Harnessing the power of topology in oxide electronics for future IT components

Jack William Harrison

Oriel College
University of Oxford

A thesis submitted for the degree of Doctor of Philosophy

Trinity 2023

Abstract

Whirling magnetic textures can have topological properties, enhancing their stability over and above that derived from energetic considerations. Such structures have been proposed as data carriers in next-generation post-Moore computing. Whilst abundantly observed in ferromagnets, their antiferromagnetic counterparts are more elusive. Interest in antiferromagnetic topological textures for device applications is growing, due to their predicted ultra-fast, deflection-free dynamics whilst being robust against external fields. In this thesis, I develop processes for imaging, nucleating and controlling topological textures in antiferromagnets, targeted towards their integration in next-generation racetrack-based oxide electronics. The prototypical canted antiferromagnet α-Fe_2O_3 is used throughout as an interesting test case, due to the family of topological textures present at room temperature that can be repeatedly nucleated via a Kibble-Zurek-like quench.

I developed analytical and micromagnetic models for topological textures in A-type antiferromagnets, focusing on the scaling of textures with relevant material parameters, allowing us to push towards the ultra-small sizes relevant for device applications. This was also used to predict the existence of the long sought-after topological antiferromagnetic skyrmions. I investigated freestanding crystalline α-Fe_2O_3 nanomembranes, a novel form of matter developed by my collaborators. One key conclusion of these experiments was that defects strongly affect the first-order Morin transition, whilst maintaining the Kibble-Zurek phenomenology observed in thin films attached to substrates. Magnetic fields cause domain repopulation in this canted AFM, but topological textures were observed to be stable in the presence of moderate field perturbations. Finally, freestanding crystal membranes can host relatively large strains compared to attached thin films or bulk crystals, which have similar lateral dimensions but the latter are drastically thicker. This was used to produce an athermal route to nucleate topological textures and tune domain populations, opening novel pathways for exploring Kibble-Zurek phenomenology in crystal membranes, as well as providing an interesting route towards device applications.

Harnessing the power of topology in oxide electronics for future IT components

Jack William Harrison
Oriel College
University of Oxford

A thesis submitted for the degree of
Doctor of Philosophy

Trinity 2023

This thesis is dedicated to my Nan, Cherry, who passed away a few months before the completion of this thesis. She always believed in me and encouraged me to follow my dreams and would have been so proud and excited to hug me after I graduate. She often jokingly told me she was looking forward to having her own doctor. She was always there for me when things were tough and she continues to inspire me to work hard. I wouldn't be where I am today without her love and support and so I dedicate this thesis in her honour.

"Look what you made me do, look what I made for you"

Linkin Park and Jay-Z, *Numb//Encore*

Acknowledgements

As is tradition, I would like to start this thesis by acknowledging the vast array of colleagues, tutors, family and friends without whom this work would not be possible. Firstly, I would like to wholeheartedly thank my supervisor, Professor Paolo Radaelli, who was absolutely integral in guiding my research towards success. From the early conception of the project through to submitting beamtime proposals, writing papers, and discussing research directions, he has been there every step of the way offering me guidance and support whilst allowing me the space to explore my own research interests. He has dedicated time to support both my physics knowledge and my career development plans, despite having a continuously packed schedule, and I am deeply grateful for all he has taught me.

Next, I want to acknowledge the contributions of several other members in our research group. Hariom Jani, originally a postdoctoral researcher in Singapore and now at Oxford, performed the vast majority of the sample growth and transfer and was invaluable in the creation of the lifted membranes so crucial to many of the experiments discussed herein. In addition to this, he has been a mentor to me throughout my PhD, offering his support and advice consistently during my projects, as well as spending many long hours conducting remote experiments with me during the COVID-19 lockdowns. Many of my experiments would have been impossible without his knowledge and support.

Jheng-Cyuan Lin (JC) is a fellow PhD student in our group and has been a good friend throughout our years working together. We have spent many long hours together filling buckets of liquid nitrogen at I06 and bouncing experimental ideas off of each other over a coffee. He was also my strong second on the holography beamtimes and that section of this thesis would have been significantly more difficult without his assistance. I wish him best of luck in the future, as he should be submitting his thesis around the same time as I have.

To mention a few others: Jiahao Chen and Jacopo Radaelli were incredibly useful contacts during the early part of the micromagnetic simulation work I undertook during the COVID-19 lockdowns and their suggestions were useful in developing my model of A-type AFM systems. Zhiyang (Paul) Zeng performed ComSol simulations of the strain profiles across membrane bends and his expertise in this area was a significant help in understanding this aspect of my strain-based STXM results. More recent additions to the team, Charlie Godfrey and Radoslaw (Radek) Kaleba, have been a pleasure to work with in the short time I've known them and have provided useful commentary and discussions on some of the later aspects of this thesis. Charlie in particular has helped me out in a couple of the later STXM beamtimes, including the final section on anisotropic strain

in membranes We both worked very long hours to perform these experiments and have this work all come together and for that I am extremely grateful.

Some other members of the physics department at Oxford also deserve recognition. Chief among these is Jason Brown, who is in charge of the cleanroom facilities in the Clarendon and performed the FIB milling integral to the mask preparation for my HERALDO experiments. His technical insight was invaluable in this process and his sharp wit and sarcasm helped lighten what was otherwise a very tricky project. In a similar vein, I would like to thank Richard Makin from the Oxford thin films facility for growing the Au masks via e-beam evaporation, which took us several attempts and quite a few long hours to iterate on the process until it was successful. The members of the Clarendon workshop also helped me to build some of the sample holders used throughout the holography mask preparation process.

As is true of any project involving substantial work at large facilities, the staff there are absolutely integral to its success. To this end, I would like to thank Francesco Maccherozzi at I06 (Diamond light source, UK), Horia Popescu and Nicolas Jaouen at SEXTANTS (SOLEIL, France), and Simone Finizio, Jorg Raabe and Tim Butcher at PolLux (PSI, Switzerland). Over and above preparing and maintaining the beamtime equipment, they have all accomodated additional requests for non-standard experiments that were incredibly useful for this research. Their training, support and advice throughout my beamtime experiments both shaped and streamlined this research project and I am eternally grateful for their help. I would like to particularly thank Simone, as we have spent a lot of time working together throughout this project and much of this work would have been impossible without his STXM expertise and continual hard work to accomodate my ever-increasing complex requests for experimental environments.

I would also like to extend my thanks to my undergraduate tutors, who taught and inspired me throughout my physics education. Special thanks should go to professors Caroline Terquem and Robin Nicholas, who both took extra time to help me with specific areas of the course I struggled with and offered me advice on a career in academia. I also acknowledge my secondary school physics teacher, Jackie Flaherty, who nurtured my love of physics and helped me prepare both for the Oxford entrance exam and subsequent interview. She also helped me secure a bursary from the Ogden trust for my undergraduate degree, who I also thank. I am, of course, appreciative of all of my teachers and tutors throughout my education, who all played their part in guiding me in my journey to this stage.

Finally, I have a long list of people from my personal life I would like to thank, but I will keep it brief. Firstly to James, Sam, and Jordan, who battled through the physics undergraduate course with me and remain very close friends. Jordan deserves special mention as my lab partner, as he kept me sane throughout many difficult experiments and helped me develop my love for novel experimental developments. I also thank Joe,

Mark, Kim, and Luke, who became close friends throughout our time together at Oxford. Additionally, I want to acknowledge my friends from earlier in my life, namely Leo, Ben, Tom, and Nathan, most of whom I remain close with and who kept me grounded throughout the years we've known each other.

From my family I want to thank my mum, my relationship with whom is summed up very nicely by this Terry Pratchett quote: "He believed in rational thinking and scientific inquiry, which was why he never won an argument with his mother, who believed in people doing what she told them, and believed it with a rock-hard certainty which dismissed all opposition." She has always loved and supported me in my ambitions, whilst ensuring that I remain kind and considerate. My dad has done so much for me over the years, including many long hours driving me to and from events that helped me develop and grow my education and career prospects, I wouldn't have got this far without him and I appreciate all he has done for me. My sister has always been there for me too and, whilst we haven't always seen eye to eye, I wouldn't trade her for anyone and I wish her all the best in her life with her new husband. My grandparents, Aunts, Uncles, Cousins, and everyone else from my family have all made my life to this point so enjoyable and full of love; I appreciate each and every one of them. The last word goes to my girlfriend of 7 years, Phoebe Hobbs. We've been through so much together, from our days as undergraduates through to buying our first flat, then spending far too much time in it during the lockdowns. She has kept me sane throughout my PhD and her hard work and dedication has repeatedly inspired me to keep pushing towards my dreams.

Abstract

Whirling magnetic textures can have topological properties, enhancing their stability over and above that derived from energetic considerations. Such structures have been proposed as data carriers in next-generation post-Moore computing. Whilst abundantly observed in ferromagnets, their antiferromagnetic counterparts are more elusive. Interest in antiferromagnetic topological textures for device applications is growing, due to their predicted ultra-fast, deflection-free dynamics whilst being robust against external fields. In this thesis, I develop processes for imaging, nucleating and controlling topological textures in antiferromagnets, targeted towards their integration in next-generation racetrack-based oxide electronics. The prototypical canted antiferromagnet α-Fe_2O_3 is used throughout as an interesting test case, due to the family of topological textures present at room temperature that can be repeatedly nucleated via a Kibble-Zurek-like quench.

I developed analytical and micromagnetic models for topological textures in A-type antiferromagnets, focusing on the scaling of textures with relevant material parameters, allowing us to push towards the ultra-small sizes relevant for device applications. This was also used to predict the existence of the long sought-after topological antiferromagnetic skyrmions. I investigated freestanding crystalline α-Fe_2O_3 nanomembranes, a novel form of matter developed by my collaborators. One key conclusion of these experiments was that defects strongly affect the first-order Morin transition, whilst maintaining the Kibble-Zurek phenomenology observed in thin films attached to substrates. Magnetic fields cause domain repopulation in this canted AFM, but topological textures were observed to be stable in the presence of moderate field perturbations. Finally, freestanding crystal membranes can host relatively large strains compared to attached thin films or bulk crystals, which have similar lateral dimensions but the latter are drastically thicker. This was used to produce an athermal route to nucleate topological textures and tune domain populations, opening novel pathways for exploring Kibble-Zurek phenomenology in crystal membranes, as well as providing an interesting route towards device applications.

Contents

List of Figures

List of Abbreviations

ADW . . . . . Antiphase domain wall

AFM . . . . . Antiferromagnet(ic)

CG . . . . . Clebsch-Gordan

DMI . . . . . Dzyaloshinskii-Moriya interaction, can be bulk (bDMI) or interfacial (iDMI)

FM . . . . . Ferromagnet(ic)

FT . . . . . Fourier transform

FWHM . . . . . Full-width at half-maximum

HERALDO . . Holography with extended reference by autocorrelation linear differential operation

HT . . . . . High temperature

IP . . . . . In-plane

KZ . . . . . Kibble-Zurek

LAO . . . . . $LaAlO_3$

LLG . . . . . Landau-Lifshitz-Gilbert

LT . . . . . Low temperature

OOP . . . . . Out-of-plane

PEEM . . . . . Photoelectron emission microscopy

PLD . . . . . Pulsed laser deposition

PMMA . . . . . Poly(methyl methacrylate)

RT . . . . . Room temperature

SAO . . . . . $Sr_3Al_2O_6$

STO . . . . . $SrTiO_3$

STXM . . . . . Scanning transmission x-ray microcopy

TTMP . . . . . Topologically trivial meron pair

XAS . . . . . X-ray absorption spectrum

XMCD . . . . . X-ray magnetic circular dichroism

XMLD . . . . . X-ray magnetic linear dichroism

"It's a dangerous business, Frodo, going out your door. You step onto the road, and if you don't keep your feet, there's no knowing where you might be swept off to." - Bilbo Baggins

J. R. R. Tolkien, *The Lord of the Rings*

1 Introduction

Contents

1.1 History of magnetic investigations of α-Fe_2O_3

Magnetic materials have been a focal point of human curiosity since our ancestors observed that certain rocks tended to attract metallic objects, or that small fragments of that rock floating in water would tend to rotate to point towards the north star (polaris) [1]. These rocks, named *magnetite* (or lodestones), were the first known ferromagnetic (FM) material and gave their name to the phenomena that would later go on to shape the course of human history. From the 19^{th} century experiments linking electric currents to magnetic fields and the subsequent development of long-range communication technology to the invention of microwaves and implementation of magnetic resonance imaging, the study of magnetism and magnetic materials have been fundamental to much of the technology that underpins modern life [1–4]. More recent techological developments such

as magnetoresistive sensors and solid state hard drives make great use of the burgeoning world of magnetism research and have enabled the technological revolution. Investigations of a wide class of magnetic materials are ongoing both at a fundamental and application-oriented level and the contributions of magnetism to technology are likely to increase even further with the continued discovery of new materials and new phenomena.

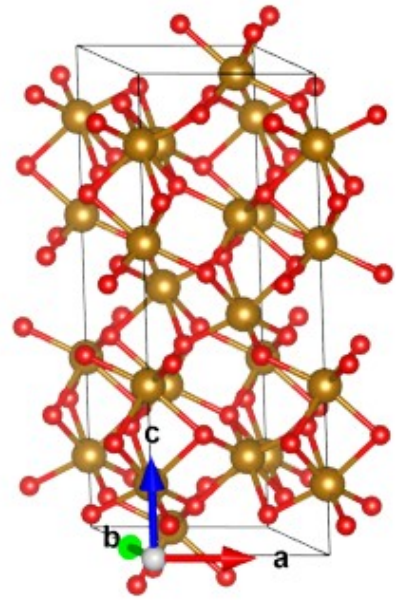

Figure 1.1: Crystal structure of α-Fe_2O_3. The brown spheres are Fe atoms and the O atoms are shown as red.

Iron-based magnetic oxide compounds (including magnetite, Fe_3O_4) have been thoroughly investigated out of practical need and pure scientific curiosity, being both abundant in nature and very stable. One such compound α-Fe_2O_3, named hematite for its blood-red colour, does not show similar magnetic properties to magnetite and, moreover, is resistant to attempts to induce a magnetisation on the scale of other iron oxides and compounds. As determined by early x-ray experiments and later refined through neutron scattering [5–7] α-Fe_2O_3 crystallises in the corundum structure with space group $R\bar{3}c$ and hexagonal lattice parameters $a = 5.04 \pm 0.01\,\text{Å}$ and $c = 13.76 \pm 0.02\,\text{Å}$ [8]. The accepted crystal structure for α-Fe_2O_3 is shown in figure 1.1 drawn using VESTA [9]. This system was identified as a prototypical canted antiferromagnet (AFM) with a high Néel temperature ($T_\text{N} = 960K$ [4, 8]) and a small magnetic moment near room temperature (RT) that disappears at lower temperatures, see figure 1.2. This disappearance coincides with a spin-reorientation transition, wherein the Néel vector of the system flips from in the a-b plane at RT to along the c-axis at lower temperatures [8, 10]. Named the Morin transition (after its discoverer), this occurs at a temperature $T_\text{M} \sim 260K$ in bulk crystals and typically lower in undoped thin films [11].

There are several different antiferromagnetic configurations that are consistent with the symmetry elements of the $R\bar{3}c$ space group of α-Fe_2O_3, hence much of the early work on the magnetic structure of this material was devoted to establishing its allowed

spin configurations. As discussed in [12], many transition metal oxides isostructural to corundum (Al_2O_3) are antiferromagnetic, with several examples such as α-Fe_2O_3 and Cr_2O_3 studied extensively with neutron diffraction and antiferromagnetic resonance in the 1980's [12–14]. This allowed their slightly different magnetic structures to be uncovered, namely the fact that the two key examples mentioned above have different magnetic space group symmetry [12, 15]. The key difference here is that α-Fe_2O_3 has a magnetic inversion centre, whereas Cr_2O_3 does not. Whilst seeming slight, this differing symmetry allows α-Fe_2O_3 to host a weak magnetic moment (discussed further below) that is absent in Cr_2O_3. Conversely, the lack of an inversion centre allows Cr_2O_3 to host a weak ferroelectric moment and exhibit the linear magnetoelectric effect, which cannot occur in α-Fe_2O_3 due to symmetry constraints.

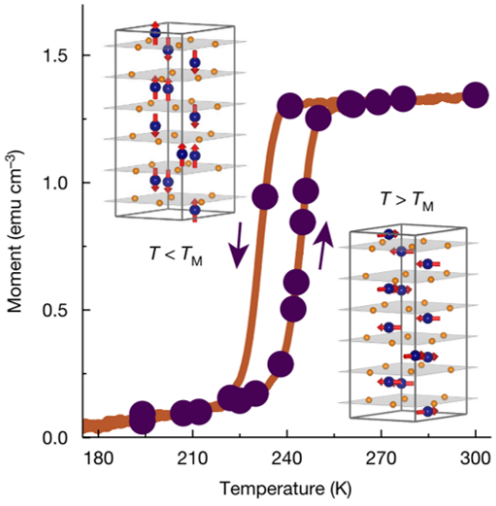

Figure 1.2: Temperature dependent magnetisation of α-Fe_2O_3 thin film on Al_2O_3 substrate with $T_M \approx 240\,K$. The magnetic structure both above and below T_M are shown as insets. Reproduced with permission from [11]

The magnetic moment present for $T > T_M$ in α-Fe_2O_3 is due to the Dzyaloshinskii-Moriya interaction (DMI) [16, 17], an asymmetric exchange coupling present in some systems. The general form of the DMI energy between a pair of spins is

$$E_{DMI} = \vec{D} \cdot \left(\vec{S_1} \times \vec{S_2} \right), \qquad (1.1)$$

where $\vec{D}$ is the DMI vector, parametrising both the strength and nature of the interaction, and $\vec{S_{1,2}}$ are the spins on two sites that are coupling via $\vec{D}$. It should be noted that $\vec{D}$, in general, could vary throughout the crystal, but its allowed orientations are constrained by symmetry [15, 17]. In α-Fe_2O_3, there is a non-zero bulk DMI (bDMI) vector $\vec{D} = D\hat{z}$. The parameter D takes different values across the various Fe-Fe bonds but has a uniform average throughout the crystal, as discussed more thoroughly in section 2.2.5. In the in-plane (IP) phase ($T > T_M$), this causes antiparallel moments in adjacent sublattices to cant towards each other (as can be seen from equation 1.1). This canting

induces a weak magnetic moment perpendicular to the local Néel vector, hence the designation of this system as a canted antiferromagnet. In the out-of plane (OOP) phase ($T < T_{\mathrm{M}}$), the cross product in the above equation ensures that the DMI interaction does not couple with the spin orientations and therefore there is no canting and no weak ferromagnetic moment. This explains the large drop in magnetic susceptibility at $T = T_{\mathrm{M}}$, which was the original signature of the Morin transition [10].

To conclude this introduction, I will discuss the origin of the Morin transition from the perspective of the various anisotropies present in α-Fe_2O_3. Firstly, the magnetic dipolar anisotropy K_{dip} is due to the long-range dipole-dipole interaction between magnetic moments in the crystal, as will be discussed further in section 3.3. This term is determined by the relative arrangements of magnetic ions and their associated moments; in this system the dipolar anisotropy favours spins lying in the a-b plane of the hexagonal structure. Additionally, there is a single-ion anisotropy K_{SI} due to the arrangements of the O^{2-} ions around the Fe^{3+} ions, which is an on-site anisotropy consistent across all atoms in a perfect system, but may be locally altered by strain or crystal defects. This term favours spins that lie along the c-axis for α-Fe_2O_3. These two anisotropy terms are roughly equal in magnitude and both have a similar temperature dependence, but have a crossover near room temperature [12] and thus the sign of the total anisotropy $K_{\mathrm{eff}} = K_{dip} + K_{SI}$ switches at this crossover point, as shown in figure 1.3. This is exactly the Morin transition and is the cause of the spin flop from the a-b plane at $T > T_{\mathrm{M}}$ to along the c-axis for $T < T_{\mathrm{M}}$. The transition point can be adjusted via chemical doping [10, 11, 13] or ion gating [18, 19] and is suppressed in undoped thin films compared to bulk systems. The origin of the transition and approaches one can take to tune this crossover will be a key part of this thesis (primarily in chapter 7).

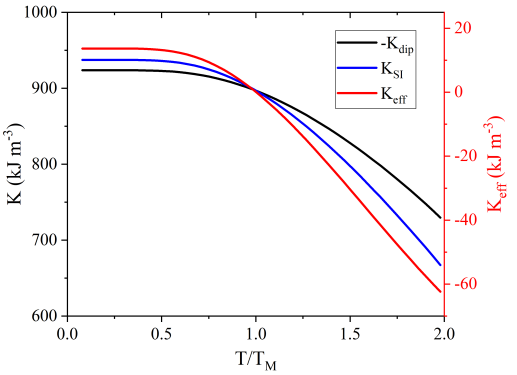

Figure 1.3: Crossover between dipolar (K_{dip}) and single-ion (K_{SI}) anisotropies as a function of reduced temperature (T/T_{M}). Also shown is the effective anisotropy ($K_{\mathrm{eff}} = K_{\mathrm{dip}} + K_{\mathrm{SI}}$), showing that the anisotropy switches sign at $T = T_{\mathrm{M}}$. Based on data presented in [18], reused with permission.

1.2 Topology and phase transitions

1.2.1 Concepts in topology

Physicists are acutely aware (thanks largely to Noether's theorem) that conservation laws and symmetries of systems are intimately related and that the presence of symmetries often lead to deep and interesting physical phenomena. In addition, spontaneously broken symmetries underpin the process of a phase transition, which has become a critical concept within condensed matter physics. Largely thanks to these developments, the somewhat esoteric mathematical field of topology became relevant to physics due to the underlying reliance on symmetry properties contained within its formalism. In general, topology is concerned with families of objects that can be smoothly deformed into each other using continuous transformations (stretching, squashing etc.); any two objects related in such a way are topologically equivalent. For example a solid sphere and a solid cube are topologically equivalent, whereas a sphere and a doughnut are not as the hole must be introduced by a discontinuous process. This can be applied not only to real-space objects, but more general N-dimensional phase spaces in order to understand the sets of objects in that space that can be connected by smooth, continuous transformations only.

T. W. B. Kibble made the connection between the topology of the ground state manifold of a system (i.e. the object comprising the set of degenerate ground states in a systems phase space) and the types of structures that can be stabilised in that system above the trivial ordered phase [20, 21]. So called topological structures result from closed loops in the ground state manifold that cannot be continuously shrunk to a point. This means there is no continuous perturbation that can remove a topological structure from a system, thereby stabilising that structure despite its non-zero energy cost above the ultimate ground state. In addition, a phase transition from a "normal" to an "ordered" phase (such as a paramagnet to a ferromagnet) that results in a change of the topology of the ground state manifold should lead to the formation of defects, trapping regions of normal phase within the ordered phase. This was originally discussed in the context of the formation of cosmic strings during the cooling of the early universe [20, 21], but was later extended by W. H. Zurek to the case of vortices in superfluid helium [22]. This lead to the general concept of the Kibble-Zurek (KZ) mechanism underpinning the

generation of topological structures in any system due to differing ground state topologies across a phase transition [23]. For second order phase transition, this mechanism also leads to a scaling law relating the density of topological textures after crossing through a phase transition to the rate at which it was traversed.

Topological structures are particularly interesting due to their inherent stability, as mentioned above. As the winding of the order parameter around such a structure is topologically distinct from the bulk ordered phase, there is no continuous transformation that can remove a topological structure. This means that in the ideal case of an infinite, perfect and continuous system they are completely thermally and temporally stable, even if they may be energetically metastable. In a real system (such as a crystal lattice), which is discrete and always contains defects, there are discontinuous mechanisms that can lead to the evaporation of a topological structure, such as annihilation at a grain boundary or collapse below the atomic scale. Nevertheless, the topological character of such structures gives them an additional level of stability over and above non-topological metastable structures as they are typically associated with a rather large energetic barrier for evaporation. This makes them particularly interesting from a practical perspective, as they typically have significantly longer lifetimes than may be predicted from a purely energetic perspective [24], and are also largely decoupled from the background ordered phase, potentially allowing them to be mobile [25–27]. Additional proposed applications of topological textures in magnetic materials will be discussed further below.

1.2.2 Classification of topological textures

Topological structures of relevance to condensed matter physics are widespread and include important classes that have been studied in great detail, such as vortex lines in superconductors, skyrmions in ferromagnets, and "cloverleaf" domains in multiferroic hexagonal manganites [23, 28–31]. In all of these cases, it is the symmetry and topology of the ground state energy landscape that allows for the formation and stabilisation of these structures, the crucial observation being that different systems with energetic ground states sharing a symmetry class should (in principle) be able to host analogous structures. To that end, topological textures are typically characterised by one of several related

numbers referred to as topological invariants. The winding number characterises the number of times the order parameter wraps the unit sphere (or N-dimensional equivalent) and is given in 3D by the integral [32–34]

$$w = \frac{1}{4\pi} \iint \hat{\psi} \cdot \left(\frac{\partial \hat{\psi}}{\partial x_1} \times \frac{\partial \hat{\psi}}{\partial x_2} \right) dx_1 dx_2. \tag{1.2}$$

Here, $\hat{\psi}$ is the normalised order parameter field (such as the magnetisation for FM textures or Néel vector for AFM textures). x_1 and x_2 are coordinates defining a closed surface surrounding the topological defect (e.g. the skyrmion). If any two structures have the same winding number then they are topologically equivalent, meaning that they can be deformed into each other by smooth, continuous transformations of the order parameter field. Typically the winding number takes integer values, corresponding to multiples of complete windings of the unit sphere; however, in certain cases, half integer values of the winding number are also allowed. This is specifically relevant for the case of (anti)merons, which will be discussed further below and are a key part of this thesis. Note that the above expression is entirely general and applies to topological structures in any system with a 3-dimensional order parameter field. In the context of real-space 2D topological magnetic structures, the winding number is often referred to as the *topological charge, Q* and, somewhat confusingly, the term "winding number" and symbol w is sometimes used to refer to a separate quantity [35], which here I will call the vorticity (following [33, 36]). This is defined as

$$Q_v = \frac{1}{2\pi} \oint_C d\phi. \tag{1.3}$$

Here, ϕ is the azimuthal component of the magnetic order parameter and the integral is taken over any closed loop C that encircles the topological defect. This integral results in an integer that corresponds to the number of complete azimuthal rotations of the order parameter completed whilst traversing the contour. Alternatively, it can be understood as the additional phase accrued by the order parameter around a closed loop surrounding the topological defect, somewhat analogous to discontinuous variations in the phase of the cooper pair wavefunction around a vortex line in a superconductor. If one also defines the polarity of the texture as $p = \pm 1$, corresponding to the orientation of the

core of the defect, then it is somewhat straightforward to see that for such structures the topological charge can be defined as $Q = pQ_v$ and that for magnetic textures spatially confined to 2D (but with 3D spin orientations) this will be identical to the definition of the winding number given in equation 1.2. A full proof of this relationship is given in appendix A.1. One can also define the helicity ξ of a topological texture to parametrise the phase offset of the magnetisation with respect to the azimuthal position, i.e. the azimuthal angle of the magnetisation can be written as $\phi' = Q_v\phi + \xi$, where ϕ is the usual azimuthal coordinate for a texture centred at the origin.

The three numbers, (Q, Q_v, ξ) give us a unique way of classifying the wide family of topological textures that can be found in magnetic systems. Note that neither the vorticity nor the helicity of the texture are topological invariants. In fact, only the topological charge Q distinguishes topologically unique textures, as any pair of textures with the same Q can be smoothly transformed into each other by a suitably chosen set of continuous rotations. Nonetheless, Q_v and ξ are still useful quantities, as these are often both experimentally accessible (whereas Q is more difficult to measure directly) and influence both the conditions for the stability and the properties of such textures under external stimuli [27, 34, 37].

1.2.3 Topological textures in antiferromagnets

I now consider the topological classification of AFM (anti)merons, the family of topological textures most relevant to this thesis, in more detail. The topological classifications for a subset of this family of textures is shown in figure 1.4, along with their designation using the (Q, Q_v, ξ) formalism discussed above. It would be remiss of me to not mention at this stage that there is some disagreement among the community as to what classifies a "meron" or an "antimeron"; specifically whether this is determined by the topological charge Q or the vorticity Q_v of the structure. Some argue that merons and antimerons should be designated by their topological charge only (i.e. $Q = +1/2$ and $Q = -1/2$ respectively) [38, 39], such that they are true antiparticles of each other and will always annihilate. Here, I adopt the convention that antiferromagnetic merons and antimerons have vorticity $Q_v = +1$ and $Q_v = -1$ respectively; however this has the side-effect

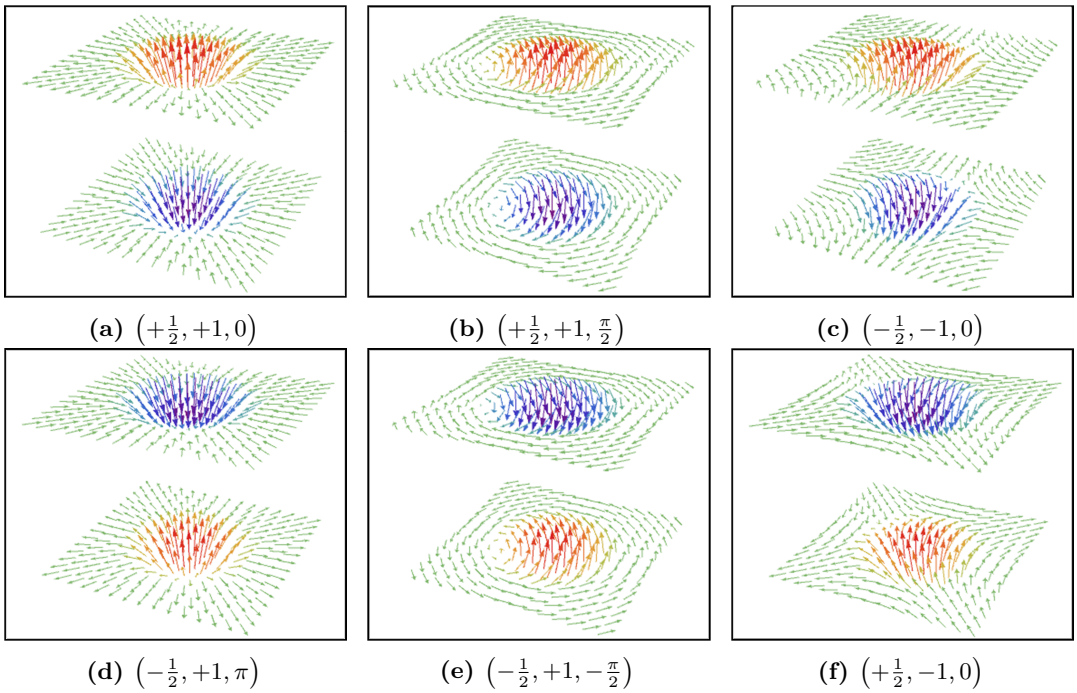

(a) $\left(+\frac{1}{2}, +1, 0\right)$ **(b)** $\left(+\frac{1}{2}, +1, \frac{\pi}{2}\right)$ **(c)** $\left(-\frac{1}{2}, -1, 0\right)$

(d) $\left(-\frac{1}{2}, +1, \pi\right)$ **(e)** $\left(-\frac{1}{2}, +1, -\frac{\pi}{2}\right)$ **(f)** $\left(+\frac{1}{2}, -1, 0\right)$

Figure 1.4: A gallery of $Q = \pm 1/2$ antiferromagnetic topological textures shown across the two sublattices labelled by their classification under the (Q, Q_v, ξ) formalism. The 3D magnetisation is shown by arrows and the colour shows the z-component with red/blue corresponding to up/down.

that core-up ($p = +1/2$) merons are topologically equivalent (i.e. have the same Q) to core-down ($p = -1/2$) antimerons, as can be seen by applying a 180° rotation about the x-axis. The reason for this choice is that, in AFMs, one cannot tell (at least, using the techniques herein) the absolute orientation of the Néel vector, but only its direction up to 180° periodicity (see chapter 4). Therefore, $p = \pm 1/2$ structures are indistinguishable; in fact, they are related by (discrete, discontinuous) time reversal symmetry or exchange of the two sublattices. It is clear, therefore, that classifying AFM topological textures by their topological charge Q is difficult through experimental data, whereas their vorticity Q_v is an accessible experimental parameter and therefore is the better choice for labelling them.

When combinations of merons and antimerons exist in close proximity a few possible composite textures can be formed. If there is a meron-antimeron pair that have the same core orientation (i.e. same polarity p), then they necessarily have opposite topological charge and therefore the total Q of the combined object is zero. Such a configuration will be referred to as a topologically trivial meron pair (TTMP). These are topologically

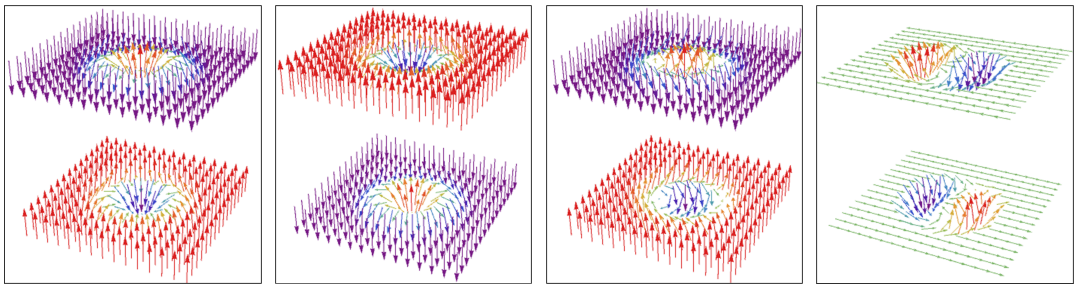

(a) $(+1,+1,0)$ **(b)** $(-1,+1,0)$ **(c)** $\left(+1,+1,\frac{\pi}{2}\right)$ **(d)** $(+1,+1,0)$

Figure 1.5: A gallery of $Q = \pm 1$ antiferromagnetic topological textures shown across the two sublattices labelled by their classification under the (Q, Q_v, ξ) formalism. The 3D magnetisation is shown by arrows and the colour shows the z-component with red/blue corresponding to up/down.

identical to the uniform AFM state and therefore are energetically unstable, but may still exist at larger separations (when the constituent particles can be considered as isolated) or for short times. When a meron-antimeron pair with opposite core orientation exist in close proximity, the compound texture has a net topological charge $Q = \pm 1$ and is called a bimeron. A bimeron is topologically equivalent to a skyrmion via a $\pi/2$ rotation about one of the IP axes and hence is an interesting quasiparticle in its own right, given the current interest in discovering antiferromagnetic skyrmions [37, 40–43]. The topological classifications for example AFM skyrmions and bimerons are shown in figure 1.5. One can also hypothesise higher-order clusters of topological textures that have $|Q| > 1$ or connected bimeron strings, but these would be expected to be less common, given the random nature of the KZ mechanism used to generate them.

1.3 Previous investigations of topological textures in α-Fe_2O_3

It was recognised (by my supervisor) that certain antiferromagnetic materials, such as α-Fe_2O_3, have the same ground state symmetry as the hexagonal manganites and therefore should be able to host magnetic analogues of the topological "cloverleaf" ferroelectric domains observed in those systems [29, 30]. Such textures were then later observed (via x-ray photoemission electron microscopy (PEEM) [44]) as flat vortices in Co capped α-Fe_2O_3 thin films [45]. Additionally, it was later demonstrated (by myself and colleagues) that in Pt-capped α-Fe_2O_3 films hosting a Morin transition one can reversibly nucleate

and destroy these textures by crossing through the phase transition, analogous to a Kibble-Zurek quench discussed above [11]. These experiments will not be discussed extensively here, but formed the basis for much of the work that is crucial to this thesis.

An additional observation we made at this stage by exploiting different polarisations of the linear x-rays was that these topological textures are not purely IP structures, but have OOP cores. This is allowed due to the relatively small energy difference between IP and OOP Néel vector orientations near T_{M}, with the core size scaling inversely with $(T - T_{\mathrm{M}})$ [11]. This allowed us to identify these textures as merons and antimerons as opposed to simple winding vortex/antivortex structures. We also identified several tightly-bound meron-antimeron pairs, which we proposed were bimerons, although definitively distinguishing these from TTMPs is not possible using x-ray magnetic dichroism directly due to the 180° ambiguity of the technique (this will be expanded on in chapter 4). Whilst the existence of these textures is interesting in its own right, both as a new class of AFM structures to study and as a new scheme for exploring Kibble-Zurek phenomena, they also have the potential to be exploited for novel spintronics devices (discussed further below).

I should point out at this stage that, whilst ours was the first concrete demonstrations of real-space topological magnetism in antiferromagnets, other examples had previously been proposed from theory and indirect measurements, and further systems have now been directly shown to host similar topological structures. Magnetic vortices and skyrmions had been predicted as the ground states of several classes of AFMs by others previously [46, 47], but no one had actually demonstrated that such textures existed. Since our initial paper, there has been a report of antiskyrmions stable in α-Fe_2O_3 below T_{M}, but the evidence is, in my opinion, rather weak [48]. As discussed in section 1.1, the related AFM Cr_2O_3 has a similar crystal structure but different magnetic structure to α-Fe_2O_3 due to the slightly different ground state symmetry, as revealed by neutron diffraction data [12]. As the system has no inversion symmetry there is no bDMI, but Cr_2O_3 can host an electric polarisation and therefore is weakly magnetoelectric. Measurements of the Hall resistivity in some Cr_2O_3|Pt bilayers at temperatures above the Néel temperature ($\sim$280 K in their samples) show an anomalous hump [49] that is often dubbed the topological Hall effect and attributed to the presence of topological objects in the system. To make an

additional comment on this case specifically, the authors argue that the presence of the anomalous hump in the Hall resistivity that appears strongly around 345 K is a signature of AFM topological spin textures in their sample. Over and above the controversial nature of attributing these anomalous features to the presence of topological textures [50, 51], no direct demonstration of the existence of these textures was made. Even more puzzling is the claim that such topological textures are present reasonably far above the Néel temperature of the system, when the system should be in the disordered paramagnetic phase. It is evident, therefore, that many authors are quick to claim to have discovered the "new thing", in this case AFM skyrmions, whilst not providing sufficient evidence to support these claims. Nonetheless, demonstrations of some topological textures in other AFM systems are starting to emerge, such as the more recent discovery that AFM CuMnAs can host vortex-antivortex strings at room temperature [52]. The Kibble-Zurek phenomenology is absent in this case as the textures are nucleated through current pulses rather than exploiting a phase transition, making it less useful as a material system to explore this aspect of fundamental physics but with a large potential for practical applications.

1.4 Spintronics and practical considerations

In the decade and a half since the initial proposal for racetrack-based platforms as a potential future for memory-in-logic computing devices [53], numerous candidate systems and materials have been proposed and trialled, with the aim of realising a commercially viable implementation of this scheme [54, 55]. Among these, skyrmions have emerged as important candidates for data "bits", as their topological nature makes them energetically stable, they can be nucleated by current pulses, and they can be moved by spin torques [28, 33, 36]. Most of the earlier work focused on skyrmion-hosting ferromagnets, but it quickly became apparent that these suffer from some fundamental limitations. FM skyrmions typically require an applied magnetic field to stabilise them, but are wiped out by larger field values meaning that they usually appear in only a relatively narrow field window. In addition, ferromagnetic domain motion driven by spin torques is usually too slow to produce competitively-fast devices (up to $\approx 100\,\mathrm{ms}^{-1}$ [28, 33, 55]). Finally, FM skyrmions driven by an applied current experience a transverse deflection known as the

skyrmion Hall effect, often leading to the annihilation of skyrmions at the boundaries of racetrack structures, further limiting their potential applications [27, 56].

In contrast, AFMs have significant advantages over FM systems for spintronics applications [25, 40, 41, 57, 58], largely stemming from the negligible stray fields that result from the zero net magnetisation present in AFM systems. Firstly, AFMs typically have a very weak coupling to external magnetic fields, therefore making them more robust against perturbation by magnetic fields compared to FM systems. Additionally, AFM systems host ultra-fast dynamics, with predicted skyrmion velocities $> 1\,\mathrm{kms}^{-1}$ [57], making them more viable for manipulations on the timescales needed for high-throughput spintronics devices. Due to the compensated sublattices, AFM skyrmions are predicted to undergo deflection-free motion with no skyrmion Hall effect, therefore making them desirable for racetrack-based devices [40, 43]. α-Fe_2O_3 is particularly promising from an applications perspective, as it exhibits ultra-low Gilbert damping and has exceptionally-long and tunable spin diffusion, shows a sizeable spin-Hall magnetoresistance and its AFM domain configurations can potentially be switched using pulsed currents through heavy-metal overlayers [48, 59–64]. Recently, there has been progress in stabilising skyrmions in synthetic AFMs, which are comprised of two ferromagnetic layers coupled through the RKKY interaction so that the two layers are antiparallel [65, 66]. Whilst these systems have some of the advantages of AFMs, namely the absence of the skyrmion Hall effect, they still do not host the ultra-fast dynamics and robustness to external fields that are present in real AFMs. Compensated ferrimagnets are also being investigated, but come with their own drawbacks, such as thermal dependence near the compensation temperature [67, 68].

There are three key components that need to be designed and optimised for racetrack-based spintronics applications. Firstly, there is the nature of the data "bit" itself, which should be ultra-small ($<10\,\mathrm{nm}$) in order to reach high density data storage necessary to compete with traditional CMOS computing [53]. This has been the motivation for topological magnetic structures in a racetrack architecture to be a focal point of research [28]. Secondly, one needs a method to read and write such topological structures using reliable approaches. As antiferromagnets are relatively immune to magnetic fields and similar perturbations, a commonly described approach is to couple the antiferromagnet

to a ferromagnetic overlayer, which can more easily be switched. A similar method has been exploited for many years in magnetoresistive random access memory (MRAM), where the AFM is used as a pinning layer and the magnetic state of a ferromagnet is read out using one of several different probes [69, 70]. One could also envision using electrical currents directly to write or read the antiferromagnet. This could be done either via spin transfer torques for a conducting AFM or spin orbit torques by interfacing the AFM with a conductive heavy metal overlayer [71–73]. Finally, in order to move topological structures in an antiferromagnet, one needs to be able to alter them with applied electrical current (using one of the two methods above). They must move reliably and without deflection, requiring them to be homochiral [25, 43], and have high enough speeds for realistic data acquisition times [26, 57].

In order to move towards racetrack-based AFM spintronic devices for α-Fe_2O_3, there are a few major outstanding hurdles that need to be overcome before the different aspects discussed above can even begin to be optimised. Firstly, one needs a way to reliably nucleate topological textures in the system. Secondly, those textures must be mobile and able to be moved reproducibly by an external stimulus, ideally an applied current. As discussed above, predictable motion of all topological textures in the system under spin torque perturbation requires that the topological textures are all homochiral, even for AFMs [43]. The system must also be thermally stable within a wide range of temperatures around RT and robust against disruption by external magnetic fields. In α-Fe_2O_3, we already have a way to reliably nucleate topological textures via a KZ quench through the Morin transition, however for this to be scaleable towards device applications we must establish an athermal route to engineer this process. We know the system is both stable at room temperature, as T_M can be adjusted to the desired value via chemical doping[10, 13], and robust in the presence of external fields to some degree [11], but the exact behaviour of the system under applied field is not well understood. As α-Fe_2O_3 is an insulator, directly switching its domain structure with electrical current is difficult; however spin torque injection through a heavy-metal overlayer is a potential route towards electrical control of this system [63, 64]. Finally, α-Fe_2O_3 can currently only be grown on symmetry-matched crystalline substrates and not on the types of materials required for

simple integration into computing systems (namely Si), making scalable manufacturing difficult to envision without progress into novel growth schemes.

1.5 Outline of thesis

This thesis will largely be devoted to developments in α-Fe_2O_3 towards spintronics applications, addressing some of the key outstanding issues mentioned at the end of the last section. There will also be discussions about how α-Fe_2O_3 can be used as a test bed for exploring fundamental physics such as the KZ process for a 1^{st} order transition and general properties of magnetic topological structures. In chapter 2, I will discuss the theoretical underpinning of much of this thesis, namely the key energy terms relevant to magnetic interactions in this system, my analytical models of topological textures, an analysis of x-ray magnetic dichroism effects, and the theoretical basis for the holographic technique to be explored later. Next, in chapter 3, I will present my micromagnetic model of A-type AFMs and apply this to the stabilisation of topological textures in α-Fe_2O_3. This, along with my analytical models, will allow me to discuss the energetic scaling of topological textures, the advantages of homochirality towards reliable spin torque induced motion of topological textures, and requirements for the stability of both bimerons and skyrmions. In chapter 4, I will discuss the different synchrotron-based techniques used to produce images of the magnetic state of α-Fe_2O_3 samples used in later chapters, as well as the development of lifted membrane samples critical to allowing these techniques to function. Chapter 5 serves as the verification that these lifted membranes have similar KZ phenomenology to attached films and can host topological textures, despite higher defect densities, as well as exploring how different growth templates affect the magnetic properties of these membranes. In chapter 6, our novel holographic technique for imaging AFM membranes is employed to explore the effects of in-situ magnetic fields on AFM domain configurations. I demonstrate that the weak ferromagnetic moment couples to the external field, leading to some domain reorientation; however the bulk of the structure is robust up to 800 mT. Finally, chapter 7 is dedicated to exploring strain-induced effect in α-Fe_2O_3 membranes. This will provide an athermal method to nucleate topological textures and to tune the populations of the otherwise degenerate trigonal domains, as well as an additional

way to tune T_{M} post-growth. I will also discuss future interesting routes of study based on the inherent flexibility of AFM crystal membranes that are hinted at by the observation of bends and folds throughout our membranes and the large inherent strains therein.

It does not do to leave a live dragon out of your calculations, if you live near him.

— J. R. R. Tolkien, *The Hobbit*

2 Theory

Contents

2.1 Introduction

In this chapter, I will present the bulk of the theoretical analysis important to this thesis. To start, in section 2.2 I discuss the origin of the different energy terms involved in the micromagnetic and analytical models of antiferromagnets studied throughout and particularly how the micromagnetic criterion underpins these models. Then, in section2.3, I present a set of analytical calculations for the energies of different topological textures in A-type antiferromagnets, with the aim of understanding the size-scaling of these textures as a function of the relevant material parameters. These will be used to

benchmark the micromagnetic models developed in chapter 3 and to understand how to engineer ultra-small textures as required for spintronics applications. Section 2.4 contains a mathematical proof of resonant magnetic x-ray dichroism, which is crucial to most of the imaging techniques utilised in this thesis. Finally, in section 2.5 I describe the theoretical underpinning of holographic imaging techniques, namely HERALDO, which is one of the key synchrotron-based X-ray techniques used throughout this work. This serves both as a rigorous introduction to the underlying principles of holographic imaging as well as to demonstrate the key methodologies, requirements and drawbacks of this technique, which will be discussed further in section 4.3.2.

2.2 Micromagnetic energy terms

Here, I will present the key energy terms relevant for micromagnetic and analytical models of magnetic materials that forms a core part of a number of discussions throughout this thesis. The presentation here will largely follow the seminal book on micromagnetic theory by Amikam [74], but with additional observations that are particularly relevant to this thesis. For simplicity, the presentation in this section will focus on the FM case and the link to AFM materials, which comes from simply replacing the magnetisation with the sublattice magnetisation throughout, will be discussed more clearly in chapter 3.

2.2.1 Exchange energy

In order to derive the micromagnetic form of the exchange interaction, start from the standard form of the Heisenberg Hamiltonian for the interaction between neighbouring spins

$$\mathcal{H}_{ex} = \sum_{\langle i,j \rangle} -J_{i,j} \vec{S}_i \cdot \vec{S}_j. \tag{2.1}$$

The sum is taken to run over all pairs of neighbouring spins, avoiding double-counting; it should be noted that some authors include a factor 1/2 and allow the double-counting of the pairs. This can also be extended to include higher-order exchange interactions (e.g. between next-nearest-neighbours), but this is not usually needed in most calculations. $J_{i,j} > 0$ gives a ferromagnetic coupling between neighbouring spins, whereas $J_{i,j} < 0$ corresponds to antiferromagnetic coupling.

In the micromagnetic regime, the lengthscale of magnetic variations is considered to be much larger than the separation between adjacent atoms, meaning that one can approximate the discrete magnetic moment distribution as a continuous magnetisation field; this is the micromagnetic criterion. Treating the spins semi-classically, one can write $\langle \vec{S}_i \cdot \vec{S}_j \rangle = S^2 \cos(\phi_{i,j}) \approx S^2(1 - (1/2)\phi_{i,j}^2)$. The first term represents an overall global energy offset, which can be removed by redefining the zero of energy. By definition, if the micromagnetic criterion is applicable, then the angle between adjacent spins $\phi_{i,j}$ is small, which allows one to Taylor expand the cosine function above. Additionally, for small angles the cosine rule can be used to approximate the angle between local magnetisation vectors as $|\phi_{i,j}| \approx |\hat{m}_i - \hat{m}_j|$, where $\hat{m}_i$ is the local magnetisation unit vector at position i. The first-order expansion of the unit magnetisation in the continuous field approximation is $|\hat{m}_i - \hat{m}_j| \approx |(\vec{r}_{i,j} \cdot \vec{\boldsymbol{\nabla}})\hat{m}|$, where $\vec{r}_{i,j}$ is the position vector pointing from point i to point j. The resulting exchange energy is

$$E_{ex} = \frac{1}{2} J S^2 \sum_i \sum_{\vec{r}_{i,j}} \left[(\vec{r}_{i,j} \cdot \vec{\boldsymbol{\nabla}}) \hat{m}_i \right]^2 \tag{2.2}$$

The sum over the set of nearest-neighbour vectors $\vec{r}_{i,j}$ results in a numerical factor that depends on the symmetry of the crystal structure, but is consistent across all atoms in a perfect crystal. Next, convert the sum over the atoms i into an integral over the magnetic body; this will be a valid approximation if the system is in the micromagnetic regime. This gives the general form for the exchange energy

$$E_{ex} = \iiint A \left[(\vec{\boldsymbol{\nabla}} m_x)^2 + (\vec{\boldsymbol{\nabla}} m_y)^2 + (\vec{\boldsymbol{\nabla}} m_z)^2 \right] dV. \tag{2.3}$$

The exchange constant is

$$A = \sum_i \frac{J_i S^2}{2 a_i}, \tag{2.4}$$

where the sum runs over the nearest neighbours of a given atom. Both the exchange coefficients J_i and nearest-neighbour interatomic distances a_i can be determined from neutron diffraction and (anti)ferromagnetic resonance measurements [7, 12]. Equation 2.3 is the standard form of the exchange interaction as used in micromagnetic and analytical studies throughout this thesis. I note briefly that the exchange parameter A given assumes

that the system is isotropic, usually applicable for higher symmetry crystals where the magnetic modulation along each axis will be similar. For many systems, such as α-Fe_2O_3, there are different exchange parameters for different crystal axes. For example, the c-axis coupling in α-Fe_2O_3 is antiferromagnetic ($A_{OOP} < 0$) whereas the exchange parameter in the $a-b$ plane is ferromagnetic ($A_{IP} > 0$). This distinction will be crucial for the micromagnetic model for A-type AFMs presented in chapter 3.

2.2.2 Anisotropy energy

Many magnetic energy terms are fundamentally spherically symmetric, such as the exchange energy discussed above, such that no magnetisation direction is inherently favoured over any other. Any anisotropies in the exchange energy result from an explicit lowering of the symmetry by the crystal structure. Anisotropy energy terms definitionally break this spherical symmetry, causing magnetic moments to preferentially align along a given direction. Here, I will describe the two key types of anisotropy relevant to α-Fe_2O_3, namely uniaxial anisotropy and triaxial basal-plane anisotropy [12, 13, 75].

Uniaxial anisotropies preferentially favour the alignment of magnetic moments either along or in a plane perpendicular to a given axis, depending on the sign of the associated anisotropy parameter. They have their origins in a number of phenomena; those relevant to this work are single-ion and dipolar contributions to the anisotropy (see section 1.1). A general uniaxial anisotropy energy can be written in the form

$$E_{An} = \iiint -K\,(\hat{u}\cdot\hat{m})^2\; d^3r, \tag{2.5}$$

where K is the uniaxial anisotropy constant and $\hat{u}$ is the anisotropy axis. $K > 0$ corresponds to an easy-axis, preferentially aligning spins along $\hat{u}$, whereas $K < 0$ leads to an easy-plane anisotropy perpendicular to $\hat{u}$. The dot product between the unit magnetisation and the anisotropy axis is squared because there is no energy difference between moments aligning or antialigning with this axis. As with the exchange energy, this form is valid provided the micromagnetic criteria applies, otherwise one has to resort to a direct sum over all atoms in the system. As the anisotropy energy involves no interatomic terms, i.e. it affects each magnetic moment in the system individually, no

approximations other than converting the sum to an integral are made in the above equation and therefore it is extremely general.

The 3-fold basal-plane anisotropy in α-Fe_2O_3 is several orders of magnitude weaker than the uniaxial anisotropy, so it can often be neglected in analytic or micromagnetic models of the system. Nevertheless, the associated energy term can be expressed as [8]

$$E_{An} = \iiint -K_{bp} \cos(6\phi) \sin^6(\theta)\, d^3r, \tag{2.6}$$

where $K_{bp} > 0$ is the basal-plane anisotropy constant, θ is a polar angle taken relative to the normal of the basal plane (i.e. the c-axis) and ϕ is the angle between the local magnetisation vector and any one of the three easy-axes, which will be related to one of the three-fold symmetry axes in a system where such an anisotropy is present. The case $K_{bp} < 0$ can be ignored as this would just correspond to swapping the easy/hard axes in the basal plane, which would be exactly the same as the $K_{bp} > 0$ case but with the angle ϕ globally rotated by 30°. As with the uniaxial anisotropy, this is a purely on-site energy and so, provided the micromagnetic criterion applies, this expression is completely general.

2.2.3 Magnetostatic energy

One of the most important magnetic energy terms, particularly in FM materials but also relevant to AFM systems, is the magnetostatic self-energy. This energy comes from the long-range dipolar interaction between all of the magnetic moments in a material. This term is often very difficult to calculate analytically and is the most time-consuming step in numerical techniques due to the fact it contains a sum that runs over all the atoms in the crystal twice. This energy term is incredibly important for understanding a wide range of magnetic phenomena, particularly as it is the underlying mechanism causing magnetic materials to tend to fracture into domains rather than maintain a monodomain state. The general form for the magnetostatic self-energy is

$$E_{Dip} = -\frac{1}{2} \sum_i \vec{\mu}_i \cdot \vec{h}_i, \tag{2.7}$$

where the factor 1/2 is introduced to account for the fact that the sum counts the interaction between each dipole pair twice. $\vec{h}_i$ is the field at point i generated by all of the *other* dipoles in the system and $\vec{\mu}_i$ is the magnetic moment at site i. In order to

make progress calculating this energy, consider a sphere of radius R, much larger than the interatomic spacing of the system but much smaller than the lengthscale of magnetic variations (referred to as a *physically small sphere*), centred on lattice point i. This is similar to the micromagnetic criterion and so mirrors the approximations involved in calculations of the exchange and anisotropy energy terms. This then means that one can treat all of the dipoles outside of this sphere as a continuum for calculating their field contribution at the centre of the sphere. Hence, the dipolar energy at point i can be found by calculating the energy due to a continuous field everywhere, subtracting off the contribution from a continuous field in a sphere of radius R about that point and adding on the contribution from the discrete lattice within this sphere. This subdivision makes sense in practise, as it is clear that the discrete nature of the system is important for the short-range part of the dipolar field, but far too complicated to allow this calculation to occur over all space.

The first of these terms can be calculated by solving Maxwell's equations in the material given the appropriate boundary condition and will be labelled $\vec{H}'$. The second term is approximately given by the demagnetisation field within a uniformly magnetised sphere $(-4\pi/3)\vec{m}$, provided the radius R has been chosen such that the magnetisation is roughly constant within the sphere (part of the "physically small" requirement). The final term will be denoted $\vec{h}'_i$ for now. Hence, the field at lattice point i is

$$\vec{h}_i = \vec{H}' + \frac{4\pi}{3}\vec{m} + \vec{h}'_i. \tag{2.8}$$

The last term of the above equation is generally the most difficult to calculate, as it is a lattice sum over the fields due to dipoles

$$\vec{h}'_i = \sum_{|\vec{r}_{ij}|<R} \left[-\frac{\vec{\mu}_j}{|\vec{r}_{ij}|^3} + \frac{3(\vec{\mu}_j \cdot \vec{r}_{ij})\vec{r}_{ij}}{|\vec{r}_{ij}|^5} \right], \tag{2.9}$$

where $\vec{r}_{ij}$ is the position vector pointing from lattice point i to point j. For a physically small sphere, $\vec{\mu}_j$ is a constant that is independent of j. One can then calculate, for example, the x-component of the field in carteesian coordinates

$$\vec{h}'_{i,x} = \sum_{|\vec{r}_{ij}|<R} \left[-\frac{\mu_x}{|r_{ij}|^3} + \frac{3x_{ij}(\mu_x x_{ij} + \mu_y y_{ij} + \mu_z z_{ij})}{|r_{ij}|^5} \right], \tag{2.10}$$

with the y- and z-components having a similar form. From the above, it can be seen that for each component of $\vec{h}'_i$ one can write the expression as a sum of components of $\vec{\mu}$ multiplied by a sum over lattice vectors (which will always just give a real number), i.e. $\vec{h}'_{i,x} = a\mu_x + b\mu_y + c\mu_z$. Hence, $\vec{h}'_i$ can be expressed as a linear function of the magnetisation $\vec{m}$, namely

$$\vec{h}'_i = \mathbf{\Lambda} \cdot \vec{m}, \tag{2.11}$$

where $\mathbf{\Lambda}$ is a matrix of real numbers that depends only on the crystal symmetry and lattice parameters.

Returning to equation 2.7, taking the continuum limit (as is appropriate given the considerations of our physically small sphere) and using the expansion of the various terms in equation 2.8 gives

$$E_{Dip} = -\frac{1}{2} \iiint \vec{m} \cdot \left(\vec{H}' + \frac{4\pi}{3}\vec{m} + \mathbf{\Lambda} \cdot \vec{m} \right) d^3r. \tag{2.12}$$

The central term is proportional to $\vec{m} \cdot \vec{m}$, which is a constant that depends only on temperature and so can be removed by simply redefining the zero of energy, particularly as we typically only care about minimising the total energy at a fixed temperature. One can also argue that, provided the system is far enough from the paramagnetic phase transition ($\approx 920\,\mathrm{K}$ for α-Fe_2O_3 [8]), $|\vec{m}|$ should be roughly constant and so this term will also be temperature independent and can be safely ignored. The last term $\vec{m} \cdot \mathbf{\Lambda} \cdot \vec{m}$ is an energy density that has the same form as a general anisotropy energy density. As this term comes from the short-range contribution to the dipolar field, it is actually the origin of a large component of the anisotropy in most systems (called a dipolar anisotropy) and so is often ignored in calculating the magnetostatic energy term and included in the anisotropy calculations instead. This is in fact the origin of the dipolar anisotropy term K_{dip} discussed in section 1.1 as one of the two anisotropy energy terms involved in the Morin transition in α-Fe_2O_3. We then have finally that the magnetostatic energy contribution to the total energy is

$$E_{Dip} = -\frac{1}{2} \iiint \vec{m} \cdot \vec{H}' \, d^3r \tag{2.13}$$

A few caveats should be noted here. Firstly, this derivation requires that the entirety of the physically small sphere is contained wholly within the material. This is reasonable

everywhere other than near the surfaces of the material, where the additional energy contributions can be calculated using a surface charge method and the largest contribution of which is an additional surface anisotropy, usually preferentially stabilising magnetic domains perpendicular to the surface. Secondly, equation 2.13 is inherently non-local due to the $\vec{H}'$ term, which has to be evaluated by another volume integral; this effectively means one has to integrate twice over the same volume. This resulting six-fold integration is the main reason that the magnetostatic energy is often the most difficult term to handle analytically and is the most time-consuming term to calculate using computational approaches such as micromagnetics.

2.2.4 Interfacial Dzyaloshinskii-Moriya energy

As originally discussed in section 1.1, the Dzyaloshinskii-Moriya interaction (DMI) is an antisymmetric exchange-type interaction that often favours magnetic structures with a fixed chirality [76, 77]. The general atomic description of the DMI energy is ([15–17])

$$E_{DMI} = \sum_{\langle i,j \rangle} \vec{d}_{i,j} \cdot \left(\vec{S}_i \times \vec{S}_j \right), \tag{2.14}$$

where $\vec{d}_{i,j}$ is the DM vector between the atoms at sites i and j and the summation runs over all nearest neighbours. The orientation of $\vec{d}_{i,j}$ depends on the crystal structure of the system, with the Moriya rules describing the allowed orientations given the symmetries involved [15, 17]. For the important case of an ultra-thin film, the symmetry of the crystal itself is less relevant and a DMI can be induced by the breaking of the crystal symmetries at the interface, specifically the inversion symmetry. When combined with a material with large spin-orbit coupling in the adjacent layer (typically a heavy metal), this symmetry breaking leads to an interfacial Dzyaloshinskii-Moriya interaction (iDMI) [78, 79]. In this case, the DMI vector is

$$\vec{d}_{i,j} = d\hat{u}_{i,j} \times \hat{z}, \tag{2.15}$$

where $\hat{u}_{i,j}$ is the unit vector between adjacent atomic sites and the film interface is considered to be perpendicular to the $\hat{z}$ axis. The constant d parametrises the strength of the interaction and is strongly dependent on the growth conditions and materials involved

in the heterostructure [78–80]. Taking the usual micromagnetic approximations discussed above allows one to treat the iDMI in a continuous form provided the micromagnetic criterion is valid. Additionally, considering the film to be much thinner than the associated magnetic exchange length along the $\hat{z}$-axis, such that all variations along this axis can be neglected, means that the iDMI can be modelled as a uniform average value throughout the film. Given the magnetisation direction $\hat{m}(\vec{r})$ at position $\vec{r}$, the continuous form of the iDMI energy is [76]

$$E_{iDMI} = \iint Dt \left[m_x \frac{\partial m_z}{\partial x} - m_z \frac{\partial m_x}{\partial x} + m_y \frac{\partial m_z}{\partial y} - m_z \frac{\partial m_y}{\partial y} \right] d^2r, \tag{2.16}$$

where D is the effective DMI constant with units J/m^2, whose relation to the constant d in equation 2.15 depends on the crystal symmetry, film thickness (t) and lattice parameters. It is assumed that D is constant across the surface of the sample, but in reality may have some spatial dependence (e.g. due to defects/grains) and will also have some depth-dependence away from the surface of the film. Unlike most of the other energy terms discussed above, the iDMI energy preferentially stabilises chiral domain structures, i.e. with a specific helicity parameter ξ as introduced in section 1.2; the favoured chirality is determined by the sign of D. This term is therefore critical to stabilise chiral magnetic textures such as skyrmions in materials without an inherent DMI [28, 37, 76] and will underpin much of the discussion in chapter 3.

2.2.5 Bulk Dzyaloshinskii-Moriya energy

There is an additional form of bulk DMI (bDMI) present in α-Fe_2O_3 that leads to a canted moment in the IP phase and is the origin of the well-known weak ferromagnetic moment found above the Morin transition in this system [8, 10, 81]. This is a homogeneous form of DMI with $\vec{d}_{i,j} = d\hat{z}$ which, given equation 2.14, favours an IP canting of magnetic moments in the IP phase ($T > T_{\mathrm{M}}$) and has no effect on magnetic moments in the OOP phase ($T < T_{\mathrm{M}}$).

To elucidate this point further, I present here my calculations for the bulk DMI in α-Fe_2O_3, similar to those performed for the symmetric exchange interaction discussed above. Each Fe^{3+} ion has 13 nearest-neighbours (see figure 2.1), 3 of which sit in the same basal plane and belong to the same AFM sublattice, whereas the other 10 sit in adjacent

planes and belong to the other sublattice. I will consider the bulk DMI interaction of the central atom with each of these two groups separately. The magnetic moments will assumed to be IP throughout here, as any OOP component of the moment on any site will only serve to reduce the interaction energy, due to the fact the DMI vector is parallel to $\hat{z}$.

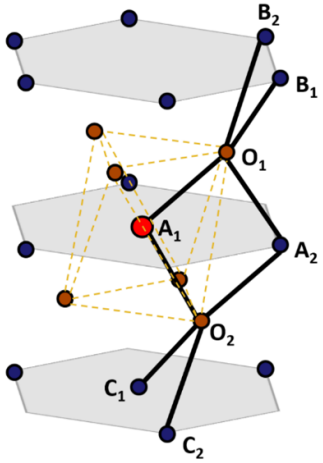

Figure 2.1: Diagram showing the 13 nearest-neighbours (blue spheres) of the central Fe atom (red sphere) in α-Fe_2O_3. The brown spheres are the O^{2-} ions arranged in an octahedron around each Fe^{3+} ion. The different interactions and associated exchange constants are given in [4, 14]. Reproduced from [11] with permission.

Firstly, for adjacent spins belonging to the same sublattice, I assume the system is in the micromagnetic regime, such that the magnetisation direction $\hat{m}$ of each atom varies only slightly across the unit cell. In this limit $\vec{S}_i \approx \vec{S}_j \Rightarrow \vec{S}_i \times \vec{S}_j \approx |S|^2 \sin(\theta_{ij})\hat{z}$, where θ_{ij} is the angle between the semi-classical spins on the two sites. Using the first-order expansion of the angle $\theta_{i,j} \approx |\hat{m}_i - \hat{m}_j|$ results in

$$E_{bDMI}^{IP} = \sum_i \sum_{\vec{r}_{i,j}} D|S|^2 \left(\vec{r}_{i,j} \cdot \vec{\boldsymbol{\nabla}}\right) \hat{m}_i \cdot \hat{z}. \quad (2.17)$$

The three relative position vectors of the nearest neighbours for a given Fe^{3+} ion are $(1,0,0), (-1/2, \sqrt{3}/2, 0)$ and $(-1/2, -\sqrt{3}/2, 0)$ in units of the IP nearest-neighbour distance. It can be easily seen that, when summing over these vectors, the $\vec{r}_{i,j} \cdot \vec{\boldsymbol{\nabla}}$ term cancels out for any given $\hat{m}_i$. Therefore, the net contribution from the IP neighbours of each atom to the bulk DMI is identically zero due to the symmetry of the crystal structure.

Secondly, for spins belonging to different sublattices, I assume that any canting angle is small (as is true for α-Fe_2O_3 and similar systems) such that adjacent spins on different sublattices are effectively antiparallel. Hence $\vec{S}_i \times \vec{S}_j \approx (|S|^2 \sin 2\phi)\, \hat{z}$, where ϕ is the canting angle of each sublattice. It can be shown that any spatial modulation of the structure (so that adjacent sublattices are close to but not exactly antiparallel) does not contribute to the bulk DMI in the thin film limit (provided $\partial\hat{m}/\partial z = 0$), although this is rather tedious and so is not presented here. See appendix A, section A.2.1 for further details if interested. There are 10 different atoms, which can be split into 3 sets

of atoms related by symmetry [8, 82], each potentially contributing different amounts of DMI energy. Therefore, I introduce 3 DMI constants D_1, D_3 and D_4 (in order to be consistent with the labelling of the exchange coefficients J_{1-4} in the literature [4, 14]). Hence, the bDMI energy is

$$E_{bDMI}^{OOP} = \sum_i (D_1 + 3D_3 + 6D_4)|S|^2 \sin 2\phi = \sum_i D_{eff}|S|^2 \sin 2\phi. \tag{2.18}$$

In order to calculate the canting angle, one must compare this energy to any terms that prefer to keep the spins anti-aligned, namely the AFM exchange between the two sublattices. This is well-known and is of the form

$$E_{ex}^{AFM} = \sum_i (J_1 + 3J_3 + 6J_4)|S|^2 \cos 2\phi = \sum_i J_{eff}|S|^2 \cos 2\phi. \tag{2.19}$$

Minimising the sum of these two energy terms allows us to calculate the canting angle, giving $\tan 2\phi = D_{eff}/J_{eff}$. Using the approximately known values of the various exchange constants and the average bDMI constant, I get a canting angle in the range 1-3 mrad (depending on the exact values used), which is consistent with the accepted experimental value of 1.1 mrad [4, 8, 14].

2.3 Analytical studies of topological textures

The analysis in this section follows the presentation in my paper on homochiral topological textures in A-type AFMs [37], but here I will provide a more thorough derivation of the equations therein. To create an analytical model of topological textures I considered the exchange, uniaxial anisotropy and iDMI energies of certain topological magnetic configurations and minimised the total energy to determine the scaling parameters of such textures. In polar coordinates, the linear ansatz (used throughout) for the unit magnetisation vector $\hat{m} = (\sin\theta\cos(\phi+\xi), \pm\sin\theta\sin(\phi+\xi), \cos\theta)$ is

$$\theta(r) = \begin{cases} \frac{\pi r}{2R} & \text{for r} \leq \text{R} \\ \frac{\pi}{2} & \text{for r} > \text{R} \end{cases} \tag{2.20}$$

where the + (−) sign in the y-component corresponds to a meron (antimeron) and R is the '(anti)meron radius', representing the typical size of the texture. The angle $\phi = \arctan(y/x)$ is the typical in-plane azimuthal angle, whereas ξ is an additional phase

angle that determines the overall chirality and was introduced under the name "helicity" in section 1.2. This was chosen as it is one of the simplest ansatz that gives the correct behaviour of the core polarisation at short and large distances, whilst crucially allowing the resulting integrals to be analytically solvable. I comment at this point that the exact functional form of the core should only affect the eventual texture scaling up to some small numerical factors, but will discuss this further in section 3.4). The dipolar energy will only be considered as a contribution to the anisotropy, so energy terms of the form in equation 2.13 will not appear explicitly in the analytical calculations below. This will be justified further in section 3.3. As all the calculations herein will be for the above-Morin state with an easy-plane anisotropy ($K_{\text{eff}} < 0$), I will drop the $-$ sign in equation 2.5 above and the absolute value $|K_{\text{eff}}| = K$ will be used throughout.

2.3.1 Analytical meron

I start by studying a linear meron, which is an extension of a calculation done in our group previously [11, 83], but with an iDMI term now included. As such, I will quote the result of the exchange and anisotropy energy calculations here, but will calculate the iDMI energy in full. This is also similar to earlier calculations of flat vortices in nanomagnets [84, 85], but with different energetic scaling due to the presence of the OOP core. The exchange and anisotropy calculation is almost identical to the case for the antimeron, which will be presented in full in section 2.3.2 to avoid unnecessary duplication. One of the key results of this calculation is that the exchange and anisotropy energy terms are independent of any phase angle ξ. This is not the case for the iDMI energy which, as we shall see, contains a term that explicitly depends on ξ. The derivatives required to apply equation 2.16 are:

$$\begin{aligned}
\frac{\partial m_x}{\partial x} &= \cos\theta\cos(\phi+\xi)\frac{\partial\theta}{\partial x} - \sin\theta\sin(\phi+\xi)\frac{\partial\phi}{\partial x} \\
\frac{\partial m_y}{\partial y} &= \cos\theta\sin(\phi+\xi)\frac{\partial\theta}{\partial y} + \sin\theta\cos(\phi+\xi)\frac{\partial\phi}{\partial y} \\
\frac{\partial m_z}{\partial x} &= -\sin\theta\frac{\partial\theta}{\partial x} \\
\frac{\partial m_z}{\partial y} &= -\sin\theta\frac{\partial\theta}{\partial y} \\
\frac{\partial\theta}{\partial x} &= \frac{\partial\theta}{\partial r}\frac{\partial r}{\partial x} = \frac{\pi}{2R}\cos\phi \\
\frac{\partial\theta}{\partial y} &= \frac{\partial\theta}{\partial r}\frac{\partial r}{\partial y} = \frac{\pi}{2R}\sin\phi \\
\frac{\partial\phi}{\partial x} &= -\frac{1}{r}\sin\phi \\
\frac{\partial\phi}{\partial y} &= \frac{1}{r}\cos\phi
\end{aligned} \tag{2.21}$$

Any terms involving $\partial\theta/\partial r$ above are valid only for $r \leq R$ and are zero for $r > R$. After substitution of the expressions above into equation 2.16, conversion of the surface element into cylindrical coordinates using $d^2r = dxdy = rdrd\phi$ and employing some trigonometric manipulations, the resulting integral is

$$E_{DMI} = -Dt\cos\xi \iint \left(\frac{\pi r}{2R} + \cos\theta\sin\theta\right) drd\phi. \tag{2.22}$$

As the first term originates from radial derivatives of θ, it is only non-zero for $r \leq R$. Moreover, it can be easily seen that for $r > R$, $\theta = \frac{\pi}{2}$ and hence $\cos\theta = 0$, so the above expression only needs to be integrated in the range $0 < r \leq R$. As the integrand is independent of ϕ, performing the angular integral just gives a factor of 2π. The radial integral is straightforward and gives the final result for the iDMI energy

$$E_{DMI} = -\frac{1}{2}DRt\left(\pi^2+4\right)\cos\xi. \tag{2.23}$$

Note that here I have assumed that the iDMI is induced only in the immediate interfacial layer for simplicity. In reality, there will be some modulation of the iDMI away from the interface but this should only slightly affect the effective iDMI strength. This will be studied further in section 3.4, in particular see table 3.2 for a verification that this simplification makes little difference to the final scaling of the textures. The

iDMI energy term needs to be added to the exchange and anisotropy energies from our previous calculations [11]:

$$E_{Ex} = 2\pi ANt\left[C - \ln\left(\frac{R}{R_c}\right)\right], \tag{2.24}$$

$$E_{An} = \left(\frac{\pi^2 - 4}{2\pi}\right) KNtR^2. \tag{2.25}$$

Where $C \approx 2$ is a numerical constant, N is the number of AFM layers such that Nt is the total thickness of the film and R_c is a large "cutoff radius" introduced to remove the infinite exchange energy contribution from the extended whirling IP background and will later be allowed to tend to infinity. One can then combine equations 2.23, 2.24 and 2.25 to get the total energy of an analytical linear meron in the presence of iDMI.

$$E_T = 2\pi ANt\left[C - \ln\left(\frac{R}{R_c}\right)\right] + \left(\frac{\pi^2 - 4}{2\pi}\right) KNtR^2 - \frac{1}{2}DRt\cos\xi\left(\pi^2 + 4\right) \tag{2.26}$$

As only the iDMI energy term has a chiral component (i.e. depends on ξ), minimising 2.23 with respect to ξ gives the equilibrium chirality. The result of this trivial calculation is that the iDMI energy is minimised when $\xi = 2n\pi$ for integer n and positive D or $\xi = (2n+1)\pi$ for negative D. I take $\xi = 0$ for convenience, which corresponds to a Néel meron of a fixed chirality and is an energy minimum under the assumption of a positive D, as is used in my simulations (see section 3.3). Rescaling the equation by a factor Nt (i.e. the film thickness) allows one to define an effective DMI strength $D_{\text{eff}} = D/N$. Minimising the total energy with respect to R gives the equilibrium meron radius

$$\frac{\partial E_T}{\partial R} = Nt\left[-2\pi A\left(\frac{1}{R}\right) + \left(\frac{\pi^2 - 4}{\pi}\right) KR - \frac{1}{2}D_{\text{eff}}\left(\pi^2 + 4\right)\right] = 0 \tag{2.27}$$

$$\Rightarrow R = \frac{\pi}{2K(\pi^2 - 4)}\left[\frac{1}{2}D_{\text{eff}}(\pi^2 + 4) \pm \sqrt{\frac{1}{4}D_{\text{eff}}^2(\pi^2 + 4)^2 + 8AK(\pi^2 - 4)}\right]$$

In the limit of no iDMI or of thick films (such that $D_{\text{eff}} \to 0$), the result above reduces to that found previously in the absence of iDMI [11]. As all the terms in the square root are positive with my conventions, the $-$ sign in the above expression would give a negative radius, which is unphysical. This motivates the choice of the $+$ sign in the expression for

R. As the z-component of the normalised magnetisation is given by $\cos(\pi r/2R)$, I find that $m_z = 0.5$ when $r = 2R/3$, hence converting the meron radius R into the full-width at half-maximum gives $FWHM = 4R/3$, which will be a useful expression for comparison between analytical results and simulated structures later (section 3.3).

It is useful to re-express these results so that they can be easily compared to previous works [86]. I introduce the characteristic lengthscale $l_w = \pi\sqrt{2A/(\pi^2-4)K} = \eta\sqrt{A/K}$, which is equivalent to the meron radius when $D_{\text{eff}} \to 0$, and a dimensionless parameter $\kappa = \left\{(\pi^2+4)/\left[4\sqrt{2(\pi^2-4)}\right]\right\} * D_{eff}/\sqrt{AK} = \kappa_0 D_{eff}/\sqrt{AK}$, which allows me to express the meron radius in a simplified form

$$R = l_w\left(\kappa + \sqrt{\kappa^2+1}\right). \tag{2.28}$$

2.3.2 Distorted antimeron

As an antimeron is composed of both Néel and Bloch sectors of varying chirality, one would expect that these textures should distort in the presence of an iDMI, as the regions with chirality that is favoured by the sign of D will enlarge over those with opposite chirality. I approach this analytically in a similar way to the meron studied above, using the linear antimeron ansatz $\hat{m} = (\sin\theta\cos\phi, -\sin\theta\sin\phi, \cos\theta)$ with $\theta(r)$ having the same functional form as before (equation 2.20). I note that the sign of $\hat{m}_y(r,\phi)$ is reversed compared to the meron and observe that here it is not necessary to include a phase factor ξ, as this would only lead to a global rotation of the antimeron. This can be easily shown by considering a 3D rotation matrix about the z-axis (R_z) by an angle ξ applied to $\hat{m}$, i.e. $R_z(\xi)\hat{m}$. I treat the distortions by introducing two additional parameters, λ and μ, which modify the mapping between (x,y) space and (r,θ) space so that constant-r lines are ellipses rather than circles. Such a distortion should in principle depend on only a single parameter; as a result, I will later enforce the criteria $\lambda\mu = 1$, which corresponds to requiring that all equal-r ellipses have the same area (see appendix A.2.2 for proof). Writing $r = \sqrt{(\lambda x)^2 + (\mu y)^2}$ and $\tan\phi = \mu y/(\lambda x)$, such that $\lambda x = r\cos\phi$ and $\mu y = r\sin\phi$, I then use equations 2.3, 2.5 and 2.16 to calculate how the relevant

energy terms are modified by these distortions. Firstly, for textures that do not vary along the z-direction the exchange energy contribution is

$$E_{Ex} = \iint ANt \left[\left(\frac{\partial \hat{m}}{\partial x} \right)^2 + \left(\frac{\partial \hat{m}}{\partial y} \right)^2 \right] d^2r. \tag{2.29}$$

Most of these terms have been calculated in 2.21, requiring only slight modifications to introduce factors of μ and λ. The relevant additional derivatives and modified versions of the derivatives found previously are:

$$\begin{aligned}
\frac{\partial m_y}{\partial x} &= -\cos\theta \sin\phi \frac{\partial \theta}{\partial x} - \sin\theta \cos\phi \frac{\partial \phi}{\partial x} \\
\frac{\partial m_x}{\partial y} &= \cos\theta \cos\phi \frac{\partial \theta}{\partial y} - \sin\theta \sin\phi \frac{\partial \phi}{\partial y} \\
\frac{\partial \theta}{\partial x} &= \frac{\partial \theta}{\partial r}\frac{\partial r}{\partial x} = \frac{\pi\lambda}{2R}\cos\phi \\
\frac{\partial \theta}{\partial y} &= \frac{\partial \theta}{\partial r}\frac{\partial r}{\partial y} = \frac{\pi\mu}{2R}\sin\phi \\
\frac{\partial \phi}{\partial x} &= -\frac{\lambda}{r}\sin\phi \\
\frac{\partial \phi}{\partial y} &= \frac{\mu}{r}\cos\phi
\end{aligned} \tag{2.30}$$

Any derivatives not included in 2.30 are identical to those in 2.21. Substituting the expressions from equations 2.21 and 2.30 into 2.29 and performing some simplification gives

$$E_{Ex} = ANt \iint \left[\left(\frac{\pi}{2R} \right)^2 \left(\lambda^2 \cos^2\phi + \mu^2 \sin^2\phi \right) + \frac{1}{r^2} \sin^2\theta \left(\lambda^2 \sin^2\phi + \mu^2 \cos^2\phi \right) \right] d^2r \tag{2.31}$$

By calculating the Jacobian, the surface element is $d^2r = dxdy = (r/\mu\lambda)drd\phi$. As the first term in the above integral comes from $\partial\theta/\partial r$ it is only non-zero in the range $0 \leq r \leq R$ and is zero outside of this range. The second term is in principle non-zero for all r, but needs to be split into two cases corresponding to the two ranges of r. The angular integrals are straightforward and give

$$\int_0^{2\pi} \left(a^2 \cos^2\phi + b^2 \sin^2\phi \right) d\phi = \pi \left(a^2 + b^2 \right), \tag{2.32}$$

where a and b can be substituted for λ and μ as required for the various terms. The relevant radial integrals are

$$\int_0^R \left(\frac{\pi}{2R}\right)^2 r dr = \frac{\pi^2}{8},$$
$$\int_0^{R_c} \frac{1}{r}\sin^2\theta dr = C' + ln\left(\frac{R_c}{R}\right), \tag{2.33}$$

where $C' \approx 0.824$ is a numerical constant. R_c is an upper limit introduced to avoid the infinite energy contribution from the whirling background as $r \to \infty$ that is an artefact of the chosen ansatz. This effectively corresponds to a long-scale relaxation of the spins away from the whirling background due to the antimeron at a radius R_c, which should have no real effect on the texture itself provided $R_c \gg R$. This is slightly different to the approach we had taken previously in the absence of iDMI and distortion [11, 83], where we subtracted the energy of an infinite flat vortex to remove the infinite exchange energy, but is more easily interpreted in the framework of micromagnetics (discussed in chapter 3) and gives the same final result. Hence, the exchange energy of the distorted antimeron is

$$E_{Ex} = \pi ANt\left(\frac{\lambda^2+\mu^2}{\mu\lambda}\right)\left[C + ln\left(\frac{R_c}{R}\right)\right], \tag{2.34}$$

where the $\pi^2/8$ term has been combined with the numerical constant C' to give $C \approx 2$, so that it is identical to the constant appearing in the exchange energy of a meron (see equation 2.24). Next I calculate the anisotropy energy, which has the general form given in 2.5 with $\hat{u} = \hat{z}$, i.e.

$$E_{An} = KNt\int_0^{2\pi}\int_0^{R_c} \cos^2\theta \frac{r}{\mu\lambda} dr d\phi. \tag{2.35}$$

Introducing an upper limit R_c again allows one to consider the two relevant regimes. For $r > R$, $\theta = \pi/2$ and $\cos\theta = 0$, hence the integration only goes up to R and the anisotropy energy is independent of the cutoff radius (provided $R_c \gg R$). The resulting integral is easy to do by parts and the anisotropy energy is

$$E_{An} = KNtR^2\left(\frac{\pi^2-4}{2\pi\mu\lambda}\right). \tag{2.36}$$

Finally, I calculate the iDMI energy using 2.16 and the method in section 2.3.1, utilising the derivatives found in 2.21 and 2.30. The resulting expression is

$$E_{DMI} = Dt \iint \left[\frac{\pi}{2R} \left(\mu \sin^2 \phi - \lambda \cos^2 \phi \right) + \frac{1}{r} \sin\theta \cos\theta \left(\mu \cos^2 \phi - \lambda \sin^2 \phi \right) \right] \frac{r}{\mu\lambda} dr d\phi. \tag{2.37}$$

As before, the terms in this expression will be zero for $r > R$, hence I only integrate up to $r = R$. The radial integrals are identical to those in section 2.3.1, the angular integrals are straightforward and similar to 2.32 and so the calculated iDMI energy is

$$E_{DMI} = DtR \left(\frac{\mu - \lambda}{\mu\lambda} \right) \left(\frac{\pi^2}{4} + 1 \right) \tag{2.38}$$

By combining 2.34, 2.36 and 2.38 I get the total energy of a distorted antimeron

$$\begin{aligned} E_T &= \pi A N t \left(\frac{\lambda^2 + \mu^2}{\mu\lambda} \right) \left[C + ln \left(\frac{R_c}{R} \right) \right] + KNtR^2 \left(\frac{\pi^2 - 4}{2\pi\mu\lambda} \right) + DtR \left(\frac{\mu - \lambda}{\mu\lambda} \right) \left(\frac{\pi^2}{4} + 1 \right), \\ E_T &= Nt \left\{ \pi A \left(\lambda^2 + \frac{1}{\lambda^2} \right) \left[C + ln \left(\frac{R_c}{R} \right) \right] + KR^2 \left(\frac{\pi^2 - 4}{2\pi} \right) - \frac{1}{4} D_{\text{eff}} R \left(\lambda - \frac{1}{\lambda} \right) \left(\pi^2 + 4 \right) \right\}. \end{aligned} \tag{2.39}$$

The second equation results from the first by enforcing the criteria $\lambda\mu = 1$ as discussed previously, thereby expressing the distortions purely in terms of λ, as well as rescaling $D_{\text{eff}} = D/N$ as before. I note that all three energy terms scale with a factor t, the thickness of each AFM layer, hence the equilibrium properties of the antimeron will be independent of this parameter. Taking the derivatives of the above expression for the total energy with respect to R and λ in order to find the minimum energy configuration gives

$$(1/Nt) \frac{\partial E_T}{\partial R} = -\pi A \left(\lambda^2 + \frac{1}{\lambda^2} \right) \frac{1}{R} + KR \left(\frac{\pi^2 - 4}{\pi} \right) - \frac{1}{4} D_{\text{eff}} \left(\lambda - \frac{1}{\lambda} \right) \left(\pi^2 + 4 \right) = 0, \tag{2.40}$$

$$(1/Nt) \frac{\partial E_T}{\partial \lambda} = \pi A \left(2\lambda - \frac{2}{\lambda^3} \right) \left[C + ln \left(\frac{R_c}{R} \right) \right] - \frac{1}{4} D_{\text{eff}} R \left(1 + \frac{1}{\lambda^2} \right) \left(\pi^2 + 4 \right) = 0. \tag{2.41}$$

One can rearrange 2.40 and solve the quartic equation resulting from 2.41 to get the equilibrium radius and distortion respectively

$$R = \frac{\pi}{2K(\pi^2-4)}\left[\frac{1}{4}D_{\text{eff}}\left(\lambda-\frac{1}{\lambda}\right)(\pi^2+4)\right. \tag{2.42}$$
$$\left. + \sqrt{\frac{1}{16}D_{\text{eff}}^2\left(\lambda-\frac{1}{\lambda}\right)^2(\pi^2+4)^2 + 4AK\left(\lambda^2+\frac{1}{\lambda^2}\right)(\pi^2-4)}\right]$$

$$\lambda = \frac{D_{\text{eff}}R(\pi^2+4)}{16\pi A\left[C+ln\left(\frac{R_c}{R}\right)\right]} + \sqrt{1+\left\{\frac{D_{\text{eff}}R(\pi^2+4)}{16\pi A\left[C+ln\left(\frac{R_c}{R}\right)\right]}\right\}^2}. \tag{2.43}$$

These coupled equations do have an exact (albeit extremely complicated) solution for R and λ, however it is easier to calculate these iteratively given values for the other parameters. It can be seen from the above equations that in the case $R_c \to \infty$ one would expect no distortion. In this case, or similarly if $D_{\text{eff}} \to 0$, the antimeron radius reduces to that found in the case of an antimeron without iDMI [11]. This is because the iDMI contributes no energy in the case of an undistorted antimeron due to the net zero energy cost of containing Néel domain walls of opposite chirality. As discussed earlier, the cutoff radius $R_c \gg R$ is an artefact of the ansatz reflecting the fact that the elliptical antimeron effectively extends to ∞, thereby providing a divergent energy contribution, which would also require no distortion as the energetic minimum. In reality, the spins far from the antimeron would relax into some other multi-domain configuration that contributes a finite energy and, somewhat obviously, no system is truly infinite, hence this divergent energy is not of practical concern. For all relevant parameter ranges it would be reasonable to set the cutoff radius as proportional to the exchange length (i.e. $\propto \sqrt{A/K} \sim 50\,\text{nm}$) and on these scales varying R_d by an order of magnitude has little effect on the actual antimeron distortion when calculated using the iterative scheme. If I re-express these formulae in terms of the same dimensionless parameter $\kappa = \left[(\pi^2+4)/4\sqrt{2(\pi^2-4)}\right]D_{eff}/\sqrt{AK} = \kappa_0 D_{eff}/\sqrt{AK}$ and lengthscale $l_w = \pi\sqrt{2A/[(\pi^2-4)K]} = \eta\sqrt{A/K}$ as for the meron, the expressions simplify slightly to

$$R = l_w\left[\frac{1}{2}\kappa\left(\lambda-\frac{1}{\lambda}\right) + \sqrt{\frac{1}{4}\kappa^2\left(\lambda-\frac{1}{\lambda}\right)^2 + \frac{1}{2}\left(\lambda^2+\frac{1}{\lambda^2}\right)}\right] \tag{2.44}$$

$$\lambda = \frac{\kappa R}{2l_w\left[C+ln\left(\frac{R_c}{R}\right)\right]} + \sqrt{1+\left\{\frac{\kappa R}{2l_w\left[C+ln\left(\frac{R_c}{R}\right)\right]}\right\}^2} \tag{2.45}$$

2.3.3 Distorted linear bimeron

Finally, I study a linear bimeron ansatz, which can be viewed as a linear skyrmion rotated by 90° about any IP axis. The form of a linear skyrmion is similar to the linear meron studied earlier, except equation 2.20 is replaced with

$$\theta(r) = \begin{cases} \frac{\pi r}{R} & \text{for r} \leq \text{R} \\ \pi & \text{for r} > \text{R}, \end{cases} \tag{2.46}$$

which ensures that the magnetization is OOP at $r = 0$ and oppositely so for $r > R$. The magnetization of a linear bimeron is then given by $\hat{\boldsymbol{m}} = (-\cos\theta, \sin\theta\sin(\phi+\xi), \sin\theta\cos(\phi+\xi))$ after rotation about the y-axis. For generality, I will allow distortions of the form $r = \sqrt{(\lambda x)^2 + (\mu y)^2}$ as was done for the antimerons discussed above. Calculating the relevant energy terms follows largely the same process as before, with the results summarised below:

$$E_{\text{Ex}} = \gamma\pi ANt\left(\frac{\lambda^2+\mu^2}{\lambda\mu}\right), \tag{2.47}$$

$$E_{\text{An}} = \frac{\pi KNtR^2}{4\lambda\mu}, \tag{2.48}$$

$$E_{\text{DMI}} = \frac{-\pi^2}{2\mu}DtR, \tag{2.49}$$

where all the symbols have the same meaning as before and $\gamma \approx 6$ is a numerical integration constant. Note that, unlike for an (anti)meron, the exchange energy is independent of the radius R as the background is uniform and there is no extended whirling structure. As before, one can minimize the total energy as a function of λ and R after enforcing the constraint $\lambda\mu = 1$ to get the equilibrium distortion and radius satisfying the equations

$$R = \frac{\pi\lambda D_{\text{eff}}}{K} \propto l_w\kappa\lambda \tag{2.50}$$

$$0 = A\gamma\left(2\lambda - \frac{2}{\lambda^3}\right) - \frac{1}{2}\pi D_{\text{eff}}R. \tag{2.51}$$

Like the antimeron, these equations do have an exact solution for any given set of parameters, however the numerical solutions are more useful for comparison with simulations. I also note, interestingly, that these solutions suggest bimerons should

collapse ($R \to 0$) if there is no iDMI and/or if there is no distortion, meaning that their energy landscape is drastically different than the (anti)meron solutions explored above. This will be discussed more thoroughly in the context of micromagnetic simulations, which largely support these conclusions, in section 3.4.3.

2.4 Magnetic dichroism in x-ray absorption

Here I present a derivation of the magnetic x-ray dichroism effects; circularly polarised x-rays are primarily sensitive to the expectation value of the atomic magnetisation, whereas linearly polarised x-rays are sensitive to the expectation value of the square of its magnetisation. This will largely follow the seminal papers on the topic [87, 88], but with significant additional discussion. To start, I will describe the approximations and assumptions used in the following derivation. Firstly, assume that in the absence of an applied electromagnetic field the atomic energy levels are described by a time-independent Hamiltonian ($\hat{H}_{\text{atomic}}$) and the total angular momentum J is a good quantum number, such that the eigenstates of $\hat{H}_{\text{atomic}}$ can be expressed in a $\{\hat{J}^2, \hat{J}_z\}$ basis. A time-varying electromagnetic field is then introduced across the atom, with associated Hamiltonian $\hat{H}_{\text{EM}}$. It is assumed that the spatial extent of the field is much larger than the atomic radius, such that the electric and magnetic fields experienced at a given time are constant across the atom. The electronic coupling to the electromagnetic field is also assumed to be much weaker than the intrinsic atomic interactions and hence time-dependent perturbation theory should be applicable. This means that, following Fermi's golden rule,

$$\Gamma_{i,f} = \frac{2\pi}{\hbar}|M_{i,f}|^2\rho \tag{2.52}$$

i.e. the light-induced transition rate $\Gamma_{i,f}$ is proportional to the square of the matrix element $|M_{i,f}|$ coupling the initial and final states through the perturbation and to the density of states ρ. The latter is often taken as $\delta(E_f - E_i)$ in a first approximation for studying resonant transitions but will ultimately determine both the linewidth of a transition and also contribute to its relative intensity; a detailed discussion of this is outside the scope of this calcultion and does not affect the conclusions related to dichroic effects. The matrix element $M_{i,f}$ will be the focus of the remainder of this section.

To calculate $M_{i,f}$, one can adopt the dipole approximation. This means that only the induced dipole moment couples to the electric field of the applied perturbation, i.e. any interactions with the magnetic field and higher-order electric field moments (e.g. quadrupole) are neglected. In this case, the relevant perturbation is the electric dipole moment $\vec{p}$ and this will induce transitions from a state $|\tau J, m\rangle$ to a state $|\tau' J', m'\rangle$, where τ labels different states with the same J. The matrix element is then

$$M_{i,f} = \langle \tau' J', m' \,|\, \vec{p} \,|\, \tau J, m \rangle = \langle \tau' J' \,\|\, \vec{p} \,\|\, \tau J \rangle \, \langle J, 1, m, q \,|\, J', m' \rangle \,, \tag{2.53}$$

where the Wigner-Eckart theorem [89–91] has been applied in going from the second to the third term, see appendix A.3 for a more detailed discussion. Assuming that the angular momentum is quantised along some axis, typically due to the presence of a crystal anisotropy or applied magnetic field, one can consider the components of the polarisation operator parallel and perpendicular to this axis. The total angular momentum of a photon $J_\gamma = 1$ has been used above and q corresponds to the component of the angular momentum along the quantisation axis and can take values $q = 0, \pm 1$. $q = 0$ corresponds to linearly polarised light parallel to the quantisation axis and $q = \pm 1$ corresponds to circularly polarised light in the plane perpendicular to this axis. $\langle J, 1, m, q \,|\, J', m' \rangle$ is a Clebsch-Gordan (CG) coefficient, generally written as $C^{j}_{m_1 m_2} = (j_1 j_2 m_1 m_2 | j_1 j_2 j m)$. These are used to convert between the two different angular momentum bases $|j_1 j_2 m_1 m_2\rangle$ and $|j_1 j_2 j m\rangle$. General forms of CG coefficients are hard to deal with, but there are standard lookup tables for some values. The CG coefficients present in this equation can be re-expressed as so-called 3j symbols of the form (see equation A.23, appendix A.4)

$$\langle J, 1, m, q \,|\, J', m' \rangle = (-1)^{-J+1-m'} \sqrt{2J'+1} \begin{pmatrix} J & 1 & J' \\ m & q & -m' \end{pmatrix}. \tag{2.54}$$

These 3j symbols are introduced as a convenient way of calculating CG coefficients, as they have useful symmetry properties and simplified forms for certain combinations of values [91, 92], this is discussed extensively in appendix A.4. I will drop the phase factor from here on, as for any value $J = n/2$ with integer n and corresponding set of allowed m this will always give ± 1 and therefore will not be relevant when the square of the matrix element is taken later. Such 3j symbols have exact non-zero values, provided that the following set of selection rules are obeyed:

1. $m + q = m'$

2. $|J - 1| \leq J' \leq J + 1$

3. $J + 1 + J'$ is an integer, and must be even if $m = q = m' = 0$

4. $m_i \in \{-J_i, -J_{i+1}, ..., J_{i-1}, J_i\}$ for each m, J

These come from the orthogonality conditions for CG coefficients (appendix A.4, equations A.20,A.21) and place limits on the allowed transitions, thereby generating the familiar dipole selection rules. Following rule 1, $m + q = m'$ and thus $\Delta m = m' - m = 0$ if $q = 0$ and $\Delta m = \pm 1$ for $q = \pm 1$. Rule 2 requires that $|J - 1| \leq J' \leq J + 1$; rules 3 and 4 are then automatically satisfied providing the above two rules are followed and the angular momentum variables are defined correctly. This gives up to 9 possible electric dipole transition for a given initial state $|\tau J, m\rangle$, 3 for each polarisation state of the x-rays. I should point out that electric dipole transitions also obey the additional selection rule $\Delta S = 0$, as photons carry no spin angular momentum. This does not affect states whose angular momentum comes purely from the orbital component, but may be relevant in general. I argue, however, that this should not affect the results below, as it only potentially limits which states transitions can occur between, but would not affect the value of the dichroism or its dependency on the atomic magnetisation. This effect, as well as more complicated interaction terms such as crystal field splitting and core hole lifetime broadening need to be accounted for in order to accurately simulate full XAS spectra, but this approach is beyond the scope of this thesis. See e.g. [87, 88] for an outline of the full process.

Additionally, there are a set of general solutions for certain sets of 3j symbols, those particularly relevant here will be when one of the angular momentum values $J = 1$, giving

the following four allowed symbols with their values [92]:

$$\begin{pmatrix} j+1 & j & 1 \\ m & -m-1 & 1 \end{pmatrix} = (-1)^{-j-m-1}\left[\frac{(j-m)(j-m+1)}{(2j+3)(2j+2)(2j+1)}\right]^{\frac{1}{2}} \quad (2.55)$$

$$\begin{pmatrix} j+1 & j & 1 \\ m & -m & 0 \end{pmatrix} = (-1)^{j-m-1}\left[\frac{(j+m+1)(j-m+1)}{(2j+3)(j+1)(2j+1)}\right]^{\frac{1}{2}} \quad (2.56)$$

$$\begin{pmatrix} j & j & 1 \\ m & -m-1 & 1 \end{pmatrix} = (-1)^{j-m}\left[\frac{(j-m)(j+m+1)}{(j+1)(2j+1)(2j)}\right]^{\frac{1}{2}} \quad (2.57)$$

$$\begin{pmatrix} j & j & 1 \\ m & -m & 0 \end{pmatrix} = (-1)^{j-m}\frac{m}{[(2j+1)(j+1)j]^{\frac{1}{2}}} \quad (2.58)$$

Given the form of the matrix element in equation 2.53, the task then becomes to calculate values for all of the relevant 3j symbols. This is particularly true if one is interested in magnetic phenomenon, for which the reduced matrix element $\langle \tau' J' \| \vec{p} \| \tau J \rangle$ does not depend on the magnetisation component m. Consider the symbol relevant for linearly polarised light ($q = 0$) with $\Delta J = 0$. Using the fact that such symbols are symmetric under even permutations of their columns [92] it can be written as

$$\begin{pmatrix} J & 1 & J' \\ m & 0 & -m' \end{pmatrix} = \begin{pmatrix} J & J & 1 \\ -m & m & 0 \end{pmatrix}. \quad (2.59)$$

One can then use the general solution 2.58 to get its value

$$\begin{pmatrix} J & 1 & J \\ m & 0 & -m \end{pmatrix} = (-1)^{J-m}\left[\frac{m^2}{(2J+1)(J+1)J}\right]^{\frac{1}{2}}. \quad (2.60)$$

Exploiting the symmetry of the 3j symbols allows one to express the other 8 symbols in one of the standard forms 2.55-2.58, thereby allowing exact values to be calculated. This process is shown in detail for all 9 3j symbols in appendix A.4. All of these terms contain phase factors given by -1 to the power of some linear function like $aJ + bm + c$ where a, b, c are integers that may be positive or negative. Crucially, a and b are found to be either both even or both odd in all cases. Given the constraints on the possible values of m for a specified J, this phase factor will always be ± 1 (i.e. a real number) and so will not be relevant when the square of the 3j symbol is taken later.

After the 3j symbols have been calculated, one needs to put this all together to calculate the square of the matrix element given in equation 2.53 in order to apply Fermi's golden rule. Assuming the magnetic splitting of the $2J + 1$ different energy levels labelled by m is much less than the experimental resolution, which should be true, the projected

component of the magnetic moment can then be replaced with a thermal average of the magnetisation, i.e. the square of equation 2.53 becomes

$$\langle S_{\tau Jm,\tau' J'm'} \rangle = \langle A^q_{J,J'} \rangle \langle \tau' J' \| \vec{p} \| \tau J \rangle^2 , \tag{2.61}$$

where

$$\langle A^q_{J,J'} \rangle = \mathcal{Z}^{-1} \sum_m (2J'+1) \begin{pmatrix} J & 1 & J' \\ m & q & -m' \end{pmatrix}^2 e^{-\frac{m}{\theta}} \tag{2.62}$$

with the partition function $\mathcal{Z}$ having its standard definition for a set of $2J+1$ magnetic energy levels and the constant $\theta = k_B T / g\mu_B B$ [87]. Evaluating this for the case $q = 0$ and $\Delta J = 0$ using equation 2.60 gives

$$\langle A^0_{J,J} \rangle = \mathcal{Z}^{-1} \sum_m (2J+1) \begin{pmatrix} J & 1 & J \\ m & 0 & -m \end{pmatrix}^2 e^{-\frac{m}{\theta}} = \frac{\langle m^2 \rangle}{J(J+1)}. \tag{2.63}$$

Thus, $\Delta J = 0$ transitions using linear light polarised parallel to the quantisation axis of the magnetisation has a transition rate and hence an absorption intensity proportional to the square of the atomic magnetisation $\langle m^2 \rangle$. Equivalent expressions for $\Delta J = \pm 1$ transitions using linear light give:

$$\langle A^0_{J,J+1} \rangle = \mathcal{Z}^{-1} \sum_m (2J+3) \begin{pmatrix} J & 1 & J+1 \\ m & 0 & -m \end{pmatrix}^2 e^{-\frac{m}{\theta}} = \frac{(J+1)^2 - \langle m^2 \rangle}{(J+1)(2J+1)}. \tag{2.64}$$

$$\langle A^0_{J,J-1} \rangle = \mathcal{Z}^{-1} \sum_m (2J-1) \begin{pmatrix} J & 1 & J-1 \\ m & 0 & -m \end{pmatrix}^2 e^{-\frac{m}{\theta}} = \frac{J^2 - \langle m^2 \rangle}{J(2J+1)}. \tag{2.65}$$

and hence all electric dipole transitions with linearly polarised x-rays are sensitive only to the thermal average of the square of the magnetisation $\langle m^2 \rangle$ along the polarisation axis. Turning to circularly polarised x-rays with $q = \pm 1$, I find very similar expressions in all 6 cases. As a representative example, $q = +1, \Delta J = 0, m' = m+1$ gives

$$\langle A^{+1}_{J,J} \rangle = \mathcal{Z}^{-1} \sum_m (2J+1) \begin{pmatrix} J & 1 & J \\ m & 0 & -m-1 \end{pmatrix}^2 e^{-\frac{m}{\theta}} = \frac{J(J+1) - \langle m^2 \rangle - \langle m \rangle}{2J(J+1)}. \tag{2.66}$$

Following this procedure through for the remaining 5 allowed dipole transitions with circularly polarised light always gives sensitivity to both $\langle m \rangle$ and $\langle m^2 \rangle$, as shown in appendix A, section A.4, hence circularly polarised x-rays are directly sensitive to the magnetisation of a sample and can be used to study ferromagnetic materials at an appropriate dipole transition. Linearly polarised x-rays, being only sensitive to $\langle m^2 \rangle$, can interact with both ferromagnets and antiferromagnets.

In order to explicitly prove the existence of *dichroic* effects, which are a difference in absorption between two different polarisations of the x-rays at a given energy, I will calculate the linear and circular dichroic effect for $\Delta J = 0$ transitions, with $\Delta J = \pm 1$ transitions following simply by applying the same process to the appropriate matrix elements. The circular dichroic effect is the difference in absorption between left- and right-handed circularly polarised x-rays [93], and therefore is proportional to

$$\begin{aligned} \langle A^{+1}_{J,J}\rangle - \langle A^{-1}_{J,J}\rangle &= \frac{J(J+1) - \langle m\rangle - \langle m^2\rangle}{2J(J+1)} - \frac{J(J+1) + \langle m\rangle - \langle m^2\rangle}{2J(J+1)} \\ &= \frac{-\langle m\rangle}{J(J+1)} \end{aligned} \tag{2.67}$$

where the solutions calculated in detail in appendix A, section A.4 have been used without proof here. This is particularly interesting, as in the dichroic calculation the terms proportional to $\langle m^2\rangle$ have cancelled out and therefore circular dichroism is sensitive only to the magnetisation. A similar calculation for $\Delta J = \pm 1$ transitions shows that circular dichroism is proportional to $\langle m\rangle$ only in all cases.

Now, turning to linear dichroism, one can get an equivalent linear polarisation in a plane perpendicular to the quantisation axis by using a linear mean of left and right circularly polarised x-rays, i.e.

$$\langle A^{x}_{J,J'}\rangle = \frac{1}{2}\left(\langle A^{+1}_{J,J'}\rangle + \langle A^{-1}_{J,J'}\rangle\right) \tag{2.68}$$

For the case $\Delta J = 0$, this gives

$$\langle A^{x}_{J,J}\rangle = \frac{J(J+1) - \langle m^2\rangle}{2J(J+1)} \tag{2.69}$$

and hence the linear dichroism is

$$\begin{aligned} \langle A^{0}_{J,J}\rangle - \langle A^{x}_{J,J}\rangle &= \frac{\langle m^2\rangle}{J(J+1)} - \frac{J(J+1) - \langle m^2\rangle}{2J(J+1)} \\ &= \frac{3\langle m^2\rangle}{2J(J+1)} - \frac{1}{2}. \end{aligned} \tag{2.70}$$

As expected, the linear dichroism is proportional only to the average of the square of the magnetisation. Calculations for the $\Delta J = \pm 1$ transitions give a similar result. I note briefly that dichroic imaging is usually done by changing the incident x-ray energy rather than the polarisation, where the dichroism comes mostly from probing transitions with different ΔJ. This will be discussed further from a more experimental perspective, including how this effect can be used to image magnetic structures, in section 4.2.

2.5 Theory of x-ray holography

Holographic techniques utilise the interference between the scattering of an object and a reference to encode detailed structural information in the diffraction pattern. A real space image of the object can then be reconstructed by applying an appropriate filter and taking an inverse Fourier transform of the resulting pattern. Here, I explain the mathematics underpinning the technique of holography with extended reference by autocorrelation linear differential operation (HERALDO), a high-resolution holography method that can be applied to a variety of illumination sources such as synchrotron-based x-ray sources and free-electron lasers. The discussion here largely follows the seminal papers by M. Guizar-Sicairos and J. R. Fienup [94, 95].

Consider a general 2D x-ray opaque plane containing within it an object and an extended reference with additive modulations given by $o(x, y)$ and $r(x, y)$ respectively. The x-ray amplitude immediately behind this plane under the paraxial approximation (i.e. close to normal incidence) is then given by $f(x, y) = o(x, y) + r(x, y)$. The Fraunhofer (far field) diffraction pattern is a product of a quadratic phase factor and the Fourier transform (FT) of $f(x, y)$, i.e.

$$F(u, v) = \iint f(x, y) exp[-2\pi i(ux + vy)]dxdy \tag{2.71}$$

where u and v are the Fourier space coordinates. A detector array in the far-field will measure $|F(u, v)|^2$, which is related to the object-space field autocorrelation by an inverse FT

$$\mathcal{F}^{-1}\left[|F(u, v)|^2\right] = f \otimes f = o \otimes o + r \otimes r + o \otimes r + r \otimes o, \tag{2.72}$$

where the cross-correlation function is

$$a \otimes b \equiv \iint a(x', y')b^*(x' - x, y' - y)dx'dy'. \tag{2.73}$$

For a given reference $r(x, y)$, define an n^{th} order linear differential operator that satisfies $\mathcal{L}^{(n)}\{r(x, y)\} = A\delta(x - x_0)\delta(y - y_0) + g(x, y)$, where A is an arbitrary complex constant and $g(x, y)$ is some other function. In general, this differential operator can be expanded as

$$\mathcal{L}^{(n)} \equiv \sum_{k=0}^{n} a_k \frac{\partial^n}{\partial x^{n-k} \partial y^k}. \tag{2.74}$$

The a_k are a set of constant coefficients that can be tweaked to obtain the desired form of $\mathcal{L}^{(n)}$. Applying this linear operator to the Fraunhofer field (equation 2.72), evaluating the terms involving δ-functions and using the identity

$$\mathcal{L}^{(n)} \{h \otimes g\} = (-1)^n \left[h \otimes \mathcal{L}^{(n)} \{g\}\right] = \mathcal{L}^{(n)} \{h\} \otimes g \tag{2.75}$$

(see Appendix A.5) gives

$$\begin{aligned} \mathcal{L}^{(n)} \{f \otimes f\} &= \mathcal{L}^{(n)} \{o \otimes o\} + \mathcal{L}^{(n)} \{r \otimes r\} + (-1)^n [o \otimes g] + g \otimes o \\ &+ (-1)^n A^* o(x + x_0, y + y_0) + A o^*(x - x_0, y - y_0) \end{aligned} \tag{2.76}$$

Provided one chooses a suitable $\mathcal{L}^{(n)}$, this reconstructs two direct images of the original object $o(x, y)$ that are inverted complex conjugates of each other. These reconstructions are centred at the position of the delta functions arising from applying the linear filter to the reference. Each reconstruction is weighted by the complex function A (or A*), which in principle is just determined by the reference and exact choice of linear differential operator and therefore is independent of any contrast present in the object. If there is no overlap between at least one of these reconstructions and any of the other cross-correlations, a direct image of the object can be obtained from the measured Fraunhofer pattern.

To determine the conditions for which at least one of the images of the object field are separated from all other cross-correlations, consider a general spatially-finite object that fits wholly within a circle of radius ρ and is centred on the origin. In order for there to be no overlap between an object reconstruction at (x_0, y_0) and any of the other cross-correlation terms, the relevant separation conditions are:

1. $o \otimes o$ will be contained wholly within a circle of radius 2ρ, and therefore so will $\mathcal{L}^{(n)} \{o \otimes o\}$. Hence, one requires that $r_0 = \sqrt{x_0^2 + y_0^2} \geq 3\rho$, which puts a lower limit on the separation between the centre of the object and the part of the reference feature that gives rise to the δ-function.

2. To get no overlap between the object reconstruction and the two cross-correlations $o \otimes g$ and $g \otimes o$, g(x,y) must have zero amplitude in a radius of at least 2ρ about the δ function at (x_0, y_0). If $\mathcal{L}^{(n)}$ generates multiple δ functions, this condition also applies between them in order to avoid overlap between different reconstructions.

3. The reference self-correlation $r \otimes r$ must be zero in a radius ρ about the δ function in order to avoid overlap with the object reconstruction. If this cannot be avoided and the reference feature r(x,y) is well known, it may be possible to subtract off this term. Additionally, in certain circumstances, such an overlap is actually a benefit, such as when the object is contained within the reference feature.

I will now describe the situation most relevant to this work, namely that when the reference is an extended slit. Other important cases can be found in the seminal work on this technique [94]. Consider an infinitely narrow line reference of length L parallel to some axis x', such as can be described using a Heaviside step function $H(x)$ via

$$r(x', y') = A\delta(y') \left[H(x' + L/2) - H(x' - L/2)\right]. \tag{2.77}$$

Given that the step function satisfies $(\partial/\partial x')H(x') = \delta(x')$, taking the partial derivative of the reference function along its axis gives

$$\frac{\partial r}{\partial x'} = A\delta(y') \left[\delta(x' + L/2) - \delta(x' - L/2)\right]. \tag{2.78}$$

Hence, defining the first order linear differential operator as $\mathcal{L}^{(1)} = \partial/\partial x'$ means that a simple line reference will recreate two copies of the object (and its complex conjugate) after the processing procedure, located at the two ends of the reference feature. In general, the axis x' may be at some angle α to the x axis of the system, usually defined in the plane of the detector with respect to the incident beam. In this case, performing a rotation will map the linear operator above onto the directional derivative along the slit $\mathcal{L}^{(1)} = \hat{\alpha} \cdot \vec{\boldsymbol{\nabla}}$, where $\hat{\alpha}$ is the unit vector pointing along the slit. Such a directional derivative is not straightforward to apply in real-space, but is equivalent to a suitable multiplicative polynomial filter applied in Fourier space (see Appendix A.5).

The set of separation conditions discussed above place the following limitations on the scaling of the object and reference features. If the object feature has radius ρ then:

1. The distance between at least one corner of the slit and the centre of the object must be at least 3ρ.
2. The slit must be at least 2ρ long.
3. Every part of the slit must be at least a distance ρ from the centre of the object.

This will lead to the design of the holography mask described in section 4.3.2 and employed in chapter 6.

Finally, I will consider the effects of an imperfect reference feature on the reconstructions. The imperfect slit reference can be described as a perfect reference convoluted with some spread function $d(x, y)$, i.e. $r_d(x, y) = r(x, y) \otimes d(x, y)$. Applying the linear differential operator to r_d and using equation 2.75 gives

$$\mathcal{L}^{(n)}\{r_d\} = [A\delta(x - x_0)\delta(y - y_0) + g(x, y)] \otimes d(x, y) = Ad(x_0, y_0) + g(x, y) \otimes d(x, y). \tag{2.79}$$

Hence, the δ function located at (x_0, y_0) becomes convoluted with the spread function $d(x, y)$, giving a smeared delta-function. As this smeared delta will lead to our reconstructions of the object, the two reconstructions are now of the form $(-1)^n A^* o_d(x + x_0, y + y_0)$ and $Ao_d^*(x - x_0, y - y_0)$, where $o_d(x, y) = o(x, y) \otimes d(x, y)$. Hence, the reconstructions are weighted by the same spread function as the original reference. For example, if the slit can be described as the cross correlation between a perfect slit and a Gaussian function of width l, the object reconstruction will be blurred by an identical gaussian and therefore the overall resolution of the reconstruction is directly related to the width of the slit. This is a key consideration when designing a HERALDO experiment, as the experimental resolution will be ultimately limited by the width of the line reference one can make, as will be discussed further in section 4.3.2.

'The Answer to the Great Question... Of Life, the Universe and Everything... Is... Forty-two,' said Deep Thought, with infinite majesty and calm.

Douglas Adams, *Hitchhiker's Guide to the Galaxy*

3 Micromagnetic simulations

Contents

3.1 Introduction

Computer modelling techniques have been utilised across the physical sciences to support and guide both experimental and theoretical developments since before computers found widespread mainstream applications. They are useful for understanding how complex systems behave under modifications of their intrinsic variables or excitation by external stimuli, specifically in cases that are too complicated for detailed theoretical studies. The

main drawback is that computer modelling techniques are ultimately only as good as the assumptions one uses to simplify and express the problem in a concise, discrete way that can be processed by a computer. As a result, it is my opinion that these techniques should primarily be used as a guide to aid and inspire additional theoretical and experimental developments, which is the approach I have taken.

One key area where computational modelling has proven to be an invaluable asset is the field of micromagnetics, where the static and dynamical behaviour of magnetic materials under a variety of external stimuli can be studied. This can be used either to support experimental studies by helping to explain the often complicated observations or to predict new behaviours and phenomena to guide future experimental developments. In this section, I will explain how the energy terms discussed in section 2.2 can be implemented in a discretised framework as required for micromagnetic programmes. I will then describe the micromagnetic model I developed to study A-type antiferromagnets such as α-Fe_2O_3, inspired by previous work conducted in our group [83], with a focus on how it accurately reproduces the relevant magnetic interactions that dominate the magnetic behaviour of the real material. The bulk of this chapter will be dedicated to discussing the important results of a series of micromagnetic simulations studying the family of topological textures in α-Fe_2O_3 and how these have guided a number of our experimental investigations, including those covered later in this thesis. I will also briefly cover a few additional sets of simulations I performed, including pinning of AFM domains at grains and interfacing α-Fe_2O_3 with a FM overlayer, the latter of which provided pathways for further experimental work beyond the direct scope of this thesis. These further simulations serve to demonstrate the flexibility of my model to investigate phenomena in antiferromagnets beyond the simple energetic stability of specific states.

3.2 Performing micromagnetic simulations

3.2.1 Discretisation of energy terms

The magnetic energy terms presented in chapter 2, section 2.2 were based on a continuum approximation for a magnetic material, which I stressed was only valid provided the lengthscale of magnetic variations was much larger than the lattice parameter of the

material (the micromagnetic criterion). Computers, unfortunately, cannot deal with a continuous parameter space and so one must ultimately implement a discretised model of the magnetic interactions. One approach would be to do away with the micromagnetic limit and deal with the real interactions between all atoms in the crystal structure, which in many cases is understood and well known. This has its benefits, but also has severe drawbacks; namely, setting up the complete crystal structure and the different atomic interactions over many unit cells becomes too complicated in all but the simplest materials. Also the calculations are extremely computationally expensive and can only model materials up to ∼100 nm in scale in a reasonable time frame. Such models have been extensively implemented in density functional theory calculations and atomistic magnetic modelling software such as VAMPIRE [96].

The approach taken by the micromagnetics community and codes such as OOMMF [97] and MuMax3 [98–100] is to divide the material up into orthorhombic boxes (hereafter referred to as cells). The key idea is that the cell size should be larger than the interatomic distance, but also smaller than the typical lengthscale of magnetic variations. This means that the magnetisation can be considered as approximately continuous inside each cell and the small-scale atomic structure can be ignored. Provided both of these criteria can be simultaneously realised, which fortuitously is the case in most materials, then this approach can accurately model both the statics and dynamics of the system. Each cell is assigned a magnetic moment equal to the saturation magnetisation of an equivalent volume of the material. The various energy terms are then calculated as interactions between the cells or with each cell and the external fields relevant to the problem, thus allowing one to model a wide range of different systems and phenomena [101].

To demonstrate the discretisation of continuous energy terms, I start with the exchange energy as derived in chapter 2

$$E_{ex} = \iiint A \left[(\vec{\boldsymbol{\nabla}} m_x)^2 + (\vec{\boldsymbol{\nabla}} m_y)^2 + (\vec{\boldsymbol{\nabla}} m_z)^2 \right] dV. \tag{3.1}$$

The constraint on magnetic moments in ferromagnetic systems is $|\hat{m}|^2 = 1$ [74, 102] (with a similar constraint on the sublattice magnetisation in antiferromagnets). Taking

the partial derivative gives the requirement $\hat{m} \cdot \frac{\partial \hat{m}}{\partial r_i} = 0$, where $r_i = \{x, y, z\}$. Considering the derivative of this requirement gives

$$\frac{\partial}{\partial r_i}\left(\hat{m} \cdot \frac{\partial \hat{m}}{\partial r_i}\right) = \left(\frac{\partial \hat{m}}{\partial r_i}\right)^2 + \hat{m} \cdot \frac{\partial^2 \hat{m}}{\partial r_i^2} = 0 \tag{3.2}$$

and hence,

$$\left(\frac{\partial \hat{m}}{\partial r_i}\right)^2 = -\hat{m} \cdot \frac{\partial^2 \hat{m}}{\partial r_i^2}. \tag{3.3}$$

Assuming the micromagnetic criterion is valid, such that one can consider the magnetic moment to be averaged over discretised cells and with very small variations between adjacent cells, the right-hand side of the above equation cab be approximated as

$$\frac{\partial^2 \hat{m}}{\partial r_i^2} \approx \frac{\hat{m_i} - \hat{m}}{\Delta_i^2}. \tag{3.4}$$

Here, $\hat{m_i}$ is the magnetisation in an adjacent cell along the r_i-axis and Δ_i^2 is the cell size along that axis. In the 6-nearest-neighbour approximation for a configuration of orthorhombic cells, only the face-sharing neighbouring cells contribute to the effective exchange field acting on a given cell. This therefore allows one to express the exchange energy density for a given cell as a sum over the contributions from the 6 neighbours using the formula above. The exchange energy per cell is then

$$\epsilon_{Ex} = \sum_{i=0}^{6} A_i \hat{m} \cdot \frac{\hat{m} - \hat{m_i}}{\Delta_i^2} = -\frac{1}{2} M_{sat}\, \hat{m} \cdot \vec{B_{eff}}. \tag{3.5}$$

The effective exchange field $\vec{B_{eff}}$ is introduced above, as different energy terms are most commonly implemented in micromagnetic codes as contributions to the total effective field acting on a given cell [97, 98]. Any exchange energy terms (such as the iDMI) can be discretised in a similar way. Energy terms which act on magnetic moments individually, such as external magnetic fields or anisotropy energies, are straightforward to discretise and result in an effective field term as described above acting on the average magnetic moment in each individual cell.

3.2.2 Evolution of micromagnetic systems

There are several different methods commonly used in the micromagnetics community to 'evolve' the magnetic state of a simulated system from its initial state to the final state, with the exact method used primarily depending on the goals of a given simulation. If one wants to study dynamical phenomena in a system, such as spin-wave propagation or domain wall motion under applied spin torques, then one needs to propagate a given magnetic state through small increments of time, which typically need to be much shorter than the relevant timescale of the dynamical effect under investigation. This is most commonly done using the Landau-Lifshitz-Gilbert (LLG) equation [97, 98, 103]

$$\frac{\partial \hat{m}}{\partial t} = \frac{\gamma}{1+\alpha^2}\left[\hat{m} \times \vec{B_{eff}} + \alpha \hat{m} \times \left(\hat{m} \times \vec{B_{eff}}\right)\right]. \tag{3.6}$$

Here, $\vec{B_{eff}}$ includes all terms that contribute to the effective field as discussed above, γ is the gyromagnetic ratio and α is a dimensionless damping parameter. Often the damping parameter is not known a-priori for a given system, meaning that a set of different values need to be tested. This method requires the divisions of time to be carefully selected such that the change in magnetisation per step is not too large, otherwise this could lead to erroneous results.

For establishing *equilibrium* configurations, dynamically propagating the magnetisation under constant external stimuli is a lengthy process for reaching the steady state. For these purposes, procedures which aim to directly minimise the energy of the system are preferred instead. These technique can also be used to study quasi-static phenomena, wherein the control parameter is varied slowly enough that the system is effectively constantly in equilibrium. One such method is to use the LLG equation presented above but with the precession term (i.e. the first term $\propto \hat{m} \times \vec{B_{eff}}$) turned off. This is equivalent to using a sufficiently strong damping parameter α, such that the effective field serves to damp the magnetisation vector towards a minimum energy configuration. This can, however, be quite slow at reaching a local energy minimum and comes with the same caveats on the suitably chosen time step. An often quicker approach is to attempt to minimise the energy of the system directly, starting from a given configuration. This is usually done using a conjugate gradient method, whereby the spins are slowly varied

along a randomly chosen direction in the $3N$-dimensional phase space (where N is the number of cells in the simulation) until the energy minimum along that line is found. After this, the next direction of variation is chosen to be orthogonal to the previous line and related to the gradient of the energy at the previously found minimum. In this way, after a number of iterations an energy minimum can be found, given some threshold energy difference per step to determine when the iteration should stop. It should be noted that energy minimisation techniques are, in general, highly dependent on the starting configuration of the system, as they will typically find the closest local energy minimum rather than the global minimum. Provided one can argue that the state reached this way does represent a true stable (or at least metastable) state of the system then this drawback can actually be utilised as a benefit of this technique for investigating the full range of magnetically stable states that the system can reach.

Throughout this work, I have used energy minimisation via the conjugate gradient method to evolve the system towards equilibrium, with the exception of the simulations presented in figure 3.6, which used time-evolution through the LLG equation presented above. In each case, I will argue that the configuration reached through energy minimisation represents at least a metastable state of the system. As this process does not allow me to consider thermal fluctuations, I therefore make no estimation of the lifetime of each state. Moreover, this process does not allow for dynamical phenomena to be studied. Nontheless, as this is the fastest and most reliable way to consistently reach local energy minima, it serves as a good method for conducting the investigations described below.

3.3 Model of A-type antiferromagnets

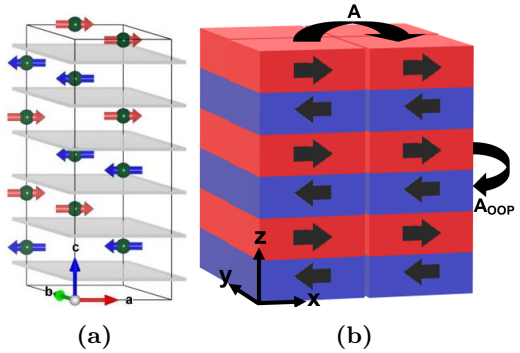

Figure 3.1: a) The crystal and magnetic structures of AFM α-Fe_2O_3. Red/blue arrows show the magnetic moment orientation

An A-type antiferromagnet such as $\alpha-Fe_2O_3$ is comprised of a set of atomic planes stacked along the c-axis of the system (figure 3.1a). Atoms within the same plane have a ferromagnetic exchange interaction ($A_{IP} > 0$) and the interaction

between atoms in adjacent layers is antiferromagnetic ($A_{OOP} < 0$). Whilst the IP interactions lend themselves well to a micromagnetic model, it is less clear that this model accurately reproduce the short-lengthscale variations along the c-axis, as this would require the cell size along this direction to be the interlayer distance of the crystal structure, which is typically much smaller than is usually acceptable in a micromagnetic model. Nevertheless, this is the approach I take; I model an A-type antiferromagnet as a set of cells, which have typical sizes in the x-y plane ($\approx$2 nm) but thicknesses on the order of the atomic spacing ($\approx$0.2 nm) along the z-axis (figure 3.1b).

In order to justify this approach, I must consider further the assumptions used in creating a micromagnetic model and explore any ramifications and caveats that occur when I violate the micromagnetic criterion along one specific axis. If the cells are smaller along one dimension than is necessary to fulfil this criterion, up to the limit of containing a single "layer" of atoms, then it is clear that the associated lengthscale approximation is not valid along that dimension. This does nothing to the approximations employed along the other two dimensions, which should still produce a good model of magnetic variations. The consequences of this are, however, not as severe as they may first seem. For a given exchange parameter along a short axis, I can say that the exchange energy is not an accurate account of the "real" exchange between atoms along this axis; however, there are certain limits for which this interaction will be good enough. In the case considered here, the layers are antiferromagnetically coupled along the z-axis and the total thickness of the film is much smaller than the magnetic exchange length along this dimension. This means that the antiferromagnetic exchange serves only to precisely anti-align the layers, such that any errors in the accuracy of the exchange energy are irrelevant provided they are not severe enough to destroy this precise anti-alignment. It

is consistently clear throughout all these simulations that the value of AFM exchange used is sufficient to enforce this anti-alignment along the z-axis.

The other key consideration needed to justify our model is the analysis of the dipolar fields, which are well understood to be the most difficult part of any micromagnetic calculations due to their long-range nature. This is discussed in detail in our paper on this topic [37], with the key arguments outlined here. The dipolar fields can be approximately decomposed into two parts (as discussed in section 2.2.3): the short-range dipole interaction, which is generally taken to contribute to the anisotropy energy and is therefore not included in the model separately, and the long-range part, which is computed directly in the form of a demagnetisation field [74]. In a natural collinear antiferromagnet, the net magnetisation is zero and so is the demagnetisation field, but the short-range component of the dipolar interaction still contributes to the anisotropy. In my 'model' A-type antiferromagnet, each magnetic cell has an exactly antiparallel counterpart in a vertically adjacent layer; therefore, the calculated demagnetisation field has a quadrupolar character and decays very rapidly. Although there are no macroscopic demagnetisation fields and no shape anisotropy, the short-range part of the quadrupolar interaction still generates an anisotropy, inducing a strong preference for the moments to lie in the x-y plane even when the on-site anisotropy energy density is set to zero. This situation is very similar to that of 'real' α-Fe_2O_3, since the Morin transition occurs precisely when the easy-axis on-site anisotropy exactly balances the perpendicular easy-plane dipolar anisotropy. As my simulations use an orthorhombic configuration rather than stacked hexagonal layers, I would not expect the dipolar anisotropy to be exactly the same as for the real material, but the order of magnitude should be correct. In fact, the simulated dipolar anisotropy is approximately 60% of the known value for α-Fe_2O_3 [12]. This argument demonstrates that a lot of the issues due to the long-range nature of the dipolar fields are largely circumvented in my model as a direct result of the stacked layer configuration that I have introduced.

Even though I have argued that this micromagnetic model of A-type antiferromagnets is valid, there are a couple of important caveats to the scope of this model that one should be aware of. Firstly, as hinted at above, it is only capable of simulating thin layers whose magnetic exchange length is much larger than the total thickness of the simulated film

in order to ensure the two sublattices remain strictly antiparallel along the z-axis of the simulation. Therefore, it cannot accurately study depth-dependent phenomena, such as the modulation of magnetic structures away from an interface. Secondly, dynamical phenomena which involve any propagation along the z-axis cannot be investigated, although those that purely involve variations in the x-y plane are allowed. Finally, it should be clear why this type of model can only reasonably be applied to antiferromagnets of the A-type (as opposed to G-type AFMs or similar). If one requires antiferromagnetic coupling along more than one dimension, then this severely limits the types of phenomena that can be accurately studied in the system and in some cases no reasonable or similar model can be built. Nonetheless, the family of A-type antiferromagnets are sufficiently rich and interesting for this model to have widespread applicability and utility.

3.3.1 Micromagnetic simulation setup

All the simulations herein were performed using MuMax3 [98–100]. Following the description of the model presented above, my simulations are comprised of a set of tetragonal boxes, significantly shorter along the z-direction than in the x-y plane (see figure 3.1b). The cell size along the z-axis was fixed at 0.228 nm, corresponding to 1/6 of the unit cell and the spacing between AFM layers [4]. The total simulation size and cell size in the x-y plane was adjusted for each different texture type to ensure a good compromise between simulation time and texture scales in each case, given that the skyrmion and bimeron simulations took an order of magnitude longer to complete than the (anti)meron simulations. In all cases, different cell dimensions and total simulation dimensions were checked and found to be consistent and all satisfied the micromagnetic guideline of a maximum angle between adjacent moments of no more than 20° (in the x-y plane)[98], hence the choices made throughout are purely a matter of convenience.

The sublattice saturation magnetisation of α-Fe_2O_3 is 920 kAm^{-1} [4]. The IP exchange constant A in α-Fe_2O_3 (i.e. the ferromagnetic interaction between cells in the same layer) is around 14-17 pJm^{-1}[11] depending on the exchange parameters used to calculate it [4, 14] and this can be altered further via doping [82], justifying the range of values A = 10-20 pJm^{-1} investigated here. The AFM coupling between adjacent layers was

similarly calculated to be $A_{\mathrm{OOP}} = -20.1\,\mathrm{pJm^{-1}}$ and is kept constant throughout. As the long-range dipolar fields are negligible, the corresponding z-axis magnetic exchange length $l_{ex} = \sqrt{2A/(\mu_0 m_s^2)} \sim 1\,\mu\mathrm{m}$ (where m_s is the weak canted ferromagnetic moment) will be much larger than the simulation size along z, so I expect negligible texture variation in this dimension (consistent with all my simulations). I additionally confirmed that altering the cell size along z has no discernible effect on the textures, discussed further below, thereby further justifying this approach.

In α-Fe_2O_3, the effective anisotropy constant K_{eff} results from a competition of on-site and dipolar interactions [8, 12, 13], with the Morin transition T_{M} occurring when these two interactions balance (see figure 1.3). This competition can be tuned by strain (see chapter 7), chemical doping and reversible ionic control to alter T_{M} or destroy the transition altogether [13, 19, 104]. As both the on-site and dipolar anisotropies are temperature-dependent, the value of K_{eff} varies systematically either side of T_{M} and these values can be calculated and directly compared with my simulation data. For example, using the representative values $A = 14\,\mathrm{pJm^{-1}}$ and $D = 0.75\,\mathrm{mJm^{-2}}$, the maximum anisotropy value for which skyrmions are stable in these simulations were $K_{\mathrm{eff}} = 3.5\,\mathrm{kJm^{-3}}$ (see figure 3.8b, section 3.4.5). Based on a thin film with $T_{\mathrm{M}} = 240\,\mathrm{K}$, similar to that used in our previous experiments [11], this corresponds to a temperature of approximately 219 K, meaning that I estimate the skyrmion stability window to be on the order of 20 K below T_{M}, which is certainly a feasible range for practical observation of these textures. As I am not aware of any work studying or engineering possible iDMI strengths in α-Fe_2O_3 systems, I have used values of D throughout that are akin to those used in theoretical studies of iDMI in other materials ([40, 78, 79, 86]) and to those found in the large body of work on topological texture hosting Co-Pt heterostructures (e.g. [80, 105]).

3.3.2 Verifying the model

In order to verify the accuracy of this micromagnetic model, I performed a set of simulations of (anti)merons in the absence of iDMI in order to compare their scaling to both the analytical calculations presented in section 2.3 and previous experimental data [11]. This is presented in figure 3.2. One can draw several key conclusions from this data; firstly, it

is clear that the analytical calculations, micromagnetic data and previous experimental results are all consistent up to numerical factors of order 1. This demonstrates that the simulation scheme is entirely reasonable for reproducing the scaling of textures that I would expect from calculations and experiments. The discrepancies can be largely put down to the quality of the experimental data (which, due to the technique used, had a resolution of ∼50 nm[11]) and the numerical constants in equation 2.28 are a result of the specific simple ansatz used. I predict that using a more complicated ansatz based on the real radial profile would more accurately reproduces the meron profile and thereby reduce this discrepancy.

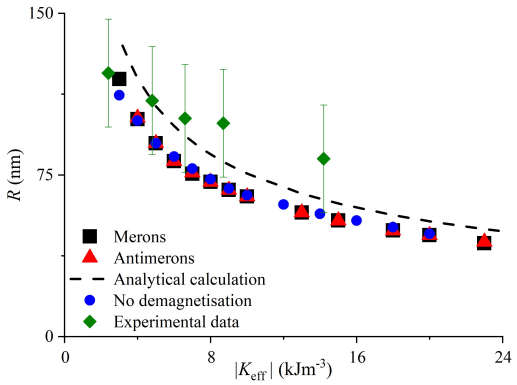

Figure 3.2: The scaling of merons (black squares) and antimerons (red triangles) as a function of the effective anisotropy without iDMI. The dashed line is an analytical calculation using eq. 2.28 in the limit $D_{\text{eff}} \to 0$. The blue circles show the radius of simulated merons with the demagnetising fields turned off and easy-plane anisotropy provided purely by K. The green diamonds show experimental data from [11].

Secondly, I performed a set of simulations both with and without demagnetising fields to demonstrate that they contribute only an effective anisotropy to first order as discussed above. This demonstrates that my model introduces no additional spurious effects due to the demagnetising fields and so I can include them organically rather than completely neglecting them, as has been done in other models of antiferromagnets [106, 107]. Finally, I note that in the absence of iDMI merons and antimerons scale identically, have no fixed chirality, and are both circularly symmetric; this is worth keeping in mind when I discuss the modifications of topological textures when iDMI is included.

As discussed in section 3.3, the size of the cells along the z-direction was chosen to be 0.228 nm. This is to accurately model the spacing between AFM layers in α-Fe_2O_3, despite technically violating the micromagnetic requirement that the cells are large enough to ignore atomic effects. I have argued that, due to the AFM coupling between cells along the z-direction and the associated long exchange length that results in no magnetic variations along $\hat{z}$, this choice is valid as a model of an A-type antiferromagnetic system.

z-axis cell size (nm)	meron FWHM (nm)
0.229	71.8 ± 0.5
0.4	71.8 ± 0.5
0.6	73.5 ± 0.5
0.8	73.5 ± 0.5
1.0	73.5 ± 0.5
1.2	73.5 ± 0.5
1.4	73.5 ± 0.5
1.6	73.5 ± 0.5
1.8	73.5 ± 0.5
2.0	73.5 ± 0.5

Table 3.1: The meron FWHM in nm stays basically constant as I vary the size of the cells in the z-direction between the value used throughout these simulations (0.229 nm) and larger values more typical of micromagnetic simulations (1−2 nm). The same micromagnetic parameter values ($A = 17\text{pJ m}^{-1}$, $K_{\text{eff}} = 15\text{kJ m}^{-3}$ and no iDMI) are used for all the above simulations.

To demonstrate this further, table 3.1 shows that altering the size of the simulation cells along the z-axis has a very minimal effect on the size of merons present in the system. This includes cell sizes in the range 1−2 nm, which are perfectly reasonable length scales in the micromagnetic regime. Hence, I am confident that this choice of a thin cell is reasonable and should have no discernable effect on my simulation results. This justifies the statement that this choice is more cosmetic (to match the simulations directly to a physically relevant system) than practically relevant. This can also be seen in the analytical calculations (section 2.3), where the (anti)meron radius is found to be independent of the layer thickness (t).

3.4 Topological textures in α-Fe_2O_3 with iDMI

3.4.1 Merons

As merons require easy-plane anisotropy and therefore are observed in α-Fe_2O_3 for $T > T_M$ [11], I use values of K_{SI} such that $K_{\text{eff}} < 0$. To study the effects of iDMI I included a non-zero D applied only to the top-most AFM layer to simulate a very short-range interaction at the interface with a heavy-metal overlayer (e.g. Pt) [78]. Comparison between the sizes of the resulting merons to the analytical expression in equation 2.28 is shown in figure 3.4. As expected, the presence of iDMI enforces a specific chirality, making all such merons Néel type (figure 3.3a). The scaling with A and $|K_{\text{eff}}|$ is, to lowest order, similar to that found for the case of a meron without iDMI and the analytical

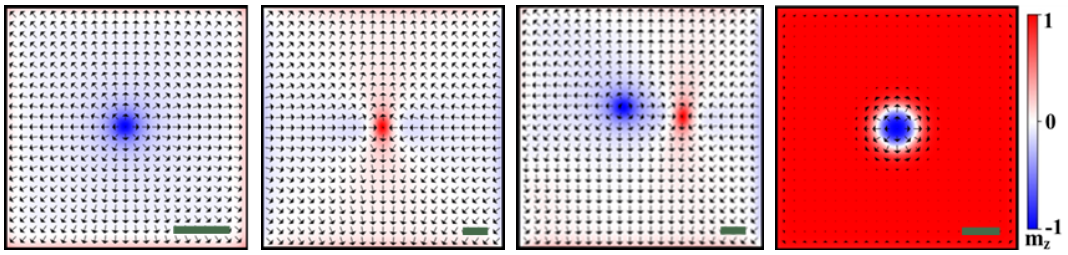

(a) Néel meron **(b)** Antimeron **(c)** Néel Bimeron **(d)** Néel Skyrmion

Figure 3.3: A gallery of topological textures stable in α-Fe_2O_3 when an iDMI is included from my micromagnetic simulations. In all cases only a single AFM layer is shown. The black arrows represent the in-plane sublattice magnetisation direction averaged over several adjacent cells and the colours correspond to the z-component of the sublattice magnetisation. The green scale bar in the bottom-right corner of each figure is 100 nm.

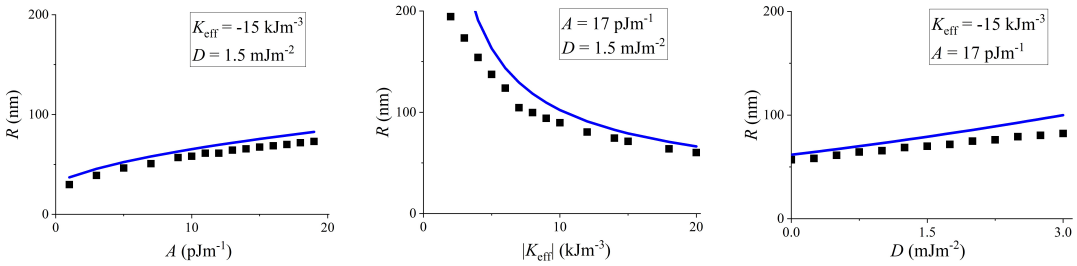

(a) **(b)** **(c)**

Figure 3.4: Radius R of *meron textures*, based on micromagnetic simulations (black points) and analytical calculations (blue lines). The iDMI was included in all cases. A, $|K_{\text{eff}}|$ and D were varied in panels (a), (b) and (c) respectively, with the rest of the parameters kept constant.

form 2.28 provides a satisfactory approximation to the simulations. The key trends are that the meron radius increases if the strength of the exchange or DMI increases, whilst decreasing rapidly with increasing IP anisotropy. There appears to be some difference in the actual FWHM values when comparing the simulations and analytics, which is not surprising, since the numerical prefactors contained in l_w and κ are strongly affected by the choice of the ansatz; calculations for a different ansatz would give different numerical factors [83]. The qualitative agreement between my computational model and analytical calculations demonstrate that this approach is both reasonable and internally consistent.

The scheme introduced above of applying the iDMI only to the top-most AFM layer was used throughout my simulations. In [78], by performing density functional theory calculations on Co/Pt interfaces they found that the largest contribution to the iDMI energy comes from the Co atoms immediately adjacent to the interface, with a significantly

Label	iDMI per layer ($\mathrm{mJm^{-2}}$)	FWHM (nm)	Description
Type 0	1|0|0|0|0|0	81.6 ± 0.5	iDMI applied only to the topmost layer as used throughout.
Type 1	1|-0.15|0|0|0|0	80.0 ± 0.5	Some iDMI penetrates into the second layer with sign reversed.
Type 2	1|0.1|0|0|0|0	81.6 ± 0.5	A small amount of iDMI penetrates into the second layer.
Type 3	1|-0.1|-0.15|0|0|0	77.5 ± 0.5	Similar to that calculated for three Co|Pt layers in [78].
Type 4	1|0.1|0.01|0.001|0|0	81.6 ± 0.5	A logarithmic penetration of the iDMI into the first 4 layers.
Type 5	1| $\frac{1}{2}$ | $\frac{1}{3}$ | $\frac{1}{4}$ | $\frac{1}{5}$ | $\frac{1}{6}$	105.6 ± 0.5	A situation where the iDMI penetrates deep beyond the top layer.

Table 3.2: A summary of the several types of alternate iDMI configurations tested for the case of a meron, along with a short description of what they represent. In each case, the numbers separated by vertical bars represent the iDMI constant of each layer working down from top layer (leftmost value), which was fixed at $D = 1\ \mathrm{mJ\,m^{-2}}$. The exchange ($A$) and anisotropy ($K_{\mathrm{eff}}$) were set at $14\ \mathrm{pJ\,m^{-1}}$ and $15\ \mathrm{kJ\,m^{-3}}$ respectively.

smaller amount coming from the second and third atomic layers. Applying the iDMI only to the topmost layer follows this scheme well, with the understanding that a small amount of iDMI penetrating into further layers will only slightly alter the effective iDMI constant. To justify this choice further, I simulated a set of merons with a set of different iDMI configurations, which are summarised in table 3.2. The goal was to test a broad range of different configurations, as the iDMI that can be generated in α-Fe_2O_3 is unknown; therefore it is reasonable to test even some extreme, physically unrealistic situations to explore the limits of this model. Type 1-3 configurations were inspired by [78] and were used to test if small variations that were physically plausible had any sizeable effects on the merons. Type 4 was used to study a deeper logarithmic iDMI penetration beyond the first layer. Type 5 was a very extreme case, where significant amounts of iDMI penetrate into the deeper layers, meaning that it is physically unrealistic but serves as a good benchmark of the worst-case scenario for how these simulations could divert from experimental data if the iDMI configuration is significantly different. It's apparent that any penetration of the iDMI beyond the first layer has a small effect on the size of the meron, up to about 25% for the most extreme case tested above. For textures such as bimerons and skyrmions, whose stability is dependent on the strength of D_{eff}, the alternative configurations would alter the stability window and texture sizes slightly but should have no other major effects.

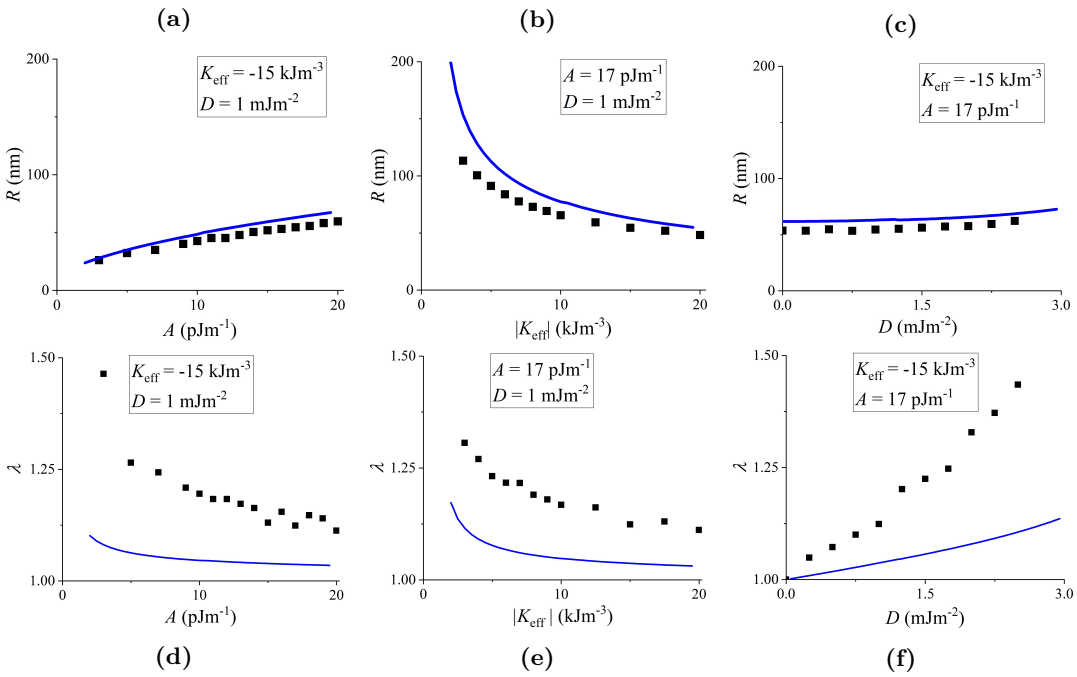

Figure 3.5: Radius R (a-c) and distortion parameter λ (d-f) of *antimeron textures*, based on micromagnetic simulations (black points) and analytical calculations (blue lines). The iDMI was included in all cases. A, $|K_{\text{eff}}|$ and D were varied in panels (a,d), (b,e) and (c,f) respectively, with the rest of the parameters kept constant.

3.4.2 Antimerons

I performed simulations of isolated antimerons with iDMI and found that they were indeed stable and distorted, as shown in figure 3.3b. Using the calculated effective radius R and distortion parameter λ of distorted antimerons from equation 2.43, I compared the simulated scaling with the analytical values, as shown in figure 3.5. The analytical curve was calculated iteratively using both parts of equation 2.43 for the same set of values of A, $|K_{\text{eff}}|$ and D used in the simulations and with the cut-off radius R_{c} set to the simulation radius. It should be noted that varying R_{c}, even by an order of magnitude, has a minimal effect on the resulting analytical radius.

Here, the antimeron radius increases with increasing exchange strength, is roughly independent of the iDMI strength and decreases rapidly as the IP anisotropy increases. The scaling of antimerons as a function of A, $|K_{\text{eff}}|$ and D is qualitatively similar to merons; however, there is again a slight difference between the analytical and simulated radius due to the ansatz choice. Whilst the scaling of the distortion with the various

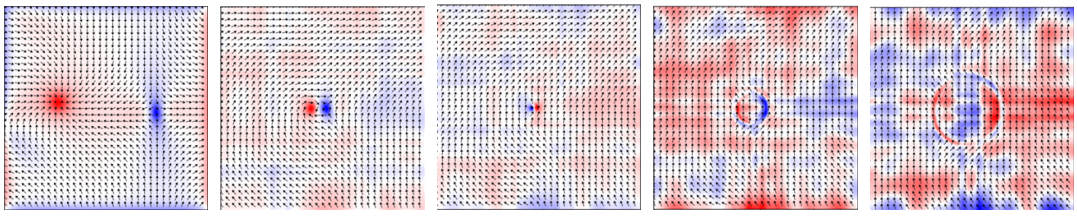

(a) (b) (c) (d) (e)

Figure 3.6: Collapse of an unstable bimeron with a weak iDMI. Snapshots of the process are presented sequentially and show (a) the initial state, (b) after the two cores have approached, (c) immediately before collapse, (d) immediately after collapse and (e) a short time after collapse.

energy terms matches qualitatively, the analytically calculated value of the distortion parameter λ is consistently smaller compared to the value extracted from the simulations, by a factor of $\approx$ 3-5. Despite these caveats, the scaling behaviour of R in both the analytical and simulated antimerons match reasonably well and they both predict that antimerons should distort in the presence of iDMI.

3.4.3 Bimerons and topologically trivial meron pairs

In a previous experimental work [11], we reported the observation of meron-antimeron pairs in α-Fe_2O_3, which could either be topologically trivial meron pairs or topologically non-trivial bimerons, depending on whether the core polarization of the constituent (anti)merons are aligned or anti-aligned respectively (as discussed in section 1.2). I note here that bimerons are topologically equivalent to skyrmions and so share all of the potential applications proposed for such structures [27, 28, 108]. Since constructing an analytical model for such compound objects using a realistic ansatz is difficult, I investigated their properties using micromagnetic simulations, noting here that the simplified bimeron calculation in equation 2.50 will be shown to inaccurately reproduce important scaling and thresholds present in the simulations. To create a bimeron, I initialised a meron-antimeron pair in the system that is either a TTMP or a bimeron in the IP state ($K_{\text{eff}} < 0$) by placing a meron in one half of the simulation and an antimeron in the other half with the desired core polarities. I then allow them to relax through the energy minimisation procedure into their preferred configuration. A structure that survives this process must be at least a local minimum and have a non-zero energy

barrier to energetic collapse into the uniform ground state, whereas any structure that collapses is not an energetic minimum.

I observe that neither TTMPs nor bimerons are stable in the absence of iDMI, or when the iDMI is weak. The observed collapse indicates that the competition between exchange and anisotropy energies alone is insufficient to stabilise such textures; this is in contrast to (anti)merons studied above and is despite the supposed topological protection of bimerons. Several stages in the collapse process of bimerons are shown in figure 3.6, performed by evolving an initial meron-antimeron pair with total topological charge $Q = 1$ as a function of time using the LLG equation 3.6. These snapshots show the meron and antimeron approaching until their inter-core distance is below the scale of the simulation, at which point they annihilate and generate a circular spin wave that propagates outwards from the annihilation point. I note that micromagnetic simulations cannot be accurately used to study these short-lengthscale collapse mechanisms, for which atomic simulations are more suitable [109, 110]. The collapse process for the topologically protected bimerons appears to be largely a consequence of the finite cell size of the system and qualitatively follows the annihilation mechanism for ferromagnetic vortices discussed by others previously [111, 112]. Given that atomic systems are ultimately finite as well, this is expected to occur for real systems and is not an artefact of the discretisation scheme used here. This collapse phenomena was studied in more detail by a colleague using atomic simulations and is presented in [96].

If I introduce a stronger iDMI into the system, bimerons become stable over a very wide parameter range as shown in figure 3.3c. By varying the initial inter-core spacing of the meron-antimeron pair, I confirmed that the final state is largely independent of this initial spacing, meaning that bimerons are now stable even when initialized at very close distances ($\leq$ 150 nm). On the other hand, TTMPs are found to only be stable if they start a long way apart, at which point they could be considered as isolated (anti)merons. This makes phenomenological sense as bimerons have a net topological charge and therefore should be prevented from collapsing due to the finite energy barrier afforded by iDMI, which is expected to be absent in TTMPs. For small values of A, the inter-core distance remains large for all values of $|K_{\text{eff}}|$, whereas for larger values of A the

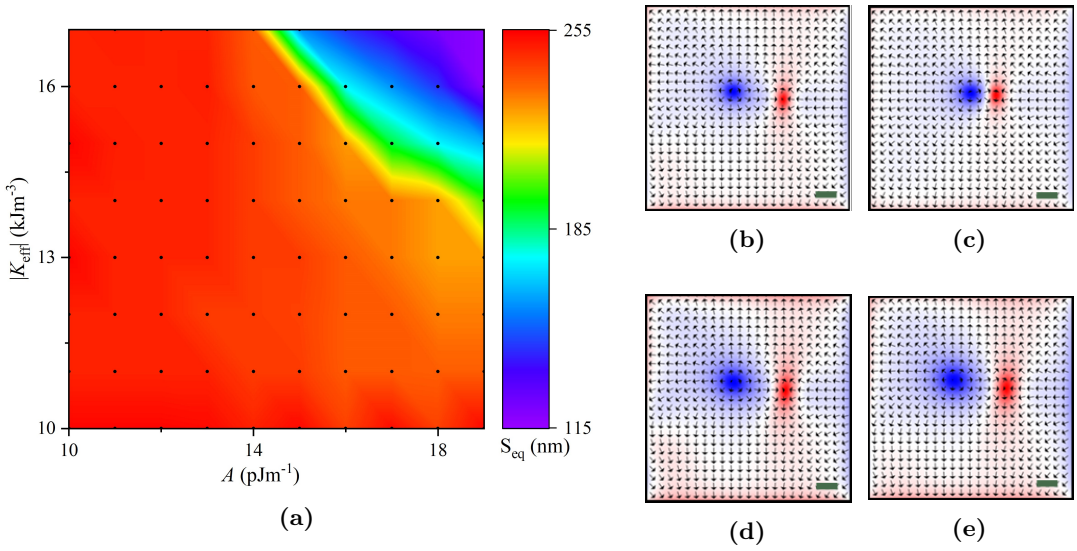

Figure 3.7: (a) Relaxed Néel bimeron inter-core distance s_{eq} as a function of A and $|K_{\mathrm{eff}}|$ for $D = 2\ \mathrm{mJ\,m^{-2}}$. The simulation points are given by black squares. (b)-(d) Snapshots of the relaxed configuration in one of the layers for several points in the diagram, where the arrows represent the IP spin direction and the colour contrast represents the z-component of the magnetisation as in figure 3.3. The green scale bar in the bottom-right corner is 100nm. The images correspond to the values: (b) $A = 14\ \mathrm{pJ\,m^{-1}}$, $K_{\mathrm{eff}} = -17\ \mathrm{kJ\,m^{-3}}$, (c) $A = 19\ \mathrm{pJ\,m^{-1}}$, $K_{\mathrm{eff}} = -17\ \mathrm{kJ\,m^{-3}}$, (d) $A = 14\ \mathrm{pJ\,m^{-1}}$, $K_{\mathrm{eff}} = -10\ \mathrm{kJ\,m^{-3}}$, (e) $A = 19\ \mathrm{pJ\,m^{-1}}$, $K_{\mathrm{eff}} = -10\ \mathrm{kJ\,m^{-3}}$.

inter-core distance is highly tunable as a function of $|K_{\mathrm{eff}}|$, see figure 3.7. Fundamentally, the size scaling of tightly-bound bimerons can depend only on the dimensionless parameter κ and the length scale l_{w} introduced in section 2.3.1. It should be noted that the antimeron component is distorted, as in the case of isolated antimerons studied above, causing the bimeron to lose circular symmetry [113].

Whilst these simulations do not address the question of the barrier height directly, one can make some general observations. Assuming a quadratic potential around the equilibrium inter-core (anti)meron separation s_{eq}, the energy of a bimeron can be approximated (up to quadratic order) as

$$E(s) = \alpha + \beta s + \gamma s^2, \tag{3.7}$$

where α, $\beta < 0$ and $\gamma > 0$ are unknown phenomenological parameters that enforce a positive-curvature quadratic with $s_{\mathrm{eq}} > 0$. For certain simple ansatz, such as the linear bimeron, one can identify these three parameters with the micromagnetic parameters

A, D_{eff} and K_{eff} respectively, up to some numerical factors (equation 2.47). As a result, the equilibrium separation is $s_{\text{eq}} = -\beta/(2\gamma) \propto D_{\text{eff}}/K_{\text{eff}}$ and the barrier height is $\Delta = E(0) - E(s_{\text{eq}}) = \beta^2/(4\gamma) = -0.5\beta s_{\text{eq}} \propto D_{\text{eff}}^2/K_{\text{eff}}$. It is clear from the simulation data that the exchange strength A does play a role in determining the bimeron size and therefore likely the barrier height, which is not accounted for in the linear bimeron solution, meaning that the relationship between the phenomenological and micromagnetic parameters is in reality more complicated. Regardless of the exact expression, these considerations indicate that the route towards experimentally realizing closely-bound, stable bimerons is to maximise Δ and minimise s_{eq} at the same time, which requires increasing both D and K_{eff}.

3.4.4 Comparison with experiments

When comparing the present results with experiments ([11, 45, 114] and as will be discussed in chapters 5-7) there is an apparent contradiction. Experimentally, it is continually observed that merons in α-Fe_2O_3 have varied chirality, which seems to rule out the presence of significant iDMI; however, I also observe meron-antimeron pairs that appear to be quite robust, demonstrating that their lifetimes must be extremely long and implying that the associated energy barrier to annihilation is large. In my simulations, this is only possible in the presence of iDMI. These contrasting observations suggest that an alternative mechanism not accounted for in this micromagnetic model might be responsible in the real system for the apparent stability of these pairs. In terms of the phenomenological model discussed earlier, this means that some additional energy term, other than the exchange, anisotropy and iDMI considered throughout, likely contributes to the barrier height Δ. An alternative explanation is that the potential landscape is locally flat, allowing both bimerons and TTMPs to be trapped by local defects even in the absence of an 'intrinsic' potential barrier. This implies that a phenomenological model would need to go beyond the quadratic approximation to accurately model these effects, such that the inter-core force need not always increase with distance from some equilibrium position.

For practical implementation of homochiral bimerons in α-Fe_2O_3 based racetrack applications, one cannot rely on defects or other local pinning mechanisms to achieve stability because the bimerons must be *mobile*. Therefore, this application requires that

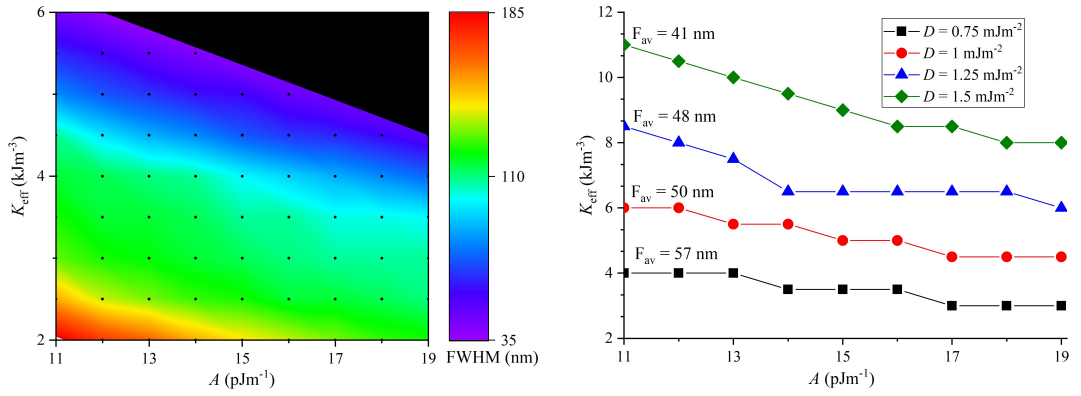

Figure 3.8: a) Néel skyrmion stability window as a function of A and K_{eff} for $D = 1\,\text{mJm}^{-2}$. The colour scale represents the relaxed FWHM of the skyrmions and the black area shows the region where the skyrmion was found to radially collapse and therefore was unstable. The A and K_{eff} values for which simulations were performed are shown by black squares. b) K_{eff} vs A curves at constant skyrmion radius, calculated for the smallest size for which a skyrmion can be stabilised in these simulations (given by the F_{av} value next to each line). Symbols/colours correspond to different iDMI strengths.

bimerons exist in a local energy minimum at a small inter-core distance s_{eq} between the meron and antimeron as well as with a large energy barrier Δ to prevent bimeron annihilation. My simulations clearly imply that it should be feasible to engineer the material parameters in such a way as to achieve this goal and that this can only be achieved by topologically protected bimerons (rather than TTMPs) in the presence of a reasonably strong iDMI.

3.4.5 Topological skyrmions

Here, I discuss the possibility to stabilise *antiferromagnetic skyrmions* in α-Fe_2O_3. These have not been observed experimentally thus far (although there has been a tenuous report of antiskyrmions , see supplementary information of [48]) but, as I demonstrate here, are stable in these simulations over a wide range of material parameter values. In α-Fe_2O_3 a skyrmion can only exist in the easy-axis phase ($T < T_{\text{M}}$) due to the symmetry requirements of the associated ground state manifold. This is interesting, as it means that their experimental discovery would significantly increase the flexibility of this material system, as topological textures have currently only been observed for $T > T_{\text{M}}$. The predictions here also apply to other A-type AFMs with OOP anisotropy, provided their

material parameters can be engineered to lie within the window of stability. It is worth pointing out that the Morin temperature can be raised well above room temperature by chemical doping [11, 19, 114], allowing practical exploitation of such skyrmions. It will also be shown later in this thesis (chapter 7) that strain is a convenient handle to tune the transition point. As in the case of bimerons and of skyrmions in other systems without bulk DMI, it is necessary to have a sizeable iDMI to stabilise these textures [76, 86, 115, 116]. I therefore initialised a Néel skyrmion with $K_{\text{eff}} > 0$ (i.e. an easy-axis anisotropy along z) in the presence of an iDMI. An example of such a skyrmion can be seen in figure 3.3d and the full stability window for a range of A, K_{eff} and D values is shown in figures 3.8a and 3.8b. For a wide range of micromagnetic parameters, the skyrmion remained stable and either grew or shrunk to an equilibrium size. As expected, these skyrmions are always Néel type, which is favoured by the iDMI. Consequently, when I initialised a Bloch type skyrmion the spins globally rotate into the Néel configuration. Some further examples of stabilised skyrmions of different sizes and the more exotic skyrmionium are shown in B.1, appendix B.

I also studied the tuning of physical parameters (A and K_{eff}) required to minimise the skyrmion size in this system for a given D (see figure 3.8b). The data in figure 3.8 points towards a threshold radius, below which the skyrmions spontaneously evaporate via radial collapse [109, 110]. This is likely due to a breakdown in the micromagnetic regime (where the finite cell size is on the same order as the length scale of variations). Hence, the sizes shown in figure 3.8b in fact represent an upper limit to the minimum achievable skyrmion size in this material system, and in fact smaller skyrmions that cannot be reasonably simulated using micromagnetics may also be stable. This shows the potential to generate ultra-small antiferromagnetic skyrmions for practical applications in α-Fe_2O_3.

As can be seen in figure 3.8b, increasing the iDMI strength D or decreasing the exchange coupling A increases the maximum anisotropy K_{eff} for which skyrmions are stable. Given the nature of the Morin transition, increasing the strength of K_{eff} for $T < T_{\text{M}}$ at fixed A corresponds to reducing the temperature of a given sample. Therefore, to maximize the thermal stability window for skyrmions in α-Fe_2O_3, one would need to engineer films with weak exchange (A) and large iDMI (D). Based on our previous data

for K_{eff} vs T (see also figure 1.3), this is already of the order of 20 K for the smallest value of D considered here. This is important to understand as applications for AFM skyrmions require a large window of thermal stability around room temperature.

To conclude this section, I emphasize a key prediction of my micromagnetic model: the long sought after *antiferromagnetic skyrmion* should be stable and therefore observable in α-Fe_2O_3 and potentially other A-type antiferromagnets. Whilst the possibility of stabilising skyrmions in easy-axis AFMs with iDMI has been studied previously, I push this further by proposing a specific system where the material parameters are appropriate, or can be engineered to be appropriate in a well-understood manner, for their stabilisation and experimental verification.

3.5 Phenomenological scaling

To conclude this presentation of simulated topological structures in α-Fe_2O_3, I discuss the size scaling of various topological textures described herein and demonstrate that these micromagnetic simulations recreate the phenomenological scaling one can expect from simple dimensional analysis. The three material parameters in my simulations have dimensions $[A] = \mathrm{J\,m^{-1}}$, $[K_{\text{eff}}] = \mathrm{J\,m^{-3}}$ and $[D_{\text{eff}}] = \mathrm{J\,m^{-2}}$. From these three parameters, one can form a *single unique* dimensionless parameter $\kappa' = D_{\text{eff}}/\sqrt{AK_{\text{eff}}}$ and a length scale $l'_{\text{w}} = \sqrt{A/K_{\text{eff}}}$. All length scales in the problem must be proportional to l'_{w} multiplied by a dimensionless function of κ', this is consistent with the analytical calculations presented earlier (equations2.28 and 2.45). Hence, if one were to divide all the relevant sizes of the textures, as extracted from these simulations, by l'_{w}, the results should scale as a function of κ' only. This is demonstrated in figure 3.9, where the texture radii are rescaled by $l_{\text{w}} = \eta\sqrt{A/K_{\text{eff}}}$, which is the relevant length scale for the linear (anti)meron ansatz as discussed above (see section 2.3.1), and then plotted as a function of κ'. This analysis has two purposes: firstly, to compare the simulated textures to various analytical models presented here and other skyrmion models [86, 116] in the literature; secondly, to establish whether or not the simulations have reached equilibrium, which is a precondition for scaling.

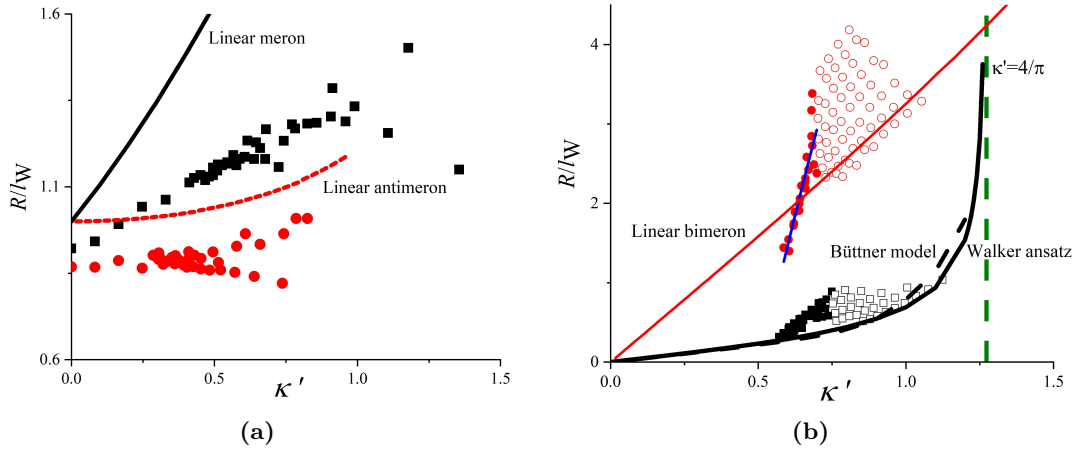

Figure 3.9: a) Rescaled radii of simulated merons (black squares) and antimerons (red circles) as a function of $\kappa' = D_{\text{eff}}/\sqrt{AK_{\text{eff}}}$ compared to the corresponding linear (anti)meron ansatz (equations 2.28, 2.45). b) Rescaled radii of skyrmions (black squares) and bimerons (red circles). In each case the filled-in symbols show the smaller textures in the approximately linear scaling regime and open symbols show larger textures where the energy landscape is predicted to be very flat. An analytical linear bimeron model and two different skyrmion ansatz [86, 116] are shown for comparison. The blue line is a linear fit to the small radii bimerons. The vertical green dashed line shows the well-known upper stability threshold for skyrmions at $\kappa' = 4/\pi$, demonstrating that my simulated skyrmions don't reach this threshold for any material parameters considered herein.

Concerning the first point, for the (anti)meron textures (figure 3.9a) it is clear that the linear ansatz models reproduce the observed functional scaling to a good approximation, only differing by numerical factors of order one, which is consistent with my discussions throughout. The same is not true for bimerons (Fig. 3.9b), which clearly display a different functional dependence from the linear approximation (see equation 2.50), although the sizes are of the correct order of magnitude. I also report the scaling for simulated AFM skyrmions, which is in good agreement with established skyrmion models in the literature within the range of stability. A straightforward observation is that skyrmions are generally much smaller than bimerons in the whole range of parameters explored herein, suggesting that they might be more suitable textures for applications of A-type antiferromagnets. Additionally, whilst many analytical skyrmion models predict a stability threshold for larger κ', they fail to predict the lower threshold for κ'. This is because these are all continuum models that do not account for the atomic nature of the system, which becomes important as the skyrmion approaches smaller length scales.

Turning to the second point, there is a clear distinction between smaller and larger

skyrmions/bimerons; whilst smaller textures scale roughly linearly with κ', larger textures do not obey any obvious scaling. This is likely because they have not reached their equilibrium radii due to the locally flat energy landscape about the equilibrium (which can be seen by studying the solutions in [86]). In this regime, a range of different sized textures are observed within the simulation tolerances for a given κ'. I remark that the textures of interest for applications, namely those that are small, are also those that fortuitously obey the expected scaling law as a function of κ'. I also note that this spread of texture sizes for a given κ' is not necessarily just an artefact of the simulations, as local strain and thermal fluctuations could also lead to this effect in a real system and this will be most pronounced when the energy landscape is locally flat near the equilibrium.

3.6 Simulations from random configurations

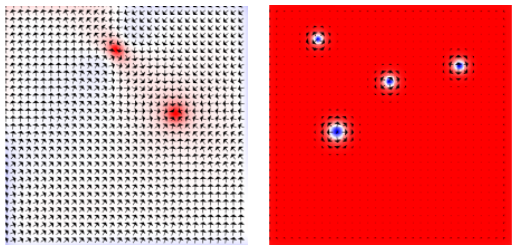

(a) $T > T_{\mathrm{M}}$ **(b)** $T < T_{\mathrm{M}}$

Figure 3.10: Example minimised simulation configurations showing (a) topological (anti)merons and (b) skyrmions in the presence of iDMI after starting from a randomised initial state. Parameters used were: $A = 17\,\mathrm{pJm^{-1}}$, $K = 15\,\mathrm{kJm^{-3}}$, and $D = 2\,\mathrm{mJm^{-2}}$.

All of the topological texture simulations above were initialised with the texture already present and I then studied their scaling and the conditions under which they were stable. Crucially though, this does not help to determine whether such structures can form in the first place. To this end, I performed a set of simulations starting from a randomised configuration and then allowed the system to energetically relax as before for a range of parameter values. This led to a variety of final configurations, including trivial fully-aligned states, multi-domain states separated by ADWs, and topological states. Some examples of the latter case are shown in figure 3.10. The minimisation process here is highly volatile, as a slight variation in the initial randomised state could in principle lead to a vastly different final state. This does, however, help to demonstrate an important point; topological textures can be generated in this system through random processes and once this occurs they can be stabilised. Such a random initial state is reminiscent of a Kibble-Zurek

quench through a phase transition [20–23] (see section 1.2). This suggests that, for an AFM with such a phase transition, topological textures may be generated by passing through the transition and then will persist provided they are energetically stable. This corresponds strongly with the process that was observed previously in α-Fe_2O_3 thin films [11] and will be explored in detail later through both thermal and athermal mechanisms of crossing the transition (chapters 5 and 7).

3.7 Grains in AFMs

In order to understand the effects crystal grains might have on domains in α-Fe_2O_3, I performed a set of simulations utilising a model of different grains in the AFM. This was done by randomly generating a set of grains through the inbuilt functionality in MuMax3 [98], keeping this consistent across the different layers along the z-axis. The average size of the grains can be adjusted, provided this is between the cell size and the total simulation size. The rest of the simulation follows the model for AFM systems used throughout this chapter, but without an iDMI for simplicity. Each grain was randomly assigned a different anisotropy strength up to 10% different from the bulk anisotropy and the anisotropy axis was randomly allowed to vary up to a few degrees from the default z-axis.

I performed a set of simulations with different grain sizes for $T > T_{\mathrm{M}}$ ($K_{\mathrm{eff}} < 0$), shown in figure 3.11. In each case, the grains were randomly generated and the system started from a random magnetic configuration and was allowed to relax through energy minimisation as usual. The colour scale for the grain configurations shows that the local anisotropy in each grain (K_g) is allowed to vary by ± 10% from the default value, set at -15 $\mathrm{kJ\,m^{-3}}$. It's clear to see that the magnetic structure strongly follows the grain structure present in the sample in each case shown here. This would be expected in any case when the lengthscale of the domains is on the same order of magnitude as the magnetic exchange length. This also demonstrates that topological textures (such as the antimeron that randomly nucleated in figure 3.11f) tend to stabilise at the intersections between several different grains, suggesting that this could cause repeatable nucleation of textures at a fixed location.

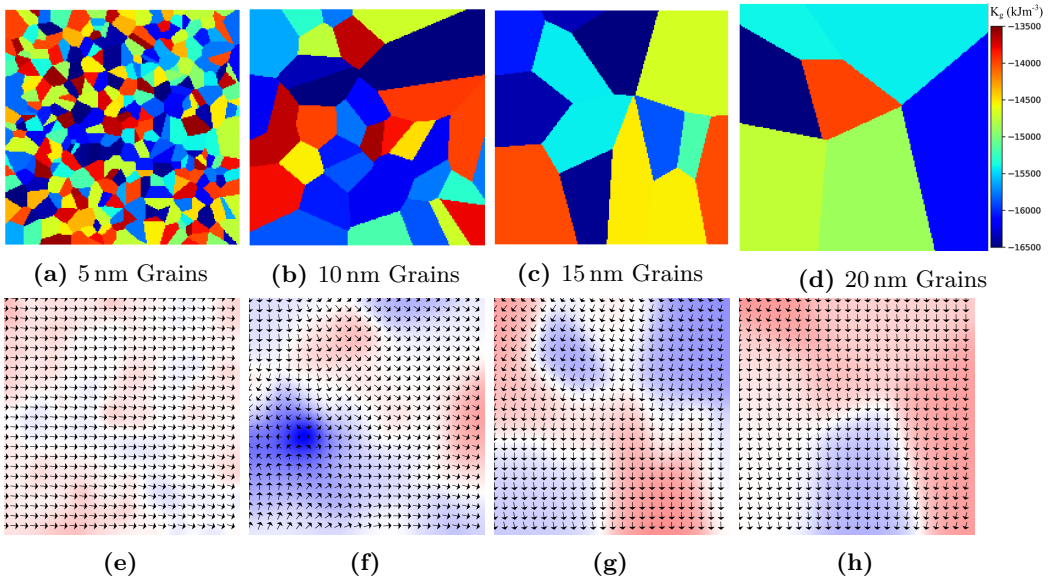

Figure 3.11: (a-d) Local anisotropy in randomly generated grain configuration and (e-h) associated AFM configuration after energy minimisation procedure, starting from a randomised initial state.

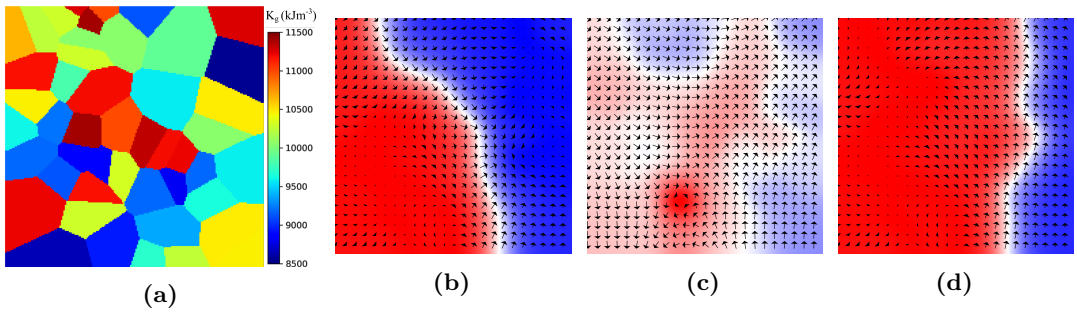

Figure 3.12: a) Randomly generated grain structure, with the colours giving the anisotropy constant K in that grain. b-d) simulated domain structures in one of the AFM layers for the three states (b) $T < T_M$, (c) $T > T_M$ and (d) back to $T < T_M$. Simulation (b) was started from a simple two-domain OOP state and (c,d) started from the end state of (b,c) respectively.

For $K_{eff} > 0$, i.e. $T < T_M$, I initialised the system with two oppositely-oriented OOP domains separated by a narrow IP domain wall, which was then allowed to relax in the presence of the grain structure shown in figure 3.12a, resulting in the configuration shown in figure 3.12b. It's clear to see here that the domain wall has distorted away from the shortest path across the simulation, which in the absence of the grain structure would minimise the energy, to more closely (but not exactly) follow the grain boundaries. The absence of an iDMI means that the domain walls and other structures observed in this section were all multichiral.

From this state, reducing the anisotropy to make $K_{\text{eff}} < 0$, but keeping the same grain structure and associated modulation allows for an approximate simulation of the Morin transition, resulting (after energy minimisation) in a stabilised antimeron at the boundary of a few grains and a spatially varying IP domain structure otherwise (figure 3.12c). Not only is this a nice demonstration of merons forming serendipitously when the simulation is allowed to pass through the transition holistically, but also clearly identifies grain boundaries or similar defects as likely nucleation centres for topological textures. This will be particularly relevant for discussions relating to defect densities in different types of AFM membranes in sections 4.4.1 and 5.4. I note that this does not happen every time, as a repeat of the simulation with a different randomised grain structure does not result in the stabilisation of a topological texture, shown in figure B.2, appendix B.

Increasing the OOP anisotropy again to return to the state with $K_{\text{eff}} > 0$ and allowing the system to once again energetically relax generates the state shown in figure 3.12d. Here, the result is a state that is pretty similar to the initial state (figure 3.12a) but with the domain wall following a slightly different path around the grains in the sample. This suggests that grains or other defects present in a sample will likely determine the paths that domains/domain walls will take through a sample and, moreover, that repeated cycles through the Morin transition may lead to some reproducibility in the state of the sample, rather than the purely random configurations expected from a typical KZ quench in an idealised system [20, 21]. This will be explored further in section 5.4.

3.8 AFM/FM interface simulations

In addition to a full set of simulations studying topological textures in α-Fe_2O_3, I also performed simulations studying the coupling between magnetic structures at an α-Fe_2O_3/Co interface. The main purpose of this was to guide a separate set of experimental investigations focused on growing thin Co layers and Co/Pt multilayers on α-Fe_2O_3 thin films and membranes, which is not otherwise within the scope of the thesis. As the coupling at the α-Fe_2O_3/Co interface is not known a priori, I explored the phase space of coupling between the two cases. Ultimately, this is a 5-dimensional phase space, with three exchange parameters and two anisotropy parameters, therefore it is only reasonable to take specific

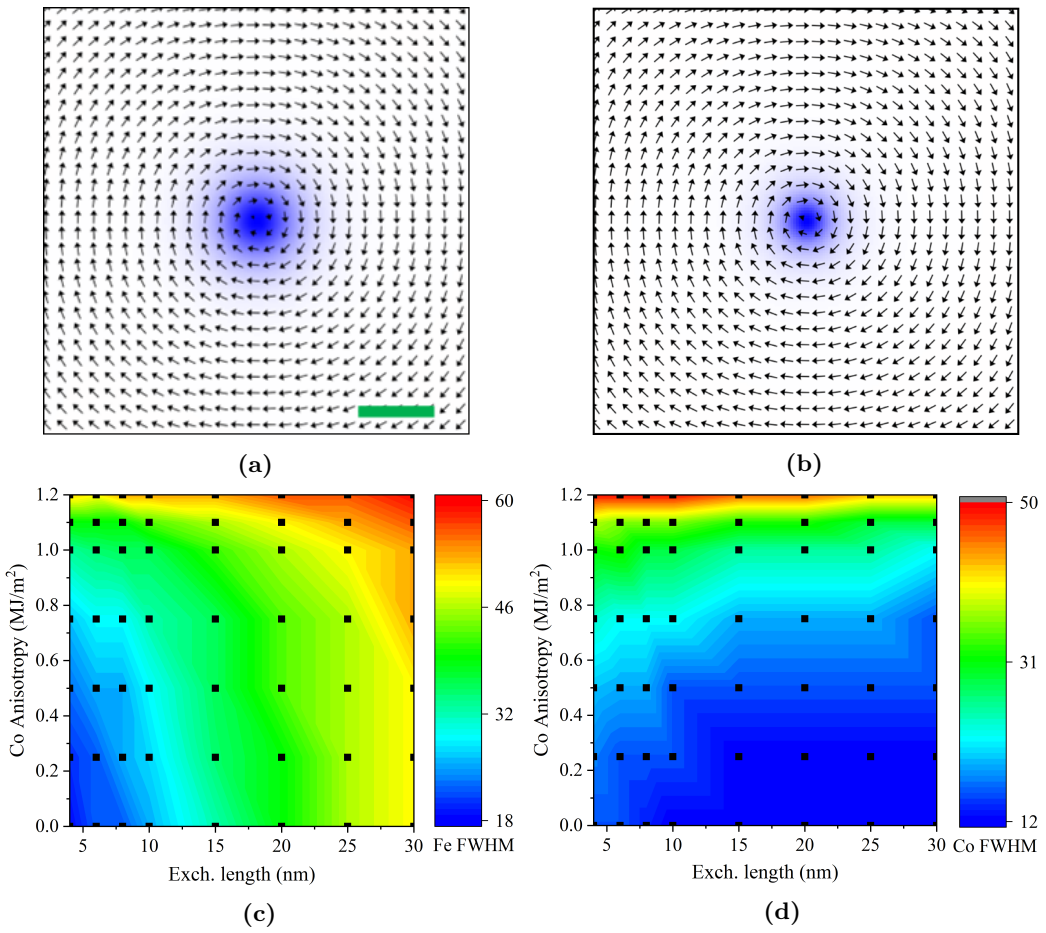

Figure 3.13: Simulated meron structure in an α-Fe_2O_3/Co interface shown as slices through (a) the top-most AFM layer and (b) the interfacial FM layer. Both (a) and (b) are on the same scale and the green bar in the bottom right corner of (a) is 50 nm. The FWHM of merons in the AFM and FM case are shown in (c) and (d) respectively as a function of the interlayer exchange and FM anisotropy. The simulated points are shown by black squares and the colours are interpolated FWHM parameters across the whole phase space.

slices through this phase space. In addition, when I introduced iDMI into the Co layer this adds an additional dimension to the phase space, thereby increasing the complexity further.

The main goal of these simulations was to explore how the sizes of merons present in the AFM and FM layers are correlated and how these depend on both the interlayer coupling and the anisotropy of the FM layer. Here, 12 AFM layers and 5 FM layers were used and the interfacial exchange between the top AFM layer and the bottom FM layer was allowed to vary. The same values for inter- and intra-layer exchange within the α-Fe_2O_3 as the rest of the simulations in this section were used and the Co-Co exchange parameter is 18 pJm^{-1}, consistent with what has been used for micromagnetic

studies of Co previously [83, 117]. The applied OOP Co anisotropy was varied, but the demagnetising fields contribute an IP anisotropy of order $1.3\,\mathrm{MJm^{-3}}$ and hence any anisotropy input less than this reduces the effective strength of the anisotropy up to the transition between IP/OOP states, i.e. the strongest IP anisotropy is when the Co anisotropy parameter $K_{Co} = 0$. Following the approach in [83], the relationship between the interfacial exchange length $L_{ex,I}$ and the associated exchange parameter $A_{ex,I}$ is

$$L_{ex,I} = \sqrt{\frac{2A}{A_{ex,I}}\, d\, D_z}, \tag{3.8}$$

where A is the exchange parameter of either the FM or AFM layer [83, 118]. d is the thickness of the interfacial region, taken to be the thickness of the Co layer, and D_z is the cell parameter along the z-axis. As the exchange parameter (A) of the FM and AFM layers are roughly the same, the interfacial exchange length is pretty similar in both systems for a given $A_{ex,I}$, which is the parameter that should be input in the simulations. iDMI was neglected entirely for this set of simulations.

As can be seen in figure 3.13, merons instantiated in the α-Fe_2O_3 and Co layers couple together. Their sizes are typically slightly different but are always a similar order of magnitude. Further examples of this behaviour for several extreme cases are shown in appendix B, figure B.3. Crucially, the FWHM of AFM merons primarily depends on the Fe-Co interfacial exchange and varies only weakly with the Co anisotropy up until close to the transition point at $1.3\,\mathrm{MJm^{-3}}$. Conversely, the meron FWHM in the FM Co layer scales directly with the Co anisotropy and is largely independent of the Fe-Co interfacial exchange. This is likely due to the fact that the inherent lengthscale in α-Fe_2O_3 is $\approx 30\,\mathrm{nm}$ and therefore longer than that due to the interfacial exchange length, see for example figure 3.4 and section 2.3.1. This suggests that AFM textures are likely to scale with the smaller of these two lengthscales. On the other hand, the inherent Co exchange length $L_{ex,Co} \propto \sqrt{A_{Co}/K_{Co}} \approx 5\,\mathrm{nm}$ is a similar order of magnitude to $L_{ex,I}$ and therefore the lengthscale of FM structures in the Co layers is expected to depend on both the Co anisotropy and $L_{ex,I}$. Therefore, in order to tune the size of textures in both coupled materials requires tuning both the Co anisotropy and ensuring a clean interface for strong exchange, requiring careful material manufacture and heterostructure design.

It doesn't stop being magic just because you know how it works

—Terry Pratchett, *The Wee Free Men*

4 Experimental techniques

Contents

4.1 Introduction

Since the initial investigations of diffraction patterns of x-rays from crystals by W. Bragg, H. Bragg and M. Laue, it's been clear that x-rays provide detailed insight into long-range real-space order in crystals [119]. For the longest time, they were primarily used to study the crystallographic order in materials, as the scattering from different atomic layers gives information about the 3D arrangements of atoms. X-ray diffraction was used, for example, for the early determination of the lattice type, symmetry and crystal structure of α-Fe_2O_3 [5, 6, 8]. More recently, developments in high-flux x-ray sources at synchrotron facilities have lead to a variety of x-ray based techniques coming to the forefront of modern research, which are able to probe new aspects of condensed matter physics such as surface chemistry,

nanostructures, and magnetism [120]. These measurements make use of the increased flux and, in some cases, developments in x-ray optics to measure effects significantly weaker than crystallographic scattering, for example: dichroic x-ray absorption, electron emission, or small-angle scattering. It is these developments, particularly the advent of several techniques for spatially-resolved studies of magnetic structures in crystalline samples, that are critical to the studies of AFM domains and topological textures in α-Fe_2O_3 that underpins the rest of this thesis.

In this chapter, I will discuss the application of synchrotron-based x-ray techniques for studying and imaging AFM domains. I will start by discussing further how x-ray dichroism provides information on the orientation of the magnetic order parameter in different materials. I will introduce several key types of measurements performed throughout this thesis, namely x-ray absorption spectroscopy, dichroic imaging and vector mapping. I will then discuss the two main techniques used for my studies of α-Fe_2O_3, which were scanning transmission x-ray microscopy and x-ray holography. Starting with a general description of each technique, I will discuss the key endstation requirements for it to be successfully implemented, limits placed on the sample, achievable resolutions, the addition of in-situ perturbations used, and any other important information one would need to recreate the experiments performed herein or utilise these techniques for investigations of similar materials. As these experiments are transmission based, the development of free-standing crystal membranes by my collaborators was crucial to their success; therefore, the end of this chapter will be devoted to discussing the preparation and characterisation of these membranes. In particular, the crystalline quality and defect density of several different membrane types will be explored, as these will be shown to have important ramifications for the position and width of the Morin transition and the associated thermal nucleation of magnetic structures in later chapters.

4.2 Magnetic dichroism

In general, dichroism is a difference in the absorption or scattering of photons by a material based on the polarisation of the incident light. Dichroism can have several different physical origins; chief among these are structural dichroism and magnetic dichroism. These occur

due to the relative orientation of the photon polarisation to either the crystal axes or magnetic order parameter respectively. I will focus on the latter here, as the bulk of this thesis is concerned with investigating the magnetic properties of α-Fe_2O_3. As presented in section 2.4, magnetic dichroic effects come from electric dipole transitions of core electrons to unoccupied higher states [93, 121]. Due to the generally high spin-orbit coupling of core states, the transition probability (calculated from Fermi's golden rule) is dependent on the polarisation of the x-rays relative to the magnetic moment of the atom, thereby altering the total absorption of x-rays. These effects are strong only near x-ray absorption edges, where the energy of the x-rays is close to the resonance energy for a dipole transition. This also allows one to perform element-specific measurements, provided the absorption edges of the elements in a material are sufficiently well-separated, which is particularly useful for samples comprised of several different magnetic layers.

The most widely used form of this effect is x-ray circular dichroism (XCD), which is the differing absorption between left- and right-handed circularly polarised x-rays [93]. This can only occur in materials wherein the space group lacks inversion or time-reversal symmetry, such as ferromagnetic alignment (which breaks time-reversal). When the effect is purely magnetic in origin, we are dealing with x-ray magnetic circular dichroism (XMCD). The maximum XMCD occurs for a fully-aligned ferromagnet (e.g. in the presence of an external magnetic field) with the x-ray propagation vector either parallel or antiparallel to the magnetic order parameter. Intermediate orientations contribute a projection, such that magnetisations perpendicular to the propagation vector result in zero XMCD signal. The XMCD contrast is therefore proportional to the expectation value of the magnetisation along the polarisation vector, i.e. $\propto \langle m \rangle$, as shown in equation 2.68. XMCD has been used extensively to study a wide array of magnetic materials, including vortices and skyrmions in ferromagnets [36, 122–124], magnetic bubbles in MnNiGa lamellae [125] and magnetic nanoparticles [93].

X-ray magnetic linear dichroism (XMLD) is an anologue to the XMCD discussed above, but with the difference in absorption being between two mutually-perpendicular orientations of the linear x-ray polarisation. The contrast is proportional to the expectation value of the square of the magnetisation, i.e. $\propto \langle M^2 \rangle$, as shown in equation 2.71, such

that both ferromagnets and antiferromagnets can have a non-zero XMLD signal [121]. Unlike other materials, there is typically found to be minimal structural contribution to the x-ray dichroism with linear polarisation in the $a-b$ plane of α-Fe_2O_3, making it incredibly useful for studying antiferromagnetic domains [11, 126]. When combined with spatially-resolved absorbative techniques (such as those discussed below), this allows one to create images of the local variation in the dichroic signal.

There are three main methods of forming dichroic images, both for XMCD and XMLD, depending on the nature of the dichroic signal in a given sample. 2P schemes are the basic form and use a difference between two images taken at the same energy but with different polarisations, either oppositely circularly polarised or 90° separated linear x-rays. In addition, the sign of the dichroic signal often switches either side of an absorption peak; therefore, by taking images at two different energies for a given polarisation and subtracting them (with some appropriate normalisation), one can remove the non-dichroic contrast from an image and therefore retain only the magnetic contrast, known as a 2E imaging mode. This technique will form the basis for many of the discussions herein and is the sole contrast mechanism used throughout. Finally, 2E2P mode uses 4 images, one at a resonance energy and one off resonance for each polarisation. Whilst this is particularly useful for imaging ferromagnets and allows for successful normalisation and calculation of sum rules [93], it is generally less useful and significantly more time consuming for XMLD imaging of AFMs.

4.2.1 Absorption spectroscopy

In addition to its use for imaging, magnetic dichroism is also useful for performing spectroscopic measurements of a system. By scanning the energy of the incident x-ray beam at a fixed polarisation, one can get an energy-dependent x-ray absorption spectrum (XAS). Standard XAS for α-Fe_2O_3, along with the dichroic signal, are presented in figure 4.1. Such XAS have many uses, but for the purposes of this thesis these spectra were used to: (i) correct for slight energy shifts between experiments, (ii) confirm the quality of the samples and (iii) identify the magnetic state of the sample at a given temperature. Concerning point (i), it is a common occurrence at beamlines, particularly

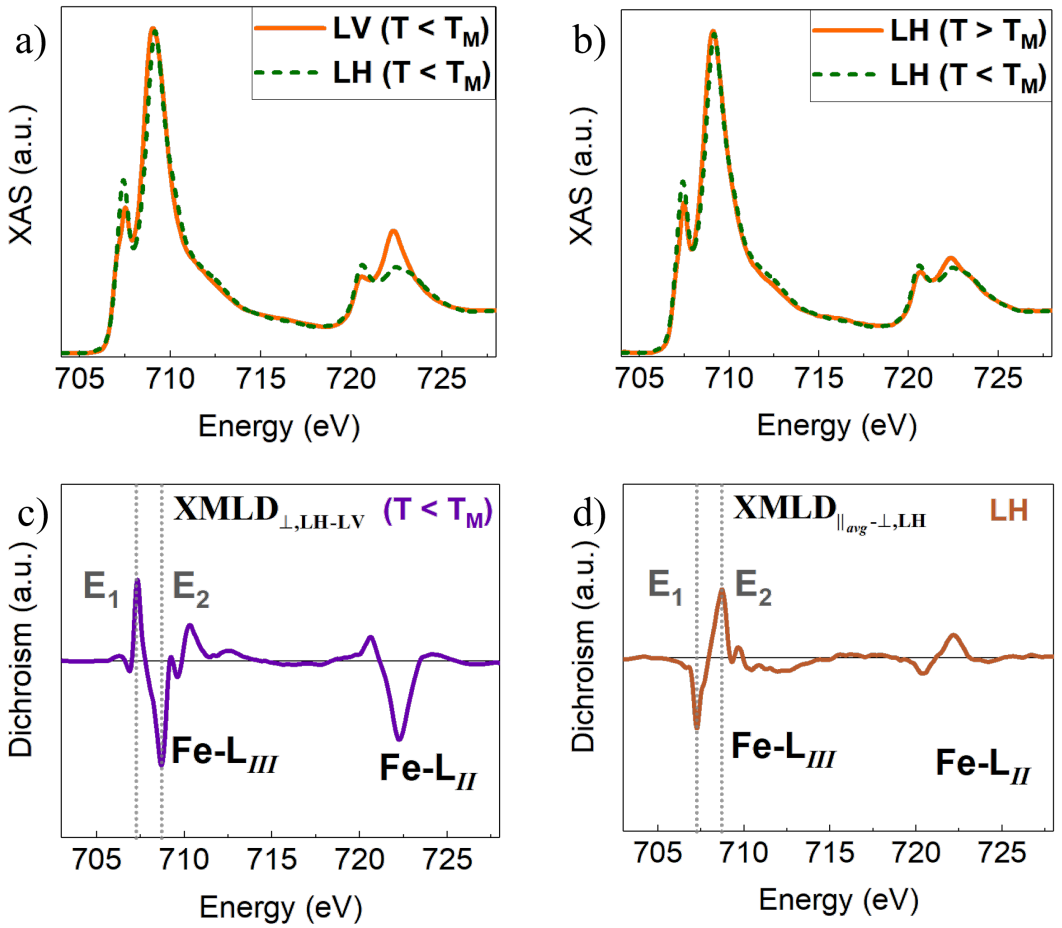

Figure 4.1: a) XAS using linearly polarised light either parallel (linear horizontal, LH) or perpendicular (linear vertical, LV) to the a-b plane taken below the Morin transition. b) Change in XAS signal with LH x-rays across the Morin transition. c) XAS dichroism below the Morin transition, found by subtracting the two curves in (a). d) Difference in XAS with LH light above/below the Morin transition, from subtracting the two curves in (b). Data reproduced from [11] with permission.

after shutdowns and maintenance periods, for there to be slight shifts in the recorded energy values between experimental runs. This is largely due to slight adjustments in the x-ray optics, which can lead to small energy variations (<0.5 eV from my experience). It is also useful for comparing results between different beamlines and techniques, when these recorded energy shifts can be larger. Under point (ii), this was largely done for sample characterisation during the growth process to confirm the absence of other oxide phases (e.g. Fe_3O_4), but is always worth keeping in mind. For typical oxide materials, particularly broad XAS peaks typically indicate poor crystalline quality and the absence of any additional peaks confirms the absence of additional oxide phases. Note that broad

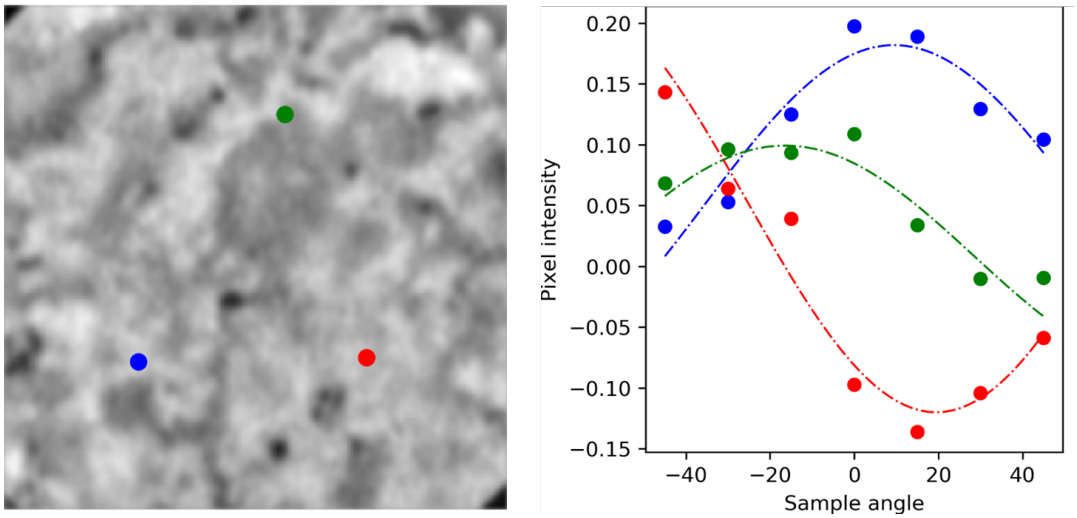

(a) Intensity image

(b) Fitted $\cos(2\theta)$ function

Figure 4.2: a) Intensity image with several points indicated by coloured dots, corresponding to the coloured angle-dependent pixel intensity and fitted $\cos(2\theta)$ function shown in (b). The phase offset of the distribution in (b) gives the angle of the local AFM order to an arbitrarily chosen 0° axis, here horizontal, and is fitted on a pixel-by-pixel basis to create a full vector map, shown in figure 5.5.

XAS peaks may arise from different effects in other material classes, such as screening in metallic ferromagnets. Concerning point (iii) it is well understood that, for a fixed linear x-ray polarisation, the relative ratio of certain XAS peaks (namely the L_3 peaks) swaps sign depending on whether the sample is above or below T_M, see figure 4.1b,d ([11, 121, 126]). Thus, this serves as an independent verification of the magnetic state of the sample at any given temperature and is particularly useful when the transition temperature varies spatially, as I will explore in section 7.2.

4.2.2 Vector mapping

For the case of α-Fe_2O_3 and similar easy-plane systems, in normal incidence the dichroic part of the x-ray absorption (typically a few % of the total absorption) is proportional to $\cos(2\theta)$, where θ is the relative angle between the polarisation axis and the magnetic order parameter (e.g. the Néel vector in AFMs) [45, 121]. By rotating the polarisation axis relative to the sample (or vice versa) one can track the variation in the dichroic signal as a function of angle. This technique should be done with a 2E dichroic imaging mode to maximise the angular dependence of the contrast. By fitting this contrast in a

pixel-by-pixel fashion to the $\cos(2\theta)$ distribution, one can extract the relative orientation of the local Néel vector to some arbitrarily chosen axis set at 0°. An example of the fitting procedure, demonstrating the angle-dependent contrast of a few different pixels along with the associated fitted $\cos(2\theta)$ function is shown in figure 4.2. Combining this procedure with a spatially resolved imaging technique generates an angle-dependent map of the dichroic contrast across a sample, hereafter referred to as a vector map, which can be used to identify real-space magnetic structures such as the winding topological textures introduced in section 1.2. This technique will be used throughout this thesis to study domain populations and topological textures in lifted membranes (chapter 5), as well as how these are altered in the presence of applied magnetic fields (chapter 6) and strain (chapter 7).

4.3 Synchrotron based techniques

4.3.1 Scanning transmission x-ray microscopy

Among the wide class of x-ray imaging techniques, scanning transmission x-ray microscopy (STXM) is probably the conceptually simplest. The basic principle is to produce a spatial map of the x-ray absorption across a region of the sample and to relate variations in the absorption to a material property of interest. As we shall see, actually implementing the technique requires a set of components that are difficult to manufacture and arrange, ultimately introducing difficulties and limits on the sample environment. Despite this, it remains both a useful and flexible technique for investigating magnetic domain structures (among other things) [128, 129].

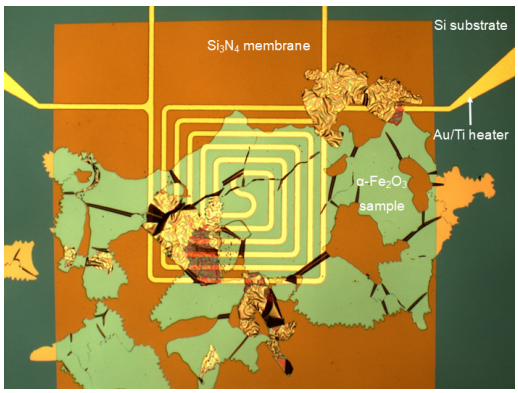

Figure 4.3: Example Si_3N_4 membrane with Au/Ti heater grown on Si substrate. The α-Fe_2O_3 membrane was transferred via the scooping technique post-growth (section 4.4).

A simplified schematic of how STXM operates is shown in figure 4.4. The x-ray beam, produced by a synchrotron to which the instrument is attached (as an endstation on a beamline), is incident on a Fresnel lens. This focuses the x-rays to a small spot on

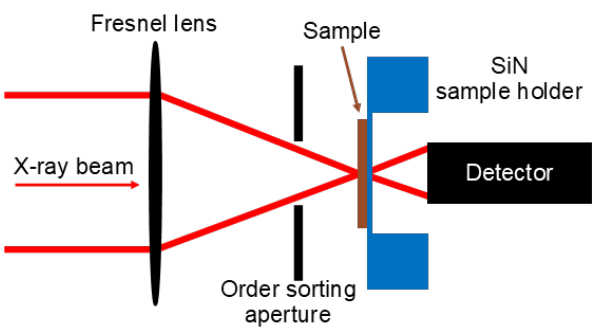

(a) Schematic diagram of the operating principle of a STXM.

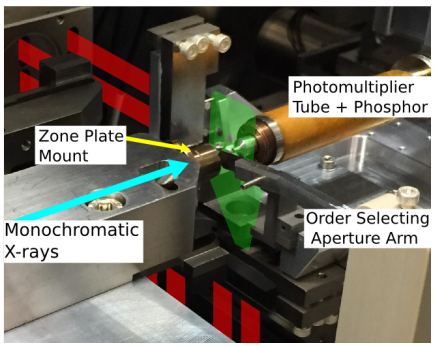

(b) Image of the STXM chamber at the PolLux beamline. [127]

Figure 4.4

the surface of the sample (typically 10-100 nm diameter, depending on the lens used) and ultimately determines the resolution limit of the instrument. A higher resolution requires a lens with a smaller outer ring diameter, which is not only more difficult to manufacture but also leads to a smaller focal distance and depth of focus, making it more difficult to mount and successfully image the sample. The focused beam passes through an order sorting aperture, which allows through only the 0^{th} order diffraction from the lens (blocking higher order diffraction), which increases the resolution of the technique. The beam is then incident on the sample, which should be carefully placed within the depth of focus of the beam, typically $\approx 2\,\mu$m, to maximise the obtainable resolution and contrast. An avalanche photodiode (or similar detector) is then placed after the sample to measure the intensity of the transmitted beam. By scanning the sample with a step size corresponding to the focused spot diameter one can build up a high-resolution spatial map of the x-ray transmission across the sample. This can then be combined with methods of extracting specific contrast, such as the x-ray magnetic dichroism discussed above, to study the topography of magnetic domains (or some other property) averaged through the sample along the beam direction. The entire chamber must be kept under a reasonably good vacuum ($\sim 10^{-6}$ mbar) to minimise the absorption of the x-rays by gas molecules; note that this is a significantly weaker vacuum than is required for electron-based imaging techniques (e.g. PEEM). Photon-in, photon-out techniques such as STXM and holography (see below) also have further advantages over electron-based imaging techniques, such as

general insensitivity to applied magnetic field and no constraints on sample conductivity, which make them ideal for studying magnetic insulators.

There are a few additional difficulties in implementing this technique that should be mentioned, particularly as they were extremely relevant throughout my experiments. Firstly, as this is a transmission technique the samples must be reasonably x-ray transparent to allow sufficient intensity through for detection, meaning that thin film samples grown on relatively thick substrates (such as those used for our PEEM experiments [11, 45]) would not be suitable. This was one of the key motivations for the push towards preparing membrane samples, as these are detached from the substrates and are therefore significantly more x-ray transparent (discussed further in section 4.4). Membrane samples can also be conveniently transferred and attached to silicon nitride membranes (Si_3N_4), which are commonly used as sample holders in STXM endstations. The thickness of the sample layers one wants to study also entails a delicate balance, as thicker samples increase the overall contrast of the technique but reduce the transmitted intensity, meaning that the ideal thickness is a compromise between these two effects and was typically about 30 nm for my samples. Finally, due to the short focal length of the x-ray optics, the sample space is tight. This means that the integration of the measurement technique with in-situ probes (such as temperature or magnetic field) is limited by these spatial constraints. These can be alleviated somewhat by careful experimental design, for example the integrated heaters on the sample holders allow me to warm the samples above the systems base temperature ($\approx 25^\circ$ C).

The 100 nm thick Si_3N_4 membranes were grown on 5x5 mm, 500 μm thick Si substrates, from which a 1x1 mm window was etched out. This leaves a very thin, soft-x-ray transparent region on which my samples were mounted. On top of the Si_3N_4 window, a Au/Ti heater was grown in some cases. The heater is connected to 4 contacts, 2 inputs and 2 outputs, to allow for both current control and resistance measurements in parallel. The heaters are designed and calibrated such that the resistance is linear with temperature in the range we are interested in ($\approx 0 - 50^\circ$ C). These sample holders were all prepared by Silson [130] and similar membranes without heaters were also used in the holography

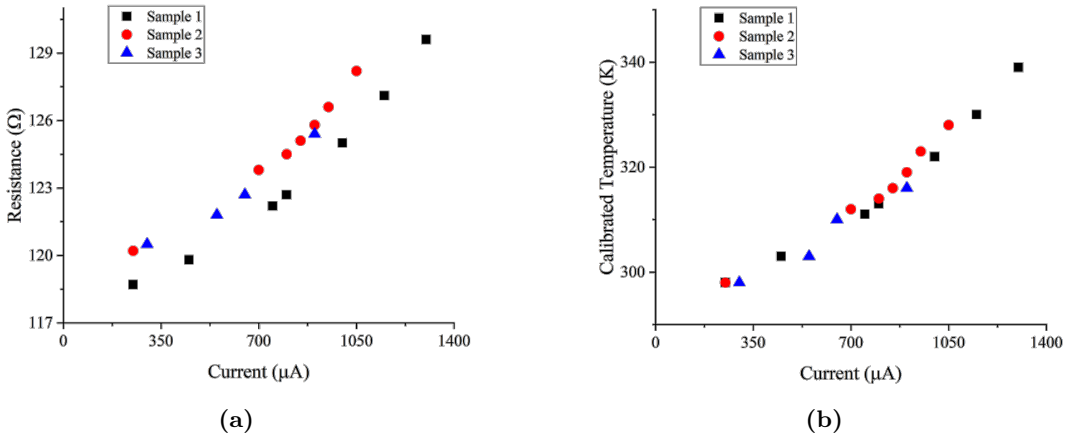

Figure 4.5: a) Measured resistance versus applied current for several different heaters and samples. (b) Calibrated temperature from data provided by Silson [130] based on measured resistance as a function of current.

experiments (discussed further below). The samples were then transferred onto the flat side of the membranes using either a scooping or directed transfer method (see section 4.4).

4.3.1.1 Gas Cell setup

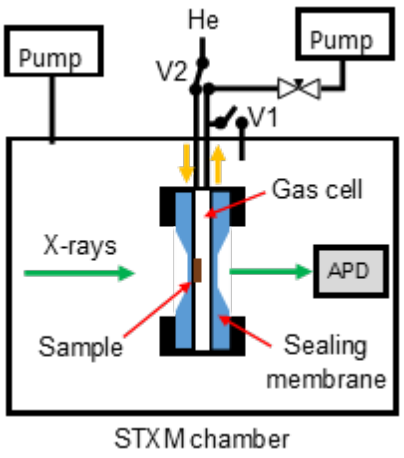

Figure 4.6: Schematic of the gas cell setup used for the strain controlled STXM experiments.

In order to systematically apply in-situ strain to α-Fe_2O_3 membranes and study the effect this has on AFM domains (see chapter 7), we utilise the custom gas cell setup developed at PolLux. The setup and operating principle is shown in figure 4.6 and will be described below; for full details, see [122, 123, 131].

The gas cell consists of a stainless steel and aluminium chamber, sealed on the back by a separate x-ray transparent membrane and on the front by my membrane on a Si_3N_4 sample holder, and connected to an external pressure system that is controlled by a computer interface. The cell is placed in the STXM chamber under vacuum and the internal pressure of the cell can be varied. A pair of valves allow the cell to be connected either directly to the chamber to ensure the internal and external pressure are equal, giving a zero-strain state (V1) or to the pressure control interface (V2). These two valves should be switched together to avoid introducing

He gas directly into the STXM chamber, which would reduce the image quality until pumped out. For the latter, a flow of He gas in the range 0-100 cc/min is admitted into the chamber and a PID controlled needle valve controls the flow rate out of the chamber via an exit tube connected to a turbo pump. Both the flow rate and the PID parameters can be tuned until a stable equilibrium pressure in the range 0-1200 mbar is obtained, although only pressures up to 800 mbar were used here. When the PID control parameters are tuned correctly, a pressure stability of better than 0.1 mbar can be obtained. In addition to the pressure variations, the temperature of the system can be controlled using a combination of a pulsed current heater and a closed loop cryostat. Due to the additional vibrations induced by the cooling system, this was turned off during imaging to maximise the resolution of the system. This meant I relied on the thermal sink provided by the cold Cu block to which the cryostat is connected to maintain the low temperature throughout the imaging period, limiting the lowest imaging temperature to around 0° C. Temperatures up to 45° C were used in these investigations, but higher temperatures are in principle reachable. The sample is mounted on a Si_3N_4 membrane and sealed with wax onto one side of the cell. The Si_3N_4 window here is 50 nm thick, allowing it to reach relatively large flexures for a given gas pressure compared to the thicker membranes used elsewhere. As above, the Si_3N_4 windows were etched out of a 5x5 mm, 500 μm thick Si substrate and were either 1x1 mm or 1x0.25 mm in dimensions in order to provide either symmetric or uniaxial strains to the sample (discussed further in chapter 7). These holders had no Au/Ti heaters, as these would significantly alter the strain profile throughout the membrane and would make it more likely to fracture under higher strains, hence the need for the awkward heating/cooling methodology discussed above.

4.3.1.2 TEY STXM

In addition to the standard bulk-sensitive imaging mode discussed above, one can also perform certain surface-sensitive measurements in a STXM by utilising the electrons emitted from the sample surface due to the x-ray absorption of the sample. To accomplish this, the sample holder is flipped so that surface of interest is facing the detector, which is replaced with a channeltron detector biased to a voltage of 2.4 kV. This allows the electrons

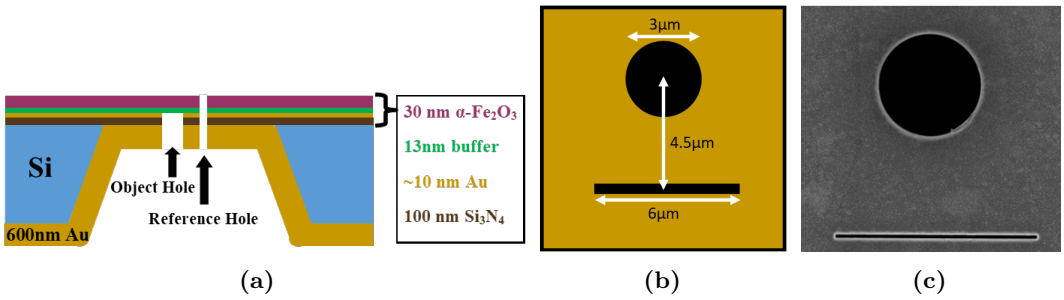

Figure 4.7: a) Cross-sectional schematic of the growth of the mask on a Si_3N_4 membrane, along with the transferred sample and object/reference structure. b) The layout of the object hole and reference slit, with appropriate dimensions marked. c) SEM image of a hole/slit milled into a mask.

emitted from the top few layers of the sample surface (i.e. $\sim 5\,\text{nm}$) to be measured and counted, whereas those from the bulk do not have sufficient energy to escape the sample. This is commonly referred to as a total electron yield (TEY) measurement. The number of electrons arriving at the detector will depend both on the x-ray intensity transmitted through the sample to the surface layer and the amount of electrons emitted due to the proportion of x-rays absorbed by the surface at a given x-ray energy. Whilst the contrast and resolution of this technique is not expected to be strong enough for dichroic imaging as required to study magnetic properties of the sample, it is sufficient for simple spectroscopic measurements and spatially resolved chemical imaging. This technique will be used for this purpose exclusively in chapter 7, where the relative orientation of the sample and buffer layer will be critical to understanding the strain profiles across different membranes.

4.3.2 Holography

As I have introduced in section 2.5, holographic techniques can be used to reconstruct high-resolution real-space images of samples by utilising the interference between the diffraction from a sample and a reference object. I demonstrated there how the specific HERALDO implementation of holographic imaging works from a theoretical perspective. Here, I will discuss the more practical aspects of implementing this technique, primarily the key benefits over the other techniques discussed above and the principal difficulties in preparing appropriate samples.

Much like STXM, HERALDO is a transmission based technique and therefore is subject to the same requirements on the x-ray transmissibility of the samples one wishes to study,

therefore requiring the same membrane samples discussed above. One major advantage, however, is the lack of focusing optics involved, meaning that there is significantly more room in the endstation chamber to incorporate various in-situ probes alongside imaging. A clear example of this is the COMET endstation at SOLEIL [132], which I used for all of my HERALDO measurements. Here, there is an extremely flexible array of Nb permanent magnets which can apply a fairly strong field (up to 1 T) to the sample in a variety of orientations relative to the sample plane. Additionally, a PID controlled heating/cooling setup is incorporated into the endstation, making variations in temperature during measurements extremely easy and the temperature very stable (within ≈ 0.1 K). These are both significant improvements over STXM and at least on par with what's possible in PEEM, with the in-situ field strength and flexibility better than what is currently available at the PEEM endstations we utilise and are aware of. It is also possible to combine HERALDO imaging with a variety of other in-situ probes, such as electric currents and ultra-fast laser pulses, some of which are currently in development at SOLEIL.

The major difficulty with HERALDO is the sample preparation, over and above the transmission requirements mentioned above. Recall that this technique requires that all the transmitted x-ray intensity comes from either the object (which is my sample) or the reference, meaning that the majority of the space needs to be opaque to x-rays. As a result, the contrast of this technique is primarily determined by the ratio of the x-ray intensity transmitted through the bulk of the structure relative to that through the object and reference. This is optimised by growing a mask, usually of a heavy-metal (Au is commonly used) of an appropriate thickness to significantly attenuate the x-rays passing through the mask, onto a Si_3N_4 holder (see figure 4.7a). We grew a 600 nm thick Au mask through e-beam evaporation of a Au wire, with a thin (≈ 10 nm) Ti layer at the interface to aid adhesion. Using an online tool [133], I calculated the attenuation length of x-rays through a Au mask at normal incidence (i.e. the thickness over which the transmitted intensity reduces by a factor 1/e) to be approximately 60 nm over the energy range relevant to these studies. For my 600 nm thick masks, this will reduce the transmitted intensity through the mask to about 0.005% of the beam intensity.

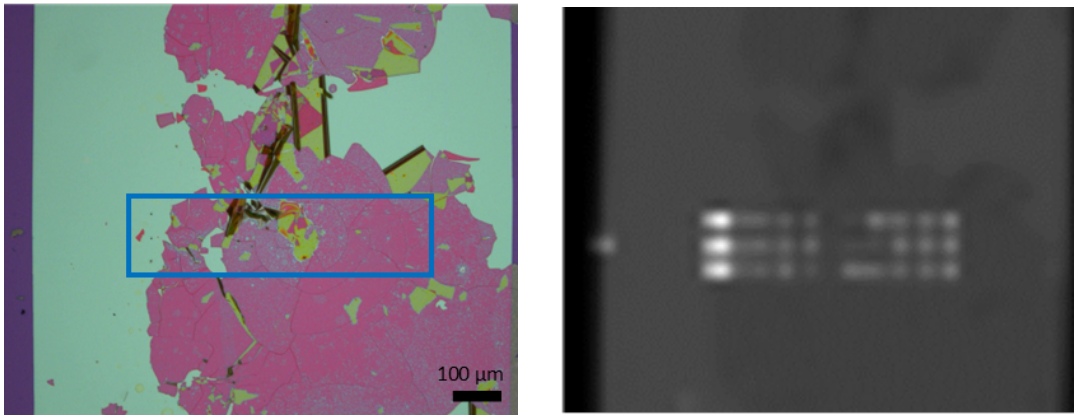

(a) (b)

Figure 4.8: a) Optical image and b) X-ray transmission intensity map of an example transferred membrane on a holography mask. The blue box in (a) highlights the region containing a 10x3 grid of object hole/reference slit pairs, which are more visible as the high-intensity regions in (b). The scale bar in (a) is 100 μm and both images are on the same scale.

The next step is to prepare an array of object holes and reference slits with an appropriate set of separations as determined by the criteria outlined in section 2.5. After Au coating, the masks were mounted in a Ga focused ion beam (FIB) system with a custom holder I designed to avoid damage to the membrane and mask during milling whilst electrically grounding the sample. The milling was performed by a collaborator following my designs and specifications. We milled a 10x3 array of 3 μm diameter holes separated by 50 μm. Along with each hole, an associated slit was milled 4.5 μm from the centre of the hole that is 6 μm long and slightly off-centre (to aid with the filter application algorithm), as shown in figure 4.7b. These dimensions were chosen to be a good compromise between milling time, field of view and slit width, as the larger the overall scale of the structure the longer the mask takes to prepare and the greater the failure rate. The dimensions also satisfy all the relevant HERALDO separation criteria in order to avoid overlap between the different reconstructions [94]. The achieved resolution, which ultimately was determined by the width of the reference slit, is discussed in section 6.2. Finally, the sample should be transferred (following the targeted process outlined below) onto the holder and the reference slits must be re-milled to remove any parts of the sample obscuring the reference slit. An optical image and x-ray transmission map of an example sample after all of the steps described above had been completed is shown in

figure 4.8. This whole process is both difficult and time consuming, forming the major drawback and technical complexity of this technique.

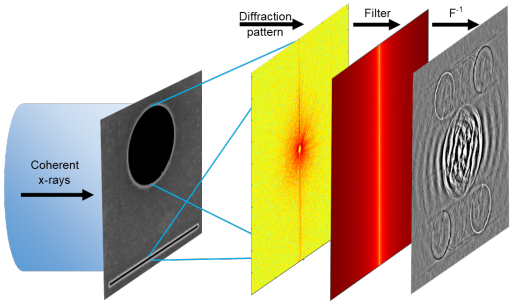

Figure 4.9: Schematic of the process of forming reconstructed images from measured diffraction pattern in HERALDO.

Once the masks are prepared and the samples transferred, the implementation of the HERALDO measurement scheme is fairly straightforward, following the process outlined theoretically in section 2.5. First, the sample is mounted in an appropriate measurement instrument, such as the COMET endstation [132], and the positions of the various object holes are identified using the mapping technique that produced figure 4.8b. The experimental and computational steps to produce the final reconstructed images are then demonstrated in figure 4.9. Firstly, the object/reference structure are simultaneously illuminated by a high-flux x-ray beam at an energy chosen to maximise the required contrast (see sections 4.2 and 6.2). This produces a diffraction pattern imaged by a spatially resolved detector in the far-field, such as the high-repetition CMOS camera installed at the COMET endstation. The rest of the image formation technique is purely computational. To make dichroic images, two diffraction patterns at different energies are taken and their background intensity is normalised to remove the energy-dependent background intensity present on most x-ray beamlines; the resulting normalised diffraction patterns are then subtracted to produce a dichroic diffraction pattern. As all subsequent processing steps are linear, in principle it doesn't matter when this process happens and the dichroic image can be formed at the end of the processing steps instead. Applying a suitably chosen linear filter (see section 2.5) and then performing an inverse Fourier transform produces a final image, in which several reconstructions of the object transmission function and its complex conjugate can be identified. This process will be used extensively to produce all the holographic images presented and discussed in chapter 6.

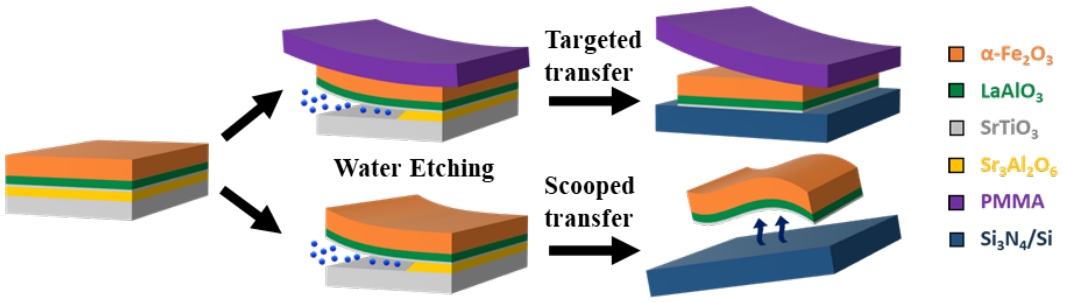

Figure 4.10: Schematic of the membrane transfer process via selective water etching of the SAO layer, adapted from [114].

4.4 Growth of crystals and membranes

The crystalline membranes were grown, characterised and transferred by my collaborators in Singapore, alongside extensive discussions and planning that I was heavily involved in. This process was described in detail in [114], based on developments in similar materials over recent years [134–136], but the key points are outlined here. The α-Fe_2O_3 used throughout was doped with 3% Rh, as this has been found to significantly raise the transition temperature from $\approx$240 K found in thin films to near or above room temperature [11, 19, 82]. The (111)-oriented $Sr_3Al_2O_6$ (SAO), $SrTiO_3$ (STO), and $LaAlO_3$ (LAO) layers were grown sequentially on either Al_2O_3 or STO substrates via pulsed laser deposition (PLD), with the (001)-oriented α-Fe_2O_3 then grown on top. In some samples, STO and LAO layers a few nm thick each were included, constituting a "buffer" layer to improve the crystallinity of the α-Fe_2O_3, due to the otherwise large lattice mismatch between the α-Fe_2O_3 and the water soluble SAO layer. This was not included in every membrane and was found not to be beneficial for membranes grown on Al_2O_3 substrates, wherein it actually hindered the successful delamination of the membrane. The PLD parameters, including laser repetition rate, oxygen pressure and substrate temperature, were adjusted for each different layer to maximise their individual crystallinity and the completed stacks were slowly cooled in an oxygen-rich environment to minimise oxygen vacancies formed during the growth. The three main types of membranes studied in this thesis are shown in figure 4.11.

To delaminate the membranes, they were placed in high purity deionised water at room temperature until the SAO layer was dissolved and the membranes detached from the

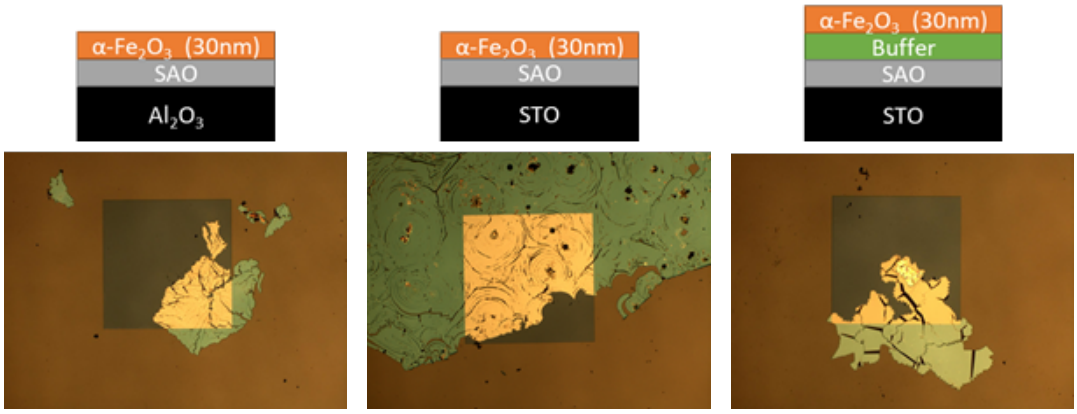

(a) Al_2O_3 substrate **(b)** $SrTiO_3$ substrate **(c)** $SrTiO_3$ substrate with buffer

Figure 4.11: Schematics of the stack configurations for several different membrane types (top row) along with optical microscope images of example membranes transfered via scooping onto Si_3N_4 holders.

substrate. There were then two processes that could be used to transfer the membranes on to the desired platform (usually Si_3N_4 membranes as discussed above), shown in figure 4.10. For the first "scooped" method the membrane floats to the water surface, the sample holder is carefully placed below the membrane and then lifted up such that the membrane sits on top of the holder. This is a rather unpredictable method, often resulting in fractured, bent or crumpled regions in the transferred membrane; many such regions can be seen in the example membrane in figure 4.3. Fortunately, there are often fairly large regions (>100 μm^2) that are crack free and so are suitable for imaging. The alternative technique, referred to here as the "targeted" method, consists of spin-coating a Poly(methyl methacrylate) (PMMA) layer then held by flexible tape before the stack is placed in the water. After the SAO layer is dissolved, the membrane remains attached to the tape, such that it can then be placed in the desired position on the sample holder. The PMMA layer and tape is then removed by a room temperature acetone wash. All samples were cooled to ≈250 K in vacuum and then allowed to slowly warm back to room temperature post-transfer but before imaging to ensure they either started below the transition or had warmed through the transition at least once (if T_M was below RT for that sample).

The magnetic properties of the three types of membranes were characterised using SQUID magnetometry as shown in figure 4.12 and from this data there are several observations one can make. Recall that, as introduced in section 1.1, a drop in the

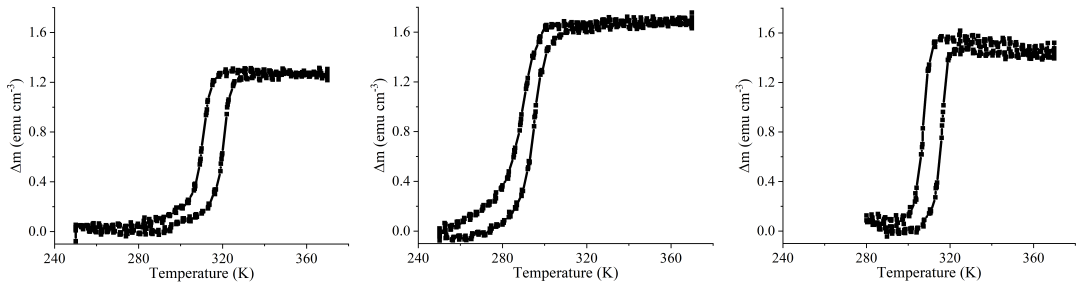

(a) Al_2O_3 substrate **(b)** $SrTiO_3$ substrate **(c)** $SrTiO_3$ substrate with buffer

Figure 4.12: SQUID magnetometry data taken on the three different membrane types before delamination from the substrate and placed on the same scale for comparison.

magnetisation signal corresponds to the vanishing canted moment as the spins flip from IP to OOP and therefore signifies the transition temperature. For these membranes, both the transition temperature and width varies slightly in each case, likely due to the differing amounts of strain inherent in each structure resulting from the different growth template. This is critical, as the transition typically sits above RT for the membranes grown on Al_2O_3 and buffered STO, whereas it sits just below RT for the membranes grown on unbuffered STO, thereby determining which magnetic state of the system dominates at room temperature. This will be evident when these different membrane types are studied via STXM in chapter 5. Additionally, the difference between the height of the step, corresponding to the total ferromagnetic magnetisation induced by the canting above the transition, differs in each case. This is potentially due to misoriented or pinned regions in some membranes, particularly the more defective ones grown on Al_2O_3, which do not fully flip across the transition. Overall though, each membrane type has been shown to host a largely similar Morin transition relatively close to RT.

In order to check if the delamination process affects the crystalline quality of the films significantly, we compared a set of x-ray diffraction (XRD) data of a membrane grown on buffered STO both before and after delamination, figure 4.13. The grey curve shows the XRD data before membrane delamination, with the largest peak corresponding to the STO substrate and smaller α-Fe_2O_3 and LAO peaks visible. After delamination (orange curve), the large STO peak is greatly suppressed as the sample is now detached from the substrate, but the α-Fe_2O_3 peak and that of the buffer layer (LAO) now present more obviously. From this data, it is clear that the crystalline quality of the membranes

is largely maintained after delamination, as the FWHM stays close to $\sim 1.1°$, but is still significantly worse than that found in thin films ($\sim 0.05°$ [11]). This suggests a significantly higher defect density in delaminated membranes compared to attached films studied previously, and this will be proposed as the explanation behind some of the phenomena observed in these membranes that differ from previous samples (e.g. in section 5.4). Furthermore, it is encouraging that the membrane quality is not significantly worsened during the transfer process, which I emphasise is quite rough, thereby making this a reasonable technique for preparing detached samples that can be successfully transferred to a variety of platforms post growth.

4.4.1 Grains and Moire patterns

Another method used to determine the crystalline quality of these membranes, as well as extract layer thickness parameters needed for our mechanical models of lifted membranes (see section 7.2), was selected-area electron diffraction (SAED). We collected atomically-resolved images in a transmission electron microscope of example membranes of each type [114]. From these images, shown in figure 4.14 along with their associated diffraction patterns, we can draw several immediate conclusions. Firstly, membranes grown on Al_2O_3 are comprised of a number of grains with typical size $\approx$100 nm, reflected in the extra satellite peaks appearing in the corresponding diffraction pattern, again confirming that these membranes have relatively poor crystallinity compared to those grown on STO. In that regards, the unbuffered samples on STO show significantly less structure but still demonstrate the existence of a number of defects and dislocations, which leads to the broadening of the corresponding diffraction spots in figure 4.14 e. The buffered STO membranes also have a high crystalline quality, with a lower density of

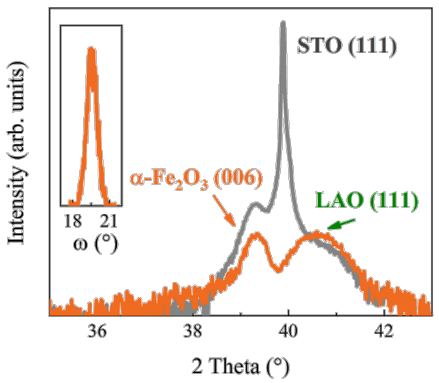

Figure 4.13: XRD of an α-Fe_2O_3 membrane grown on buffered STO both before delamination (grey curve) and after delamination and transfer to a Si support (orange curve). The inset shows the rocking curve of the detached sample, giving a FWHM of $\sim 1.1°$. Reproduced with permission from [114]

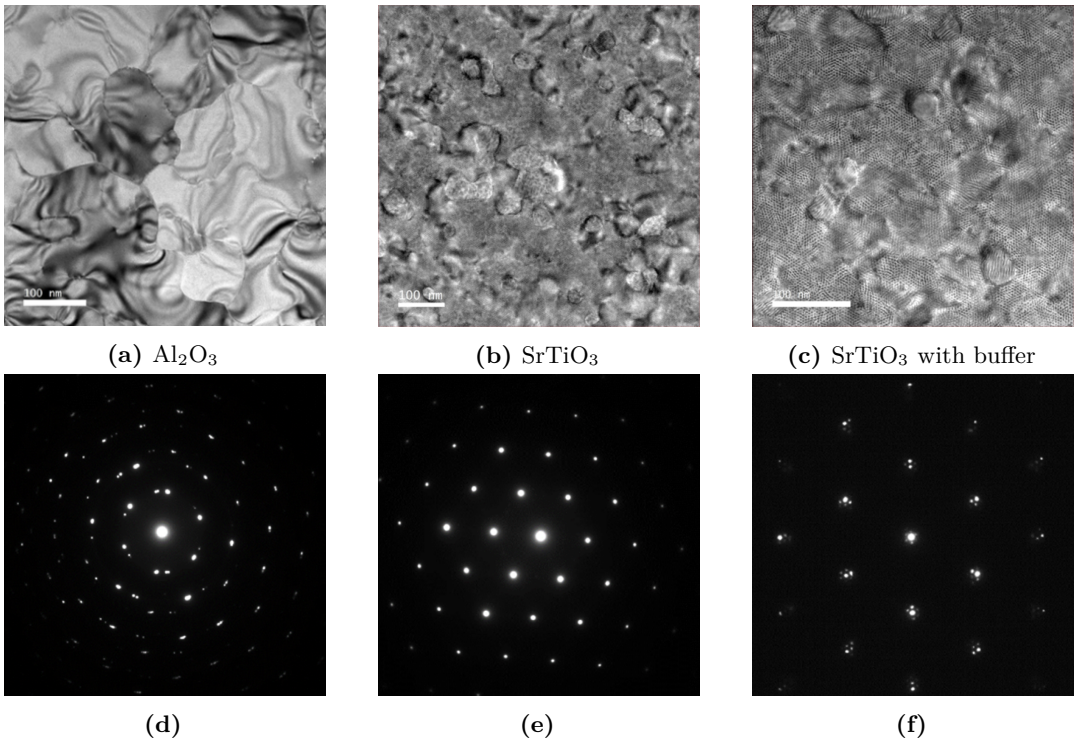

(a) Al_2O_3 **(b)** $SrTiO_3$ **(c)** $SrTiO_3$ with buffer

(d) **(e)** **(f)**

Figure 4.14: (a-c) SAED images and (d-f) associated diffraction patterns taken across the three key types of membranes relevant to this work. Scale bars are 100 nm in each case.

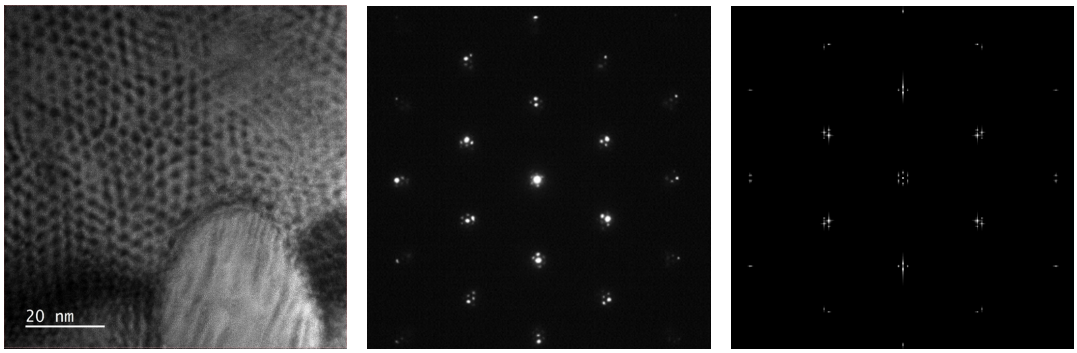

(a) Image **(b)** Diffraction pattern **(c)** Simulation

Figure 4.15: a) high-resolution SAED image of the membrane grown on buffered STO. The scale bar is 20 nm. b) measured and c) simulated diffraction pattern generated by the moiré structure due to the lattice mismatch between the buffer layer and the sample.

visible defects than in the unbuffered case. The diffraction spots in figure 4.14 f are also noticeably narrower than in the other two cases, which further supports this observation. There are, however, additional peaks in the diffraction pattern for the membrane grown on buffered STO that need accounting for, as well as some structure in the background of the images that becomes clearly visible at higher resolutions.

As shown in the high-resolution SAED image on the membrane grown on buffered STO (figure 4.15 a), there is a clear repetitive hexagonal pattern with a lengthscale of ≈5 nm. This is similar to mismatch moiré patterns seen in other material systems [137, 138], which are believed to be useful for atomic-scale tuning of parameters of 2D systems. I hypothesised that the origin of this pattern was similar here, as the LAO buffer layer remains attached to the membrane after delamination from the water soluble SAO (this will be important when studying strain profiles in chapter 7). LAO has a cubic structure, but the (111) projection looks hexagonal and it is this orientation that is used to grow the (001) oriented α-Fe_2O_3. The equivalent hexagonal lattice parameter of LAO is 5.35 Å and that of α-Fe_2O_3 is 5.03 Å, leading to a repeat distance of ≈ 8 nm along the hexagonal axes, consistent with the lengthscale of the additional hexagonal structure shown above. I constructed a simulated mismatch moiré pattern using python and the formalism described in [137] and took its 2-dimensional Fourier transform to calculate the predicted diffraction pattern, the results of which are shown in figure 4.15 c. The simulation is performed by constructing two lattices with the correct relative lattice parameters using the function

$$f(\vec{r}) = \frac{1}{9} + \frac{8}{9}\cos\left(\frac{1}{2}\vec{k_1}\cdot\vec{r}\right)\cos\left(\frac{1}{2}\vec{k_2}\cdot\vec{r}\right)\cos\left(\frac{1}{2}\vec{k_3}\cdot\vec{r}\right), \tag{4.1}$$

where $\vec{k_{1,2,3}}$ are three appropriately chosen lattice vectors with magnitude $k = 4\pi/\sqrt{3}a$ and a the hexagonal lattice parameter of the system. Summing these two lattices gives a simulated moiré pattern and the Fourier transform of this pattern produces the simulated diffraction pattern shown in figure 4.15 c. Whilst this pattern likely has no direct consequences on the phenomenon studied throughout this thesis, namely the nucleation and stability of topological textures, it opens up interesting routes for atomic scale modulation of the properties of ultra-thin AFM membranes through interface engineering.

"See first, think later, then test. But always see first. Otherwise you will only see what you were expecting."

Douglas Adams

5

Domain morphologies and topological textures in AFM membranes

Contents

5.1 XAS and initial characterisation

As discussed extensively in sections 1.1 and 4.4, α-Fe_2O_3 samples show a characteristic magnetic (Morin) transition that is typically an indicator of good crystalline quality. Given that the magnetic characterisation of our membrane samples suggest a similar transition slightly above room temperature (figure 4.12), I would expect the magnetic state of the system at RT to be similar to that in thin film samples at lower temperatures [11]. XAS of a membrane taken in STXM with linearly polarised x-rays in the plane of the sample is shown in figure 5.1. By comparison with figure 4.1b, this measurement supports the earlier SQUID measurements by demonstrating that the ratio of the L_2 peaks switch between RT and 330 K, the telltale signature that the Morin transition temperature sits in this range

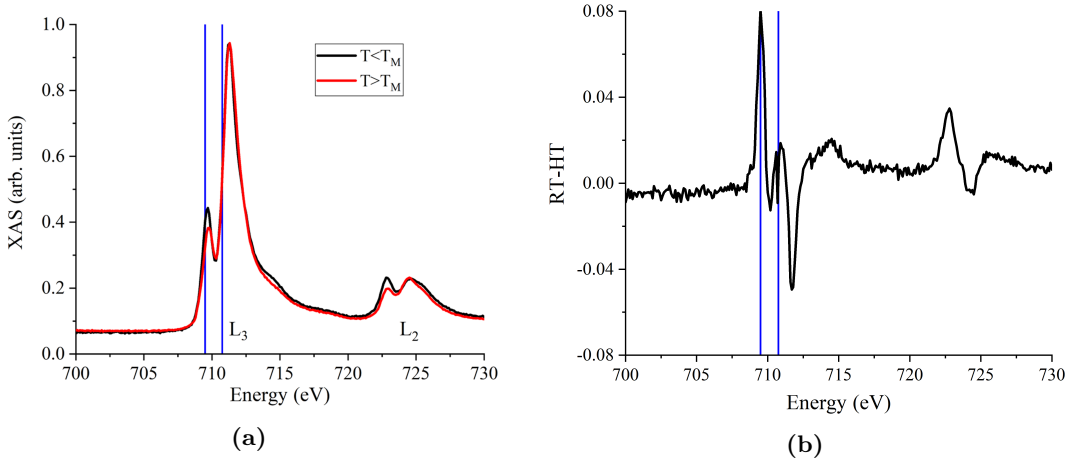

Figure 5.1: a) XAS of a membrane grown on buffered STO, taken at RT ($T < T_M$, black line) and 330K ($T > T_M$, red line). The $L_{2,3}$ sets of peaks are labelled and the blue vertical lines mark the energies used for the STXM images in the rest of this chapter. b) Difference between RT and HT spectra, emphasising the dichroic signal at the blue lines and the contrast reversal at the L_2 peaks.

[19, 126]. The lack of any additional peaks confirms that there is minimal mixing of other Fe oxide phases in these samples, further supporting the characterisation in section 4.4.

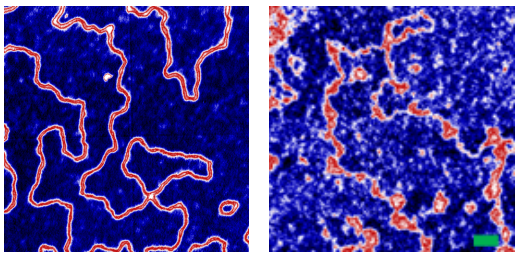

Figure 5.2: a) Previous PEEM XMLD image of ADWs in α-Fe_2O_3 thin films at low T, adapted from [11] with permission. b) Image taken in STXM on α-Fe_2O_3 lifted membrane at RT. The scale bar in (b) is 1 μm long and both images are on the same scale.

The first milestone in STXM imaging of membranes was demonstrating the similarity between the low temperature state of attached thin films and lifted membranes, shown in figure 5.2. Here, the blue/red colours correspond to OOP/IP regions respectively; this colour scheme will be used throughout this thesis. This not only represents one of the first examples of STXM images of AFM domains, but also helps to confirm that the magnetic structure of our membranes is not significantly changed during the rough sample transfer process. It is known that poor quality α-Fe_2O_3, characterised either by low crystallinity or high defect density, can suppress the Morin transition entirely, hence the presence of the OOP phase in our samples is testament to both the quality of the growth and the reliability of our transfer process. Here, I will focus on LAO/STO buffered α-Fe_2O_3

membranes grown on STO substrates, which were found to have the highest structural quality among the sets of membranes we grew (see section 4.4). Membranes grown on unbuffered STO and Al_2O_3 substrates will be discussed briefly at the end of this chapter (sections 5.5.1 and 5.5.2). Upon warming the membranes above RT, I would expect the sample to pass through the Morin transition into the IP phase, which we had shown to be topologically rich in our thin film samples [11]. The aims of this chapter are to explore the nucleation of the high temperature phase in this KZ analogue system and to verify the presence of topological textures in our new membranes, largely to prove that the topological phase had not been 'wiped out' by the higher lattice strain or defect density present in these membranes compared to thin films.

5.2 Thermal evolution of AFM membranes

For $T < T_M$ the α-Fe_2O_3 Néel vector is largely OOP due to the competition between the two anisotropy terms that lies at the heart of the transition. Our previously studied α-Fe_2O_3 thin films demonstrated this phenomenology, as the low-temperature (LT) magnetic state ($T < T_M$) consisted of a pair of time-reversal AFM domains oriented OOP separated by IP anti-phase domain walls (ADWs) [11]. This morphology can clearly be seen in the RT image of our AFM membranes, figure 5.3a, confirming that these membranes are below the Morin transition at room temperature as a result of the 3% Rh doping included during growth. Once this was established, I warmed the samples up by applying a current through the on-chip heater (see section 4.3.1) and studied the evolution of the magnetic state as a function of temperature, as shown in detail in figure 5.3. It is clear that the phenomenological evolution of the magnetic structure follows what would be expected for a 1st order magnetic phase transition. I observed the formation of IP domains both through the widening of the ADWs present in the OOP phase at RT as well as the nucleation of IP islands out of the OOP background at $T \approx T_M$, which then expand at higher T. Once the system reached $T > T_M$, being mindful that the transition has a width of ≈10 K, I observed spatially varied IP domains (red/white) with a few small OOP regions (blue) remaining. This phenomenology is remarkably similar to that in attached films [11], but in a system with significantly higher

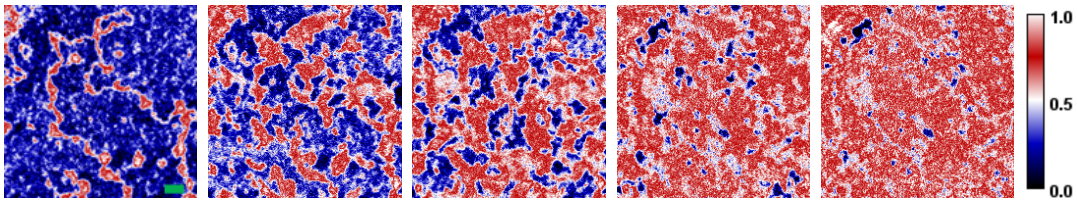

(a) 300 K **(b)** 307 K **(c)** 309 K **(d)** 312 K **(e)** 314 K

Figure 5.3: STXM images of the magnetic state of a 10x10 μm region of an α-Fe_2O_3 membrane at different temperatures taken by STXM. The green scale bar in (a) is 1 μm long. Each image throughout is seperately normalised and the colourbar shown will be excluded henceforth for brevity.

defect densities after a fairly rough transfer process, suggesting that the topological phase and the presence of the transition is more robust than previously expected. Additionally, the transition is spatially homogenous, which is to be expected due to the lack of any significant grain structure seen in these membranes as discussed in section 4.4.1. A further set of images taken on a different region in the same sample are shown in appendix B, figure B.4, showing the same phenomenology upon warming.

In order to verify that the observed contrast was antiferromagnetic in origin, I performed both an XMLD and XMCD measurement in the same area of the sample for $T > T_M$. The latter follows the standard 2E-2P measurement scheme [45, 93] taken at the same energies as the XMLD images throughout and using positive/negative circular polarisations. Full XMCD spectra were not taken and so different energies were not checked. Nonetheless, if XMCD contrast were present then one would expect to at least see some signature of it at the energies used here as they are close to the main resonance peak (see figure5.1). This is consistent with similar checks we have performed previously on substrate-attached thin film samples [11, 45]. These images are shown in figure 5.4. It is clear to see that the XMLD contrast is identical to that in figure 5.3e, whereas the XMCD image is remarkably different. The large white/blue region at the top left of the two figures is a crack in the sample used for focusing. The XMCD image is comprised

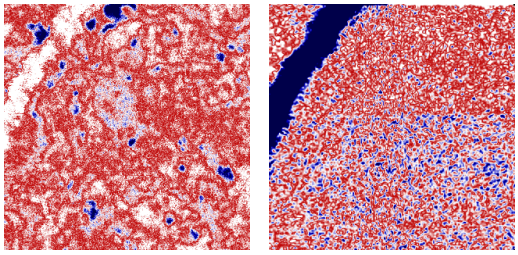

(a) XMLD image **(b)** XMCD image

Figure 5.4: a) XMLD and (b) XMCD STXM image in an 8x8 μm area.

entirely of short-lengthscale noise, indicating that the sample has zero XMCD signal due to the AFM domain structure. This confirms that the sample is definitely antiferromagnetic (rather than ferromagnetic) and also that the XMLD contrast is magnetic in nature, as one would expect structural dichroism to occur in the XMCD image also.

5.3 Observing topological textures

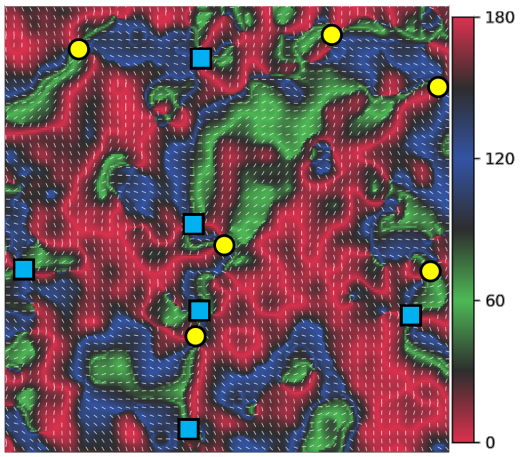

Figure 5.5: Vector map at 314 K on a 5.6x5.6 μm area towards the top left of the region in figure 5.3. The colourbar shows the angles corresponding to the colours in the image.

The OOP regions discussed above and observed in figure 5.3e can be of two possible types, either topologically trivial bubbles or whirling topological textures (i.e. (anti)merons). These can be distinguished by performing a vector map of the magnetic state as discussed in section 4.2.2, as topological textures will host a complete winding of the Néel vector around the core whereas a trivial bubble would not. Two example vector maps taken on this membrane are shown in figure 5.5 for part of the region shown in the warming cycle above and in figure B.5 (appendix B) for a different region on the same sample.

The blue/red/green (B/R/G) colours demarcate the three sets of 120° separated IP domains and their time-reversed counterparts, which are indistinguishable with this technique. The small white bars show the local Néel vector orientation. The yellow circles and blue squares are guides to the eye and highlight the locations of topological textures in these images, determined by tracing the pattern of domains in a closed loop around a point. The yellow circles are the cores of merons, with vorticity $Q_v = +1$ and topological charge $Q = \pm 1/2$, corresponding to a clockwise $R - \bar{G} - B - \bar{R} - G - \bar{B}$ winding of the domains. Here $R/G/B$ correspond to red/green/blue sectors and $\bar{R}$ denotes a time-reversal domain. Recall that, as discussed in section 1.2, due to the 180° ambiguity of the technique the topological charge Q of a given texture cannot be uniquely determined,

but the vorticity Q_v can and so is the primary number used to label topological textures here. The blue squares show antimerons, with vorticity $Q_v = -1$ and topological charge $Q = \pm 1/2$, corresponding to a clockwise $R - \bar{B} - G - \bar{R} - B - \bar{G}$ winding of the domains. Both texture types appear in approximately equal numbers here, suggesting that they are roughly equal in energy and therefore statistically equi-probable to nucleate. Additionally, I note here that the merons exhibit a variety of helicities ξ, as to be expected for a system with no symmetry-breaking iDMI interaction as discussed in sections 2.3 and 3.4.

In figure 5.5 it's clear that there are a number of meron-antimeron pairs in close proximity, but at a variety of distances (from 200 nm to 600 nm). I also note that there are a few regions that could potentially constitute a very tightly bound pair of topological textures based on the local winding of the Néel vector, but the resolution of this technique is not high enough to clearly identify them. As discussed in section 3.4.3, these pairs could either be TTMPs or bimerons. TTMPs are not likely to be stable at close distances, whereas bimerons have a preferred inter-core distance that depends on the material parameters but is on the order of 200 nm (figure 3.7). Whilst the more distant pairs could feasibly be either TTMPs or bimerons, the closest pairs are most likely stable bimerons with $Q = \pm 1$. The vector map taken on a different region of the same membrane shown in figure B.5 also appears to show a connected string of several merons and antimerons, similar to what has been observed in CuMnAs [52]. Hence, I am confident in saying that we have the full topological family present in our membranes for $T > T_{\mathrm{M}}$, after nucleation through the K-Z quench.

5.4 Thermal reproducibility

Another interesting observation I made when studying these α-Fe_2O_3 membranes is that, upon cooling back to RT ($T < T_{\mathrm{M}}$) after the warming and vector mapping process discussed above, the low temperature magnetic state recovered was remarkably similar to the initial state of the sample. I warmed the sample back to $T > T_{\mathrm{M}}$ and also noticed that the high temperature state was also quite similar to that found earlier. To investigate this effect further, I imaged the same position on the sample after an additional set of cooling and warming cycles. The STXM images of the initial state and the state after 1, 3 and 10

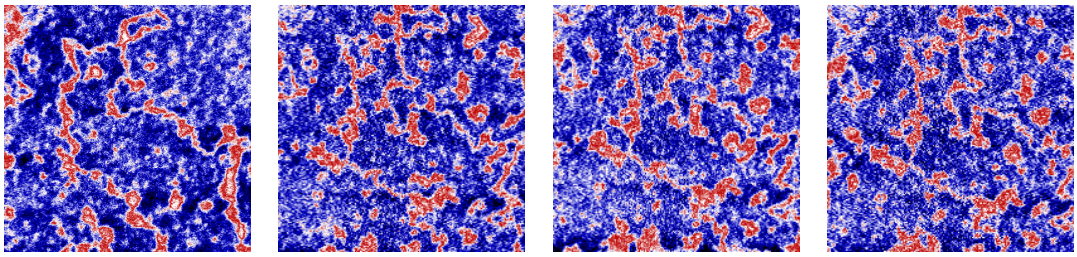

(a) Initial state **(b)** After 1 cycle **(c)** After 3 cycles **(d)** After 10 cycles

Figure 5.6: STXM images of the magnetic state of a 10x10 μm region at room temperature after a different number of thermal cycles to $T > T_M$ and back.

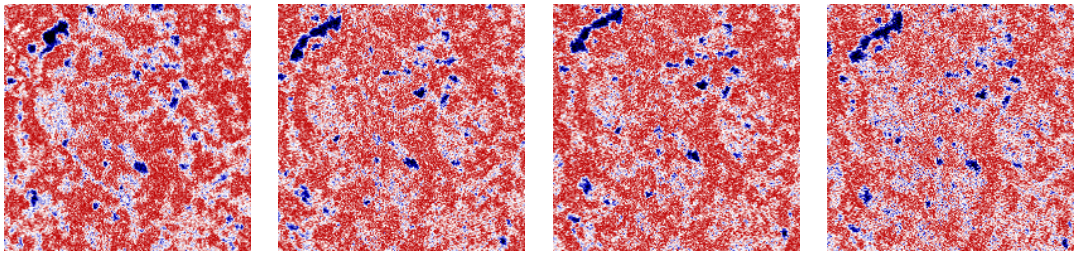

(a) Initial state **(b)** After 1 cycle **(c)** After 3 cycles **(d)** After 10 cycles

Figure 5.7: STXM images of the magnetic state of a 10x10 μm region at 314K after a different number of thermal cycles to $T < T_M$ and back.

total warming/cooling cycles is shown for $T < T_M$ in figure 5.6 and for $T > T_M$ in figure 5.7. In each case, it is clear that the large-scale structure of the domains is similar throughout, but smaller features do vary between each set of cycles. This is particularly evident in the small IP (red) islands in the RT state, some of which are consistent across the images but others are not. The OOP (blue) bubbles in figure 5.7 are also largely consistent across all images. Recalling that some of these bubbles are the cores of the topological textures seen in figure 5.5 strongly suggests that these are repeatedly nucleating at the same position.

The simplest explanation for this reproducibility, seen in a significantly reduced amount in our previous thin film samples [11], is the increased defect density present in our lifted membranes compared to the attached films. These defects will likely act as local pinning centres with a different anisotropy to the bulk. The exact nature of the defects (surface, structural etc.) cannot be determined from this STXM data itself, but is an interesting route for future exploration. Reproducibility of topological texture nucleation is an important prerequisite for some spintronics applications such as racetrack-based memory [28, 53] and so techniques to engineer these pinning sites

should be explored. This also supports the conclusions of section 3.7, where simulations containing different grains showed that these boundaries tend to act as nucleation centres for topological textures and pin domain walls. A similar effect is likely to occur for point/line defects, which are expected to be the most dominant defect type in this group of membranes, as discussed in section 4.4.1.

5.5 Unbuffered membranes

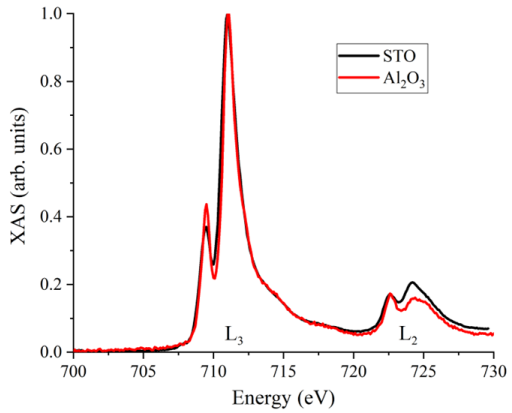

Figure 5.8: XAS of membranes grown on STO (black) and on Al_2O_3 (red), taken at RT. The $L_{2,3}$ sets of peaks are labelled. Both curves are arbitrarily scaled to lie between 0 and 1 and the red curve is shifted horizontally by 0.4 eV to correct for the slight energy shift between samples and to aid with direct comparison.

In addition to the membranes grown on buffered STO discussed extensively above, I also studied some other membrane types we produced, namely membranes grown on unbuffered STO and on Al_2O_3. As discussed in section 4.4, both of these membrane types have a greater defect density than the buffered ones, so their magnetic properties and evolution are not necessarily similar to the above case. Additionally, the membrane grown on unbuffered STO was found to have a transition slightly below RT, whereas T_M for the Al_2O_3 grown membrane was slightly above RT. This was confirmed initially via XAS taken at RT, shown in figure 5.8, where it is clear that the L_2 peaks have opposite ratios in these two membranes. By comparing these with figure 5.1, it is evident that, as expected, the membrane grown on unbuffered STO sits just above the transition (i.e. in the IP state) at RT whereas the Al_2O_3 grown membrane is comfortably below the transition (i.e. in the OOP state). The rest of this chapter is then devoted to some simple measurements on these two membrane types to confirm that their magnetic properties are not significantly altered, other than the modulation of the transition, despite the significantly higher defect densities present in these samples.

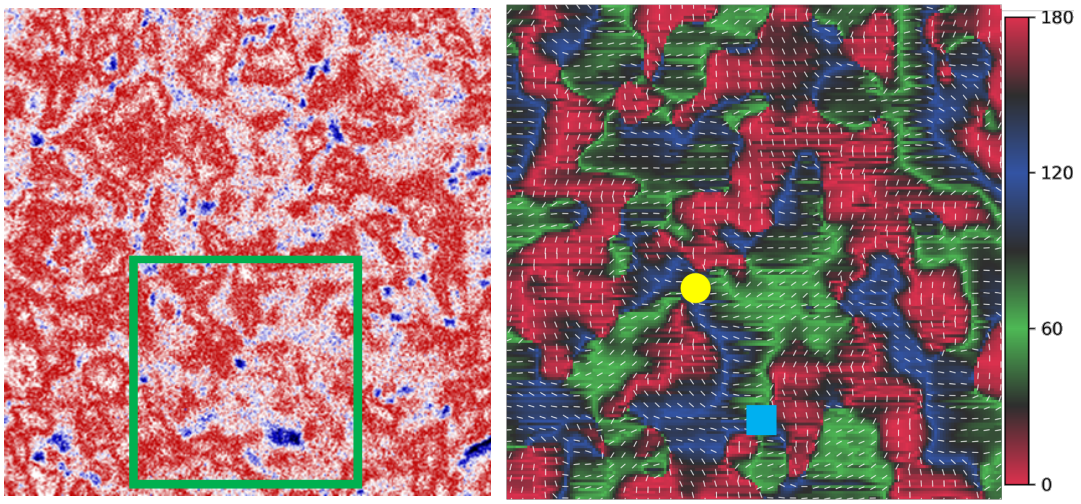

(a) XMLD image **(b)** Vector map

Figure 5.9: a) 10x10 μm area XMLD image in an unbuffered α-Fe_2O_3 membrane grown on STO. b) Vector map taken in a 4x4 μm region in the same area, shown by the green box in (a).

5.5.1 STO substrate

When studying a lifted α-Fe_2O_3 membrane grown on an unbuffered STO substrate, the key question is whether topological textures are stable in this system near room temperature, given that the transition sits slightly below RT as discussed above. This is interesting both from an applications perspective, as magnetic textures stable at RT are a key component of racetrack-based devices [28, 33], but also from a more fundamental perspective to understand the role of structural defects during a KZ quench.

In figure 5.9, I present an image of the magnetic state of the sample taken slightly above room temperature (≈302 K) along with the associated vector map taken in the green boxed region in the lower half of the larger image. A slightly warmed state was used in order to shrink some of the large OOP bubbles that were still present in order to make the vector map easier to construct. Two things are immediately clear. Firstly, this sample has very similar domain morphologies to the higher temperature state in the buffered sample (e.g. in figure 5.3e), consistent with the transition being slightly suppressed in this sample compared to the buffered membranes discussed above. Secondly, the fact that this sample can also host topological textures suggests that they are more robust to the presence of defects than we initially believed, although their areal density

is seemingly reduced compared to the buffered case (compared to figure 5.5). Thus, I have demonstrated here that the existence of the buffer layer in films grown on STO is not necessary to allow for the stabilisation of topological textures in lifted membranes, but does generally increase the crystalline quality and texture density. It will also be shown in chapter 7 that the absence of a buffer layer will mitigate some strain effects across bends in the membranes compared to the case with a buffer, making these types of samples very useful for benchmarking membrane strain experiments.

5.5.2 Al_2O_3 substrate

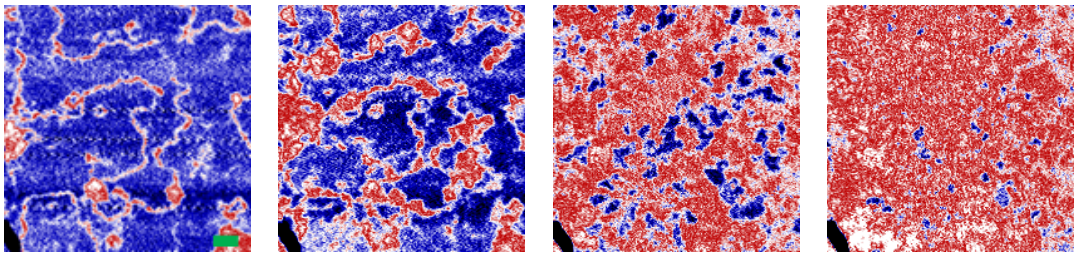

(a) 300 K **(b)** 311 K **(c)** 314 K **(d)** 322 K

Figure 5.10: STXM images of the magnetic state of a 10x10 μm region on a lifted membrane grown on Al_2O_3 at different temperatures. The green scale bar in (a) is 1 μm long.

Finally, I studied a lifted α-Fe_2O_3 membrane grown on Al_2O_3, to see if the phase transition was similar to the buffered STO membranes, despite the significantly higher defect density and larger transition width present in these samples (see section 4.4). From figure 5.10, it is clear that the general phenomenology of the transition is similar to that in buffered films grown on STO (figure 5.3), with a second example taken at a different position in the same sample shown in figure B.6 (Appendix B). The sample sits below the transition at RT and then, as the temperature is increased, the IP (red) domains nucleate and become abundant, whereas the OOP (blue) regions continue to shrink upon warming. As before, the remaining OOP regions at higher temperatures could either be non-topological bubbles, which would be expected to collapse at higher temperatures, or the cores of topological textures as seen previously in attached films grown on Al_2O_3 [11]. Given the similarities between the magnetic behaviour of the different types of membranes studied here, I would expect this system to host topological textures also, but perhaps at a reduced density compared to the other classes of membranes studied above.

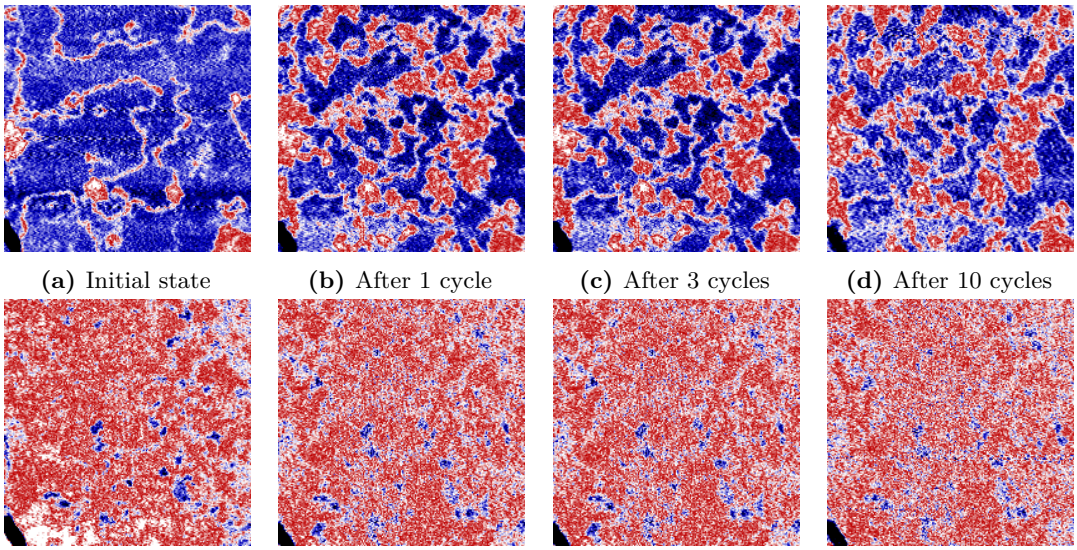

(a) Initial state **(b)** After 1 cycle **(c)** After 3 cycles **(d)** After 10 cycles

(e) Initial state **(f)** After 1 cycle **(g)** After 3 cycles **(h)** After 10 cycles

Figure 5.11: STXM images of the magnetic state of a 10x10 μm region at room temperature (a-d) and 320 K (e-h) after a different number of thermal cycles to $T > T_M$ and back to RT.

To further emphasise the effects that the increased defect densities have in the membranes grown on Al_2O_3, I performed a set of thermal cycles to 320 K ($T > T_M$) and back to RT on the same 10x10 μm region as figure 5.10, imaging the sample at both RT and 320 K in each case. This is shown in figure 5.11. Here, the similarity between the images after each set of cycles is drastic. For the RT state, the system is not fully below the transition at this temperature (due to the greater defect-induced thermal hysteresis compared to the other sample types) and therefore after the first thermal cycle some IP islands always remain upon returning to RT. What is remarkable is that the location and structure of these islands remains remarkably similar even after a large number of complete thermal cycles. Contrast this with figure 5.6, wherein there was some similarity between the ADWs remaining at RT, but they were not identical. Similar conclusions can be drawn about the thermal reproducibility of the HT state. Whilst the different IP domains are difficult to distinguish from single XMLD images, the locations of OOP bubbles (some of which are likely the cores of topological textures) are reproduced almost exactly after each cycle. This is clear evidence that the main difference between buffered membranes grown on STO and these ones grown on Al_2O_3 is in the thermal reproducibility of the state of the sample. As discussed above, it is difficult to argue that this should be caused

by anything other than the greater amount of defect pinning present in these samples, as well as due to the grain structure shown in figure 4.14 and as modelled in section 3.7.

This discussion has served to demonstrate that there is some flexibility in the crystalline quality allowable in these membranes both for the existence of the Morin transition and the stability of topological textures, ultimately allowing them to be nucleated via a KZ-like mechanism in any of these membrane types. This could be crucial from a future device perspective for scalable growth and transfer of AFM membranes. It is also fundamentally interesting, as the general KZ mechanism assumes a perfect system with a homogeneous ground state manifold [20–23], whereas I have demonstrated that the texture generation across a transition is robust even in the presence of relatively large defect densities and grain structures. This potentially broadens the scope of the effect to a wider class of materials and phenomena when ideal conditions cannot be realised.

The search for the truth might be flawed, but the search itself is priceless.

Terry Pratchett, *The Science of Discworld: Judgement Day*

6 Holographic imaging of AFM membranes

Contents

6.1 Introduction

In this chapter, I will present the results of my holographic imaging experiments based on the HERALDO technique described in sections 2.5 and 4.3.2. After discussing a few of the key difficulties in implementing this technique, this chapter will focus on the effects of magnetic fields applied to AFM membranes. Here, I studied α-Fe_2O_3 membranes grown on buffered STO only, similar to those investigated in chapter 5, as these form a good test bed for proof-of-principle studies. Firstly, by creating vector maps of the low temperature state in the presence of an applied magnetic field, I'll show that the effect on the structure within ADWs are largely immune to perturbation by external field. In addition, I will show that XMCD leads to ADW contrast in this imaging mode, which is unique in the sense that the compensated sublattices typically lead to zero XMCD signal in AFMs, potentially opening up novel imaging pathways. Magnetic fields

applied to the high temperature state lead to domain repopulation, imaged through both a standard XMLD approach and by vector mapping. I discuss how an applied field provides a symmetry-breaker between otherwise indistinguishable AFM domains related by time-reversal symmetry due to the presence of the canted moment. An example topological pair found in these membranes is studied as a function of field through several loops with interesting semi-reversible behaviour. I emphasise at the outset that this is an underdeveloped technique for studying AFM samples and the key goal here is to explore the potential for investigating AFM samples with in-situ perturbations utilising the major advantages inherent in the HERALDO scheme.

6.2 Optimising AFM imaging method

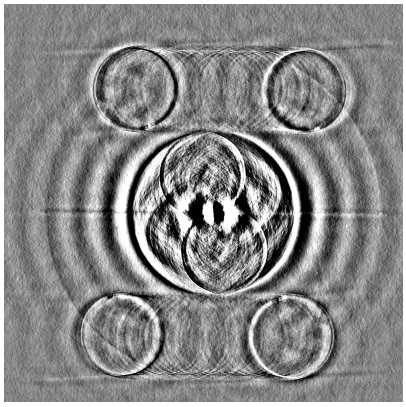

Figure 6.1: HERALDO image taken on one of the holes, showing extra reconstructions due to an improperly milled reference slit.

There were a few initial technical hurdles that had to be overcome before I could successfully image AFM membranes using HERALDO, over and above the inherent difficulties involved in preparing the mask and transferring the sample described in chapter 4. Firstly, I had to identify which of the holes milled through the mask were suitable for imaging. By taking holographic images across several different holes using the usual XMLD contrast method described in section 4.2, it is evident that there are additional weak reconstructions present in some areas due to discontinuities in the slits, for an example of this see figure 6.1. This rules out some of the areas as good-quality imaging sites and is a major downside of the difficult to reproduce mask preparation process. I stress that it is not easy to establish *a priori* which holes will be suitable without resorting to high-resolution imaging that is likely to damage the sample. This is one of the main reasons why a large array of holes was prepared, rather than a few isolated ones, in order to maximise the number of useable imaging sites. Nonetheless, I identified several object holes that were suitable for imaging through these initial trials, which had either no or very few extra reconstructions.

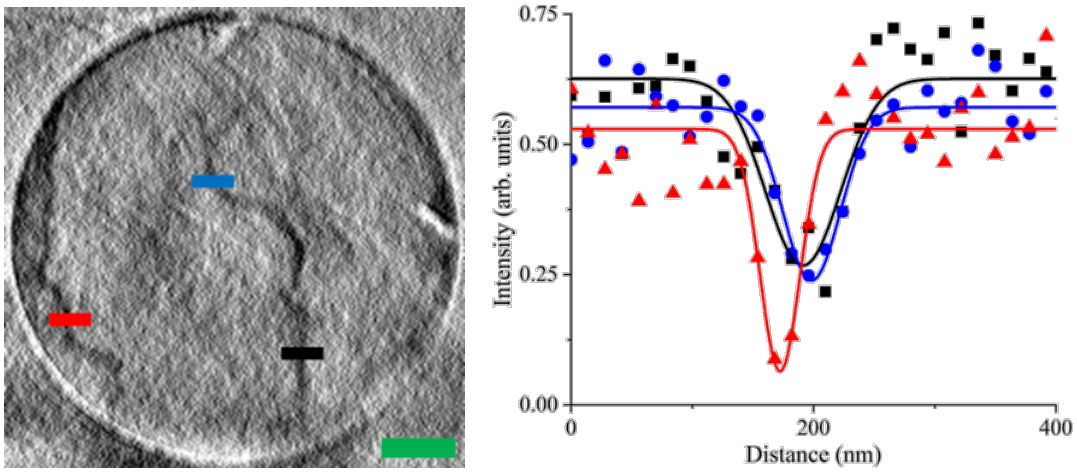

Figure 6.2: a) XMLD image of a domain wall taken at $T < T_M$. b) Linecuts and associated Gaussian fits of the pixel-by-pixel intensity taken across the corresponding coloured lines in (a).

Once the appropriate regions were identified, the next step was to optimise the x-ray energies to maximise the image contrast. As with our previous experiments [11] and our STXM work (chapter 5 [114]), this was done by considering pairs of energies close to the absorption peaks of the α-Fe_2O_3 XAS and identifying the energy pairs that produced the greatest contrast in XMLD imaging mode. The additional difficulty here is that single images cannot be used to identify the best energies, instead several pairs of energies must be checked to maximise the XMLD contrast. Once selected, that energy pair was utilised throughout all subsequent images. I note here that a slightly different energy pair was chosen for $T < T_M$ compared to $T > T_M$, as the optimised contrast for OOP vs IP domains is different to that for perpendicularly oriented IP domains. Additionally, for the entirety of this chapter, XMLD HERALDO images will be presented in greyscale, as direct IP/OOP attribution is more difficult than in STXM and the contrast is usually weaker. Finally, I should point out that only the parts of the images within the bounds of the circles are the reconstructions we care about, the circles themselves corresponding to the reconstructed boundaries of the object hole. The rest of the reconstructions correspond to the additional terms in equation 2.77 and so are not useful for imaging the magnetic state of the samples.

It is important to determine the resolution obtained with the masks and samples prepared here, as well as with the specific experimental configuration used. To this end, I

took a set of linecuts perpendicular to domain walls imaged below T_{M} (discussed further below) and performed a Gaussian fit of the pixel-by-pixel intensity, as shown in figure 6.2. Each pixel corresponds to ∼14 nm in real space after the reconstruction, as the 3 μm diameter holes are found to be 210 pixels wide. The extracted width of the Gaussian fit to each line cut was at least 40 nm in all cases, with larger widths found across some sections of the domain wall. Thus, the mask preparation resulted in an approximately 40 nm resolution here, which corresponds closely to the width of the reference slits as extracted from SEM images similar to figure 4.7c. The 14 nm pixel size results from the lateral dimensions of the camera used and the separation between the sample and detector, as the scattering vector corresponding to the furthest pixel from the image centre as well as the pixel density will also ultimately limit the instrument resolution. These parameters can in principle be optimised over and above what was used in these experiments and are usually less relevant to determining the ultimate resolution of the technique than the size of the reference feature given current manufacturing capabilities.

6.3 Imaging domain walls below T_{M}

As discussed previously, when $T < T_{\mathrm{M}}$ α-Fe_2O_3 hosts a set of AFM domains oriented along the c-axis, related by time-reversal symmetry and connected by ADWs. For our membranes, the c-axis is oriented OOP of the films, and therefore the domains at this temperature are oriented along the x-ray k-vector in normal-incidence geometry. Therefore, XMLD contrast allows us to clearly distinguish between the two OOP domains and the ADWs, although the pair of time-reversed OOP domains have the same contrast and so are indistinguishable. Figure 6.3a shows an example ADW separating two OOP domains, with the associated vector map taken in the boxed region shown in figure 6.3b. The white regions are OOP domains, which have been masked out by applying a binary filter to the vector map based on an average pixel intensity calculated from the set of angle-dependent images and with a threshold applied. The small coloured bubbles are nucleation sites, likely pinned at defects, and are expected to shrink further if the sample is cooled further below T_{M}. In general the domain walls are not homochiral and have a spatially-varying in-plane orientation. They also do not have a consistent width, likely due to the relatively

weak OOP anisotropy alongside local fluctuations in the anisotropy due to inhomogeneous strain caused by defects or imprinted surreptitiously during membrane transfer [114]. This is somewhat contrasted to what was observed previously in attached thin films, which had more consistent domain wall widths but were also multichiral [11]. This supports the attribution of the defect density to the variations in wall width, whereas the varied chirality is due to the absence of any symmetry-breaking chiral energy terms, e.g. an iDMI, similar to what was discussed in section 3.7.

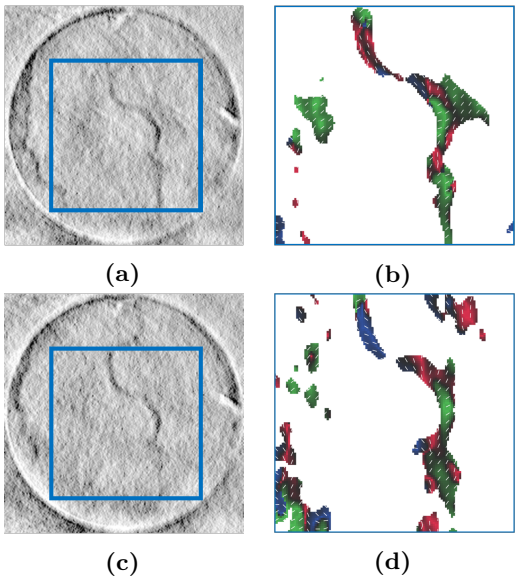

Figure 6.3: Holographic images (a,c) and vector maps (b,d) taken at 280 K (below T_M) in the absence of an applied field (a,b) and with a 650 mT field applied towards the right of the image (c,d).

Under application of magnetic fields up to 650 mT along the in-plane direction, the ADWs are seen to be structurally robust to change, as can be seen from the almost identical profiles in the XMLD images (figure 6.3c). This could be partly due to the relatively high defect density present in α-Fe_2O_3 membranes acting as pinning centres for the ADWs, meaning that relatively larger fields would be needed to affect them compared to less-defective samples. Moreover, as the fraction of the ADW that is fully in plane is relatively small, the canted moment and associated coupling with the external field is expected to be fairly weak; hence, the ADWs are not expected to completely reorient themselves to align the weak FM moment with the external field except at much larger field. Nonetheless, by analysing the vector map of the ADW (figure 6.3d) at 650 mT compared to the zero field case, I observe some reorientation of the IP component of the ADW. This suggests that the coupling is non-zero and that higher fields could potentially cause complete reorientation within the ADW. Whilst this would not enforce homochirality, as the orientation relative to the domain wall vector would still spatially vary as the wall itself wound through the sample, it could have potential uses for racetrack-type devices, wherein ADWs perpendicular to

(a) (b) (c)

Figure 6.4: a) XMLD image of ADWs for $T < T_{\mathrm{M}}$. b,c) XMCD image of the same ADWs using b) circular left and c) circular right polarised x-rays.

the long axis of the racetrack are favoured. I emphasise here that observing such AFM ADW reorientation in the presence of an steady-state in-situ magnetic field is significantly easier in holography compared to similar synchrotron-based x-ray techniques, due to the absence of focusing objectives and larger space in the experimental chamber.

More interestingly, and contrary to what can usually be observed in AFMs, ADWs lead to clear contrast with *circularly* polarised x-rays in our samples for $T < T_{\mathrm{M}}$ when imaged in the HERALDO geometry (figure 6.4 and B.9). These are 2E mode XMCD images rather than conventional 2E2P XMCD images, as left- and right-handed circular x-rays lead to the same contrast here and the image is formed by subtracting two images with the same polarisation at different energies. Nonetheless, the fact that contrast is observed at all with circular light is interesting and in stark contrast to what we had observed previously in PEEM and STXM [11, 114], wherein XMCD imaging of AFM structures shows zero contrast for both $T < T_{\mathrm{M}}$ and $T > T_{\mathrm{M}}$ in both 2E mode and 2E2P mode. These images were taken at the same pair of energies as the XMLD images above (but on a different object hole) and show clear contrast between the ADWs and the OOP background. Additionally, the two time-reversed OOP domains are still indistinguishable with XMCD imaging and I also note that the fact that both right-handed and left-handed circular light produces the same ADW contrast is opposed to what is typically seen in FM materials using absorption techniques [36, 93]. This is likely due to the additional coherent scattering effects that are absent in standard absorption-based techniques and is a major new imaging scheme that has, up to now, been absent in AFMs. The downside is

that the variation in IP contrast observed with XMLD imaging and used to construct vector maps is absent with XMCD HERALDO imaging and therefore this technique is only useful for observing ADWs in an OOP background when $T < T_{\mathrm{M}}$.

6.4 Imaging domains above T_{M}

After warming the sample to 320 K ($T > T_{\mathrm{M}}$), I expect the ADWs to widen and form an IP matrix of 3-fold domains separated by 120° and their time-reversed counterparts, akin to what was observed previously in thin films [11]. Indeed, our XMLD HERALDO images change drastically compared to what was observed at low temperature, with a large domain oriented perpendicular to the incident x-ray beam clearly visible before any field is applied (figure 6.5a). Due to the three-fold domain structure in these materials, only one domain is seen clearly in the reconstruction, as the other two domains contribute equally to the x-ray scattering at a given polarisation and so are indistinguishable. Under application of a magnetic field up to 800 mT, the largest field used here, this clear domain appears to shrink systematically with applied field. The end state of this procedure is shown in figure 6.5b and this process will be explored in more detail using vector mapping below. Reversing the field direction leads to a drastic change in the domain configuration, as the previously favoured domains are now anti-favoured with respect to the applied field and this becomes apparent by comparing images at -300 mT (figure 6.5c) and -650 mT (figure 6.5d) to the two previous states. Interestingly, returning to a positive value of field (400 mT) recreates a domain structure that is somewhat similar to the initial state, see figure 6.5e, suggesting that the field-dependant processes may be semi-reversible. This could be an effect of defect

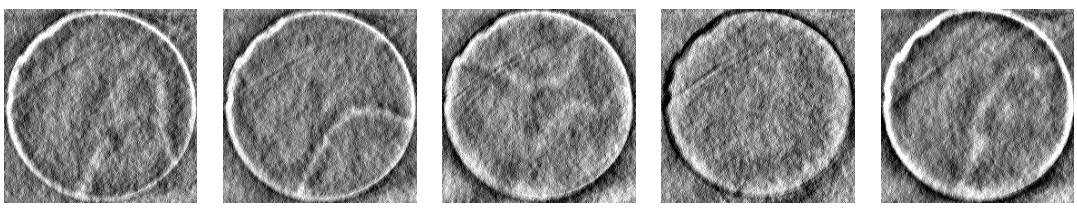

(a) Initial state **(b)** 800mT **(c)** -300mT **(d)** -650mT **(e)** 400mT

Figure 6.5: XMLD HERALDO images taken at 320 K ($T > T_{\mathrm{M}}$) as a function of field applied to the right/left of the image for positive/negative fields.

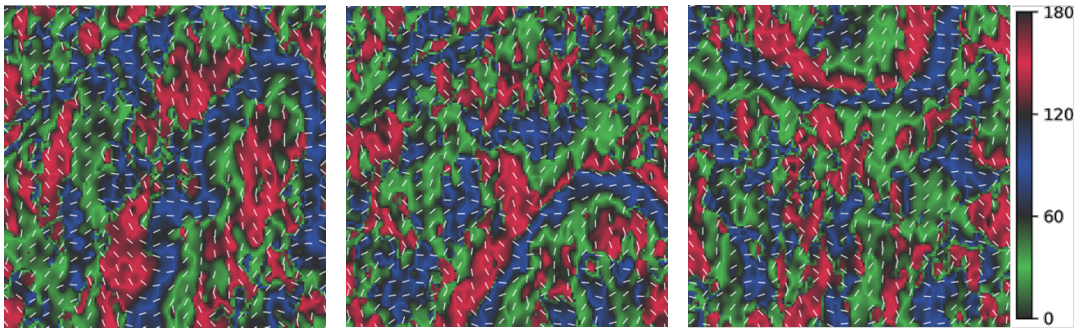

(a) 0 mT **(b)** 550 mT **(c)** -400 mT

Figure 6.6: XMLD vector map images of AFM domains taken at 320 K (above T_M) at different field values for the same sample position as figure 6.5 and taken during that sweep. The colourbar in (c) shows how the colours shown across the vector maps relate to the Néel vector angle relative to the vertical axis.

pinning, as discussed in section 3.7, or could hint at some more complicated underlying mechanism for domain repopulation in the presence of an applied field.

To better understand the field-dependent behaviour of these IP domains, I performed an XMLD vector map at several points during the above field sweep, allowing me to clearly identify the three pairs of 120° domains (figure 6.6a) at each point and understand their behaviour. An additional example of the phenomenology discussed herein is shown in figure B.10, taken on a different object hole. I note at the outset that no topological textures can be seen in these images, which is not an issue as this section is devoted to the behaviour of non-topological AFM domains under an applied external field. The effect of field on topological textures will be studied later. The "blue" domain, which is clearly recognisable as a bright region in the zero-field intensity image (figure 6.5a), appears to connect two pairs of green/red domains, which are likely to be time-reversed counterparts. I note at this stage that XMCD images taken at this temperature show no contrast, due to the lack of any OOP regions. This is a further signature that there are not any topological textures visible in this image, as is clear from the vector map. I would predict that topological merons observed previously in similar samples would be visible using such contrast due to their OOP cores, provided these were larger than the resolution limit of the masks used.

Under application of a 550 mT IP field, the bright domain appears to shrink drastically in the vector map (figure 6.6b), consistent with what was shown in figure 6.5b for higher

field values. Due to the discontinuity of the process, it is difficult to tell from the vector map alone whether this corresponded to an actual shrinkage of that domain or it fracturing into several smaller domains. Moreover, there is a large-scale redistribution of the domains compared to the zero-field case. Interestingly, whilst it is the large blue domain that shrinks, I also note the apparent nucleation of many smaller vlue domains out of the mostly red/green background. Crucially, an applied field provides a symmetry-breaker between the two time-reversal domains with Néel vector perpendicular to the applied field, as these have opposite canted moment and therefore have inverted coupling to the external field. Hence, the newly nucleated blue domains can be identified as those with a magnetic moment parallel to the applied field, whereas the shrunken blue domain must be its time-reversed counterpart. The green/red domains serve as pathways for this domain repopulation, as these pairs of domains are all roughly equal in energy with regards to the applied field.

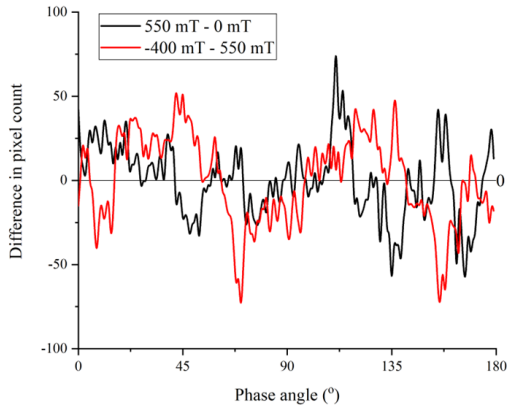

Figure 6.7: Plot of difference in distribution of phase angle under different applied fields for the three vector maps shown in figure 6.6. The black curve shows the difference between the 500 mT and 0 mT vector maps and the red curve shows the difference between the -400 mT and 500 mT vector maps.

When the field direction is reversed to -400 mT, there is a stark change in the overall domain structure and populations (figure 6.6c), corresponding to the midpoint of the two states shown in figure 6.5d,e. Clearly, blue domains dominate the image at this field, however these are likely to be the time-reversal counterparts of the domains studied at positive field values. These images serve to demonstrate that the field-dependent behaviour of AFM membranes is distinctly non-trivial and that the mechanism for domain repopulation is tricky to study. Nonetheless, I can make a few immediate observations. Firstly, it is clear that the domains oriented perpendicular to the field direction (with an associated canted moment parallel to the field) are favoured. Secondly, the saturation magnetisation must be larger than the 800 mT field used here, consistent with the full hysteresis loops

studied for thin films previously [11]. The plot of the variation in phase angle distribution during the steps studied in figure 6.6 is shown in figure 6.7. From this figure, it is clear that the change in phase angle distribution is largely reversed when the field direction is reversed, but no further major conclusions can be straightforwardly drawn. On the positive side, this represents the first clear imaging of AFM domain repopulation in the presence of an applied magnetic field (that I am aware of) and therefore opens up the route to more detailed investigations of these phenomena in future through the use of HERALDO or similar transmission-based techniques.

6.5 Topological textures in magnetic fields

Similar to what was observed in AFM membranes using STXM, as discussed extensively in chapter 5, topological textures were also found to be stable (although seemingly less abundant) in the membranes prepared for holography. Both a single XMLD image and the associated vector map for a pair of topological textures is shown in figure 6.8, taken at 320 K in the absence of an applied field. As before, merons and antimerons are shown by yellow circles and blue squares respectively, as determined by the winding of red/blue/green domains around the core. This meron-antimeron pair are fairly separated spatially (≈ 1.7 μm), therefore I would not categorise them as a bound bimeron system as they may also comprise a topologically trivial structure. They are, however, directly connected by a string of red/green/blue/red domains, similar to the "half-moon" structures previously observed in thin film samples [11, 45]. This verification of the presence of topological textures in AFM membranes further supports the results and conclusions of chapter 5, but also offers a unique opportunity to study the effect of magnetic fields on such textures due to the flexibility of the HERALDO technique.

Under application of a 500 mT magnetic field in the IP direction, the pair of topological textures shown in figure 6.8 show an obvious shrinking in the domains connecting the two cores, as seen in figure 6.9b compared to the initial zero field state (figure 6.9a). This occurs without much modification to the textures themselves, as their inter-core distance remains constant across all the images. This appears to be a somewhat reversible process, as reducing the field down to 100 mT returns the connecting domains to roughly

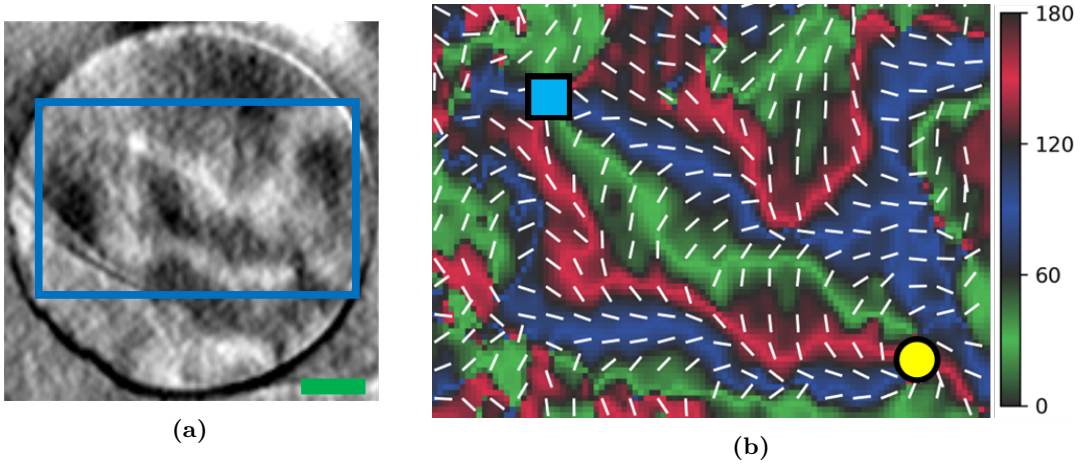

Figure 6.8: a) XMLD HERALDO image and (b) corresponding vector map of topological textures in the absence of an applied field. The vector map is taken in the blue boxed region in (a).

their original position (figure 6.9c). A further cycle to 500 mT and back shows an almost identical behaviour (figure 6.9d,e). This suggests that the main effect these fields have on topological texture pairs is to alter the energy cost of different domain orientations surrounding or connecting the textures, without affecting the cores themselves. This is due to the fact that some of the connecting domains are less energetically favourable than others in the presence of the applied field and therefore would tend to contract, whereas the time-reversed counterpart domain would expand due to the field-induced symmetry breaking. To describe phenomenologically the process occuring under applied field, assume that the initial configuration around the meron core is $R-\bar{G}-B-\bar{R}-G-\bar{B}$ as in figure 6.8. Upon application of a magnetic field along the positive x direction, one would expect the configuration to become $\boldsymbol{R}-\bar{\boldsymbol{G}}-B-\bar{r}-g-\bar{B}$, where bold/lowercase symbol indicate greater/lower angular range for a given domain. This is due to the fact that the canted moment, which couples to the applied magnetic field, is always in-plane and perpendicular to the local Néel vector.

The reproducibility under field cycles is probably a result of defect pinning of the domains, making it more energetically favourable for them to return to their original positions when the applied field is weaker. Unfortunately, due to the relatively small field of view of the technique and the restriction on the number of imaging positions available, no isolated topological textures were observed in this membrane (even after

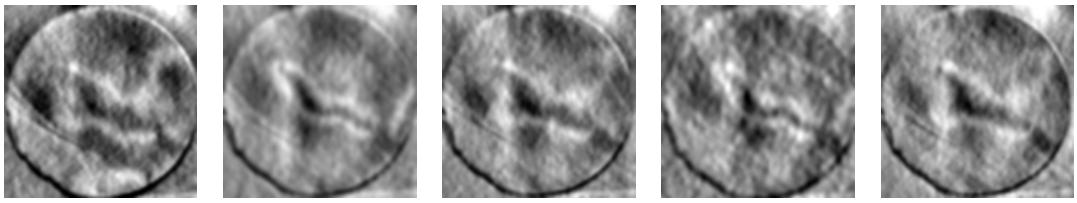

(a) Initial state **(b)** 500mT **(c)** 100mT **(d)** 500mT **(e)** 100mT

Figure 6.9: Images taken at the position of the pair of topological textures shown in figure 6.8 as a function of field, cycling to 500mT and back down to 100mT twice.

several thermal cycles) and thus the effects of field on isolated textures could not be studied. This experiment has reinforced the stability of topological textures to external perturbations, as well as providing a major advantage for AFM systems over FMs for spintronics applications, where much lower fields tend to fully align FM states. Detailed field-dependent investigations of the full topological family present in α-Fe_2O_3 remains an interesting and open route for future studies.

"I feel thin, sort of stretched, like butter scraped over too much bread"- Bilbo Baggins

J. R. R. Tolkien *The Fellowship of the Ring*

7 Strain in membranes

Contents

7.1 Introduction

It is an intuitive realisation most children make that certain objects tend to stretch or deform when you pull on or squash them, whereas many are resistant to such changes. Secondary school physics teaches us that, due to the arrangements of atoms or molecules in specific materials and the types of bonds involved, their respective bond strengths determine this resistance. One of the key parameters describing the deformation of an object under tension or compression is *strain*, typically defined as the fractional length change of an object when a force is applied. In 1D, such as the case of a classical spring (the context in which this concept is usually introduced), this is written as

$$\epsilon = \frac{\Delta l}{l}, \tag{7.1}$$

whereas in higher-dimensions this is represented by a 2-dimensional strain tensor

$$\epsilon_{ij} = \frac{1}{2}\left(\frac{\partial d_i}{\partial x_j} + \frac{\partial d_j}{\partial x_i}\right). \tag{7.2}$$

Here, $\partial d_i/\partial x_j$ represents the way the distortion along the i-axis depends on the length of the j-axis of the system. The diagonal elements of the above tensor (i.e. ϵ_{ii}) correspond to direct analogues of the 1D case, whereas the off-diagonal components are called shear strain. Such off-diagonal components are only allowed in certain crystal symmetry classes (space groups), as this also determines the number of independent components of the strain tensor. When there is a direct relation between elastic deformations of a material and applied forces, such as in a material obeying Hooke's law, one can also use the strain tensor to relate the elastic deformations of a body to the applied forces.

A critical field of condensed matter physics is the study of materials where combinations of electric, magnetic and elastic order parameters are coupled together. This can lead to a variety of extremely interesting phenomena, such as the buildup of a voltage across certain crystals when they are compressed (the famous piezoelectricity), which also have wide-reaching practical applications[139]. Magnetoelectric materials such as $BiFeO_3$, in which the magnetic order parameter can be switched by applying a voltage across the material (or vice-versa), have also been proposed as the bedrock of novel, low-energy memory-in-logic computing devices [140–142]. Given this, we are then faced with the question of whether we can couple the antiferromagnetic order parameter found in our α-Fe_2O_3 samples with applied external strain. This would provide an additional athermal handle to control the magnetic state of this material in-situ.

Here, I discuss my investigations of the effects of strain on AFM domains in α-Fe_2O_3 membranes, wherein I study serendipitously formed bends in lifted membranes as well as utilise the gas cell setup discussed in section 4.3.1.1 to systematically explore strain-induced effects. These bent regions will lead to spatially varied domain morphologies, which are then explained by exploring the effect of strain on the Morin transition. We shall see that bends in lifted membranes can either host compressive or tensile IP strain, depending on

the sample morphology and orientation. I will discuss how crucial the presence of the buffer layer in our samples is to allowing these strain-induced effects and will explain this through finite-element analysis and studying bends in an unbuffered membrane. Additionally, symmetrically applied IP strain can be used to systematically tune the Morin transition temperature, whereas asymmetric strain can lead to the development of an additional uniaxial IP anisotropy, allowing the preferential stabilisation one of the three-fold IP domains typically observed in unstrained films. I will explore the temperature-strain phase space for α-Fe_2O_3 membranes for symmetrically applied strain. Finally I studied the effects of uniaxial strain on AFM domains above the Morin transition by utilising rectangular Si_3N_4 sample holders. I observed that uniaxial strain tends to preferentially stabilise one or two trigonal domains over the others, depending on the relative orientation between the strain axis and the trigonal domains. This chapter will lead to interesting possibilities for strain engineering the transition temperature and domain morphology post growth with potential technological applications, as well as a unique athermal method for studying KZ-like phenomenology.

7.2 Strain across membrane bends

7.2.1 Temperature dependence

As discussed in section 4.4, our α-Fe_2O_3 membranes can be transferred onto various platforms post-growth via either directed transfer or scooping from water. As the latter is a fairly rough and random process, the transferred membranes often have varied morphology, which includes cracks, folds and bends (see figure 4.3). Due to the flexible nature of our thin lifted membranes, I would expect regions involving bends to induce strain in the membrane. In fact, one would expect *a priori* relatively large crystal strains to be present in these extreme regimes, much larger than can typically be obtained in thin films or bulk samples [143–146]. Thus, these membranes act as an interesting test bed for exploring the effects of moderately large strain on antiferromagnetic domain structures in α-Fe_2O_3 (and potentially other systems that can be grown on similar platforms). It could also serve as a launching point for exploring more exotic geometrically induced effects, such as flexoelectricity or curvilinear magnetism [147–150].

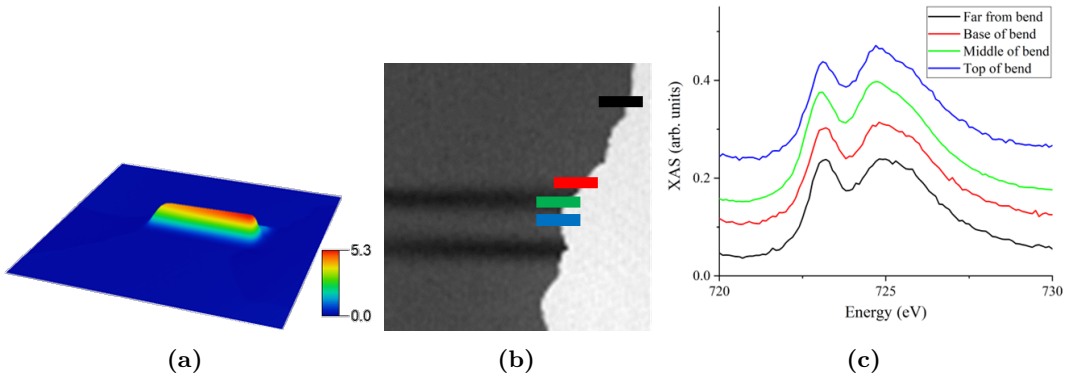

Figure 7.1: a) Confocal microscopy image across a membrane bend, the colour scale shows the local height of the membrane in μm. b) 40x40 μm STXM intensity image across the same bent region. c) XAS at the L_2 edge taken at RT at different focus heights at several positions along the bend. The curves have been arbitrarily offset vertically for clarity and the colours correspond to the positions marked by the lines in (b).

We prepared several α-Fe_2O_3 membranes grown on buffered STO and then transferred via the scooping technique and studied their magnetic properties via STXM. The methodology was largely the same as in chapter 5, but here I focused on regions containing strong membrane bends. An example bend, imaged by confocal microscopy (figure 7.1a), was studied in detail to understand how this spatial variation would affect the magnetic properties of the system. I emphasise at the outset that the existence of such bent regions is a unique property of our lifted membrane samples not found in bulk crystals or attached thin films. As is clear from the XAS at different positions (figure 7.1c), the magnetic state of the system at RT varies across the bend. From the relative heights of the L_2 peaks, the bulk of the film away from the bend appears to be below the transition (as $T < T_M$), whereas the peak of the bend is above the transition.

In order to further investigate the variations in the XAS shown in figure 7.1, I took a set of STXM images across the bend at different temperatures, shown in figure 7.2. The sample was rotated so that the x-ray polarisation vector was always perpendicular to the direction of the bend, i.e. along the horizontal axis in figure 7.2. This therefore ensures that there should be no geometrical effects, as the polarisation remains parallel to the IP sample axis at all points across the bend. Due to the $\approx 2\,\mu$m depth of focus of the STXM at these energies and the $\approx 6\,\mu$m bend height, only part of the bend can be in focus in any given image. As a result, I took a set of images focused in the far

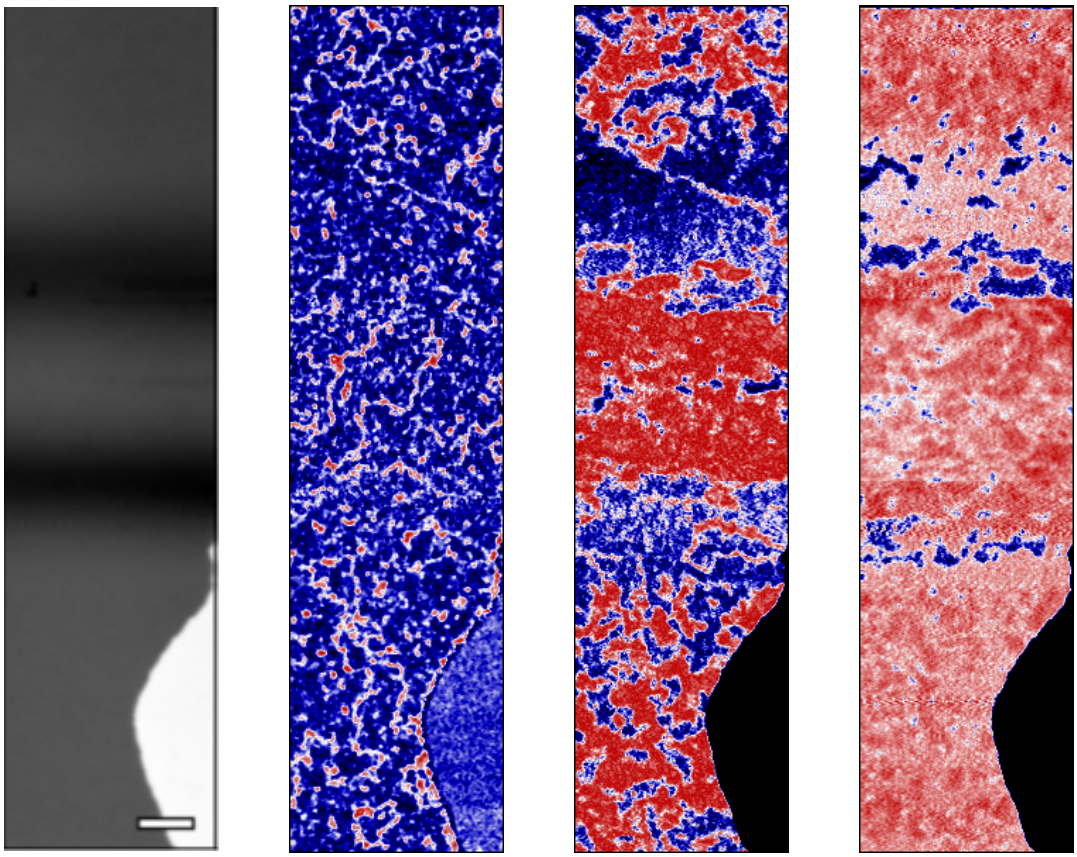

(a) Sum image **(b)** $T < T_M$ **(c)** RT, $T \approx T_M$ **(d)** $T > T_M$

Figure 7.2: a) Intensity image showing the same membrane bend as figure 7.1, with the darker regions corresponding to the area of steepest slope along the bend. The scale bar 2 μm long. (b-d) XMLD images across the bend as a function of temperature.

field, on the side, and at the peak of the bend. I then stitched these together, such that every part of the bend was in focus in at least one of these images and therefore the magnetic structure across the bend was consistently sharp in the final image. The images were smoothed and mutually rescaled prior to stitching to ensure the contrast across the final stitched image was consistent.

At low temperature ($\approx$ 250K), the entire membrane is clearly below the transition (figure 7.2b), showing that the strain across the bend is not sufficient to suppress the transition entirely. Upon warming to RT, there emerges a spatial modulation of the contrast, such that the top of the bend is clearly above the transition whilst the sides of the bend remain below the transition, shown by the relative proportion of IP/OOP (red/blue) domains across these regions. The bulk of the membrane is in the intermediate state at

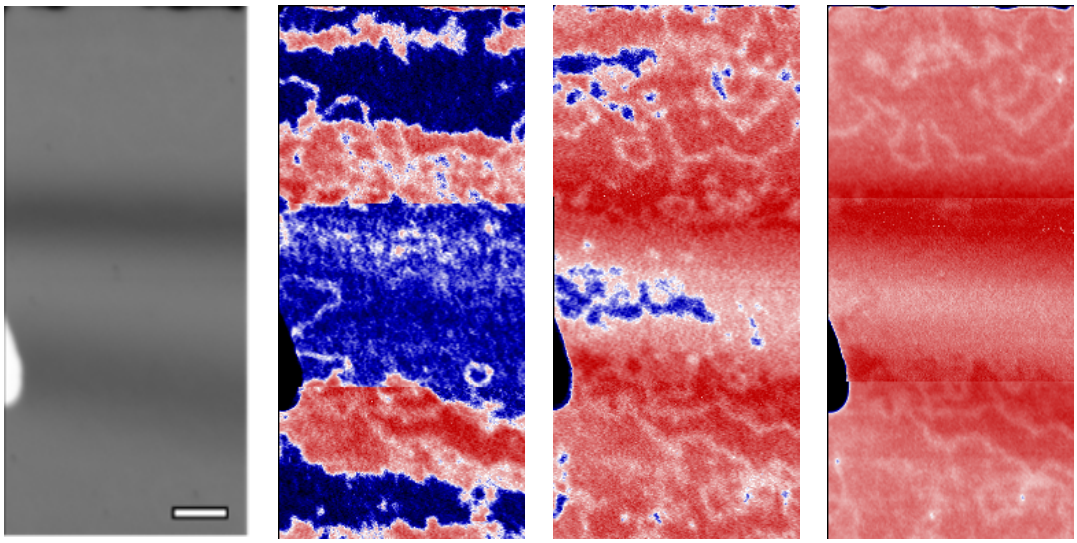

(a) Sum image **(b)** RT, $T \approx T_M$ **(c)** $T > T_M$ **(d)** $T >> T_M$

Figure 7.3: a) Intensity image showing a bend in a "flipped" membrane, with the darker regions corresponding to the steepest slope. The scale bar 2 μm long. (b-d) XMLD images across the bend as a function of temperature.

this temperature, i.e. $T \approx T_M$, such that the regions away from the bend show a roughly equal mixture of IP and OOP domains, similar to what was seen in chapter 5. This is consistent with what was observed in the XAS data across the bend as shown in figure 7.1c. At 315 K the bulk of the membrane is comfortably above the transition (as $T > T_M$), along with the top of the bend. The sides of the bend are largely through the transition but it is clear that there is still a sizeable OOP fraction at this temperature, which I would expect to shrink further at even higher temperatures. It is therefore clear that the top/sides of the bend are experiencing an inverted modification of the local T_M compared to each other and relative to the T_M in the membrane bulk. This is the first major signature of strain-based magnetic modulations in freestanding AFM membranes, and shows that the main effect the strain appears to be having is to vary the local transition temperature. Recalling that the Morin transition occurs due to a competition between single-ion and dipolar energy terms (see section 1.1), both of these terms will be adjusted as the atoms in the crystal move closer together/further apart, depending on the nature of the strain involved. Thus, the variation in local T_M occurs as a result of the differing ratio of these two anisotropy terms due to the strain-induced alteration of the local crystal structure.

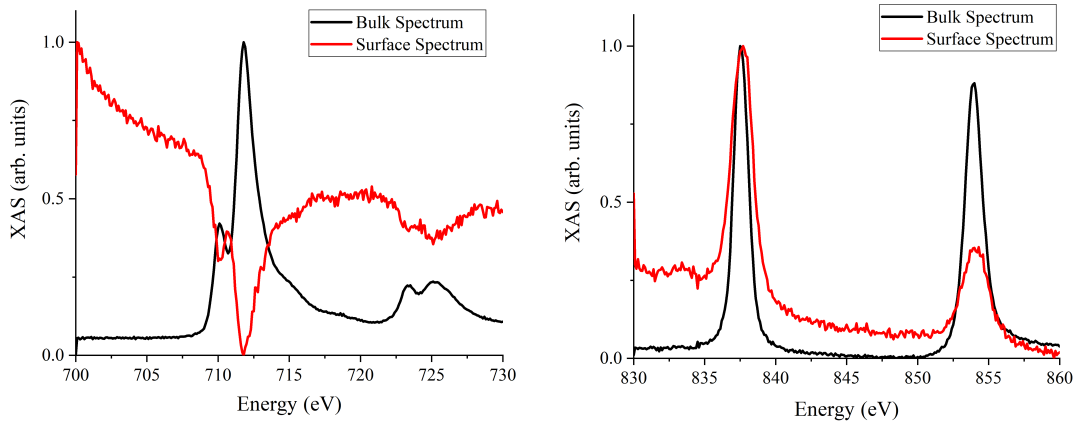

(a) Fe spectrum **(b)** La spectrum

Figure 7.4: Bulk-sensitive XAS (black) and surface-sensitive TEY XAS (red) taken across the "flipped" membrane discussed above. These XAS are taken across the Fe L-edges (a) and the La M-edges (b). Each spectrum is linearly rescaled to lie in the range {0,1}.

To clarify this discussion further, I also studied a bend in a "flipped" membrane, such that the buffer layer was on the top and the α-Fe_2O_3 was underneath. I note that this flipping happened spontaneously during the scooped transfer of this particular membrane, as will be demonstrated definitively below (figure 7.4). As seen in figure 7.3, the top of the bend now has an enhanced transition temperature, whereas the sides of the bend are above the transition even at room temperature. By comparing this to figure 7.2, the situation is clearly reversed. At higher temperatures, the entire sample can be brought comfortably above the transition, again demonstrating that the transition is only shifted, rather than wholly destroyed, by the strain across these bends. These observations add an interesting facet to the work, as now one can in principle tune not only the strength of the strain (by adjusting the curvature of the bend) but also its sign by utilising the relative orientation of the buffer and AFM layers. This could in principle be used to locally tune the T_M in a region, e.g. by using an AFM tip to create an indent in a membrane, likely inducing inversed effects in membranes that are identical except for the different buffer positions relative to the sample surface.

Additionally, I used surface-sensitive TEY STXM to directly confirm that the buffer layer was on top for this membrane (see section 4.3.1.2). Performing TEY XAS scans across the "flipped" membrane studied above and comparing these to the standard bulk-sensitive XAS (figure 7.4) clearly shows that the La signal from the surface is strong, corresponding

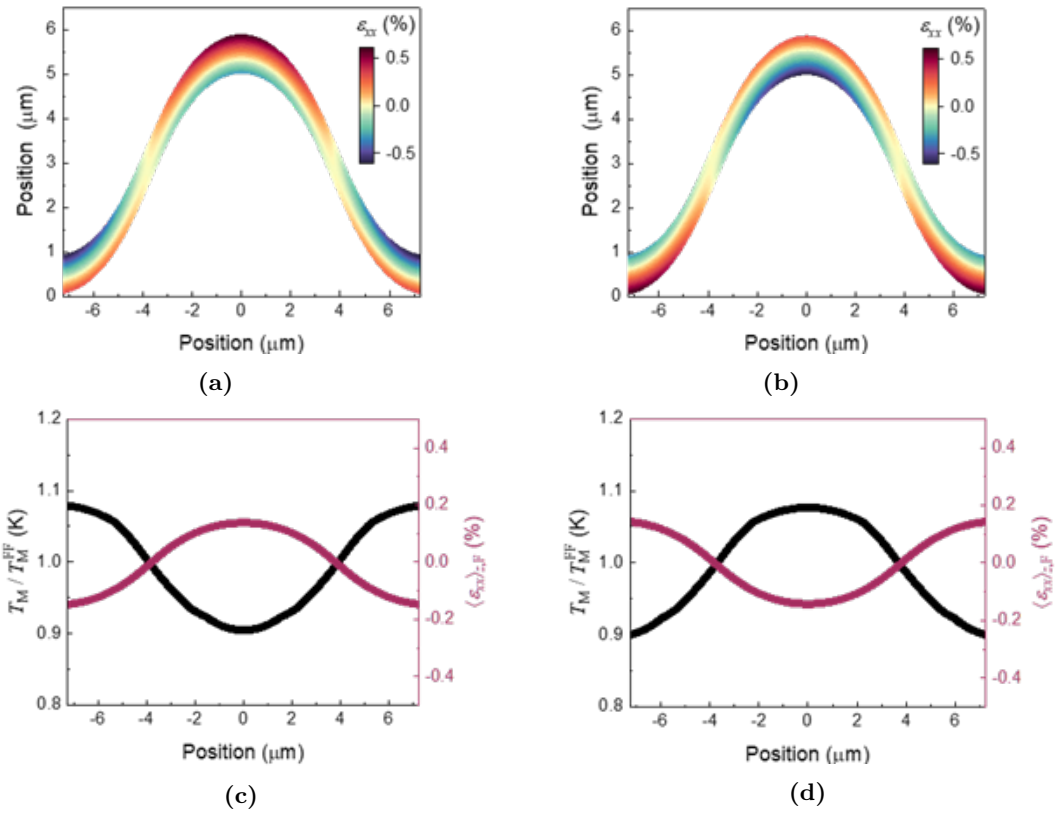

Figure 7.5: a,b) Simulated strain profiles across an (STO/LAO) buffer/α-Fe_2O_3 stack, with the α-Fe_2O_3 layer on the top/bottom in (a)/(b) respectively. (c,d) Thickness-averaged strain and corresponding local T_M across the corresponding simulated membrane bends. Reproduced with permission from [114].

to the LAO buffer layer on top, whereas the Fe spectrum is significantly suppressed. In fact, the Fe TEY spectrum appears inverted compared to the bulk spectrum. This is because a greater proportion of the x-rays are absorbed on the path through the sample to the surface region near the Fe absorption edges, such that the background electron emission from the surface is reduced at these energies and therefore the TEY signal is reduced. This is direct evidence that the membrane in figure 7.3 is "flipped" compared to that in figure 7.2, suggesting that this is the cause of the reversed effect on T_M across the bends in each case.

7.2.2 Mechanical model of membrane bends

To understand the strain profile across the membranes, a colleague performed time-dependent finite-element simulations of our membranes, with data and discussions provided by me. The key points will be outlined here, as these are crucial to explaining the effects of strain in AFM membranes, with full details provided in [114]. The membrane dimensions,

including the height and base of the bend, were extracted from the confocal microscopy measurements (figure 7.1) and approximate material parameters from the literature for the different materials involved were used [151–153]. By applying an upward impulse to the flat membrane and then allowing it to mechanically relax, membrane bends of similar shapes and dimensions to those found from confocal microscopy mapping were stabilised and the simulated strain profiles within the bends were extracted.

Figure 7.5 shows clear thickness-dependent strain profiles that also vary spatially across the bend for the two cases studied above, i.e. with the buffer layer below (7.5a) or above (7.5b) the α-Fe_2O_3. The colour scales show both the magnitude and type (+ve tensile, -ve compressive) of the strain in each part of the membrane. In each case, the strain was then averaged through the thickness of the α-Fe_2O_3 layer to get the net strain profile across the bend and this was then compared to strain-dependent T_M data for thin films from the literature [104], with the bulk transition temperature of the film in the far-field (T_M^{FF}) set at 300 K. This leads to a variation of the local T_M across the membrane of $\pm 10\%$, roughly consistent with what was seen in our earlier images (figures 7.2 and 7.3).

These simulations demonstrate that our membrane bends have a roughly symmetric strain profile either side of the "neutral line". This would be expected to pass through the centre of the membrane in the case of a uniform material, leading to zero net strain when averaged across the thickness. In the case with the STO/LAO buffer layer underneath the α-Fe_2O_3, the buffer accommodates some of the strain, such that the neutral line lies near the bottom of the α-Fe_2O_3 layer and thus a net strain is present in the antiferromagnetic layer. For the flipped membrane, with the buffer layer of top and α-Fe_2O_3 underneath, the neutral line instead lies near the top of the α-Fe_2O_3. This comparison emphasises the role the buffer layer plays in accommodating part of the strain and leading to the spatial modulation of the transition temperature. For the case of figure 7.2, the simulations give a net tensile strain at the top of the bend and a compressive strain on the side of the bends and this is reversed for the case of figure 7.3. Based on previous studies on the effects of strain in bulk systems and thin films [13, 82, 104], one would expect tensile strain to reduce T_M, whereas a compressive strain would enhance it. Thus, our simulated strain profiles are consistent with our observations of the variations in local T_M across the bend. This serves

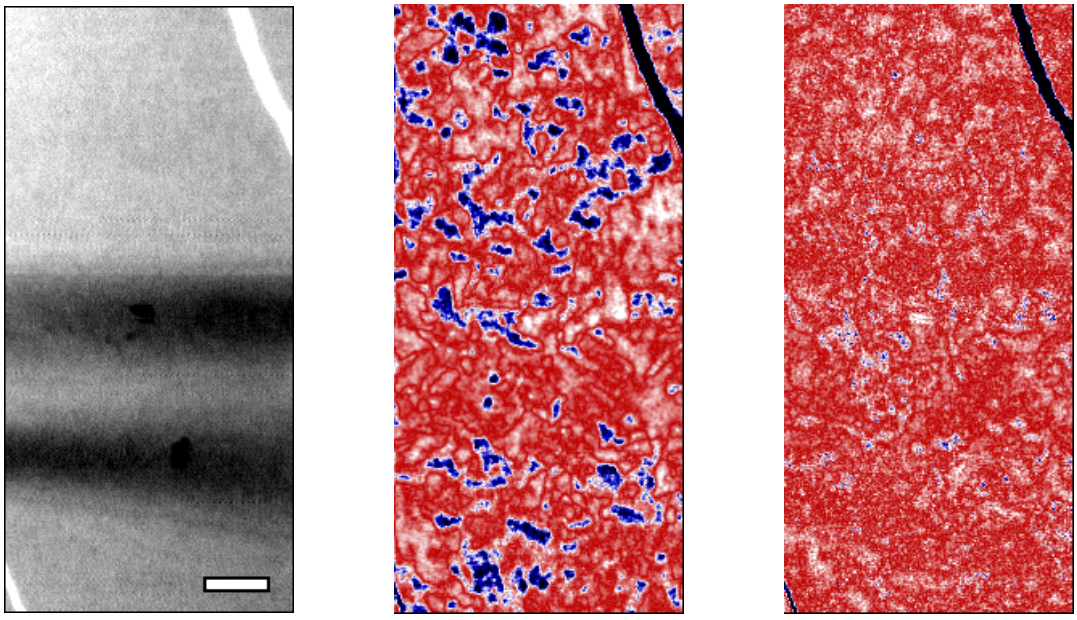

(a) Sum image **(b)** RT, $T > T_M$ **(c)** $T >> T_M$

Figure 7.6: a) Intensity image showing a membrane bend in an unbuffered membrane, with the darker regions corresponding to the steepest slope. (b,c) XMLD images across the bend at two different temperatures.

to demonstrate concretely that local variations in strain across the bend is the key factor leading to the spatial modulation of the local transition temperature observed in our films.

7.2.3 Strain across a bend in an unbuffered membrane

In order to further verify the mechanical model and to solidify the importance of the buffer layer, I studied a bend in an unbuffered membrane grown on STO, similar to the one discussed in section 5.5.1. The STXM intensity image and XMLD images taken at two different temperatures are shown in figure 7.6. Looking at these images, it is difficult to argue that there is any spatial dependence of the transition temperature. This is particularly true based on the figure taken at RT (7.6b), which is only slightly above the transition and so the spatial modulation of T_M should be apparent if there is a non-negligible local strain variation across this bend, through comparison with figures 7.2c and 7.3b. This is consistent with the discussion above, as in a membrane without the buffer layer the neutral line should sit roughly at the centre of the α-Fe_2O_3 across the entirety of the bend and therefore the average strain across the membrane thickness would be zero everywhere. This has interesting potential applications: if one wants to minimise local

fluctuations in T_M in a membrane due to inhomogeneities in the strain then that sample should be grown without a buffer layer, e.g. for transferring the membrane to a textured substrate post-growth. Alternatively, if one wants to exploit an inhomogeneous strain to locally tune T_M then the existence of the buffer layer, its thickness, and its position relative to the α-Fe_2O_3 need to be taken into account to achieve the desired strain profile.

7.2.4 Extreme bends and topological textures

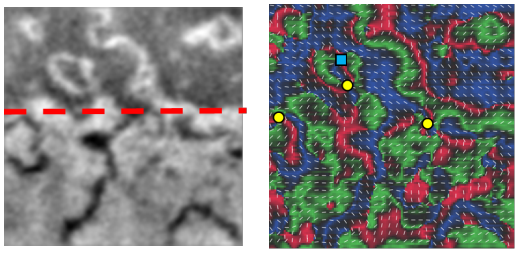

(a) XMLD image **(b)** Vector map

Figure 7.7: a) Single XMLD image and (b) vector map across a different part of same bend shown in figure 7.3, showing the trigonal domain imbalance and topological textures found on the bend. The dashed red line in (a) shows the position of steepest slope of the bend.

Most interestingly, on the top/base of the bend studied in figure 7.3 for $T >> T_M$, there seems to be no internal structure to the IP contrast, suggesting that the three trigonal domains are not equally favoured in this region. Additionally, performing a vector map of the Néel vector across a different part of the same bend (chosen to aid with the focusing procedure) at the same temperature demonstrates a strong imbalance of the relative trigonal domain fractions on top of the bend compared to at the base (figure 7.7). The dashed line in 7.7a shows the position of the steepest slope, roughly corresponding to the zero-strain position where the strain swaps from compressive to tensile based on the earlier simulations. It is clear that the blue domains are favoured at the top of the image (corresponding to the base of the bend), whereas green domains are favoured in the bottom half of the image (on top of the bend). This suggests that, in additional to local variations of the IP/OOP anisotropy, the strain has here induced an IP easy/hard axis favouring perpendicularly oriented domains on the top relative to the base of the bend. This is an interesting observation, as it opens the possibility of nucleating monodomain AFM states for $T > T_M$ by exploiting anisotropic IP strain applied to otherwise triaxial membranes to generate a uniaxial anisotropy. An additional observation that can be made based on the vector map performed on the second membrane is that topological textures (including a

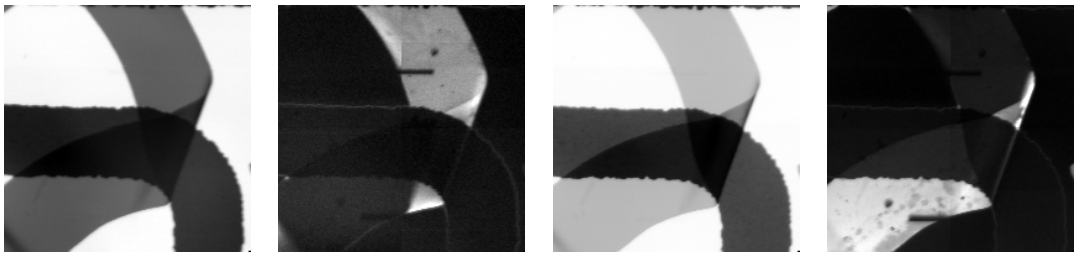

(a) Fe-edge STXM **(b)** Fe-edge TEY **(c)** La-edge STXM **(d)** La-edge TEY

Figure 7.8: a,c) normal STXM images and (b,d) surface-sensitive TEY images taken across a 180° fold at either Fe (a,b) or La (c,d) edge energies. The white/black regions in (a,c)/(b,d) are the bare Si_3N_4 holder and the arc that appears dark in all 4 images is part of the Au heater.

bimeron) are stable even in the presence of this anisotropic strain. This is encouraging for device applications, as utilising bimerons for racetrack-based storage devices require them to be stable in an otherwise uniform AFM background, such as that we would expect to stabilise with enhanced uniaxial strain.

I also demonstrated an instance of full reversal of a different membrane across a 180° fold, marking this as a region with potentially drastic strains. Some membranes prepared through the scooped method form such extreme structures serendipitously during the transfer process. This was confirmed by imaging the membrane at the Fe (711.6 eV) and La (837.4 eV) peaks using both standard STXM and TEY STXM, as shown in figure 7.8. In the TEY images, the brighter regions correspond to an increased electron emission at the chosen energy and therefore show the part of the fold that has the corresponding element (Fe or La) at the surface closest to the detector. This clearly shows that the LAO buffer layer is on top in one part of the membrane (7.8d), but the α-Fe_2O_3 is on top in an adjacent region connected by the fold (7.8b), thereby demonstrating full reversal across this fold. Unfortunately, the magnetic orientations of such 3D structures cannot be easily studied via STXM, due to the extremely small thickness of the α-Fe_2O_3 layer compared to the depth of focus of the technique. Nonetheless, this earmarks crystal membranes as an interesting test bed for exploring the effects of extreme strain in magnetic materials.

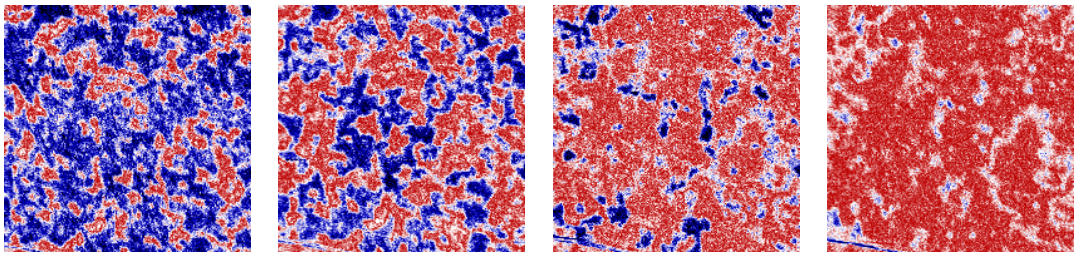

(a) 0 mbar **(b)** 100 mbar **(c)** 150 mbar **(d)** 200 mbar

Figure 7.9: STXM images of the magnetic state of a square membrane at 33 °C as a function of gas cell pressure.

7.3 Systematic Strain evolution

7.3.1 Symmetrically Applied Strain

By utilising the gas cell mounted in the STXM (described in section 4.3.1.1) and appropriately grown and transferred membranes, we can systematically vary the membrane strain in-situ whilst imaging. For these purposes, the samples were mounted on a 1x1 mm square Si_3N_4 holder via a directed transfer method (see section 4.4). This ensures that the strain is roughly homogeneous and isotropic in the plane of the sample near the centre of the square provided the flexure is not too severe. Whilst varying the pressure differential between the gas cell and the STXM vacuum to flex the membrane, I took a sequence of images of the AFM state of the system. As shown in figure 7.9, as the pressure differential between the cell and the vacuum chamber is increased with the temperature fixed at 33 °C (just below T_M for this membrane), the system passes through the Morin transition; this can only be purely due to the induced strain. This strongly indicates that the strain is tensile in nature, as it was consistently found above that tensile strain tends to suppress T_M. This is also an important milestone, constituting the first time that α-Fe_2O_3 membranes have been demonstrated to cross through the Morin transition completely athermally. Further examples of similar sweeps at fixed pressure or fixed temperature are shown in appendix B, figures B.7 and B.8 respectively. The nucleation of IP domains in each case is remarkably similar to that seen through temperature variations, signifying the underlying similarity between the two mechanisms, albeit with a varied transition temperature. Ultimately, both temperature and strain primarily affect the system by altering the ratios of the different anisotropy terms already present in the system (see figure

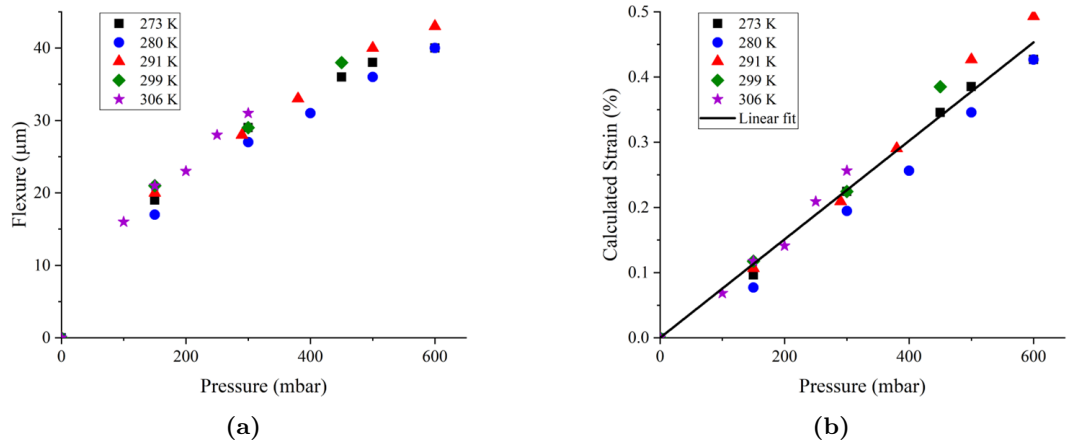

Figure 7.10: a) Measurement of the membrane flexure at the imaging position as a function of pressure at different temperatures. b) Corresponding estimated strain at the same set of temperatures and pressures, with an associated linear fit used to estimate strain values at each pressure.

1.3). Strain therefore shifts the crossover position between the otherwise roughly opposite dipolar and single-ion anisotropy terms relative to the zero-strain transition temperature.

In addition, I used the focal distance of the STXM to track the membrane flexure as a function of pressure at different temperatures, figure 7.10a. This clearly shows that the membrane flexure is roughly independent of temperature across the range used here. This characterisation was then used to estimate the percentage IP tensile strain within the membrane at each point. As presented in the original paper on the membrane flexure setup [122], a mechanical model for the radial component of the IP strain in a circular membrane gives

$$\epsilon_r = \frac{2h^2}{3r^2}, \tag{7.3}$$

where h is the deflection height at the centre of the membrane and r is the radius of the membrane. ϵ_r is the radial strain near the centre of the membrane. For our square membranes, this model likely estimates the strain accurately only close to the centre of the membrane, hence all of the measurements presented here were performed within 100 μm of the membrane centre (i.e. $<$10 % of the membrane width). By applying the formula above to the data in figure 7.10a, one can create an approximate pressure-strain calibration, which is extracted from a linear fit of the strain estimates as a function of pressure with the intercept fixed at 0, shown in figure 7.10b. Note that these strain values

are only estimates, as the material parameters of the membrane and Si_3N_4 holder may vary with temperature, leading to different deflections at a given pressure dependent on the temperature. These variations are demonstrated to be small (and at least not systematic, therefore likely the result of random errors) over the temperature range investigated here.

By varying both the temperature of the sample and the pressure differential between the gas cell and the vacuum, one can construct cross sections through the 2D temperature-strain phase space. I took a set of XMLD STXM images of a membrane along several isothermal and isobaric slices, crossing from below to above the Morin transition each time. Consistently traversing the transition in the same direction is critical to avoid the hysteresis effects inherent in the transition and the sample was cooled to at least 15 °C or lower after each set of measurements with the gas cell depressurised, which was found to be far enough below T_M in each case to fully reach the OOP state. By applying a binary filter to the normalised images based on the pixel-by-pixel intensity, I extracted the fraction of the image that was comprised of IP domains. Applying the fitted pressure-strain calibration shown in figure 7.10b allowed me to generate a phase space diagram of the magnetic state of the system as a function of temperature and strain, shown in figure 7.11.

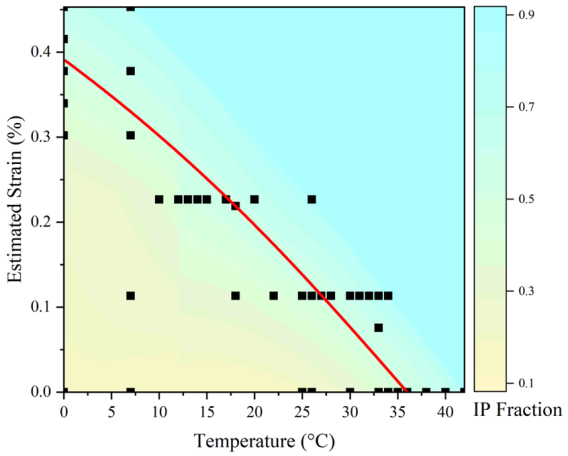

Figure 7.11: Phase diagram of the magnetic state as a function of temperature and strain.

Here, the yellow/blue colours correspond to a majority OOP/IP state. The red curve is the fitted transition temperature as a function of strain, discussed more thoroughly below and shown in detail in figure 7.13. This curve corresponds well to the area of phase space where the IP/OOP fraction is approximately 50%, defining the transition point. The data points are indicated by black squares and the values at intermediate regions are linearly interpolated from the values at the data points. The extremes of the graph are far from the transition and are set at the minimal/maximal IP fraction for simplicity, although a data point at 0 °C/0 mbar was taken. From this, it

is clear that in-situ strain applied post-growth can be used to systematically tune the transition temperature of α-Fe_2O_3 membranes. This could potentially have several specific uses, for example to fix T_M at a particularly useful value (e.g. near room temperature) post-growth in order to account for slight deviations across different membranes. It could also be used for athermal nucleation of topological textures in AFM membranes, as this was the major drawback of our KZ-like nucleation procedure (see chapter 5).

In order to demonstrate this latter point, I performed a vector map of the state of the sample at room temperature (26 °C) with the cell pressurised at 450 mbar, corresponding to an approximate strain of 0.34% and sufficient to be comfortably above the transition at this temperature. This vector map is presented in figure 7.12 and clearly shows a family of topological textures very similar to those shown earlier, e.g. in figures 5.5 and 6.8. Therefore, this serves to demonstrate that the phenomenology of the Morin transition is the same regardless of whether it is crossed through either strain or temperature. Crucially, this also provides an athermal pathway to performing a K-Z quench in α-Fe_2O_3, which is necessary for any topological texture based device architectures that one may propose.

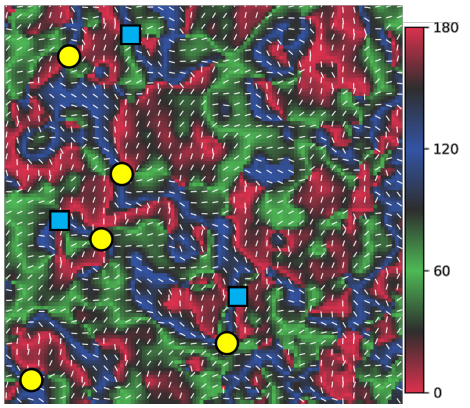

Figure 7.12: Vector map of α-Fe_2O_3 at room temperature ($T < T_M$) under 0.34% tensile strain.

It is important to further understand the interplay between temperature and strain in crossing the Morin transition. To that end, I consider a general Landau model of a first order phase transition. Close to the transition, one can perform a Taylor expansion on the free energy of the system expressed as a function of the order parameter. In the case considered here, the relevant order parameter is the sine of the angle of the Néel vector to the c-axis (θ), as this should be 0 or π for $T < T_M$ and $\pm\pi/2$ for $T > T_M$. As the system under consideration is an antiferromagnet, time reversal symmetry corresponds to exchange of the sublattices and reversal of the sign of the Néel vector angle, hence the

free energy should be symmetric under $F(\theta) \rightarrow F(-\theta)$ and so I exclude any odd-order terms from the expansion. This means that the free energy can be written as

$$F = A\sin^2(\theta) + B\sin^4(\theta) + C\sin^6(\theta) + ... \tag{7.4}$$

Here, A, B and C are phenomenological constants with values constrained by the desired form of the free energy. The highest-order term in the expansion must be strictly positive, i.e. $C > 0$, in order to get a minimum at zero for $T < T_{\mathrm{M}}$. To model a first-order transition in this formalism, I require $B < 0$. Initially, I let the coefficient A be purely temperature dependent, i.e. $A = A_0(T_{\mathrm{M}} - T)$. The details of this model are commonly included as part of a condensed matter physics or theoretical physics course, so will not be reproduced in full here. The crucial point is that one gets a first-order phase transition from $\theta = 0$ to $\theta = \pm\pi/2$ at $T = T_{\mathrm{M}}$ due to the fact that the coefficient A swaps sign at this temperature.

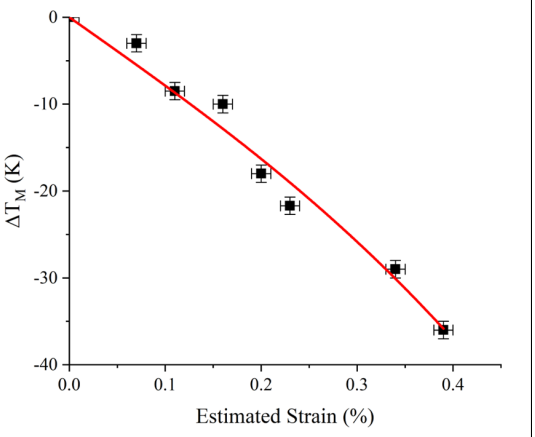

Figure 7.13: Modulation of the transition temperature T_{M} as a function of strain (black dots), along with a 3$^{\mathrm{rd}}$order fit of the function $f(\epsilon_r)$. This is the same fitted curve plotted in figure 7.11

Now, assume instead that A is a function of both the temperature and strain, namely

$$A = A_0(T_{\mathrm{M}} - f(\epsilon_r) - T), \tag{7.5}$$

where $f(\epsilon_r)$ is some general function of the radial component of the strain tensor, as relevant for the experiments conducted with square membranes in the gas cell. It's easy to see that this simple change has no real effect on the general Landau model for this phase transition, other than to effectively modulate the transition temperature, i.e. $T_{\mathrm{M}} \rightarrow T'_{\mathrm{M}} = T_{\mathrm{M}} - f(\epsilon_r)$, as seems to be the case based on the experimental data presented in figures 7.9 and 7.11 as well as the discussion in section 7.2. Without knowing the exact functional form of $f(\epsilon_r)$ not much progress can be made, but a few simple observations unveil some of its properties. Firstly, I would expect that compressive and tensile strains,

corresponding to $\epsilon_r < 0$ and $\epsilon_r > 0$ respectively, should have roughly opposite effects on the Morin transition, requiring that $f(-\epsilon_r) = -f(\epsilon_r)$. This is the consistent with the discussion in section 7.2. Secondly, I require by definition that $f(\epsilon_r = 0) = 0$, as the zero strain state corresponds exactly to the case when the Landau model should give a transition temperature at exactly T_M. Finally, for the entirety of the experiments here the strain is relatively small (<0.5%) and therefore it is reasonable to Taylor expand the function $f(\epsilon_r)$ around the zero-strain state. Given the constraints on the form of $f(\epsilon_r)$ above, I neglect all even powers of ϵ_r in the expansion, including any zero-order term, to give

$$f(\epsilon_r) = a\epsilon_r + b\epsilon_r^3 + c\epsilon_r^5 + ... \tag{7.6}$$

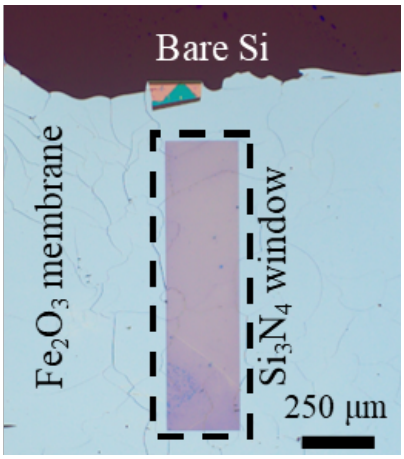

Figure 7.14: Optical image of an α-Fe_2O_3 membrane transferred onto Si with a 1 mm x 0.25 mm x 50 nm Si_3N_4 window.

As shown in figure 7.13, the above function cut off at 3rd order fits the data for the modulation of the transition temperature quite well. This data is acquired by taking each of the individual isothermal or isobaric sweeps and establishing the strain at which the in-plane domain fraction reaches 50%, linearly interpolating the data within the sweep as required. Higher-order fits are not sufficiently constrained by the data points to converge, but it is fairly clear that the strain-dependence of the transition temperature is largely linear within the range considered here. From this fit, the coefficients a and b can be extracted and can then be used with the expansion of $f(\epsilon_r)$ to create a full Landau model of this phase transition, which has all the desired behaviours. This model allows one to better understand the strain-dependent behaviour observed above and predict how to use strain to systematically tune the Morin transition, as well as the expected effects of compressive strain in the system, which are otherwise inaccessible due to the geometric constraints of the gas cell approach.

7.3.2 Anisotropic strain

In addition to the square Si_3N_4 holders, which allowed for a roughly symmetrically applied IP strain near the membrane centre, I performed a set of measurements on rectangular Si_3N_4 holders. These sample holders used were similar to those above, except with dimensions 1x0.25 mm, and with α-Fe_2O_3 membranes grown in the same batch transferred on top via the targeted approach. As a result of the different radius of curvature along the long and short axes, the strain model originally described in [122] and presented in equation 7.3 above predicts a 16x larger strain along the short axis compared to the long axis for a given membrane deflection, thereby making the strain largely uniaxial. As mentioned in section 1.1, α-Fe_2O_3 has a weak 6-fold basal plane anisotropy due to its inherent trigonal structure. I hypothesised that a uniaxial strain would distort this trigonal structure and preferentially enhance or suppress one of the anisotropy axes at the cost of the others, depending on the direction of the uniaxial strain relative to the threefold axes. This would therefore rebalance the relative domain populations towards a monodomain state. This is in addition to the modulation of T_M due to strain as discussed in detail above, which is also expected to be relevant in this case.

An example optical image of an α-Fe_2O_3 membrane transferred onto a rectangular Si_3N_4 holder is shown in figure 7.14. In order to ensure that the strain is close to uniaxial and is as large as possible, images were taken within 50μm of the centre of the membrane. The sample is below the Morin transition at room temperature (figure 7.15a) and so was first warmed to 313 K, which is above the Morin transition in this sample, in order to nucleate the usual triaxial monodomain state (figure 7.15b). A vector map of this state (figure 7.16a) shows its triaxial nature, which is further emphasised by taking a pole plot of the fitted phase (figure7.16b). These both clearly demonstrate

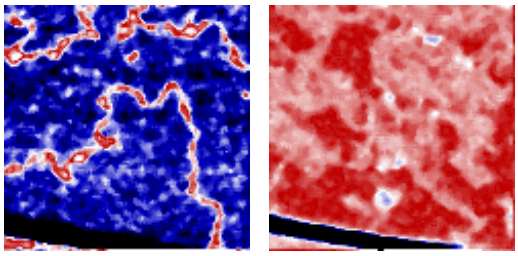

(a) 26 °C **(b)** 40 °C

Figure 7.15: STXM images of the magnetic state of the α-Fe_2O_3 membrane on a rectangular holder in an unstrained state at (a) $T < T_M$ and (b) $T > T_M$.

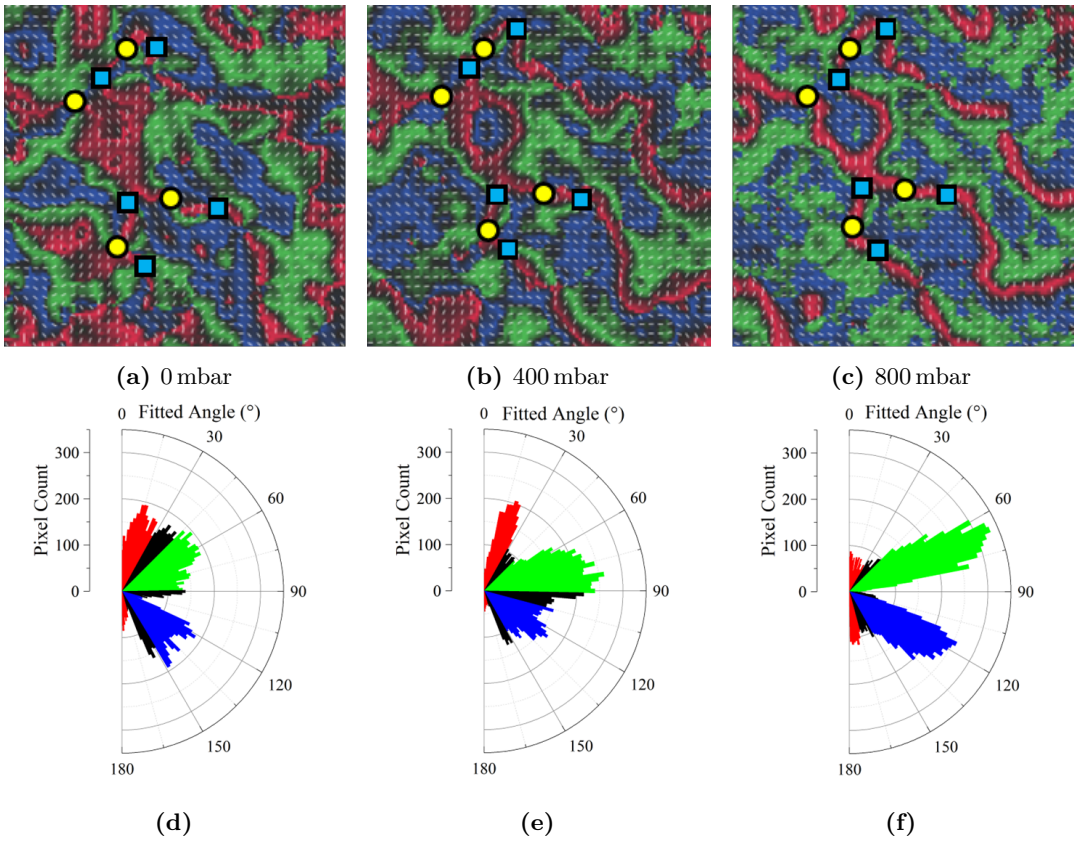

Figure 7.16: a-c) Vector maps and (d-f) corresponding pixelwise distribution of phase angle in the same region of an α-Fe_2O_3 membrane near the centre of a rectangular Si_3N_4 holder as a function of pressure.

the three preferential orientations of the Néel vector, which are rather broad due to the weakness of the basal plane anisotropy responsible for this.

Pressurising the cell flexes the sample and thereby induces a uniaxial strain as discussed above. At 400 mbar and 800 mbar, the sample flexure is 9 μm and 17 μm respectively. From the model presented in equation 7.3, this predicts that the strain along the short/long axis is 0.35%/0.022% at 400 mbar and 1.23%/0.077% at 800 mbar. Performing vector maps (figure 7.16c,e) and extracting pole plots (figure 7.16d,f) of the angular dependence at these two pressures makes the resulting uniaxial tendency clear, although the state is not fully polarised even at the highest pressure. Given that uniaxial strain does not discriminate between a domain and its time-reversed counterpart, even at extreme strains one would still expect to see domain walls separating otherwise identical domains, although these should shrink drastically at high strain values. This tendency can be seen by comparing

the images taken at 400 mbar and 800 mbar and I would expect this to continue to be true if higher strain values could be reached, noting here that this last measurement was nearly at the pressure limit of the gas cell setup ($\approx$1 bar).

The vector map at 0 mbar clearly shows an abundance of topological textures as is usually seen after performing a temperature-dependent KZ quench, with merons and antimerons indicated by yellow circles and blue squares respectively. Interestingly, these textures are robust even up to the highest strain value. Whilst the exact winding around the cores varies with strain, as some of the regions shrink while others are enhanced, the topological textures themselves remain largely fixed in space. This could be due to defect pinning, but is also likely a result of the topological protection afforded to such structures. As emphasised throughout this thesis, topologically protected structures cannot (in perfect, continuous systems) be wiped out by continuous processes, such as domain reorientation due to strain-induced anisotropy. As a crystal is not a perfect system, this topological protection is not exact, but still appears to contribute to the stability seen across the images here. This supports the proposal that topological textures could be stabilised in a largely uniform background, as required for racetrack-based device applications, by applying large strains to crystal membranes post-growth.

His job was to make sense of the world, and there were times when he wished that the world would meet him halfway.

Terry Pratchett, *Snuff*

8 Conclusions and Outlook

To finish this work I will provide a summary of the key concepts and results discussed throughout this thesis and my outlook for the field as a whole. The focus of this paper has been the study of domains and topological textures in antiferromagnetic materials, with the prototypical canted AFM α-Fe_2O_3 serving as a convenient and useful test bed for exploring their phenomenology. A large amount of space has been devoted to exploring emerging techniques for modelling and imaging AFM materials as these unveil useful pathways to investigations of other interesting materials in similar magnetic classes.

After giving a general introduction to the fields of antiferromagnets, topological structures and spintronics, I devoted chapter 2 to a thorough discussion of critical theoretical concepts. I presented derivations of the continuum forms of the most relevant magnetic energy terms, namely exchange, anisotropy, dipolar fields, and iDMI, largely following work presented in [74] and [76]. I expanded on this by demonstrating that interactions between α-Fe_2O_3 atoms within the same crystal plane (along the c-axis) do not contribute to the bulk DMI energy; however, atoms in adjacent planes belonging to different AFM sublattices do contribute and the calculated canting angle is consistent with the experimentally-derived literature values. Next, I presented my analytical calculations for the scaling of topological merons, antimerons and bimerons utilising a linear ansatz in the presence of iDMI. The main goal of this section was to gain an understanding for the scaling of AFM topological textures for comparison with micromagnetic simulations. A

calculation of resonant x-ray dichroism effects demonstrated that circular dichroism is proportional to the magnetisation of a system, whereas linear dichroism is proportional to the square of the magnetisation. This discussion is crucial to understanding the dichroic imaging techniques used for my experimental studies later in the thesis. I finished this chapter by presenting the underlying theory for the HERALDO technique, following the seminal paper on the subject [94], which is critical to understanding the advantages and drawbacks of this technique, which was implemented practically later in this thesis.

Chapter 3 is an important part of this thesis, during which a model for A-type AFMs in micromagnetics is developed and applied to the study of topological textures. After demonstrating how the continuum forms of the different energy terms from chapter 2 can be discretised for computer simulations in the micromagnetic regime, I presented my micromagnetic model with a specific focus on the application to α-Fe_2O_3. The model was verified by comparing the scaling of (anti)merons in the absence of iDMI with previous experimental data and the analytical calculations from chapter 2. The modifications of topological textures in the presence of iDMI was then studied in detail, particularly their altered scaling and the distortion caused to some textures by this chiral interaction. The stability of AFM bimerons and the possibility to stabilise the long sought-after AFM skyrmion was discussed in detail, including the phenomenological scaling of these simulated textures. Finally, a few other examples of applications of this simulation scheme were presented, including nucleating topological textures from a randomised configuration (analogous to a KZ quench), understanding the effects of grains on AFM domains, and the scaling of textures at the interface of AFM/FM heterostructures.

Next, in chapter 4 I introduced the experimental techniques used throughout the remainder of the thesis and the methodology for the growth, transfer, and characterisation of the freestanding crystal membranes necessary for their successful application. The crucial concepts there were the notion of dichroism (particularly XMLD), XAS and vector mapping techniques. I then discussed the details of the two primary experimental techniques, STXM and HERALDO, used through the rest of this thesis. The focus here was on the technical details of the implementation of these techniques, including the primary benefits, constraints, and drawbacks of each. I also discussed the key steps

in preparing samples for each. Finally I discussed the preparation of lifted α-Fe_2O_3 membranes grown on several different platforms, as developed by my collaborators. The different types of samples were found to have different defect densities, which manifested in shifted Morin transition temperatures and transition widths. These defect densities were confirmed by SAED, which also uncovered unusual moiré patterns in buffered membranes. These were explained by a lattice mismatch model, which I suggested had potential for short-lengthscale engineering of periodic structures at interfaces for ultra-thin materials.

Following this, chapter 5 explored the characterisation of the AFM states found in these novel α-Fe_2O_3 membrane samples via STXM. Here, the focus was on demonstrating the Kibble-Zurek-like phenomenology across the Morin transition for the first time on this sample type and for proving the existence of topological textures therein, which previously had only been observed in much more pristine thin films. Vector mapping of topological textures in transmission was demonstrated for the first time, with topological texture densities similar to that observed previously in thin films [11]. The defects present in these samples were found to play a large role both in the modulation of the transition and in the thermal reproducibility of the magnetic states both above and below the transition. This was emphasised by comparing three membranes grown on different substrates and with/without a buffer layer, where a greater defect density was attributed to leading to a greater amount of thermal reproducibility. Nonetheless, the KZ phenomenology was found to be more robust than previously believed, as the quenching pathway was similar in all three cases.

Chapter 6 was a slight detour. Rather than focusing on topological textures explicitly, I demonstrated that x-ray HERALDO is a promising technique for studying AFM domains in the presence of in-situ perturbations. As introduced in chapters 2 and 4, the lensless imaging technique allows for extra space in the experimental chamber that can be used to incorporate additional components. After detailing the principle difficulties with implementing HERALDO, I showed how it can be used to image AFM domains in membrane samples. The bulk of the chapter was dedicated to exploring how magnetic fields alter the energetic landscape of AFM domains, leading to domain repopulation by breaking the symmetry between otherwise indistinguishable AFM domains related by

time-reversal symmetry. Interestingly, an unconventional form of XMCD imaging was shown to give contrast between IP and OOP AFM domains in this geometry, opening up novel imaging pathways for AFM materials in scattering experiments. A pair of topological textures was identified through vector mapping and their field behaviour was demonstrated to be semi-reversible under field, serving as an interesting investigation of their robustness, which is a major advantage of topological textures in AFM systems over FMs for spintronics applications.

To finish, chapter 7 explored the effects of strain on AFM domains in crystallographic membranes. This project was initiated by the observation of bends in lifted membranes formed serendipitously post-growth during transfer onto Si_3N_4 holders. It was observed that there was a spatial modulation of the transition temperature across the membrane bend, which led to pinning of magnetic states outside of their usual thermal stability window. This spatial variation was found to depend on the relative orientation of the buffer layer and sample relative to the bend direction. A finite-element model of the strain in such membrane bends led to an understanding of the strain profiles across these bends and the associated local modulation of T_M. TEY STXM was used to demonstrate the role of the buffer layer on this strain, as well as through comparison with an unbuffered membrane. This also established crystal membranes as interesting test beds for extreme strain modulation, flexomagnetism and curvilinear magnetism. Following these experiments, I showed how the gas cell setup can be used to explore systematic strain modulation of the Morin transition. I demonstrated the first example of an athermal Kibble-Zurek quench in this system, resulting in the nucleation of a network of topological (anti)merons and bimerons. An extensive temperature-strain phase diagram was produced by taking several isothermal and isobaric measurement series. A simple Landau model of the phase transition was employed in order to explore the modulation of the transition temperature as a function of strain and predict the effects of larger strain and of compressive strain. Finally, I used rectangular Si_3N_4 holders mounted in the gas cell to study the effects of uniaxial strain on α-Fe_2O_3 applied above the Morin transition. It was found that applying this strain reorients the otherwise degenerate sixfold domains towards a pair of the trigonal axes, due to the relative orientation of the strain direction

to these axes. This process preserved topological textures nucleated during the thermal transition up to the highest pressures, indicating that strain only distorts the winding around the cores and cannot destabilise them due to their inherent topological protection.

Looking towards the future, I would like to make a few observations about the potential for topological textures in α-Fe_2O_3 (and AFMs in general) for fundamental explorations and spintronics applications. I am more sceptical than some of my colleagues on whether α-Fe_2O_3 is the ideal candidate material for topological texture based AFM spintronics. Despite being made from incredibly cheap materials, an often understated consideration for device applications, its practical drawbacks are likely to outweigh this benefit without significant advancements in material design. Among these drawbacks, I believe the insulating nature of the system is the most immediate challenge, as this hinders the control of topological textures through spin torques, which is currently how this is done in metallic FMs and how proposed racetrack devices are designed to work [28, 33]. Whilst some progress has been made in switching α-Fe_2O_3 domains through spin-orbit torque injection from a heavy-metal overlayer [63, 64], our own attempts to get this to work on systems hosting topological textures have so far been unsuccessful. Difficulties like the quality of the interface, relative thickness of the different layers and defect pinning of AFM states have prevented us from making much progress towards this goal. Additionally, whilst significant progress was made in this thesis towards an athermal method of nucleating topological textures in α-Fe_2O_3, there is still a lot of work to be done if a strain based method is to be integrated into device architectures, as this would likely have to involve ultra-small piezo based heterostructures rather than the bulky gas cell employed here.

From a fundamental perspective, I am more optimistic. One major advantage of α-Fe_2O_3 and similar AFMs is that they act as useful test-beds for investigating interesting phenomena with a broad applicability even beyond condensed matter physics. The wide family of topological textures present in this system allows them to be used productively to study the scaling properties and interactions between analogous structures; significant progress was made towards this goal through my micromagnetic modelling (chapter 3) and studies of topological textures and AFM domains in the presence of applied field and strain (chapters 6 and 7). α-Fe_2O_3 has also served to further demonstrate

the universality of the Kibble-Zurek mechanism [20–23] (in chapter 5 and elsewhere throughout). This may be interesting from a theoretical perspective, as a first-order analogue of the KZ scaling across a transition has not been studied in detail. Moreover, the similarity in the transition process whether it is crossed through temperature or strain potentially opens the door to more exotic transitions being utilised to explore these effects. Both the developments in experimental techniques and the micromagnetic model for simulating A-type AFMs presented throughout this thesis can additionally be applied to a wide array of interesting materials, some of which are progressing currently through developing discussions and collaborations, therefore constituting both a substantial and valuable contribution to the field as a whole.

Appendices

Sometimes, if you pay real close attention to the pebbles you find out about the ocean.

— Terry Pratchett, Lord and Ladies

A

Further theoretical proofs

Contents

A.1 Topological charge in 2D

During the discussion in section 1.2, I stated that if one takes the general form of the topological charge Q given in equation 1.2 and the definition of the vorticity in equation 1.3, then by also defining the polarity p of the topological texture one gets the relationship $Q = pQ_v$. Here, I will prove that this is generally true for topological textures in 2D, uncover the functional form of p and prove that (anti)merons have $Q = \pm 1/2$. I start with the general form of a circularly symmetric topological texture centred on the origin, similar to the form used to describe (anti)merons in chapter 2.

$\hat{m} = (\sin\theta\cos(\phi'), \sin\theta\sin(\phi'), \cos\theta)$ where θ is the angle to the $\hat{z}$ axis (assumed to be OOP) and $\phi' = Q_v\phi + \xi$, where Q_v is the vorticity and ξ is the helicity, as introduced in section 1.2, and ϕ is the normal azimuthal angle. I take the general equation for the topological charge (equation 1.2) and use the 2D case for the magnetisation $\hat{m}$:

$$Q = \frac{1}{4\pi}\iint \hat{m}\cdot\left(\frac{\partial\hat{m}}{\partial x}\times\frac{\partial\hat{m}}{\partial y}\right)dxdy. \tag{A.1}$$

I note at this point that the discussions herein will apply equally well to an AFM as a FM if one replaces the magnetisation $\hat{m}$ with the sublattice magnetisation or the Néel vector. Calculating the required derivatives for the general form of $\hat{m}$ is rather tedious, but many of them are similar in form to those presented in equation 2.21. Substituting these into equation A.1 and converting the carteesian coordinates to cylindrical ones gives

$$\begin{aligned} Q = \frac{1}{4\pi}\iint \begin{bmatrix}\sin\theta\cos(\phi')'\\ \sin\theta\sin(\phi')\\ \cos\theta\end{bmatrix}\cdot\left(\begin{bmatrix}\frac{\partial\theta}{\partial r}\cos\theta\cos\phi\cos\phi' + \frac{Q_v}{r}\sin\theta\sin\phi\sin\phi'\\ \frac{\partial\theta}{\partial r}\cos\theta\cos\phi\sin\phi' - \frac{Q_v}{r}\sin\theta\sin\phi\cos\phi'\\ -\frac{\partial\theta}{\partial r}\sin\theta\cos\phi\end{bmatrix}\right. \\ \left.\times\begin{bmatrix}\frac{\partial\theta}{\partial r}\cos\theta\sin\phi\cos\phi' - \frac{Q_v}{r}\sin\theta\cos\phi\sin\phi'\\ \frac{\partial\theta}{\partial r}\cos\theta\sin\phi\sin\phi' + \frac{Q_v}{r}\sin\theta\cos\phi\cos\phi'\\ -\frac{\partial\theta}{\partial r}\sin\theta\sin\phi\end{bmatrix}\right) r dr d\phi \end{aligned} \tag{A.2}$$

Fortunately, most of the terms in this vector triple product either cancel out or simplify, resulting in the final equation

$$Q = \frac{1}{2\pi}\int_0^{2\pi} Q_v\, d\phi \int_0^{\infty}\frac{1}{2}\left(\frac{\partial\theta}{\partial r}\sin\theta\right)dr. \tag{A.3}$$

Here, the first term gives an integer, the vorticity, corresponding to the number of times the phase of the texture completes a full cycle of 2π around a closed loop, as discussed in section 1.2. The second term can be trivially integrated to give

$$p = \left[\frac{1}{2}\cos\theta\right]_{r=0}^{r=\infty} = \left[\frac{1}{2}\hat{m}_z\right]_{r=0}^{r=\infty}. \tag{A.4}$$

For a skyrmion, we have that $\hat{m}_z = \pm 1$ at $r = 0$ and $\hat{m}_z = \mp 1$ at $r = \infty$, giving $p = \mp 1$ respectively. For an (anti)meron, $\hat{m}_z = \pm 1$ at $r = 0$ and $\hat{m}_z = 0$ at $r = \infty$, giving $p = \mp 1/2$. It is therefore trivial to see that $Q = p \times Q_v$ as required, and higher-order topological textures can be equivalently described with this formalism. I have also

demonstrated that the topological charge of skyrmions and (anti)merons are $Q = \pm 1$ and $Q = \pm 1/2$ respectively, which has otherwise just been stated without proof throughout.

A.2 Energy terms and analytical models

A.2.1 Spatial modulation and bulk DMI

Following the discussion in section 2.2.5, here I demonstrate that any spatial modulation between atoms in adjacent sublattices that causes them to not be exactly antiparallel does not lead to a difference in the bulk DMI energy. This not only reinforces the earlier calculations, but also serves to demonstrate that any spatially-varied magnetic structure (such as the topological textures discussed throughout) do not affect the canting angle and, conversely, the bulk DMI energy is not relevant to the stability of scaling of such textures. This justifies why this energy term was excluded from the analytical calculations and micromagnetic simulations throughout. I start with the general form of the DMI given in equation 2.14 and the form of the homogeneous DMI vector relevant for α-Fe_2O_3, i.e. $\vec{d}_{i,j} = d\hat{z}$. If I assume that any deviations due to a spatial modulation in the Néel vector orientation is small then $(\vec{S}_i \times \vec{S}_j)_z \approx \left(|S|^2 \sin(2\phi + \chi_{i,j})\right)$, where ϕ is the canting angle as before and $\chi_{i,j}$ is a small angle corresponding to the spatial variation in the Néel vector between atoms i and j. This is only valid provided the micromagnetic criterion applies, ensuring that the variation in the orientation between adjacent spins is small. Thus, the bulk DMI can be written

$$E_{bDMI}^{OOP} = \sum_{i,j} D_{i,j}|S|^2 \sin(2\phi + \chi_{i,j}) \approx \sum_{i,j} D_{i,j}|S|^2(2\phi + \chi_{i,j}), \tag{A.5}$$

where the second equation follows from the first by expanding the $\sin(2\phi + \chi_{i,j})$ function for small angles, which will be valid here. The sum can then be split into two terms. The first term directly corresponds to equation 2.18 and gives the same canting angle as calculated earlier, whereas the second needs more careful consideration. Using the expansion $\chi_{i,j} \approx |\hat{L}_i - \hat{L}_j| \approx |(\vec{r}_{i,j} \cdot \vec{\boldsymbol{\nabla}})\hat{L}|$, where $\hat{L}$ is the local Néel vector taken under a continuum approximation, allows me to expand the energy difference due to this spatial variation as

$$\delta E_{bDMI}^{OOP} = \sum_{i,j} D_{i,j} |S^2| (\vec{r}_{i,j} \cdot \vec{\boldsymbol{\nabla}}) \hat{L}. \tag{A.6}$$

In order to calculate this term, one must sum over all the position vectors for the different ions belonging to the alternate sublattice surrounding any individual atom, labelled B_1, B_2, C_1 and C_2 in figure 2.1. There are 10 such position vectors. For example, the three vectors belonging to neighbours of type B_1 are,

$$\{\vec{B_1}\} = \begin{pmatrix} a \\ 0 \\ \frac{c}{6} \end{pmatrix}, \begin{pmatrix} -\frac{a}{2} \\ \frac{\sqrt{3}a}{2} \\ \frac{c}{6} \end{pmatrix}, \begin{pmatrix} -\frac{a}{2} \\ -\frac{\sqrt{3}a}{2} \\ \frac{c}{6} \end{pmatrix}, \tag{A.7}$$

where a and c are the lattice parameters of the system. The other 7 vectors are similar in form but are excluded for brevity. It turns out that, when summing over all 10 of these lattice vectors, $(\vec{r}_{i,j} \cdot \vec{\boldsymbol{\nabla}}) = 0$ and thus such a spatial variation in the Néel vector orientation does not affect the canting angle or contribute any additional energy. I note briefly that any distortions of the system away from this ideal structure may introduce a bulk DMI contribution to the energy of spatial variations in the Néel vector, but such effects are likely to be too small to be relevant here.

A.2.2 Distortion parameters

To expand on the discussion in section 2.3.2, here I discuss some aspects of the distortion parameter formalism that was glossed over for brevity there. Recall that the distortion parameters λ, μ were introduced to modify the mapping between (x, y) space and (r, θ) space via $\lambda x = r\cos\phi$ and $\mu y = r\sin\phi$. The Jacobian is therefore given by

$$J = \begin{pmatrix} \frac{\partial x}{\partial r} & \frac{\partial x}{\partial \phi} \\ \frac{\partial y}{\partial r} & \frac{\partial y}{\partial \phi} \end{pmatrix}. \tag{A.8}$$

The 2D area element is then $dx\,dy = |J| dr\,d\phi = (r/\lambda\mu) dr\,d\phi$ and the area of the ellipse is then given by integrating this element, i.e.

$$Area = \int_0^{2\pi} \int_0^R \frac{r}{\lambda\mu}\, dr\, d\phi = \frac{2\pi R}{\lambda\mu}. \tag{A.9}$$

Therefore, I have justified the earlier statement that the condition $\lambda\mu = 1$ corresponds to all equal-R ellipses having equal area.

A.3 Wigner-Eckart Theorem

Here, I will give a brief demonstration of the Wigner-Eckart theorem needed to calculate the matrix elements relevant for electric dipole transitions in section 2.4. This is meant to be neither detailed nor exhaustive, as a full proof requires extensive details of irreducible tensor operators that are not otherwise discussed in this thesis, but rather should serve to illustrate that its application to this problem is at least valid. For a more detailed discussion, see [91] and the references therein.

Consider a k^{th} order irreducible tensor operator T^k with components T^k_q operating on a state described by basis vectors $|\tau J, M\rangle$. This results in a set of $(2k + 1)(2J + 1)$ vectors given by

$$T^k_q \,|\tau J, M\rangle \text{ with } (q = -k, -k+1, ..., +k; M = -J, -J+1, ..., +J) \tag{A.10}$$

A new state formed from a linear of combination of these vectors can be written as

$$|\tau' J', M'\rangle = \sum_{q,M} T^k_q \,|\tau J, M\rangle \,\langle JkMq \,|\, J'M'\rangle \tag{A.11}$$

where $\langle JkMq \,|\, J'M'\rangle$ is a Clebsch-Gordan coefficient introduced in section 2.4 and discussed in more detail below in section A.4 of this appendix. Rewriting this equation by using the orthogonality condition A.21 gives

$$T^k_q \,|\tau J, M\rangle = \sum_{J',M'} |\tau' J', M'\rangle \,\langle JkMq \,|\, J'M'\rangle \tag{A.12}$$

Now, acting on equation A.11 with the angular momentum raising operator $\hat{J}^+$ gives

$$\begin{aligned} \hat{J}^+ \,|\tau' J', M'\rangle = \sum_{q,M} T^k_q \,|\tau J, M\rangle \,[&\sqrt{k(k+1) - q(q-1)}\,\langle JkM(q-1) \,|\, J'M'\rangle \\ &+ \sqrt{J(J+1) - M(M-1)}\,\langle Jk(M-1)q \,|\, J'M'\rangle] \end{aligned} \tag{A.13}$$

where properties of the commutator $\left[J^+, T^k_q\right]$ have been used without proof in order to simplify this expression, see [91] for details. Applying the recursion relation A.22 to the bracketed function in the equation above gives

$$\begin{aligned} \sqrt{k(k+1) - q(q-1)}\,\langle JkM(q-1) \,|\, J'M'\rangle + \sqrt{J(J+1) - M(M-1)}\,\langle Jk(M-1)q \,|\, J'M'\rangle \\ = \sqrt{J'(J'+1) - M'(M'+1)}\,\langle JkMq \,|\, J'M'+1\rangle \end{aligned} \tag{A.14}$$

and therefore one can use equation A.11 to write

$$\hat{J}^{+}\left|\tau' J', M'\right\rangle = \sqrt{J'(J'+1) - M'(M'+1)}\left|\tau' J' M'+1\right\rangle. \tag{A.15}$$

Relations for the other angular momentum operators can be calculated in a similar way and are

$$\begin{aligned}\hat{J}^{-}\left|\tau' J', M'\right\rangle &= \sqrt{J'(J'+1) - M'(M'-1)}\left|\tau' J' M'-1\right\rangle,\\ \hat{J}^{z}\left|\tau' J', M'\right\rangle &= M'\left|\tau' J' M'\right\rangle.\end{aligned} \tag{A.16}$$

Thus $|\tau' J', M'\rangle$ are a set of standard $(2J'+1)$ angular momentum eigenfunctions connected in the usual way by angular momentum operators. Thus all scalar products of the form $\langle \tau J M \,|\, \tau' J' M'\rangle$ are all necessarily zero, except the $(2J+1)$ products $\langle \tau J M \,|\, \tau' J M\rangle$, i.e. those for which $J' = J$ and $M' = M$. Crucially, these products are entirely independent of M. The matrix elements of the operator T^k_q can then be written as

$$\left\langle \tau J M \left| T^k_q \right| \tau' J' M' \right\rangle = \sum_{J'' M''} \langle \tau J M \,|\, \tau'' J'' M''\rangle \,\langle J' k M' q \,|\, J'' M''\rangle, \tag{A.17}$$

where equation A.12 has been used to introduce a third set of angular momentum eigenfunctions that are effectively summed over. As discussed above, the products $\langle \tau J M \,|\, \tau'' J'' M''\rangle$ are zero unless the two J and M are identical, and therefore the CG coefficient on the right of the above equation is equivalent to $\langle J' k M' q \,|\, J M\rangle$. The sum over the products $\langle \tau J M \,|\, \tau'' J'' M''\rangle$ are therefore necessarily independent of M and q, and so can be written as a reduced matrix element, resulting in the standard form of the Wigner-Eckart theorem

$$\left\langle \tau J M \left| T^k_q \right| \tau' J' M' \right\rangle = \left\langle \tau J \left\| T^k \right\| \tau' J' \right\rangle \langle J' k M' q \,|\, J M\rangle. \tag{A.18}$$

A.4 Wigner 3j symbols

In this discussion I will expand on the principles of 3j symbols introduced in section 2.4, discuss their symmetry properties and demonstrate complete proofs for the values for each of the 9 3j symbols relevant for electric dipole transitions. This will let me derive the relationship between the transition rate and expectation values of the magnetisation for each transition type.

To start, I will make the relationship between CG coefficients and 3j symbols more clear. CG coefficients are introduced when converting between two alternate descriptions of angular momentum $|j_1 m_1 j_2 m_2\rangle$ and $|j_1 j_2 j m\rangle$ such that one can write [89, 90]

$$|j_1 j_2 J m\rangle = \sum_{m_1 m_2} C^{j}_{m_1 m_2} |j_1 j_2 m_1 m_2\rangle . \tag{A.19}$$

Such CG coefficients have standard orthogonality conditions due to the fact they correspond to unitary transformations [91], namely

$$\sum_{m_1,m_2} \langle j_1 j_2 m_1 m_2 \,|\, j m\rangle \langle j_1 j_2 m_1 m_2 \,|\, j' m'\rangle = \delta_{j,j'}\delta_{m,m'} \tag{A.20}$$

$$\sum_{m} \langle j_1 j_2 m_1 m_2 \,|\, j m\rangle \langle j_1 j_2 m_1' m_2' \,|\, j m\rangle = \delta_{m_1,m_1'}\delta_{m_2,m_2'}. \tag{A.21}$$

Furthermore, CG coefficients obey a set of recursion relations, namely:

$$\begin{aligned}\sqrt{j(j+1)-m(m+1)}\,\langle j_1 j_2 m_1 m_2 \,|\, J m+1\rangle = \sqrt{j_1(j_1+1)-m_1(m_1-1)}\,\langle j_1 j_2 m_1-1 m_2 \,|\, J m\rangle \\ + \sqrt{j_2(j_2+1)-m_2(m_2-1)}\,\langle j_1 j_2 m_1 m_2-1 \,|\, J m\rangle\end{aligned} \tag{A.22}$$

Wigner 3j symbols are, at their core, simply a different way of expressing CG coefficients, but in a way that brings out inherent symmetries that makes it easier to perform calculations with them. Given the general definition of a CG coefficient above, the corresponding 3j symbol is

$$C^{j}_{m_1 m_2} = (-1)^{-j_1+j_2-m}(2j+1)\begin{pmatrix} j_1 & j_2 & j \\ m_1 & m_2 & -m \end{pmatrix}. \tag{A.23}$$

As mentioned above, one of the main advantages of using 3j symbols is their inherent symmetry properties. Firstly, 3j symbols are unchanged under even permutations of the columns, but an additional phase factor is introduced under odd permutations.

$$\begin{pmatrix} j_1 & j_2 & j \\ m_1 & m_2 & -m \end{pmatrix} = \begin{pmatrix} j_2 & j & j_1 \\ m_2 & -m & m_1 \end{pmatrix} = (-1)^{j_1+j_2+j}\begin{pmatrix} j_2 & j_1 & j \\ m_2 & m_1 & -m \end{pmatrix}. \tag{A.24}$$

The other three possible permutations trivially follow from the symmetry relationships above. A similar phase factor is introduced upon inversion of the second row, i.e.

$$\begin{pmatrix} j_1 & j_2 & j \\ m_1 & m_2 & -m \end{pmatrix} = (-1)^{j_1+j_2+j}\begin{pmatrix} j_1 & j_2 & j \\ -m_1 & -m_2 & m \end{pmatrix}. \tag{A.25}$$

These two symmetry properties taken together allow one to express a large number of 3j symbols in alternate forms, which sometimes have simple closed solutions for their values.

This makes them significantly easier to work with than Clebsch-Gordan coefficients and the associated multi-dimensional lookup tables. The selection rules required for non-zero 3j symbols and standardised solutions for certain cases relevant to dipole transitions were already discussed in section 2.4. Utilising these along with the symmetry properties above, I will present a full derivation of the thermally averaged transition weight $\langle A^q_{J,J'}\rangle$ introduced in equation 2.62 for all allowed q, J'. I remind you that such symbols are directly related to the transition rate through a reduced matrix element independent of the atomic moment.

A.4.1 q=0: Linearly polarised x-rays

The case $\Delta J = 0$ was shown in section 2.4 through equations 2.60 and 2.63, so will not be reproduced here. Recall that the result was

$$\langle A^0_{J,J}\rangle = \frac{\langle m^2\rangle}{J(J+1)}. \tag{A.26}$$

Now, consider the case $\Delta J = +1$. The goal is to rearrange the 3j symbol into one of the standard forms 2.55-2.58, thereby allowing a value for the associated expectation value $\langle A^0_{J,J+1}\rangle$ to be calculated. This process is as follows:

$$\begin{pmatrix} J & 1 & J+1 \\ m & 0 & -m \end{pmatrix} = \begin{pmatrix} J+1 & J & 1 \\ -m & m & 0 \end{pmatrix} \overset{(2.56,m'=-m)}{=\!=} (-1)^{J+m-1}\left[\frac{(J+m+1)(J-m+1)}{(2J+3)(J+1)(2J+1)}\right] \tag{A.27}$$

The third term follows from the second through the standard form 2.56 and using the substitution $m \to m' = -m$, which I have indicated with "$\overset{(2.56,m'=-m)}{=\!=}$"; I will use this notation from here onwards. The absorption rate is then proportional to

$$\langle A^0_{J,J+1}\rangle = \mathcal{Z}^{-1}\sum_m (2J+3)\begin{pmatrix} J & 1 & J+1 \\ m & 0 & -m \end{pmatrix}^2 e^{-\frac{m}{\theta}} = \frac{(J+1)^2 - \langle m^2\rangle}{(J+1)(2J+1)}, \tag{A.28}$$

as stated without explicit demonstration in section 2.4. The equivalent derivation for $\Delta J = -1$ is

$$\begin{pmatrix} J & 1 & J-1 \\ m & 0 & -m \end{pmatrix} = (-1)^{2J}\begin{pmatrix} J & J-1 & 1 \\ m & -m & 0 \end{pmatrix} \overset{(2.56,J'=J-1)}{=\!=} (-1)^{3J-m-2}\left[\frac{(J+m)(J-m)}{J(2J+1)(2J-1)}\right]$$

$$\langle A^0_{J,J-1}\rangle = \mathcal{Z}^{-1}\sum_m (2J-1)\begin{pmatrix} J & 1 & J-1 \\ m & 0 & -m \end{pmatrix}^2 e^{-\frac{m}{\theta}} = \frac{J^2 - \langle m^2\rangle}{J(2J+1)}. \tag{A.29}$$

A.4.2 q=+1: Right-handed circularly polarised x-rays

The example solution $q = +1, \Delta J = 0, m' = m + 1$ was given briefly in section 2.4. Here, I will demonstrate the solution of this and the $\Delta J = \pm 1$ terms explicitly, highlighting the dependence of the transition rate on the expectation value of the magnetisation. Firstly

$$\begin{pmatrix} J & 1 & J \\ m & 1 & -m-1 \end{pmatrix} = (-1)^{2J+1} \begin{pmatrix} J & J & 1 \\ m & -m-1 & 1 \end{pmatrix} \overset{(2.57)}{=\!=} (-1)^{3J-m+1} \left[\frac{(J-m)(J+m-1)}{2J(2J+1)(J+1)} \right]$$
$$\langle A^{+1}_{J,J} \rangle = \mathcal{Z}^{-1} \sum_m (2J+1) \begin{pmatrix} J & 1 & J \\ m & 1 & -m-1 \end{pmatrix}^2 e^{-\frac{m}{\theta}} = \frac{J(J+1) - \langle m \rangle - \langle m^2 \rangle}{2J(J+1)}. \tag{A.30}$$

This was the result presented briefly in equation 2.66, now fully justified. The equivalent process for $\Delta J = +1$ is

$$\begin{pmatrix} J & 1 & J+1 \\ m & 1 & -m-1 \end{pmatrix} = \begin{pmatrix} J+1 & J & 1 \\ -m-1 & m & 1 \end{pmatrix} \overset{(2.55, m'=-m-1)}{=\!=} (-1)^{m-J} \left[\frac{(J+m+1)(J+m+2)}{(2J+3)(2J+2)(2J+1)} \right]$$
$$\langle A^{+1}_{J,J+1} \rangle = \mathcal{Z}^{-1} \sum_m (2J+3) \begin{pmatrix} J & 1 & J+1 \\ m & 1 & -m-1 \end{pmatrix}^2 e^{-\frac{m}{\theta}} = \frac{(J+1)(J+2) + (2J+3)\langle m \rangle + \langle m^2 \rangle}{(2J+2)(2J+1)}. \tag{A.31}$$

For $\Delta J = -1$, the calculation is

$$\begin{pmatrix} J & 1 & J-1 \\ m & 1 & -m-1 \end{pmatrix} = (-1)^{2J} \begin{pmatrix} J & J-1 & 1 \\ m & -m-1 & 1 \end{pmatrix} \overset{(2.55)}{=\!=} (-1)^{3J-m-2} \left[\frac{(J-m-1)(J-m)}{(2J+1)(2J)(2J-1)} \right]$$
$$\langle A^{+1}_{J,J-1} \rangle = \mathcal{Z}^{-1} \sum_m (2J-1) \begin{pmatrix} J & 1 & J-1 \\ m & 1 & -m-1 \end{pmatrix}^2 e^{-\frac{m}{\theta}} = \frac{J^2 - (2J-1)\langle m \rangle + \langle m^2 \rangle}{2J(2J+1)}. \tag{A.32}$$

A.4.3 q=-1: Left-handed circularly polarised x-rays

Finally, I will round out these calculations by performing the remaining three derivations for the final set of allowed transitions with left-handed circularly polarised light, i.e. $q = -1, \Delta J = 0, \pm 1, m' = m - 1$. All of these require exploiting the symmetry property A.25 along with permuting columns. Firstly,

$$\begin{pmatrix} J & 1 & J \\ m & -1 & -m+1 \end{pmatrix} = (-1)^{2J+1} \begin{pmatrix} J & J & 1 \\ m-1 & -m & 1 \end{pmatrix} \overset{(2.57, m'=m-1)}{=\!=} (-1)^{3J-m+2} \left[\frac{(J-m+1)(J+m)}{2J(2J+1)(J+1)} \right]$$
$$\langle A^{-1}_{J,J} \rangle = \mathcal{Z}^{-1} \sum_m (2J+1) \begin{pmatrix} J & 1 & J \\ m & -1 & -m+1 \end{pmatrix}^2 e^{-\frac{m}{\theta}} = \frac{J^2 - (2J-1)\langle m \rangle + \langle m^2 \rangle}{2J(J+1)}. \tag{A.33}$$

Then,

$$\begin{pmatrix} J & 1 & J+1 \\ m & -1 & -m+1 \end{pmatrix} = (-1)^{2J+2} \begin{pmatrix} J+1 & J & 1 \\ m-1 & -m & 1 \end{pmatrix} \overset{(2.55, m'=m-1)}{=\!=} (-1)^{J-m+2} \left[\frac{(J-m+1)(J-m+2)}{(2J+3)(2J+2)(2J+1)} \right]$$

$$\langle A^{-1}_{J,J+1} \rangle = \mathcal{Z}^{-1} \sum_m (2J+3) \begin{pmatrix} J & 1 & J+1 \\ m & -1 & -m+1 \end{pmatrix}^2 e^{-\frac{m}{\theta}} = \frac{(J+1)(J+2) - (2J+3)\langle m \rangle + \langle m^2 \rangle}{(2J+2)(2J+1)}. \tag{A.34}$$

Finally,

$$\begin{pmatrix} J & 1 & J-1 \\ m & -1 & -m+1 \end{pmatrix} = \begin{pmatrix} J & J-1 & 1 \\ -m & m-1 & 1 \end{pmatrix} \overset{(2.55, m'=-m, J'=J-1)}{=\!=} (-1)^{-J+m-2} \left[\frac{(J+m-1)(J+m)}{(2J+1)(2J)(2J+-)} \right]$$

$$\langle A^{-1}_{J,J-1} \rangle = \mathcal{Z}^{-1} \sum_m (2J-1) \begin{pmatrix} J & 1 & J-1 \\ m & -1 & -m+1 \end{pmatrix}^2 e^{-\frac{m}{\theta}} = \frac{J(J-1) + (2J-1)\langle m \rangle + \langle m^2 \rangle}{2J(2J+1)}. \tag{A.35}$$

A.5 Concepts in holography

A.5.1 Application of polynomial filters

Here, I will present a quick proof that applying a polynomial filter in Fourier space is equivalent to taking the directional derivative in real space. For a general function $f(x, y)$ and its Fourier transform $F(u, v)$, I define their relationship as:

$$f(x,y) = \iint_{-\infty}^{\infty} F(u,v) exp\left[2\pi i(ux+vy)\right] \, dudv \tag{A.36}$$

Now consider the linear polynomial multiple $u^a v^b F(u, v)$, the inverse Fourier transform of this function is

$$\begin{aligned} \mathcal{F}^{-1}\left[u^a v^b F(u,v)\right] &= \iint_{-\infty}^{\infty} u^a v^b F(u,v) exp\left[2\pi i(ux+vy)\right] \, dudv \qquad (A.37) \\ &= \iint_{-\infty}^{\infty} \frac{\partial^a}{\partial x^a} \frac{\partial^b}{\partial y^b} F(u,v) exp\left[2\pi i(ux+vy)\right] \frac{1}{(2\pi i)^{a+b}} \, dudv \\ &= \frac{1}{(2\pi i)^{a+b}} \frac{\partial^a}{\partial x^a} \frac{\partial^b}{\partial y^b} f(x,y) \end{aligned}$$

Hence, applying a polynomial filter in Fourier space is equivalent to the application of a linear differential operator in real space, up to numerical factors. It's straightforward to see that any linear differential operator can be formed by applying an appropriate sum/product of polynomial filters to the Fourier pattern before the inverse Fourier transform is performed in order to generate the real-space reconstructions.

A.5.2 Linear differential operators on cross-correlations

Here, I will prove the identity in equation 2.75, i.e. $\mathcal{L}^{(n)}\{f \otimes g\} = (-1)^n \left[f \otimes \mathcal{L}^{(n)}\{g\}\right] = \mathcal{L}^{(n)}\{f\} \otimes g$, used to derive equation 2.77. Given the definition of the cross-correlation of two generic functions f(x) and g(x) presented in equation 2.73, the application of a simple n$^{\text{th}}$ order linear differential operator on $f \otimes g$ gives

$$\begin{aligned} \mathcal{L}^{(n)}\{f \otimes g\} &= \iint \frac{\partial^n}{\partial x^n} f(x')g(x'-x)\,dx' \\ &= \iint f(x')(-1)^n \frac{\partial^n g(x'-x)}{\partial (x'-x)^n}\,dx' \\ &= (-1)^n f \otimes \mathcal{L}^{(n)}\{g\} \end{aligned} \tag{A.38}$$

This proves the first term in the above identity. The second term follows similarly by considering the alternative (but equivalent) form of the cross correlation function

$$\begin{aligned} \mathcal{L}^{(n)}\{f \otimes g\} &= \iint \frac{\partial^n}{\partial x^n} f(x'+x)g(x')\,dx' \\ &= \iint \frac{\partial^n f(x'+x)}{\partial (x'+x)^n} g(x')\,dx' \\ &= \mathcal{L}^{(n)}\{f\} \otimes g \end{aligned} \tag{A.39}$$

B
Supplementary figures

Contents

In this appendix, I will present several further images and examples of some of the key phenomena discussed throughout this thesis. As most of the important details were already discussed in the relevant chapter, the commentary here will be light. These figures are largely provided for reference only and to demonstrate that the images presented in this thesis were not just one-off occurances but are common across different samples or different regions on the same sample. This section can be skipped entirely or referred to at appropriate points during the main text.

B.1 Additional simulation images

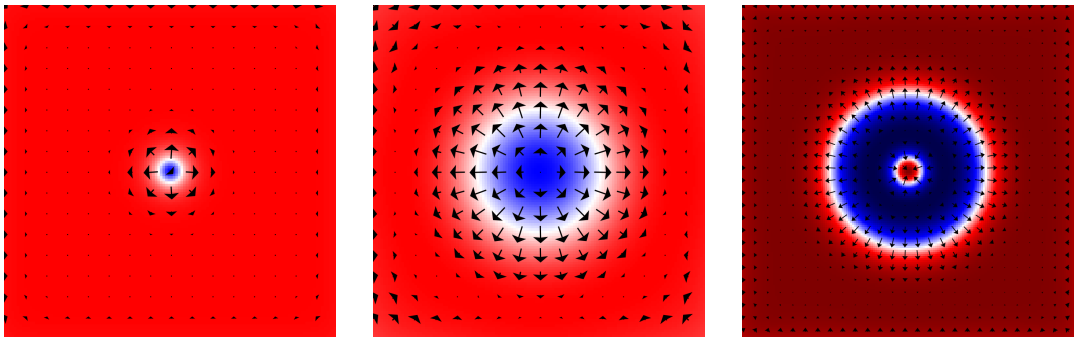

(a) Small Skyrmion **(b)** Large Skyrmion **(c)** Skyrmionium

Figure B.1: Further example skyrmion textures stabilised in my micromagnetic simulations for $T < T_{\mathrm{M}}$ in the presence of an iDMI.

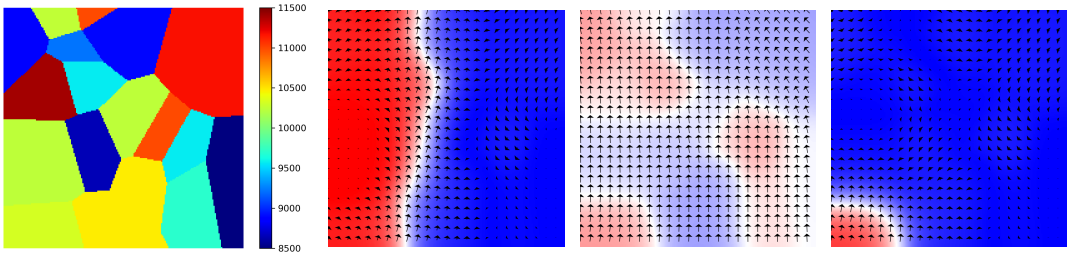

(a) **(b)** **(c)** **(d)**

Figure B.2: a) Randomly generated grain structure, with the colours giving the total anisotropy constant K_{eff} in that grain. b-d) Simulated domain structures in one of the AFM layers for the three states (b) $T < T_{\mathrm{M}}$, (c) $T > T_{\mathrm{M}}$ and (d) back to $T < T_{\mathrm{M}}$. Simulation (b) was started from a simple two-domain OOP state and (c,d) started from the end state of (b,c) respectively.

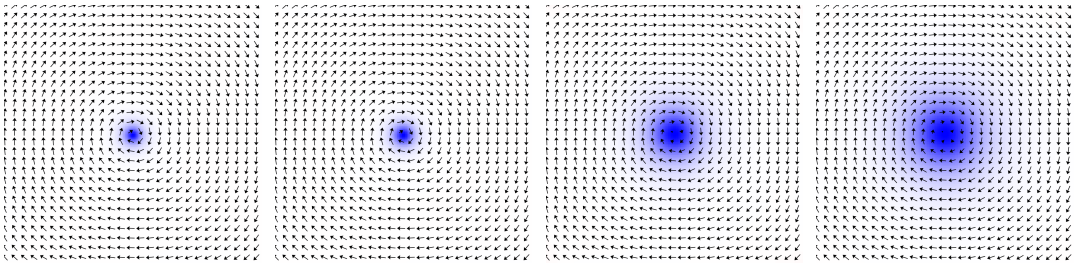

(a) **(b)** **(c)** **(d)**

Figure B.3: Further simulations of merons in an AFM/FM system showing two extreme cases from the phase diagram in figure 3.13. a,b) Weak AFM-FM exchange and strong IP FM anisotropy and (c,d) strong AFM-FM exchange and weak IP FM anisotropy.

B.2 Additional STXM images

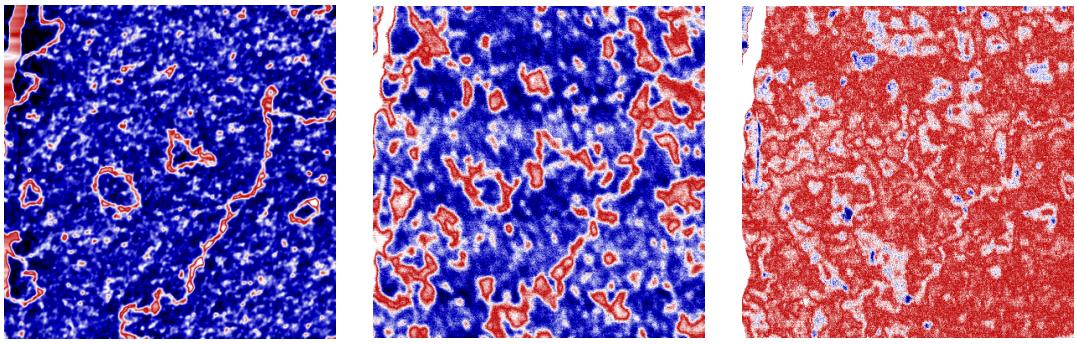

(a) 300 K **(b)** 312 K **(c)** 322 K

Figure B.4: Warming sequence taken in a 13x13 μm area at a different position on the same sample as figure 5.3 following the same colour scheme. This demonstrates that the phenomenology of the phase transition is similar across the bulk of the sample.

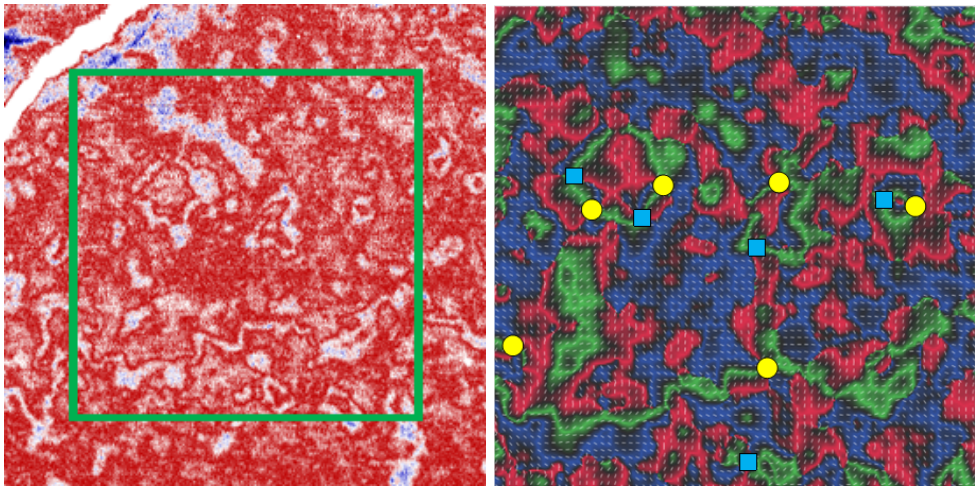

(a) XMLD image **(b)** Vector map

Figure B.5: a) XMLD image and (b) corresponding vector map taken in the boxed region shown in (a). Both images were taken at 330 K in the same area as figure B.4. This is a second example of a complete topological family, including a tightly bound bimeron, in our α-Fe_2O_3 membranes measured by STXM.

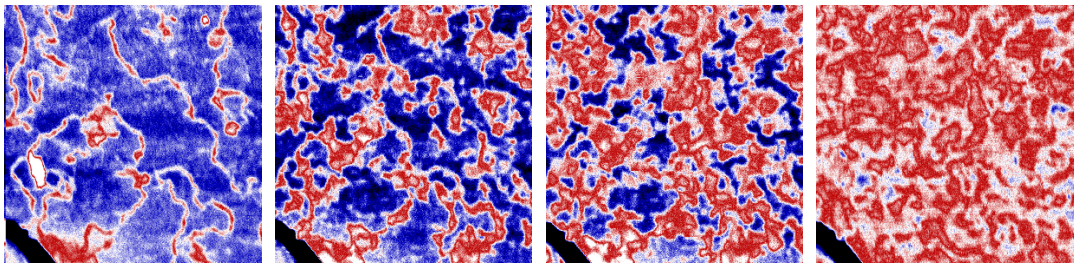

(a) 300 K **(b)** 312 K **(c)** 318 K **(d)** 335 K

Figure B.6: Warming sequence taken in a 10x10 μm area at a different position on the same sample as figure 5.10.

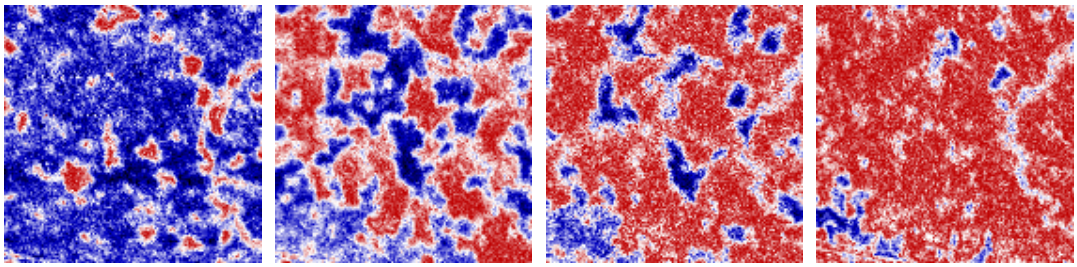

(a) 283 K **(b)** 288 K **(c)** 290 K **(d)** 293 K

Figure B.7: STXM images of the magnetic state of a square membrane at a fixed gas cell pressure of 300 mbar as a function of sample temperature.

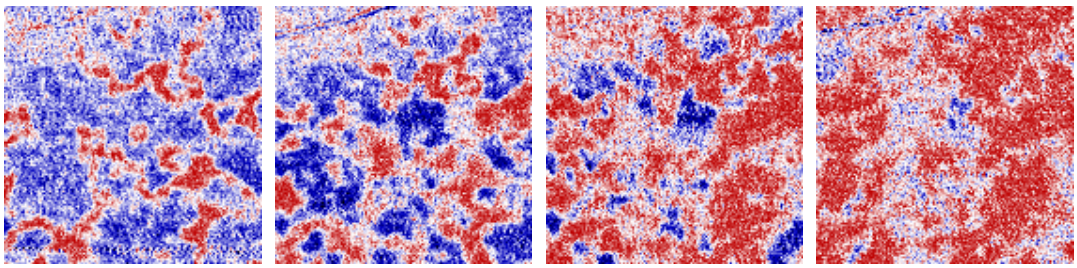

(a) 400 mbar **(b)** 500 mbar **(c)** 550 mbar **(d)** 650 mbar

Figure B.8: STXM images of the magnetic state of a square membrane at a sample temperature of 273 K as a function of gas cell pressure.

B.3 Additional HERALDO images

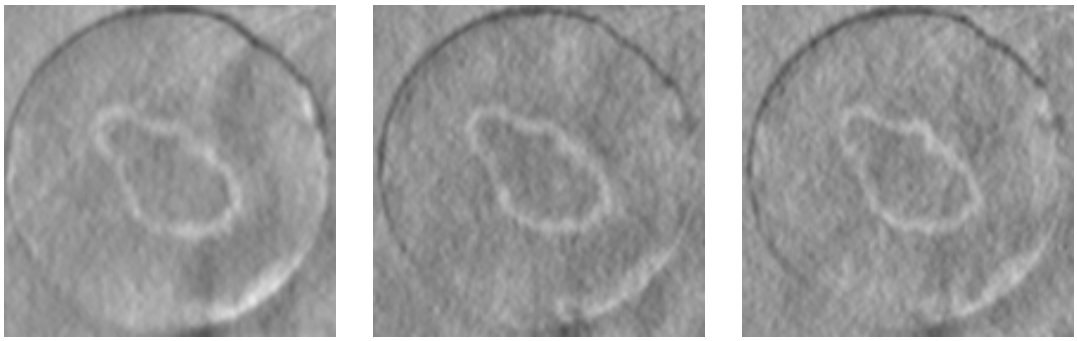

(a) **(b)** **(c)**

Figure B.9: a) XMLD image of a different closed ADW for $T < T_M$. b,c) XMCD image of the same ADW using b) circular left and c) circular right polarised x-rays.

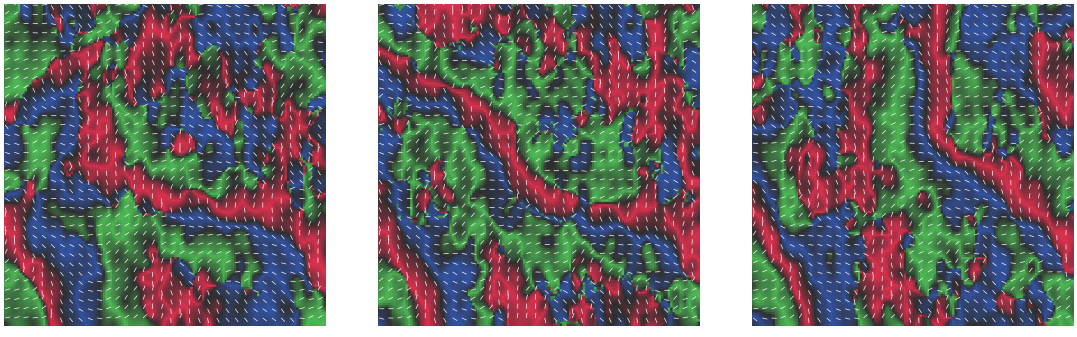

(a) 0 mT **(b)** 400 mT **(c)** 550 mT

Figure B.10: XMLD vector map images of AFM domains taken at 320 K (above T_M) at different field values at a different position but during the same field sweep as for figure 6.5.

"Don't adventures ever have an end? I suppose not. Someone else always has to carry on the story." – Bilbo Baggins

J. R. R. Tolkien *The Fellowship of the Ring*

References

[1] G. L. Verschuur. *Hidden attraction: the mystery and history of magnetism.* Oxford University Press, 1993.

[2] J. M. D. Coey. "Magnetism in future". In: *Journal of Magnetism and Magnetic Materials* 226–230 (2001), pp. 2107–2112.

[3] Alex Hubert and Rudolf Schäfer. *Magnetic domains: the analysis of magnetic microstructures.* Springer, 1998.

[4] J. M. D. Coey. *Magnetism and magnetic materials.* Cambridge Universiy Press, 2009, pp. 418–420.

[5] W. H. Bragg and W. L. Bragg. *X-ray and crystal structure.* G. Bell and Sons, London, 1924, p. 183.

[6] L. Pauling and S. B. Henricks. In: *J. Am. Chem. Soc.* 47 (1925), p. 781.

[7] C. Shull, W. Strauser, and E. Wollan. "Neutron diffraction by paramagnetic and antiferromagnetic substances". In: *Physical Review* 83 (2 1951), pp. 333–345.

[8] A. H. Morrish. *Canted Antiferromagnetism: Hematite.* World Scientific, 1994.

[9] K. Momma and F. Izumi. "VESTA 3 for three-dimensional visualization of crystal, volumetric and morphology data." In: *J. Appl. Crystallogr.* 44 (2011), pp. 1272–1276.

[10] F. J Morin. "Magnetic Susceptibility of α-Fe_2O_3 and α-Fe_2O_3 with added titanium". In: *Physical Review* 78 (6 1950), pp. 819–820.

[11] H. Jani et al. "Antiferromagnetic half-skyrmions and bimerons at room temperature". In: *Nature* 590 (7844 2021), pp. 74–79.

[12] J. Artman, J. Murphy, and S. Foner. "Magnetic anisotropy in antiferromagnetic corundum-type sesquioxides". In: *Physical Review* 138 (3A 1965), pp. 1958–1963.

[13] P. J. Besser, A. H. Morrish, and C. W. Searle. "Magnetocrystalline anisotropy of pure and doped hematite". In: *Physical Review* 153 (2 1967), pp. 632–640.

[14] E. Samuelsen and G. Shirane. "Inelastic neutron scattering investigation of spin waves and magnetic interactions in α-Fe_2O_3". In: *Physica Status Solidi* 42 (1 1970), pp. 241–256.

[15] D. I. Khomskii. *Transition Metal Compounds.* Cambridge University Press, 2014.

[16] I. Dzyaloshinsky. "A thermodynamic theory of "weak" ferromagnetism of antiferromagnetics". In: *Journal of Physics and Chemistry of Solids* 4.4 (1958), pp. 241–255.

[17] T. Moriya. "Anisotropic Superexchange Interaction and Weak Ferromagnetism". In: *Phys. Rev.* 120 (1 1960), pp. 91–98.

[18] H. Jani. "Tuning ground state of oxides via hydrogen doping to enhance functionalities." PhD thesis. National University of Singapore, 2019.

[19] H. Jani et al. "Reversible hydrogen control of antiferromagnetic anisotropy in α-Fe_2O_3". In: *Nature Communications* 12 (1 2021), p. 1668.

[20] T. W. B. Kibble. "Topology of cosmic domains and strings". In: *Journal of Physics A: Mathematical and General* 9.8 (1976), pp. 1387–1398.

[21] T. W. B. Kibble. “Some implications of a cosmological phase transition”. In: *Physics Reports* 67.1 (1980), pp. 183–199.

[22] W. H. Zurek. “Cosmological experiments in superfluid helium?” In: *Nature* 317.6037 (1985), pp. 505–508.

[23] A. del Campo and W. H. Zurek. “Universality of phase transition dynamics: topological defects from symmetry breaking”. In: *International Journal of Modern Physics A* 29.08 (2014), p. 1430018.

[24] M. Hoffmann, G. P. Müller, and S. Blügel. “Atomistic perspective of long lifetimes of small skyrmions at room temperature”. In: *Physical Review Letters* 124 (24 2020).

[25] H. Velkov et al. “Phenomenology of current-induced skyrmion motion in antiferromagnets”. In: *New Journal of Physics* 18 (7 2016), p. 075016.

[26] Laichuan Shen et al. “Current-induced dynamics and chaos of antiferromagnetic bimerons”. In: *Physical Review Letters* 124 (3 2020), p. 037202.

[27] A. S. Araújo et al. “Typical skyrmions versus bimerons: a long-distance competition in ferromagnetic racetracks”. In: *Physical Review B* 102 (2020), p. 104409.

[28] C. Back et al. “The 2020 skyrmionics roadmap”. In: *Journal of Physics D: Applied Physics* 53 (2020), p. 363001.

[29] Q. N. Meier et al. “Global formation of topological defects in the multiferroic hexagonal manganites”. In: *Physical Review X* 7 (2017), p. 041014.

[30] S. M. Griffin et al. “Scaling behaviour and beyond equilibrium in the hexagonal manganites”. In: *Physical Review X* 2 (2012), p. 041022.

[31] T. Choi et al. “Insulating interlocked ferroelectric and structural antiphase domain walls in multiferroic $YMnO_3$”. In: *Nature Materials* 9 (3 2010), pp. 253–258.

[32] T. Lancaster. “Skyrmions in magnetic materials”. In: *Contemporary Physics* 60 (3 2019), pp. 246–261.

[33] X. Zhang et al. “Skyrmion-electronics: writing, deleting, reading and processing magnetic skyrmions toward spintronic applications”. In: *Journal of Physics: Condensed Matter* 32 (14 2020), p. 143001.

[34] B. Göbel, I. Mertig, and O. A. Tretiakov. “Beyond Skyrmions: Review and perspectives of alternative magnetic quasiparticles”. In: *Physics Reports* 895 (2021), pp. 1–28.

[35] N. Gao et al. “Creation and annihilation of topological merons in in-plane magnetized films”. In: *Nature Communications* 10 (1 2019), pp. 1–9.

[36] Y. Tokura and N. Kanazawa. “Magnetic skyrmion materials”. In: *Chemical Reviews* 121 (5 2020), pp. 2857–2897.

[37] J. Harrison, H. Jani, and P. G. Radaelli. “Route towards stable homochiral topological textures in A-type antiferromagnets”. In: *Physical Review B* 105 (2022), p. 224424.

[38] M. Augustin et al. “Properties and dynamics of meron topological spin textures in the two-dimensional magnet $CrCl_3$”. In: *Nature Communications* 12 (1 2021), pp. 1–9.

[39] X. Yu et al. “Transformation between meron and skyrmion topological spin textures in a chiral magnet”. In: *Nature* 564 (2018), pp. 95–98.

[40] J. Barker and O. A. Tretiakov. “Static and dynamical properties of antiferromagnetic skyrmions in the presence of applied current and temperature”. In: *Physical Review Letters* 116 (14 2016), p. 147203.

[41] X. Zhang, Y. Zhou, and M. Ezawa. “Antiferromagnetic skyrmion: stability, creation and manipulation”. In: *Scientific Reports* 6 (1 2016), pp. 1–8.

[42] P. F. Bessarab et al. “Stability and lifetime of antiferromagnetic skyrmions”. In: *Physical Review B* 99 (14 2019), p. 140411.

[43] Robin Msiska et al. “Nonzero skyrmion Hall effect in topologically trivial structures”. In: *Phys. Rev. Appl.* 17 (2022), p. 064015.

[44] Alessandro Sala. “Imaging at the Mesoscale (LEEM, PEEM)”. In: *Springer Handbook of Surface Science*. Ed. by Mario Rocca, Talat S. Rahman, and Luca Vattuone. Springer International Publishing, 2020, pp. 387–425.

[45] F. P. Chmiel et al. “Observation of magnetic vortex pairs at room temperature in a planar α-Fe_2O_3/Co heterostructure”. In: *Nature Materials* 17 (7 2018), pp. 581–585.

[46] A. N. Bogdanov et al. “Magnetic structures and reorientation transitions in noncentrosymmetric uniaxial antiferromagnets”. In: *Phys. Rev. B* 66 (2002), p. 214410.

[47] E. G. Galkina et al. “Magnetic vortex as a ground state for micron-scale antiferromagnetic samples”. In: *Physical Review B* 81 (18 2010), p. 184413.

[48] A. Ross et al. “Structural sensitivity of the spin Hall magnetoresistance in antiferromagnetic thin films”. In: *Physical Review B* 102 (9 2020), p. 094415.

[49] Y. Cheng et al. “Evidence of the Topological Hall effect in Pt/antiferromagnetic insulator bilayers”. In: *Phys. Rev. Letters* 123 (2019), p. 237206.

[50] A. Gerber. “Interpretation of experimental evidence of the topological Hall effect”. In: *Physical Review B* 98 (2018), p. 214440.

[51] L. Tai et al. “Distinguishing the two-component anomalous Hall effect from the topological Hall effect”. In: *ACS Nano* 16 (2022), pp. 17336–17346.

[52] O. J. Amin et al. “Antiferromagnetic half-skyrmions electrically generated and controlled at room temperature”. In: *Nat. Nano.* 18 (2023), pp. 849–853.

[53] Stuart S. P. Parkin, Masamitsu Hayashi, and Luc Thomas. “Magnetic domain-wall racetrack memory”. In: *Science* 320 (2008), pp. 190–194.

[54] Z. Luo et al. “Current-driven magnetic domain-wall logic”. In: *Nature* 579 (7798 2020), pp. 214–218.

[55] A. Manchon et al. In: *Rev. Modern Phys.* 91.035004 (2019).

[56] N. Nagaosa and Y. Tokura. “Topological properties and dynamics of magnetic skyrmions”. In: *Nature Nanotechnology* 8 (2013), pp. 899–911.

[57] Hua Bai et al. “Functional antiferromagnets for potential applications on high-density storage and high frequency”. In: *J. of Appl. Phys.* 128 (21 2020), p. 210901.

[58] Takayuki Shiino et al. “Antiferromagnetic domain wall motion driven by spin-orbit torques”. In: *Physical Review Letters* 117 (8 2016), p. 087203.

[59] R. Lebrun et al. “Electrically tunable long-distance transport in crystalline antiferromagnetic iron oxide”. In: *Nature* 561 (2018), pp. 222–225.

[60] R. Lebrun et al. “Long-distance spin-transport across the Morin phase transition up to room temperature in ultra-low damping single crystals of the antiferromagnet α-Fe_2O_3”. In: *Nature Communications* 11 (2020), p. 6332.

[61] R. Lebrun et al. “Anisotropies and magnetic phase transitions in insulating antiferromagnets determined by a spin-Hall magnetoresistance probe”. In: *Communications Physics* 2 (2019), p. 50.

[62] J. Fischer et al. “Large spin Hall magnetoresistance in antiferromagnetic α-Fe_2O_3/Pt heterostructures”. In: *Phys. Rev. Applied* 13 (2020), p. 014019.

[63] Yang Cheng et al. “Electrical switching of tristate antiferromagnetic Néel order in α-Fe_2O_3 epitaxial films”. In: *Physical Review Letters* 124 (2 2020), p. 027202.

[64] Egecan Cogulu et al. “Direct imaging of electrical switching of antiferromagnetic Néel order in α-Fe_2O_3 epitaxial films”. In: *Physical Review B* 103 (10 2021), p. 100405.

[65] W. Legrand et al. “Room-temperature stabilization of antiferromagnetic skyrmions in synthetic antiferromagnets”. In: *Nature Materials* 19 (2020), pp. 34–42.

[66] X. Zhang, Y. Zhou, and M. Ezawa. “Magnetic bilayer-skyrmions without skyrmion Hall effect”. In: *Nature Communications* 7 (2016), p. 10293.

[67] L. Caretta et al. “Fast current-driven domain walls and small skyrmions in a compensated ferrimagnet”. In: *Nature Nanotechnology* 13 (2018), pp. 1154–1160.

[68] Y. Hirata et al. “Vanishing skyrmion Hall effect at the angular momentum compensation temperature of a ferrimagnet”. In: *Nature Nanotechnology* 14 (2019), pp. 232–236.

[69] D. Xiong et al. “Antiferromagnetic spintronics: an overview and outlook”. In: *Fund. Res.* 2.4 (2022), pp. 522–534.

[70] T. Jungwirth et al. “Antiferromagnetic spintronics”. In: *Nat. Nano.* 11 (2016), pp. 231–241.

[71] E. V. Gomonay and V. M. Loktev. “Spintronics of antiferromagnetic systems”. In: *Low Temp. Phys.* 40 (2014), p. 17.

[72] V. Baltz et al. “Antiferromagnetic spintronics”. In: *Rev. Mod. Phys.* 90 (2018), p. 015005.

[73] H. Yan et al. “Electric-field-controlled antiferromagnetic spintronic devices”. In: *Adv. Mat.* 32 (12 2020), p. 1905603.

[74] Amikam Aharoni. *Introduction to the theory of ferromagnetism*. Oxford Universiy Press, 1996.

[75] R. Lebrun et al. “Anisotropies and magnetic phase transitions in insulating antiferromagnets determined by a spin-Hall magnetoresistance probe”. In: *Communications Physics* 2 (1 2019), pp. 1–7.

[76] S. Rohart and A. Thiaville. “Skyrmion confinement in ultrathin film nanostructures in the presence of Dzyaloshinskii-Moriya interaction”. In: *Physical Review B* 88 (18 2013), p. 184422.

[77] J. Mulkers, B. Van Waeyenberge, and M. V. Milosević. “Effects of spatially engineered Dzyaloshinskii-Moriya interaction in ferromagnetic films”. In: *Physical Review B* 14.144401 (2017).

[78] Hongxin Yang et al. “Anatomy of Dzyaloshinskii-Moriya interaction at Co/Pt Interfaces”. In: *Physical Review Letters* 115 (26 2015), p. 267210.

[79] P. Jadaun, L. F. Register, and S. K. Banerjee. “The microscopic origin of DMI in magnetic bilayers and prediction of giant DMI in new bilayers”. In: *NPJ Computational Materials* 6.88 (2020).

[80] A. Cao et al. “Enhanced interfacial Dzyaloshinskii-Moriya interactions in annealed Pt/Co/MgO structures”. In: *Nanotechnology* 31.15 (2020).

[81] V. V. Mazurenko and V. I. Anisimov. “Weak ferromagnetism in antiferromagnets: α-Fe_2O_3 and αLa_2CuO_4”. In: *Physical Review B* 71 (2005), p. 184434.

[82] J. M. D. Coey and G. A. Sawatzky. “A study of hyperfine interactions in the system $(Fe_{1-x}Rh_x)_2O_3$ using the Mössbauer effect”. In: *Journal of Physics C: Solid State Physics* 4 (15 1971), pp. 2386–2407.

[83] P. G. Radaelli et al. “Micromagnetic modeling and imaging of vortex vertical bar meron structures in an oxide vertical bar metal heterostructure”. In: *Physical Review B* 101 (14 2020), p. 144420.

[84] G.-W. Chern, H. Youk, and O. Tchernyshyov. “Topological defects in flat nanomagnets: The magnetostatic limit.” In: *Journal of Applied Physics* 99.08Q505 (2006).

[85] H. Youk et al. “Composite domain walls in flat nanomagnets: The magnetostatic limit.” In: *Journal of Applied Physics* 99.08B101 (2006).

[86] F. Buttner, I. Lemesh, and G. S. D. Beach. "Theory of isolated magnetic skyrmions: from fundamentals to room temperature applications". In: *Scientific Reports* 8.1 (2018), p. 4464.

[87] B. T. Thole, G. Van der Laan, and G. A. Sawatzky. "Strong magnetic dichroism predicted in the $M_{4,5}$ x-ray absorption spectra of magnetic rare-earth materials". In: *Physical Review Letters* 55 (19 1985), pp. 2086–2088.

[88] G. Van der Laan and B. T. Thole. "Strong magnetic x-ray dichroism in 2p absorption spectra of 3d transition metal ions". In: *Physical Review B* 43.13401 (16 1991).

[89] B. Cagnac and J. C. Pebay-Peyroula. *Quantum theory and its applications*. The Macmillan Press, 1975.

[90] A. I. M. Rae and J. Napolitano. *Quantum Mechanics Sixth Edition*. CRC Press, 2016.

[91] A. Messiah. *Quantum mechanics volume II*. North Holland Publishing Company, 1962.

[92] I. I. Sobelman. *Atomic spectra and radiative transitions*. Springer-Verlag, 1979.

[93] G. Van der Laan and A. I. Figueroa. "X-ray magnetic circular dichroism - A versatile tool to study magnetism". In: *Coordination Chemistry Reviews* 277 (2014), pp. 95–129.

[94] M. Guizar-Sicairos and J. R. Fienup. "Holography with extended reference by autocorrelation linear differential operation". In: *Optics Express* 15 (26 2007), p. 17592.

[95] M. Guizar-Sicairos and J. R. Fienup. "Direct image reconstruction from a Fourier intensity pattern using HERALDO". In: *Optics Letters* 33 (22 2008), p. 2668.

[96] J. Chen. "Switching and imaging of magnetic structures in iron oxides". Chapter 6. PhD thesis. University of Oxford, 2023.

[97] M. J. Donahue and D. G. Porter. *OOMMF User's Guide, Version 1.0*. Interagency Report NISTIR 6376. National Institute of Standards and Technology, Gaithersburg, MD, 1999. URL: `https://math.nist.gov/oommf/oommf.html` (visited on 11/30/2022).

[98] Arne Vansteenkiste et al. "The design and verification of MuMax3". In: *AIP Advances* 4.10 (2014), p. 107133.

[99] Lukas Exl et al. "LaBonte's method revisited: an effective steepest descent method for micromagnetic energy minimization". In: *Journal of Applied Physics* 115.17 (2014), p. 17D118.

[100] Jeoroen Mulkers, Bartel Van Waeyenberge, and Milorad V. Milošević. "Effects of spatially-engineered Dzyaloshinskii-Moriya interaction in ferromagnetic films". In: *Physical Review B* 95.14 (2017), p. 144401.

[101] J. Leilaert and J. Mulkers. "Tomorrow's micromagnetic simulations". In: *Journal of Applied Physics* 125.180901 (2019).

[102] M. J. Donahue. "A variational approach to exchange energy calculations in micromagnetics". In: *Journal of Apllied Physics* 83 (1998), pp. 6491–6493.

[103] A. De Lucia et al. "Multiscale model approach for magnetization dynamics simulations". In: *Physical Review B* 94.184415 (2016).

[104] S. Park et al. "Strain control of Morin temperature in epitaxial α-Fe_2O_3(0001) film". In: *EPL* 103 (2 2013), p. 27007.

[105] Anni Coa et al. "Enhanced interfacial Dzyaloshinskii-Moriya interactions in annealed Pt/Co/MgO structures". In: *Nanotechnology* 31 (15 2020), p. 155705.

[106] Jonas De Clercq, Jonathan Leliaert, and Bartel Van Waeyenberge. "Modelling compensated antiferromagnetic interfaces with MuMax3". In: *Journal of Physics D: Applied Physics* 50 (2017), p. 425002.

[107] D. Suess et al. "Micromagnetic simulation of antiferromagnetic/ferromagnetic structures". In: *IEEE Transactions on Magnetics* 38 (5 2002).

[108] Börge Göbel et al. "Magnetic bimerons as skyrmion analogues in in-plane magnets". In: *Physical Review B* 99 (6 2019), p. 060407.

[109] Andrea De Lucia et al. "Multiscale simulations of topological transformations in magnetic-skyrmion spin structures". In: *Physical Review B* 96 (2 2017), p. 20405.

[110] L. Cai, E. M. Chudnovsky, and D. A. Garanin. "Collapse of skyrmions in two-dimensional ferromagnets and antiferromagnets". In: *Physical Review B* 86 (2 2012), p. 24429.

[111] Riccardo Hertel and Claus M. Schneider. "Exchange explosions: magnetization dynamics during vortex-antivortex annihilation". In: *Physical Review Letters* 97 (17 2006), p. 177202.

[112] S. S. P. K. Arekapudi et al. "Direct imaging of distorted vortex structures and magnetic vortex annihilation processes in ferromagnetic/antiferromagnetic disk structures". In: *Physical Review B* 103 (1 2021), p. 14405.

[113] A. O. Leonov and I. Kézsmárki. "Asymmetric isolated skyrmions in polar magnets with easy-plane anisotropy". In: *Physical Review B* 96 (1 2017), p. 14423.

[114] H. Jani, J. Harrison, et al. "Spatially reconfigurable topological textures in freestanding antiferromagnetic nanomembranes." In: *preprint arXiv:2303.03217* (2023).

[115] Y. Q. Guo et al. "Dzyaloshinskii-Moriya interaction and skyrmions in antiferromagnetic-based heterostructures". In: *Journal of Magnetism and Magnetic Materials* 170594 (2023).

[116] X. S. Wang, H. Y. Yuan, and X. R. Wang. "A theory on skyrmion size". In: *Communications Physics* 1 (1 2018), p. 1.

[117] G. S. Abo et al. "Definition of magnetic exchange length". In: *IEEE Transactions on Magnetics* 49.8 (2013), pp. 4937–4939.

[118] G. S. Abo et al. "Definition of magnetic exchange length." In: *IEEE Transactions on Magnetics* 49.8 (2013).

[119] C. Hammond. *The basics of crystallography and diffraction.* Oxford University Press, 2001.

[120] D. H. Bilderback, P. Elleaume, and E. Weckert. "Review of third and next generation synchrotron light sources". In: *Journal of Physics B* 38 (2005), S773–S797.

[121] E. Arenholz et al. "Anisotropic x-ray magnetic linear dichroism at the Fe $L_{2,3}$ edges in -Fe_3O_4". In: *Phys. Rev. B* 74 (9 2006), p. 094407.

[122] S. Finizio et al. "In situ membrane bending setup for strain-dependent scanning transmission x-ray microscopy investigations". In: *Rev. Sci. Instrum.* 87 (2016), p. 123703.

[123] S. Finizio et al. "Control of the gyration dynamics of magnetic vortices by the magnetoelastic effect". In: *Physical Review B* 96 (2017), p. 054438.

[124] N. Bukin et al. "Time-resolved imaging of magnetic vortex dynamics using holography with extended reference autocorrelation by linear differential operator". In: *Scientific Reports* 6 (2016), p. 36307.

[125] L. A. Turnbull et al. "Tilted x-ray holography of magnetic bubbles in MnNiGa lamellae". In: *ACS Nano* 15 (1 2021), pp. 387–395.

[126] P. Kuiper et al. "X-ray magnetic dichroism of antiferromagnetic Fe_2O_3: the orientation of magnetic moments observed by Fe 2p x-ray absorption spectroscopy". In: *Phys. Rev. Lett.* 70 (1993), pp. 1549–1552.

[127] *PolLux endstation homepage.* `https://www.psi.ch/en/sls/pollux`. Last accessed: 2022-12-09.

[128] F. Pfeiffer. "X-ray ptychography". In: *Nature photonics* 12 (2018), pp. 9–17.

[129] A. Sakdinawat and D. Attwood. "Nanoscale X-ray imaging". In: *Nature photonics* 4 (2010), pp. 840–848.

[130] *Silson ltd.* `https://www.silson.com/`. Last accessed: 2022-12-24.

[131] T. Huthwelker et al. “An in situ cell to study phase transitionsin individual aerosol particles on a substrate using scanning transmission x-ray microspectroscopy”. In: *Rev. Sci. Instrum.* 81 (2010), p. 113706.

[132] H. Popescu et al. “COMET: a new end-station at SOLEIL for coherent magnetic scattering in transmission”. In: *Journal of Synchrotron Radiation* 26 (1 2019), pp. 280–290.

[133] *X-ray attenuation length calculator*. `https://henke.lbl.gov/optical_constants/atten2.html`. Last accessed: 2023-09-06.

[134] P. Singh et al. “Large-area crystalline $BaSnO_3$ membranes with high electron mobilities”. In: *ACS Appl. Electron. Mater.* (1 2019), pp. 1269–1274.

[135] D. Lu et al. “Synthesis of freestanding single-crystal perovskite films and heterostructures by etching of sacrificial water-soluble layers.” In: *Nature Materials* 15 (2016), pp. 1255–1260.

[136] H. S. Kum et al. “Heterogeneous integration of single-crystalline complex-oxide membranes.” In: *Nature* 578 (2020), pp. 75–81.

[137] P. Zeller and S. Günther. “What are the possible moiré patterns of graphene on hexagonally packed surfaces? Universal solution for hexagonal coincidence lattices, derived by a geometric construction”. In: *New J. Phys.* 16 (2014), p. 083028.

[138] K. Reidy et al. “Direct imaging and electronic structure modulation of moiré superlattices at the 2D/3D interface”. In: *Nat. Comms.* 12 (2021), p. 1290.

[139] G. Gautschi. *Piezoelectric Sensorics*. Springer Berlin, 2002.

[140] N. Waterfield Price et al. “Electrical switching of magnetic polarity in a multiferroic $BiFeO_3$ device at room temperature”. In: *Physical Review Applied* 8 (2017), p. 014033.

[141] S. Manipatruni et al. “Scalable enery-efficient magnetoelectric spin-orbit logic”. In: *Nature* 565 (2019), pp. 35–42.

[142] N. A. Spaldin and R. Ramesh. “Advances in magnetoelectric multiferroics”. In: *Nature Materials* 18 (2019), pp. 203–212.

[143] G. Dong et al. “Super-elastic ferroelectric single-crystal membrane with continuous electric dipole rotation”. In: *Science* 366 (6464 2019), pp. 475–479.

[144] R. Xu et al. “Strain-induced room-temperature ferroelectricity in $SrTiO_3$ membranes”. In: *Nature Communications* 11 (2020), p. 3141.

[145] S. S. Hong et al. “Extreme tensile strain states in $La_{0.7}Ca_{0.3}MnO_3$ membranes”. In: *Science* 368 (6486 2020), pp. 71–76.

[146] Y. Ohashi, Y. Matsushima, and H. Kaiju. “Modulation of magnetic anisotropy by bending in Ni and$Ni_{78}Fe_{22}$ thin films on polycarbonate organic substrates.” In: *Journal of Magnetism and Magnetic Materials* 570.170497 (2023).

[147] H. Gomonay and V. M. Loktev. “Magnetostriction and magnetoelastic domains in antiferromagnets”. In: *Journal of Physics: Condensed Matter* 14 (2002), pp. 3959–3971.

[148] E. A. Eliseev et al. “Spontaneous flexoelectric/flexomagnetic effect in nanoferroics”. In: *Physical Review B* 79 (2009), p. 165433.

[149] V. P. Kravchuk et al. “Multiplet of skyrmion states on a curvilinear defect: reconfigurable skyrmion lattices”. In: *Physical Review Letters* 120 (2018), p. 067201.

[150] D. Makarov et al. “New dimension in magnetism and superconductivity: 3D and curvilinear nanoarchitectures”. In: *Advanced Materials* 34 (2022), p. 2101758.

[151] D. Chicot et al. “Mechanical properties of magnetite (Fe_3O_4), hematite (Fe_2O_3) and goethite (α-FeO·OH) by instrumented indentation and molecular dynamics analysis.” In: *Materials Chemistry and Physics* 129 (3 2011), pp. 862–870.

[152] A. Khan, J. Philip, and P. Hess. “Young’s modulus of silicon nitride used in scanning force microscope cantilevers”. In: *Journal of Applied Physics* 95 (2004), p. 1667.

[153] X. Luo and B. Wang. "Structural and elastic properties of $LaAlO_3$ from first-principles calculations." In: *Journal of Applied Physics* 104 (2008), p. 073518.